Novel strategies for biosensing with DNA origami and solid-state nanopores

Gayathri Mohanan

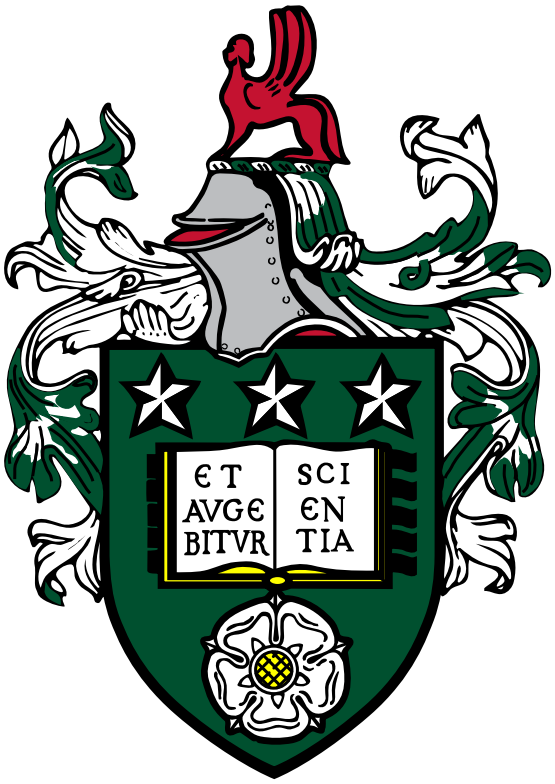

Submitted in accordance with the requirements for the degree of

Doctor of Philosophy

University of Leeds

The Pollard Institute

School of Electronic and Electrical Engineering

Bragg Centre for Materials research

July, 2025

In Loving Memory of my Father (Acha),

Mohanan

Who showed me the value of kindness and staying grounded.

Dedicated to my Mother (Amma)

Sheela

Whose unwavering support, strength and love that gave me confidence to pursue my dreams.

Intellectual Property and Publication Statements

The candidate confirms that the work submitted is their own, except where work which has formed part of jointly authored publications has been included. The contribution of the candidate and the other authors to this work has been explicitly indicated below. The candidate confirms that appropriate credit has been given within the thesis where reference has been made to the work of others.

The work in Chapter 3 of the thesis includes contents and figures that have appeared in publication as follows:

- Chau, C., Mohanan, G., Macaulay, I., Actis, P. and Wälti, C., 2024. Automated purification of DNA origami with SPRI beads. *Small*, *20*(20), p.2308776.

The work in Chapter 6 results of the thesis includes preliminary experimental work and data that led to the publication as follows:

- Confederat, S., Sandei, I., Mohanan, G., Wälti, C. and Actis, P., 2022. Nanopore fingerprinting of supramolecular DNA nanostructures. *Biophysical Journal*, *121*(24), pp.4882-4891.

I am the equally shared first author in the above stated Small publication, “Automated purification of DNA origami with SPRI beads” – I contributed equally with Chau, C., I performed the experiments and analysed the data. I also drafted the manuscript. All advisors including Macaulay, I., Actis, P. and Wälti, C., helped and provided advice throughout the process.

For the Biophysical journal publication, “Nanopore fingerprinting of supramolecular DNA nanostructures”, I am one of the co-author and I contributed to conducting the preliminary experiments that led to this work. I performed nanopore sensing and analysed data. All advisors including Actis, P. and Wälti, C., helped and provided advice throughout the process.

Abstract

Protein sensing is crucial in understanding biological processes and diagnosis of diseases as many relevant biomarkers are proteins. Sensitive and specific detection of such proteins is crucial for disease diagnosis and studying molecular interactions at nanoscale in complex biological systems. Traditional methods for such detection involves ensemble or bulk measurement which average out the output lacking sensitivity in detecting proteins that are in low abundance. Here, a sensitive biosensor based on nanopipette is developed which can detect the precise positioning of proteins on DNA origami.

DNA origami can be precisely functionalised with proteins at varying positions enabling spatial control and signal enhancement facilitating the detection of proteins which are otherwise difficult to detect. In this work, I show the specific attachment of protein binders called affimers at multiple location which are specific to the infection biomarker C-Reactive protein (CRP). For this, I have developed a DNA origami frame with a central pocket in which different combinations of affimers can be functionalised that capture CRP to observe that at least half of the origami structures are functionalised by CRP protein when captured with one or more affimers. The formation of a stable affimer-oligonucleotide conjugate is demonstrated of which the oligonucleotide is complimentary to the DNA strands in the central pocket of DNA origami.

The oligonucleotides or functional molecules like proteins are always added in excess during origami folding and functionalisation. There needs to be a strategy for removing these excess molecules to prevent their interference in downstream applications, at the same time provide high functionalisation efficiency, reduced structural damage and high yield. I have shown the use of SPRI beads, which are traditionally used in DNA sequencing, for the purification of DNA origami from excess biomolecules. I have discussed about the optimum ratio of beads to be utilised and demonstrated the successful purification of DNA origami while maintaining the structural integrity and high yield comparing with column purification.

Finally, I demonstrate the difference in the ion current signals in percentage based on the number of affimer-functionalised origami structures using nanopipette. I notice an increasing trend in the percentage of origami occupied with affimer proteins with increasing number of functionalisation. Thus, it enables the detection of precise positioning of proteins opening up possibilities of developing highly sensitive label-free sensors for biosensing.

Acknowledgement

I would like to thank my supervisors, Prof. Christoph Wälti and Dr. Paolo Actis, for their guidance and unwavering support throughout my PhD. After every supervisory meeting, I felt motivated and encouraged, which kept me excited about my work and made the entire journey deeply enjoyable. Thank you both for generously sharing your knowledge, for your thoughtful feedback on my experiments, presentations and for supporting me in every way over the past four years. You have truly been the best supervisors I could have asked for, and I have cherished every discussion and interaction with you. Christoph - Thank you for your kindness, sharing your wisdom and for always standing by me. A special thanks to Christoph for training me in the art of making the perfect cheese fondue with the "right" consistency - an unexpected but delightful skill I've picked up during my time here. Paolo - Thank you for your cool ideas, thoughtful advice and for keeping me on track throughout. A special thanks to Paolo for the kind gesture of sending me Kerala meals during my quarantine time, when I was new to the UK.

I would also like to thank Dr. Chalmers Chau for his mentorship, guidance, training and valuable feedback on my reports. I truly enjoyed working with you and learned so much from you, especially during our work on DNA origami purification. I fondly remember our lunch conversations and the cooking recipes we exchanged, in addition to origami preparation recipes. The conference trips to Germany were truly enjoyable - from trying local food to exploring new places. Importantly, thank you for 3D printing magnetic racks for me in my favourite colour and for ordering the colourful reaction tubes I so fancy.

I gratefully acknowledge Dr. Martin Walko for running the mass spectrometry experiments, and Alexander Kulak for his help with SEM measurements in the Department of Chemistry. I thank Dr. George Heath and Dr. Varun Gupta for helping me with high speed AFM measurements. I also appreciate the work of Dr. Oksana Degtjarik for running cryo-EM measurements with DNA origami. I would like to acknowledge the use of Open AI's ChatGPT and Microsoft Copilot for proofreading my thesis document.

To all my colleagues and friends in the Bioelectronics group – Virginia, Ana, Chalmers, Elena, Zijing, Tim, Ellen, Sam, Ila, George, Fabio, Eren, Dylan, Dimi, Dela, Rachel, Andreia, Parisa, Federica, Maria, and Miguel – thank you for your support. I enjoyed all our group meetings, interactions and fun lab activities. Thanks to Miguel for being a fantastic lab mate; working alongside you at the happiest place in Leeds (Miguel's clean room) and chatting during our coffee breaks was always a highlight of my day. Ana, thank you for constantly checking on me. The time you spent with us for those three months

was incredibly fun and special for me, and you've been part of my PhD journey ever since.

A heartfelt shout-out to Nizzy, who started this journey with me – thank you for always being there, through all the research and non-research ups and downs. Thanks also to Sandra and Ambili for their companionship in the past years, Vaishak and Jyothi for making me feel at home when I missed mine, Srijoni for our many fun break-time conversations, and Payal, my gym buddy. I would also like to thank my dear friends Nidhin and Ruchitha for all the wonderful holidays and road trips we've shared in the UK - those relaxing moments meant so much, and Devika, Poornendhu, Arathy, Akash, Mythili, and Neneh for celebrating my small wins even from afar.

I also extend my thanks to the PGR-representative team at school of electronic and electrical engineering - I thoroughly enjoyed organising the internal PGR conferences as a PGR rep from the Pollard Institute. My time at The Edge doing Zumba, BodyPump, and spin classes added a healthy and enjoyable rhythm to my routine, both before and after work.

To my family: My heartfelt thanks to my sister, Athira, from planning my first trip to the UK for this PhD to always surprising me with thoughtful gifts. Your advice and presence have been constant sources of support. My brother, Srigovind, thank you for encouraging me to dream big and always making sure I had what I needed to chase those dreams. Your pride in my little wins and your inspiration from childhood has meant everything. You always told me that dreams have no limit, and I still remember how you both were more excited than I was when I got this position. I would also like to thank my uncle, Anil Karamal for his positive influence and encouragement throughout my life.

To my wonderful husband, Arun - thank you for moving 5000 miles from your hometown so we could be together while I finished my PhD. You were never worried about this degree because you believed I could do it with ease, and I am still amazed by the confidence you have in me. Thank you for constantly reminding me that I am amazing, and especially for all the little surprises and thoughtful gifts that made thesis writing feel a little lighter. I would also like to thank my in-laws for their love and support.

Finally, I dedicate this degree to my mother, Sheela. Thank you for making sure that, despite every challenge, I received the best education. You gave me everything I needed to pursue my dreams, and your constant reassurance that you'd be there when things got tough gave me strength. You taught me kindness, resilience, and how to find joy even in the hardest moments - lessons that helped me through every step of this journey.

Table of Contents

Intellectual Property and Publication Statements III
Abstract V
Acknowledgement VII
Table of Contents IX
List of Figures XIII
List of Abbreviations XIX
List of Tables XX
Chapter 1 Introduction 1
Thesis Aim 4
Chapter outline 5
DNA and DNA nanotechnology 7
Deoxyribonucleic acid (DNA) 7
1.1 Structure of DNA 8
DNA Nanotechnology 12
1.2 DNA origami 17
1.2.1 DNA origami design and synthesis 20
1.2.2 DNA origami functionalisation 22
1.2.3 DNA origami purification 26
1.2.3.1 Sedimentation purification 27
1.2.3.2 Affinity purification 28
1.2.3.3 Membrane purification 29
1.2.3.4 Retention purification 29
Nanopores 32
1.3 Types of nanopores 33
1.3.1 Biological nanopores 34
1.3.2 Solid-state Nanopores 35
1.3.3 Hybrid nanopores 37
1.3.4 Glass nanopores or Nanopipettes 39
1.3.5 Properties of nanopipettes 40
1.3.5.1 Double diffuse layer (DDL) 40
1.3.5.2 Electrophoretic and electro-osmotic forces in nanopipette 41
1.3.5.3 Nanopipette fabrication 42
1.3.5.4 Nanopipette morphological characterisation 43

1.3.5.5 Nanopipette electrochemical characterisation 44
1.4 Nanopipette in Biosensing 44
1.5 Carrier molecules in Biosensing 46
1.5.1 Carrier molecules in nanopipette biosensing 47
1.6 Affimer proteins 53
1.7 Protein-oligonucleotide conjugation 55
1.8 DNA origami and nanopores in biosensing 55
1.9 Conclusion 57
Chapter 2 Materials and Methods 59
2.1 DNA origami production 59
2.1.1 4-Fold Symmetrical Tile and the biotinylated tile origami 59
2.1.1.1 Dimeric 4-Fold Symmetrical Tile 60
2.1.1.2 4-Fold Symmetrical Frame origami 60
2.1.1.3 Frame origami 60
2.1.2 DNA origami purification 60
2.1.2.1 SPRI beads selection 60
2.1.2.2 S-400 HR spin column filtration 61
2.1.3 DNA origami yield measurement 62
2.1.3.1 Absorption spectroscopy 62
2.1.4 Agarose Gel analysis 62
2.1.5 Origami-protein mixture clean up 63
2.1.5.1 SDS-PAGE analysis 63
2.1.6 Intact origami percentage calculation 64
2.1.7 Protein functionalised origami percentage calculation 64
2.2 Affimer purification 65
2.2.1 Expression of CRP affimer in E.coli 65
2.2.2 Transformation 65
2.2.3 Selection, growth and storage 66
2.2.4 CRP affimer extraction and purification 66
2.2.5 Sodium dodecyl Sulphate-Polyacrylamide Gel electrophoresis 67
2.3 Mass spectrometry 68
2.4 Surface Plasmon resonance 68
2.5 CRP functionalisation on DNA origami 69
4FSF with oligo attachment points 70
2.6 Atomic Force Microscopy (AFM) 72
2.7 Nanopore fabrication 72

2.7.1 Nanopore detection of origami monomer and tetramer.....72
2.7.2 Nanopore detection of functionalised origami.....73
2.7.3 Event Data Analysis.....74
Chapter 3 DNA origami purification using Solid phase reversible immobilisation beads (SPRI).....77
Introduction.....77
Result and Discussion.....78
3.1 DNA origami folding and purification using SPRI beads. 78
3.2 SPRI purification of protein-functionalised DNA origami.....88
Conclusion.....98
Chapter 4 Conjugation and Purification of Oligonucleotide-Protein Complexes. 101
Introduction.....101
Results and Discussion 102
4.1 Affimer purification 102
4.2 Affimer binding affinity.....105
4.3 Affimer-oligonucleotide conjugation.....106
Conclusions.....115
Chapter 5 Functionalisation of DNA origami with CRP using affimer.....117
Introduction.....117
Result and Discussion 119
5.1 Origami design.....119
5.2 Origami functionalisation with Streptavidin 121
5.3 Origami functionalisation with CRP 122
Conclusion.....128
Chapter 6 Nanopipette detection of functionalized origami 130
Introduction.....130
Results and Discussion 133
6.1 Nanopore characterisation 133
6.2 Analyte translocation through nanopipette.....137
6.2.1 Nanopore detection of origami structures.....139
6.2.2 Nanopore detection of functional origamis.....145
6.2.2.1 Detection of CRP functionalised DNA origami.....146
6.2.2.2 Detection of affimer functionalised DNA origami 151

Conclusion **164**
Chapter 7 Thesis Conclusion and Future outlook **167**
7.1 Conclusion 167
7.1.1 DNA origami purification 167
7.1.2 Protein-functionalised DNA origami carrier development 168
7.1.3 Biosensor development 168
7.2 Ongoing and Future work 169
7.2.1 Automation of SPRI purification of DNA origami 169
7.2.2 DNA origami for protein interaction study 171
7.2.3 Mechanical properties of functionalised DNA origami 177
Bibliography **180**
Chapter 8 : Appendix for Chapter 3 ..... **209**
8.1 caDNAno file 209
8.2 Quantification of intact and broken origami 213
Chapter 9 :Appendix for Chapter 4 ..... **214**
9.1 Mass Spectrometry analysis in phosphate buffer 214
9.2 SDS-PAGE analysis of purified Affimer-oligonucleotide 214
Chapter 10 :Appendix for Chapter 5 ..... **215**
10.1 caDNAno file 215
10.2 AFM Images of streptavidin functionalisation to 4FSF 216
10.3 AFM Images of CRP functionalisation to 4FSF 218
Chapter 11 :Appendix for Chapter 6 ..... **219**
11.1 SEM analysis 219
11.2 Nanopore optimisation for translocation of 4FSF origami with affimers. 220

List of Figures

Figure 1:1 Diagram of DNA published in 1953. 7
Figure 1:2 Illustration of structure of B-DNA. 9
Figure 1:3 Structure of DNA. 10
Figure 1:4 Surface representation of DNA in which bases are coloured as purple. 11
Figure 1:5 Central dogma of molecular biology. 12
Figure 1:6 A) A replicational junction. 13
Figure 1:7 Sticky ended cohesion. 14
Figure 1:8 Self-assembly of branched structures to form larger structures. 15
Figure 1:9 Motif generation by reciprocal exchange. 16
Figure 1:10 Early topological structures built from DNA. 17
Figure 1:11 Illustration of DNA origami design.. 19
Figure 1:12 DNA origami shapes. 20
Figure 1:13 DNA origami functionalisation strategies. 22
Figure 1:14 Chemical cleavage reactions on DNA origami. 24
Figure 1:15 Cysteine-Bearing Protein of Interest (POI) is conjugated to the Azide-Modified Oligo. 25
Figure 1:16 The heterobifunctional crosslinker azido-PEG3-maleimide is incubated with reduced urease. 26
Figure 1:17 Illustration of methods to purify DNA origami. 27
Figure 1:18 Magnetic beads modified with poly-T oligonucleotides 29
Figure 1:19 Assembly and purification of functionalised DNA nanostructures. 31
Figure 1:20 Illustration of nanopore set-up. 32
Figure 1:21 Illustration of nanopore set-up. 33
Figure 1:22 Illustration of types of nanopores. 33
Figure 1:23 Biological nanopores: Structure of biological nanopore with their constricted pore size 35
Figure 1:24 Fabrication of solid state nanopores 37
Figure 1:25 Illustration of hybrid nanopore set-up. 38
Figure 1:26 Hybrid nanopores 39
Figure 1:27 Schematic of electrical double layer. 41
Figure 1:28 Image of a laser puller (Sutter Instruments). 43
Figure 1:29 Image of a nanopipette filled with a red coloured solution. 44
Figure 1:30 Control and DNA translocation experiments 46
Figure 1:31 Illustration of molecular carriers used for target detection. 48

Figure 1:32 Working principle for single molecule detection of AuNP LBA/lysozyme complexes through a nanopipette. 49

Figure 1:33 Schematic representation of a DNA carrier (48.5 kbp) engineered to contain aptamer sequences 50

Figure 1:34 DNA origami carrier based biosensors. 52

Figure 1:35 AFM image of DNA origami frame used in [13]. 53

Figure 1:36 X-ray crystal structure of Adhiron92 scaffold 54

Figure 1:37 Design of DNA origami containing 8 aptamer sites for ATP binding.. . 56

Figure 2:1 Illustration of protocol used for Affimer expression, purification and characterisation. 65

Figure 2:2 Illustration of DNA origami frame 4FSF demonstrating the binding points. 71

Figure 2:3 Flow chart representing the step-wise process of bootstrapping. 75

Figure 3:1 Illustration of DNA origami with excess oligonucleotides 78

Figure 3:2 Illustration of DNA origami folding from single stranded scaffold DNA (M13mp18) and short oligonucleotides (staples) followed by purification. 79

Figure 3:3 The schematic illustration of the SPRI DNA origami purification routine.80

Figure 3:4 Purification of DNA origami using different ratio of SPRI beads,..... 81

Figure 3:5 The yield of the DNA origami measured by absorbance at A_{260}. 82

Figure 3:6 500 nm scan size AFM images of 4FST origami tiles purified using 4X, 0.8X and 0.4X ratio of SPRI beads to DNA origami. 82

Figure 3:7 AFM images of 4FST origami structures at 0.4X, 0.6X, 0.8X, 1X, 2X, 3X, and 4X ratio of SPRI beads to DNA origami volume. 83

Figure 3:8 Bar graph indicating the percentage of intact origami for different volume ratios of SPRI ranging from 0.4X to 4X ratio. 84

Figure 3:9 Agarose gel of origami structures loaded after SPRI purification at 0.8X volume ratio. 86

Figure 3:10 The impacts of thermal de-clumping step in the SPRI beads-based DNA origami purification method. 88

Figure 3:11 Schematic illustration of removal of excess protein from DNA origami using SPRI method. 89

Figure 3:12 Silver-stained SDS-PAGE gel of 1st, 2nd and 3rd round cleaned and uncleaned origami, CRP as loading control. 90

Figure 3:13 AFM images of CRP-DNA origami sample before (left) cleaning and after 1st round of SPRI bead cleaning (right). 90

Figure 3:14 AFM images of the SPRI beads purification of the 4FST to remove background CRPs. 91

Figure 3:15 Bar graph depicting the percentage of intact origamis after multiple rounds of SPRI purification of excess CRP protein from 4FST origami tiles. 92

Figure 3:16 Illustration of DNA origami purification using S-400 filtration columns. 92

Figure 3:17 Yield of DNA mass of origamis after three rounds of purification using 0.8X ratio beads and S-400 columns. 93

Figure 3:18 AFM micrographs of 4FST origami tiles purified using S-400 and SPRI bead technique. 94

Figure 3:19 Illustration of streptavidin functionalisation to DNA origami via biotinylated oligonucleotide and its purification.....95

Figure 3:20 Bar graph indicating total yield of streptavidin functionalised 4FST origami tiles purified using S-400 columns and 0.8X volume ratio SPRI beads. 97

Figure 3:21 Schematic illustration of coupling SPRI bead purification with liquid handling robot. 99

Figure 4:1 Illustration of reaction between a free thiol (-SH) and maleimide producing thiosuccinimide. 101

Figure 4:2 Illustration of oligonucleotide-affimer conjugation using maleimide chemistry. 102

Figure 4:3 SDS-PAGE analysis of affimer. 102

Figure 4:4 The mass spectra of purified CRP affimer displaying monomer peaks 104

Figure 4:5 SPR Analysis. 106

Figure 4:6 Mass spectra of affimer conjugated with 5'maleimide oligonucleotide. 107

Figure 4:7 Mass spectra of affimer in TE buffer 109

Figure 4:8 Mass spectra of affimer-5'-maleimide oligonucleotide conjugate in TE buffer. 110

Figure 4:9 Mass spectra of affimer conjugated with 3'-maleimide oligonucleotide in TE buffer. 110

Figure 4:10 Relative intensity in percentage for affimer and affimer-oligonucleotide conjugate estimated from mass spectra in different buffer conditions.....111

Figure 4:11 Mass spectra of conjugation of 22 nt long 5' maleimide oligonucleotide with cys labelled affimer. 112

Figure 4:12 SDS-PAGE gel for confirmation of conjugate formation. 113

Figure 4:13 A) Agarose gel electrophoresis of 20-nt oligo nucleotide after Ni-NTA purification. 114

Figure 5:1 AFM image of origami frame used in [13]. 117

Figure 5:2 Illustration of functionalised origami in this study. 118

Figure 5:3 DNA origami design and folding. 120

Figure 5:4 Illustration of DNA origami with 12 binding points. 121

Figure 5:5 Streptavidin modified DNA origami. 122

Figure 5:6 Functionalisation of 4FSF DNA origami using CRP. 124

Figure 5:7 CRP attachment for 1, 4 and 10 binding points in 4FSF DNA origami. 125

Figure 5:8 Bar graph demonstrating the percentage of CRP bound DNA origami 4FSF. 127

Figure 6:1 Ion current traces observed during analyte translocation through nanopores. 130

Figure 6:2 Overall aim of the study 132

Figure 6:3 Scanning electron microscopy images of two nanopipettes pulled using Program 1 (A and B), and Program 2 (C and D). 134

Figure 6:4 I-V characterisation of nanopipette.. 135

Figure 6:5 IV curve of nanopipette shown. 136

Figure 6:6 Box plot representation of resistance values measured from nanopipettes fabricated using Program 1 and Program 2. 137

Figure 6:7 Illustration of nanopore set up for analyte translocation. 138

Figure 6:8 Illustration of monomer (88 x 88 nm) and tetramer (170 x 170 nm) design of DNA origami. 139

Figure 6:9 Ion current traces of monomer tile translocation through nanopore A. without PEG, B. with PEG in electrolyte at -300 mV. 140

Figure 6:10 Scatter plot and histogram of monomer tile translocated through nanopipette with PEG in electrolyte bath. 141

Figure 6:11 Ion current traces of A. monomer tile at positive voltage, B. monomer tiles at zero voltage, C. without any analyte at negative voltage. 142

Figure 6:12 Ion current traces of 2 x 2 origami at – 500 mV A. without PEG B. with PEG in electrolyte bath. 142

Figure 6:13 Ion current traces for monomer tile (left) shaded in green colour and tetramer tiles shaded in lavender. 143

Figure 6:14 Scatter plot and histogram of monomer tile (n = 287) and 2 x 2 tile (N = 327) 144

Figure 6:15 Ion current trace of origami frame (4FSF) and respective scatter plot and histogram (plotted from 1274 events). 146

Figure 6:16 Ion current trace for 4FSF origami, 4FSF origami-Affimer and 4FSF origami-CRP recorded for 200 s. 147

Figure 6:17 Scatter plot for A) Empty 4FSF-origami with a single binding point (280 events). B) 4FSF origami + Affimer (886 events) C) 4FSF origami + Affimer + CRP (435 events) 148

Figure 6:18 Bootstrapping analysis of empty 4FSF origami, affimer-functionalised 4FSF origami and CRP-functionalised 4FSF origami. 149

Figure 6:19 Plot showing percentage of ion current peaks in each range. 150

Figure 6:20 Plot showing percentage of ion current peaks in range 1 and 2 for empty 4FSF, 4FSF + CRP, and 4FSF + 10 Affimers. 151

Figure 6:21 Illustration of 4FSF origami with A) one affimer, B) two affimers C) four affimers, D) six affimers, E) eight affimers, F) ten affimers, G) twelve affimers. 153

Figure 6:22 Raw ion current traces for 4FSF origami functionalised with A) no affimers, B) 1 affimers, C) 2 affimers, D) 4 affimers, E) 6 affimers, and F) 8 affimers, G) 10 affimers, and H) 12 affimers. 155

Figure 6:23 Scatter plot of Dwell time (ms) vs Peak amplitude (nA) 156

Figure 6:24 Ion current traces of 4FSF origami with 0, one and ten affimer binding points. 157

Figure 6:25 Graph showing percentage of origami in range 1 and range 2 for sample 4FSF + 1 Affimer translocated through two different pipettes. 158

Figure 6:26 Plot denoting the percentage of origami in range 1 and range 2.. 159

Figure 6:27 Plot denoting the percentage of origami in range 1 and range 2. 160

Figure 6:28 Percentage of origami in range 2 corresponding to increasing concentration of affimer-oligo constructs added to DNA origami with one binding point. 161

Figure 6:29 Ion current trace for origami + 1 binding point incubated with 100x excess of affimer-oligonucleotide. 161

Figure 6:30 percentage of origami in range 2 corresponding to affimer oligo excess conjugated to DNA origami with 10 binding points. 162

Figure 6:31 Percentage of origami in range 1 and range 2 for origami mixed with affimer without oligo-maleimide. 163

Figure 6:32 Percentage of origami in range 1 and range 2 for origami with complimentary strand bound to oligo binding point to affimer. 164

Figure 7:1 Illustration of liquid handling robot performing parallel purification of multiple samples of DNA origami 170

Figure 7:2 Agarose gel electrophoresis image of origami purified using SPRI technique coupled to robot. 170

Figure 7:3 AFM images of samples taken from random wells of 96 well plate spot check. 171

Figure 7:4 High speed AFM images of 4FSF-CRP captured with 4 affimers in the centre.....172

Figure 7:5 Analysis indicating preliminary evidence of resolving the subunits of CRP protein within DNA origami. 173

Figure 7:6 Exported frames from video of CRP interacting with affimer within a DNA origami frame. 174

Figure 7:7 High speed AFM images of DNA origami with CRP captured in the centre using four affimer-oligonucleotide conjugates. 176

Figure 7:8 Preliminary evidence of detection of 4FSF-CRP with 4 affimers.....178

Figure A:1 caDNAno file image of DNA origami tile used in Chapter 3 for SPRI purification study. 209

Figure A:2 AFM image of example demonstrating how counting of intact and broken origami was done. 213

Figure B:1 Mass spectra of affimer conjugate formation in 40 mM phosphate buffer. 214

Figure B:2 SDS PAGE gel of purified affimer-oligonucleotide. Lane 1 – ladder, Lane 2-6 – multiple rounds of elutions during purification. 214

Figure C:1 caDNAno image for 4FSF origami frame used for functionalisation studies. 215

Figure C:2 AFM images of 4FSF origami frame functionalised with streptavidin via four biotins. 216

Figure C:3 AFM images of 4FSF origami attached with streptavidin via 2 binding sites (2 biotins) 217

Figure C:4 Quantification of CRP bound to 4FSF origami. 218

Figure D:1 SEM images of nanopipettes pulled with different parameters. 219

List of Abbreviations

4FSF	Four fold symmetry frame
AFM	Atomic force microscopy
BP	Binding point
CEA	Carcinoembryonic antigen
CRP	C-reactive protein
Da	dalton
DMSO	Dimethyl sulfoxide
DNA	Deoxyribonucleic acid
EDTA	Ethylenediaminetetraacetic acid
ELISA	Enzyme linked immunosorbent assay
kbp	kilo basepair
MWCO	molecular weight cut-off
Ni-NTA	Nickel-nitrilotriacetate
nM	nanomolar
nt	nucleotide
PBS	Phosphate buffered saline
PEG	Polyethylene glycol
SDS-PAGE	Sodium dodecyl sulfate-Polyacrylamide gel electrophoresis
SEM	Scanning electron microscopy
SPR	Surface plasmon resonance
SPRI	Solid phase reversible immobilisation
TCEP	Tris(2-carboxyethyl) phosphine
TE	Trisacetate-EDTA

List of Tables

Table 2-1 SPRI volume ratio for DNA origami purification. 61

Table 2-2: composition of SDS gel 67

Table 2-3 Universal binding strands for DNA origami functionalisation 70

Table 2-4 Sequence of affimer plug. 70

Table 2-5 Combination of binding points for achieving multiple points of functionalisation on DNA origami. 71

Table 2-6 Table with parameters for pulling nanopipettes. 72

Table 2-7 Parameters for pulling nanopipettes 73

Table 3-1 Table indicating the percentage of intact origami for different volume ratio of SPRI beads. 84

Table 3-2 Table indicating the percentage of intact origami for different designs after 0.8X SPRI bead purification. 86

Table 3-3 The quantification of streptavidin functionalised origami from AFM images for S-400 filtration and 0.8X SPRI method. 97

Table 4-1 Computed theoretical parameters for CRP affimer using Expasy ProtParam [302]. 104

Table 5-1 Percentage of CRP-bound origami quantified from AFM images 127

Table 6-1 Parameters used for pulling nanopipette with program 1 133

Table 6-2 Parameters used for pulling nanopipette with program 2. 133

Table D-1 Pulling Parameters for nanopipette. 219

Table D-2 Changes in the heat parameter in line 2 for producing different size of nanopores. 220

Table D-3 Table representing the different programs used for optimisation of right nanopore for discrimination of number of affimers. 220

Table D-4 Table representing the parameters for program no. 64. 220

Table D-5 Table representing the parameters used for pulling nanopipettes with different programs. The pull time is shown in column 3, resistance in 0.1 M KCl in column 4, and resistance in 50% 35K PEG, 0.1 M KCl in column 5. 221

Table D-6 Table demonstrating the percentage of origami in range 1 and 2 for the same construct (4FSF + 10 Affimers) translocated through nanopores pulled with different parameters. 222

Chapter 1 Introduction

Proteins are essential biomolecules in living systems, playing a fundamental role in regulating various molecular mechanisms. The upregulation or downregulation of proteins can alter metabolic pathways, leading to disease. Composed of amino acids, proteins adopt a hierarchical structure—primary, secondary, tertiary, and quaternary - each contributing to their functional activity [1]. Various biophysical and biochemical methods are employed to analyse protein structure and composition. Techniques such as X-ray crystallography, NMR spectroscopy, and mass spectrometry provide structural insights; however, they offer only ensemble averages and require large protein concentrations, which poses challenges in clinical settings [2]. Conventional biochemical assays such as ELISA are widely used in clinical diagnostics to quantify cumulative protein interactions but provide only ensemble-average measurements [3]. While ELISA is considered as a simple, scalable and quantitative method, it lacks the ability to resolve molecular heterogeneity or dynamic interactions at single molecule level. In contrast, single-molecule techniques have emerged as powerful tools for studying individual protein molecules and their dynamic interactions in real time [4]. These approaches offer unprecedented sensitivity and resolution, paving the way for protein-based molecular diagnostics with applications in both research and clinical settings. Single molecule protein detection techniques such as optical or magnetic tweezers and atomic force microscopy can detect the folding and unfolding of proteins and protein-ligand interaction by an external applied force [5]. AFM technique consist of a probe embedded on a cantilever which deflects in response to interaction between tip and sample due to attractive and repulsive forces allowing the study of biological molecules with 1-10 nm resolution [6].

A technique in the forefront of single molecule sensing is the nanopore technology. A nanopore sensor is composed of a nanometre sized pore embedded within a membrane separating two compartments filled with an electrolyte solution. These compartments are fitted with electrodes which produce a current when a voltage is applied due to the flow of ions in solution. If no analyte is present, the measured current depends only on the size, geometry and surface chemistry of the nanopore while the flow of the ions is obstructed when a biomolecule is electrophoretically pulled through the pore from one compartment to other due to applied voltage. This generates ion current blockages, the characteristics of which define the properties of the analyte. This method provides enhanced sensitivity at single molecule level enabling detection and quantification of proteins in solution, analysing the charge and size, and monitoring binding interaction between protein and a ligand.

Nanopore sensors are used for biomolecule detection due to their single molecule sensitivity, label-free and high-throughput real time detection. DNA detection using nanopores is well-established and has been further extended to detect other biomolecules, including proteins. Unlike DNA which has a uniform structure and high negative charge, proteins offer complexity in terms of structure and charge making them challenging candidate for analysis using nanopipettes. The size of the analyte need to be comparable with the size of the nanopore to yield a good signal-to-noise ratio to get a large ion current signal. Proteins are typically 2-10 nm in size hence an ideal pore size of a sensor should be in the same range. Proteins with smaller size and heterogenous charge fails to give good signal-to-noise ratio resulting in smaller peaks too small to detect using glass nanopores. Moreover, single, unbound proteins pass too quickly through the nanopore often making them undetectable [7]. It has been reported previously that the use of DNA carriers attached to proteins can help in improving signal to noise ratio while detecting proteins. DNA provides a uniform negative charge to the conjugate enabling controlled movement enhancing the ion current signals specific to proteins [8].

DNA has unique base pairing properties enabling self-assembly which has been utilised in DNA nanotechnology to generate programmable nanostructures called DNA origami. DNA origami utilised self-assembly of scaffold and short staple strands to fold into the designed scaffold route at set temperature [9]. DNA origami can be an ideal candidate to target proteins because of their massive size and negative charge enabling high signal to noise ratio. DNA origami is widely used for functionalising biomolecules due to its engineerability and has been used for applications like biosensing, studying enzyme cascades and drug delivery [10-12]. It has been previously reported that C-reactive protein (CRP) can be attached to DNA origami, producing large ion current signals during translocation through nanopores, thereby enabling its detection, which would otherwise be difficult [13]. This approach utilised molecular DNA-based binder molecule called aptamers specific to CRP protein incorporated into DNA origami enabling site-specific attachment of CRP protein. Though aptamers are excellent candidate for biosensing due to its high specificity and smaller size, they are prone to degradation and difficult to synthesise in large scale [14, 15]. Therefore, there needs to be a better molecular binder which offers ease of synthesis, stability and diverse range of targets. Protein based molecular binders are gaining importance due to its ease of production and ability to produce diverse range of binders against various targets.

Functionalised origami structures have gained prominence in protein biosensing, offering precise control over biomolecule attachment, which facilitates highly sensitive and specific protein detection. Origami structures are used to detect biomarkers previously

at single molecule level as they can capture individual molecule per structure especially at low concentrations [13]. Functionalised DNA origami structures can be immobilised on mica substrate and subsequently detected using atomic force microscopy [16]. However, the excess oligo or functional molecules while folding and functionalising origami could interfere with the characterisation. Though there are several methods established for DNA origami purification, they require tedious procedures, handling times and could disintegrate the origami structures resulting in low yields.

There needs to be reliable and sensitive nanopore strategy capable of protein sensing, and the question here is how can small proteins be detected with high resolution at single molecule level. A strategy needs to be implemented for functionalising proteins on nanostructures if they are to be used as carriers for protein detection in combination with nanopore technology. For that, a stable design of DNA origami is required, and should be characterised well. Moreover, functionalisation should not mean the excess of molecules would interfere with characterisation. Therefore, an efficient purification method for DNA origami should be established that give high functionalisation yield, at the same time, remove background materials.

Recent advancements in nanopore technology have enabled reliable analysis of DNA and RNA, but protein sequencing remains a major challenge due to the structural complexity and functional diversity of proteins. Proteins play central roles in cellular processes and serve as critical biomarkers for early diagnosis, prognosis, and monitoring of therapeutic responses. Sensitive, rapid, and selective protein detection is therefore increasingly important for both healthcare and personalized medicine.

Building on strategies such as the DNA origami-assisted nanopore sensing proposed by Raveendran et al., which enabled selective capture and detection of CRP at picomolar concentrations, this work aims to develop a nanopore-based protein biosensing platform using a four-fold symmetry DNA origami frame (4FSF) functionalized with affimer proteins as high-affinity CRP binders. This platform leverages the structural stability of the origami frame and the specificity of protein binders to investigate single-molecule capture and translocation events, with enhanced signal-to-noise ratios achieved via PEG-modified electrolytes. The approach seeks to address the challenges of detecting low-abundance proteins with high sensitivity and specificity.

Thesis Aim

This thesis aims to develop a DNA origami-nanopipette based detection system for sensitive detection of proteins. It also answers the question whether protein binders-specifically affimers could be incorporated into origami based carriers and enable detection of target analytes by ensuring high specificity. Additionally, this work establishes a robust and novel method for purification of DNA origami structures to remove excess oligonucleotides and functional molecules, to make sure it does not interfere with further applications.

Chapter outline

Chapter 1: Introduction to DNA nanotechnology, DNA origami purification techniques, nanopore sensing, carriers in nanopore sensing and affimer proteins.

Chapter 1 introduces key concepts including DNA, its structure and function, DNA nanotechnology, and DNA origami. A brief history of DNA and the emergence of DNA nanotechnology is also presented. Furthermore, strategies for the functionalization of DNA origami are discussed, followed by a detailed review of purification techniques, highlighting their advantages and limitations. The second section of this chapter introduces the concept of nanopore sensing, discussed the different type of nanopores that can be fabricated, with a particular emphasis on nanopipettes which will be the class of nanopores used in this thesis. Subsequent sections review the research conducted on DNA origami and nanopipettes as biosensors, as well as the carrier molecules used in biosensing, all of which form the foundation for the work presented in this thesis.

Chapter 2: Materials and method

This chapter presents a detailed methodology, and materials used in this work. Materials and method are written separately for each chapter.

Chapter 3: DNA origami purification using solid phase reversible immobilisation beads (SPRI)

One of the aim of this thesis was to develop a purification protocol to remove excess oligonucleotides and functional molecules from DNA origami. To achieve this, a novel method called solid-phase reversible immobilization (SPRI) was developed for the purification of both non-functionalized and functionalized DNA origami. This chapter presents the optimization of the technique, its application to various DNA origami designs, and the evaluation of its effectiveness in purifying functionalized DNA origami structures.

Chapter 4: Conjugation and purification of oligonucleotide-protein complexes.

The second aim of this thesis was to incorporate protein binders for the functionalization of DNA origami, which is presented in this chapter. This chapter details the conjugation of oligonucleotide with affimer proteins and its characterisation. This construct is then used in Chapter 5 for attaching CRP on DNA origami.

Chapter 5: Functionalisation of origami with CRP protein using affimers.

This chapter details the results obtained from the functionalization of DNA origami with affimer proteins and CRP molecules. It provides evidence for the successful attachment of a model affimer to DNA origami and demonstrates its use for subsequent binding of

CRP. Atomic force microscopy (AFM) data are presented to confirm the binding of affimer and CRP to the DNA origami structures.

Chapter 6: Nanopipette detection of functionalised origami.

In this chapter, a sensitive nanopipette biosensor is developed for the detection of small proteins. The fabrication and characterization of the nanopipette are described in detail. The ability of the nanopipette sensor to discriminate proteins with a molecular weight difference of 12,000 Da is demonstrated. This chapter also presents the analysis of ion current peaks obtained from measurements of DNA origami and functionalized DNA origami.

Chapter 7: Thesis conclusion and future outlook.

The final chapter of this thesis summarizes all experimental findings in the context of the wider scientific literature. It also outlines potential future directions for further development of this work.

DNA and DNA nanotechnology

Deoxyribonucleic acid (DNA)

DNA as a chemical substance was first identified by Friedrich Miescher in 1869 from leucocytes in pus which he named as nuclein [17]. Later in 1874, he observed that nuclein was different from other chemical substances as it contained high amount of phosphorous and confirmed using salmon milt that nuclein contained phosphorous in the form of phosphoric acid [18]. Meanwhile, Richard Altmann identified the same substance and named it nucleic acid as it behaved like an acid in chemical reactions in 1899 [19]. In 1893, Albrecht Kossel and Albert Neumann demonstrated that DNA is made up of four bases and Kossel identified that DNA was part of the chromosome together with proteins such as histone [19, 20]. In 1944, Oswald Avery identified DNA as a genetic material and the carrier of hereditary characters [21]. In the late 1940s, Erwin Chargaff demonstrated the specificity of the structure of DNA and discovered an important rule called Chargaff's rule concerning the proportion of bases in DNA. According to the rule, DNA contained equal amounts of Adenine (A) and Thymine (T) on the one hand and guanine (G) and cytosine (C) on the other [22, 23]. These findings, combined with the biophysical studies of Maurice Wilkins and Rosalind Franklin with Raymond Gosling, led Watson and Crick to the discovery of double helical structure of DNA in 1953 (Figure 1:1) [24-26].

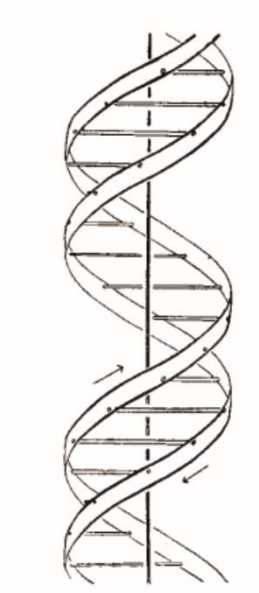

Figure 1:1 Diagram of DNA published in 1953. The two ribbon symbolises the phosphate-sugar backbone and the horizontal rods represent the pairing between bases holding the chains together. Vertical line represents the axis. (Adapted from [26]).

1.1 Structure of DNA

The DNA structure described by Watson and Crick is called B-DNA which is the most biologically relevant and prevalent conformation of DNA under physiological conditions. According to Watson-crick model of DNA, the DNA structure has two helical chains each coiled around the same axis and each chain consist of phosphodiester groups joining β-D-deoxyribofuranose residues with 3'5' linkages [26]. In each chain, residues are spaced 3.4 Å (0.34 nm) apart, and along the z-axis. With an assumed rotational angle of 36° between successive residues in a single chain, the structure completes a full helical turn after 10 residues, corresponding to a repeat distance of 34 Å (3.4 nm). The phosphorus atom is located 10 Å from the central fiber axis. The diameter of the DNA double helix is 2 nm [27]. The two chains of a DNA are held together by purine and pyrimidine nitrogenous bases by hydrogen bonding. The purine bases consist of guanine (G) and adenine (A), while pyrimidine bases consist of cytosine (C) and thymine (T) [28]. A purine on one chain always base pair with a pyrimidine on the other chain and only specific bases can pair with each other; adenine base pairs with thymine via two hydrogen bonds, cytosine pairs with guanine with three hydrogen bonds (Figure 1:3 C). These bases are flat heterocyclic rings consisting of carbon and nitrogen. Pyrimidines are single six membered heterocyclic rings whereas purines are bicyclic structures with five and six membered heterocyclic rings. The carbon and nitrogen in the bases are numbered as shown in Figure 1:3 B. Pyrimidines are joined to the 1' position of the sugar by glycosidic linkage via nitrogen at position 1 whereas purine is linked via nitrogen at position 9 [29]. The ratio of amount of adenine to thymine and guanine to cytosine is always close to one for DNA. The sugar of the sugar-phosphate is linked to the base via a glycosidic linkage and phosphate is linked to sugar via a phosphor ester linkage. As the phosphates are linked to sugars through two ester linkages, it is called as a phosphodiester bond [28]. Sugar-phosphate attached to a base is called a nucleotide which is the building blocks of DNA (Figure 1:2).

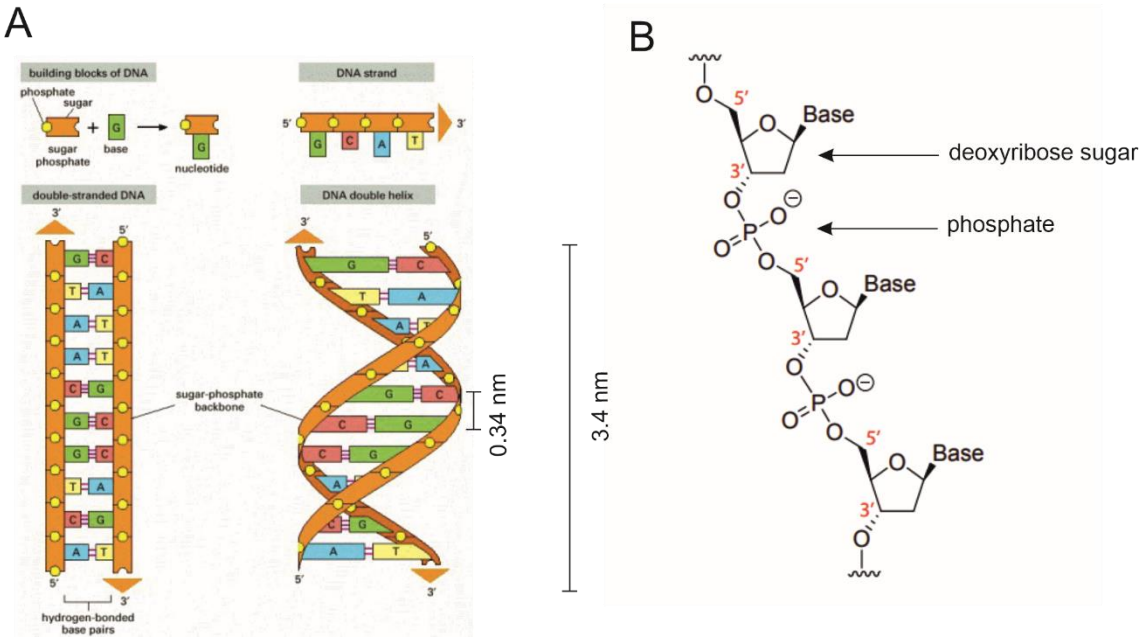

Figure 1:2 Illustration of structure of B-DNA. A) sugar-phosphate when attached to a base is called nucleotide which is the building block of a DNA molecule. Nucleotides are connected in a sequence to form a DNA strand. The bases on one strand complimentarily bind to bases on the other strand via hydrogen bonds to form a double stranded DNA helix. B) structure of DNA backbone. Deoxyribose sugar linked with a nitrogenous base is attached to each other via phosphate groups (Adapted from [28]).

An important characteristic of the DNA polynucleotide chain is the structural asymmetry of its ends. One end, known as the 5’ end, features a 5’-OH group, while the opposite end, termed the 3’ end, carries a 3’-OH group. Since DNA consists of two complementary strands, the 5’-3’ direction of one strand aligns with the 3’-5’ direction of the other, resulting in an anti-parallel arrangement of the polynucleotide strands in double-stranded DNA (Figure 1:3 A).

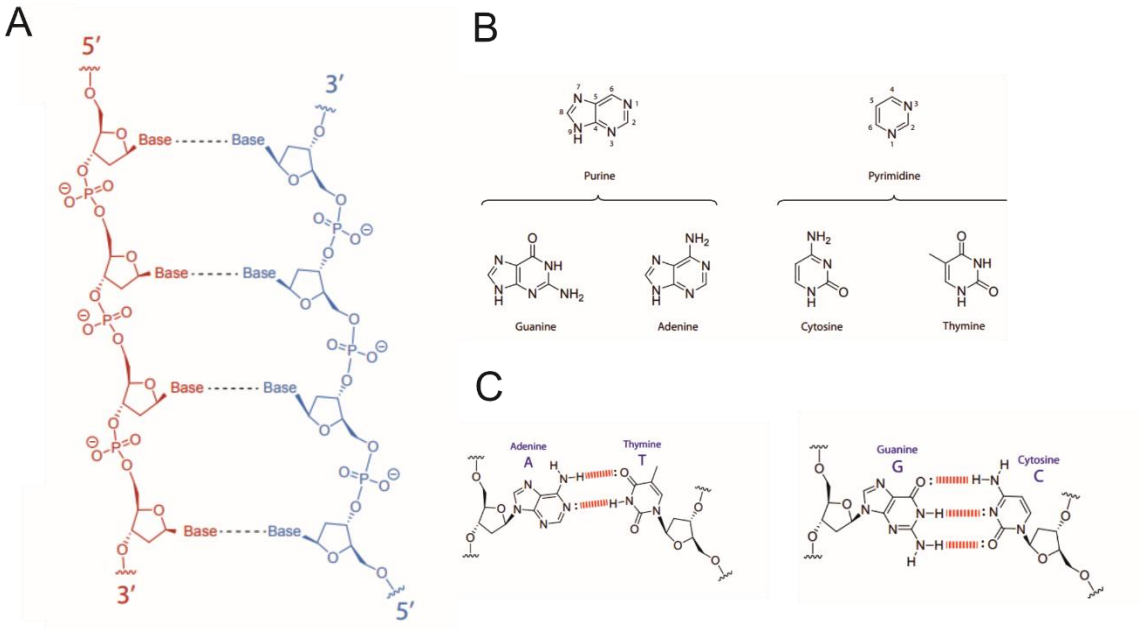

Figure 1:3 Structure of DNA A) Anti-parallel structure of double stranded DNA. B) structure of nitrogenous bases in DNA, the numbers denote the positions of carbon and nitrogen. C) pairing of purine and pyramidines; adenine pairs to thymine via two hydrogen bonds, guanine pairs to cytosine via three hydrogen bonds (Adapted from [28]).

The double helical structure has two asymmetrical grooves, the major groove and minor groove which arises due to the antiparallel orientation of DNA strands and the angle at which bases are linked to sugar-phosphate. The difference in width between the major and minor grooves arises from the angles at which the glycosidic bonds attach the bases to the sugar backbone. These bonds are positioned approximately 120° apart, resulting in an asymmetrical arrangement of the bases that creates two grooves of unequal size when stacked along the helical axis. The major grooves are wider, around 22 Å enabling higher access to protein for fundamental molecular processes such as replication and transcription whereas minor grooves are shorter around 12 Å [29].

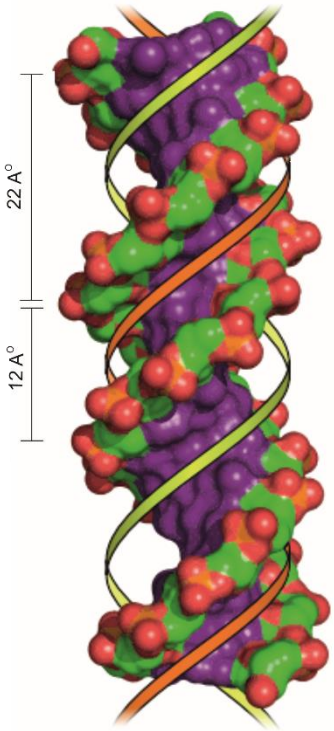

Figure 1:4 Surface representation of DNA in which bases are coloured as purple. Sugar-phosphate backbone is coloured as follows; carbon : green, oxygen : red, phosphorous: orange. DNA grooves create two continuous surfaces that encircle the helical structure. These grooves are formed by the exposed edges of the base pairs, as illustrated in the figure. The major groove (highlighted by the yellow ribbon) is broader and more accessible, whereas the minor groove (marked by the orange ribbon) is narrower (Adapted from [28]).

The model of DNA proposed by Watson and Crick qualified the characteristics necessary for a genetic material such as auto-replication, specificity, information content and the ability of genes to mutate. The auto-replication is possible based on Chargaff's rule called base pairing, adenine always pair to thymine and guanine to cytosine. According to the Watson-Crick model, DNA is linear structure accounting for its specificity and information content; the sequence of the nucleotides constitute the genetic information [19]. The genetic information in a DNA is transferred to ribonucleic acid (RNA) which serve as the template for production of proteins. This was envisioned by Francis Crick as central dogma of molecular biology and formed the basis of gene expression and molecular regulation [30].

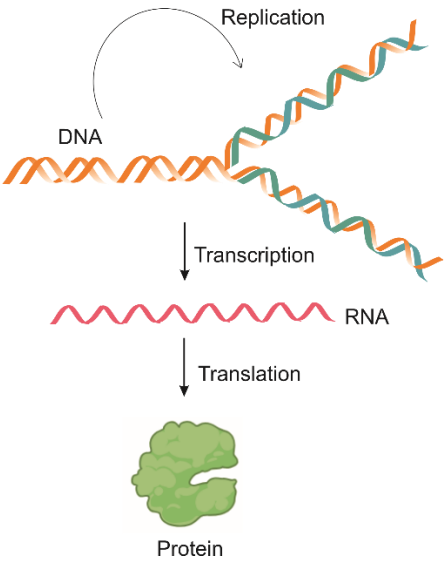

Figure 1:5 Central dogma of molecular biology. DNA is capable of auto replication, and the genetic information is transcribed to RNA and translated to proteins forming the basis of gene expression. The arrows indicate the direction of transfer of genetic information.

While the role of DNA as the carrier of genetic information has been extensively studied and remains fundamental to molecular biology, this aspect is beyond the scope of this thesis. Instead, this work focuses on DNA as a structural nanomaterial, leveraging its programmability, sequence-specific hybridization, and nanoscale self-assembly properties for biosensing applications.

DNA Nanotechnology

The field of DNA nanotechnology uses the programmability and specificity of the base pairs interactions of DNA to build nanostructures with nanoscale precision. This idea was first put forward by Nadrian C. Seeman in the 1980s who introduced the concept of DNA self-assembly by designing synthetic DNA structures that could form precisely controlled DNA nanostructures. According to Seeman, the conformational variability and backbone flexibility of DNA could facilitate the formation of nucleic acid junctions which is essential to their biological function [31]. One such example is the replication junction, site where the parent ds DNA unwinds and new complimentary strands are synthesised by DNA polymerases, which was inherently suggested in Watson and Crick's proposal for DNA replication mechanism (Figure 1:6 A) [32]. Another example is the Holliday structure (1964), the intermediate structure that forms during DNA recombination and repair and is crucial in genetic recombination [33]. A Holliday junction is a key intermediate in homologous recombination, enabling the exchange of genetic material between homologous DNA molecules. It consists of a four-stranded structure where two DNA

duplexes are linked at a crossover point. The migration of this junction occurs through a stepwise exchange of base pairs, moving the crossover point along the DNA. This process, known as branch migration, can proceed in either direction, leading to different recombination outcomes. The Figure 1:6 B illustrates the symmetry of the Holliday junction, with half-arrows indicating the 5' to 3' directionality of DNA strands and a lens-shaped object representing the two-fold sequence symmetry. The transition between different conformations of the junction is driven by base-pairing rearrangements, ultimately leading to either the restoration of the original DNA pairing or the formation of newly hybridized helices. In 1982, Seeman proposed using Holliday junctions as the foundation for constructing DNA lattices and nanostructures [31]. In 1991, he created the first 3D DNA cube nanostructure proving that DNA could be used for structural engineering [34].

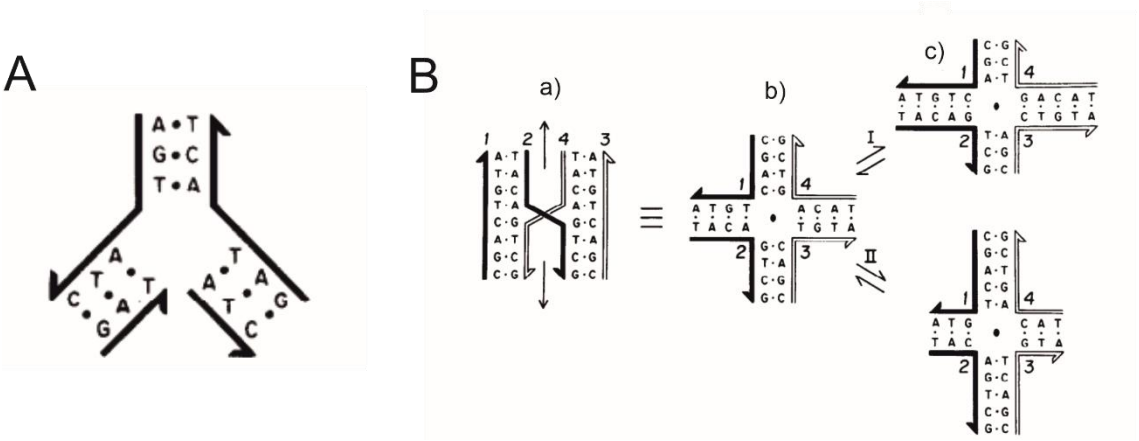

Figure 1:6 A) A replicational junction. The half-arrows indicate the 5' to 3' directionality of the individual DNA strands. The outer strands represent the parental double helix, while the inner strands correspond to newly synthesized DNA. This disjoint junction structure exhibits sequence symmetry between the two newly formed double-helical segments, reflecting the intermediate stage of DNA replication. B) The recombination junction (a) The Holliday structure as originally proposed by Holliday (1964) [35], where the shaded backbones were initially paired with each other, as were the unshaded backbones. The half-arrows indicate the 5' to 3' directionality of the strands, while the full-headed arrows represent the two-fold symmetry axis. The junction itself is the point where the strands cross, and its migration corresponds to the movement of this crossover point along the DNA. (b) This representation highlights the potential four-fold backbone symmetry, as suggested by Emerson (1969) [36], Broker & Lehman (1971)[33], and Sobell (1972) [37]. The two-fold sequence symmetry is depicted by the lens-shaped object at the centre of the structure. The migration of the branch point, as indicated by reactions I and II, leads to different recombination outcomes: repeated reaction I restores the original pairing, while repeated reaction II results in the formation of newly hybridized double helices (Adapted from [31]).

Structural nanotechnology relies on three factors; hybridisation, stably branched DNA and synthesis of DNA sequences [27]. Hybridisation is crucial for any sequence dependent formation of nanostructures. The important aspect in hybridisation of nucleic acid is the sticky end cohesion to join pieces of linear duplex DNA. Sticky ends are short,

single-stranded overhangs created when a double-stranded DNA molecule is cut by certain restriction enzymes. These overhangs can base pair with complementary sticky ends from another DNA molecule, allowing for specific and efficient recombination or ligation [38]. Sticky end cohesion relies on coherence of two double helical molecule by hydrogen bonding as illustrated in Figure 1:7. Two sticky ends will adhere to each other in a programmable and specific fashion to form a Watson-crick double helix.

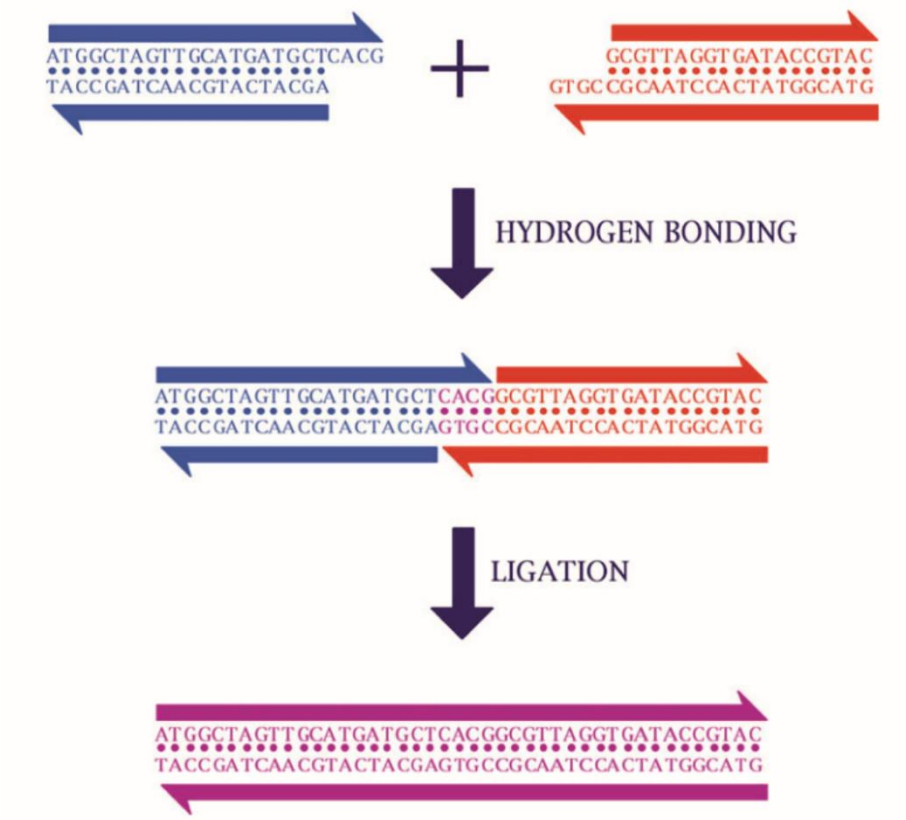

Figure 1:7 Sticky ended cohesion. The illustration depicts two unwound double helices with strands of slightly different lengths, forming overhanging single-stranded regions, known as sticky ends. When these complementary sticky ends encounter suitable conditions, they can anneal through base pairing, as shown in the middle. The final step involves covalent joining of the DNA strands, achieved through enzymatic (or sometimes nonenzymatic) ligation, resulting in a continuous double-helical structure (Adapted from [39]).

A stably branched DNA is crucial in nanotechnology and also for biological process. The processes of replication and genetic recombination occur due to the involvement of the triple-branched replication fork and the four-armed Holliday junction. The combined effect of hybridisation and branching of DNA makes DNA an eligible construction material. For example, four copies of four-armed DNA can be attached by sticky cohesion to form a quadrilateral where only the inner sticky ends are used. This structure can be extended to form an infinite lattice (Figure 1:8) [31].

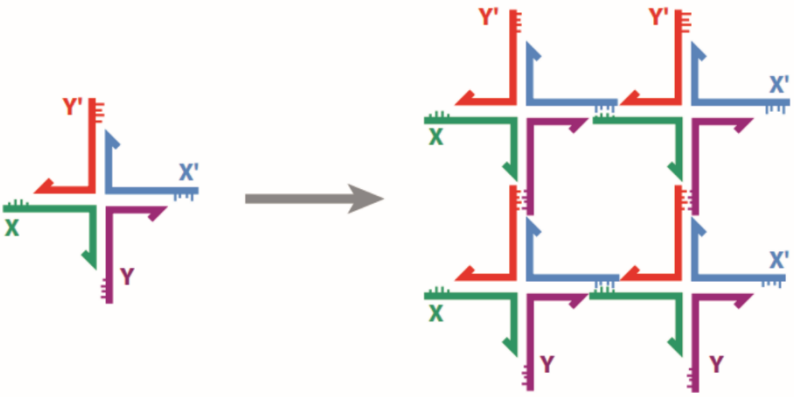

Figure 1:8 Self-assembly of branched structures to form larger structures. The structure on left is individual four-armed structure consisting of 4 strands coloured differently and named X, Y', X' and Y. The sticky ends are represented by small protrusions on the ends of each strand. The sticky ends adhere to each other, for example Y to Y' and X to X' to form a tetrahedral structure. Note that not all sticky ends are used hence if bound to more structures it can form an infinite 2D or 3D lattice (Adapted from [27]).

The branch points in inherently branched structures like Holliday junctions can migrate allowing relocation hence they are unstable. This is due to the sequence symmetry, that is two pairs of strands within the four strands of a Holliday junction have the same sequence. To build stable DNA structures, branch migration has to be eliminated which can be done by choosing sequences that lack symmetry within the vicinity of branch point. These sequences are not available naturally, hence are synthesised artificially in laboratories. Nowadays, it is possible to order required DNA sequences and even DNA sequences with modifications such as biotinylated DNA are readily available [27].

A fundamental step in DNA nanotechnology is the motif design. Motif design involves altering the connections between DNA strands in two distinct double helices to create a new pattern of connectivity. This is called as reciprocal exchange. For example, in the Figure 1:9, reciprocal exchange occurs between the red and blue strands resulting in a single structure comprising of red-blue and blue-red strands. This is designed in computer and the resulting strands are synthesised to carry out the reaction. A single recombinase enzyme reciprocal exchange result in the same topologies whereas if two or more happens, it result in structures with different topologies. Reciprocal exchange can be carried out with strands of same polarity or different polarity, however, the best-behaved molecules are those formed from different polarity [27, 31]. One important motif is the DX motif where exchange happens between strands of different polarity. It arises from two reciprocal exchanges between double stranded helices [40]. In DX + J motif, there is an extra domain which is perpendicular to the plane of the two helices and serve as a topographic marker (Figure 1:9) [41].

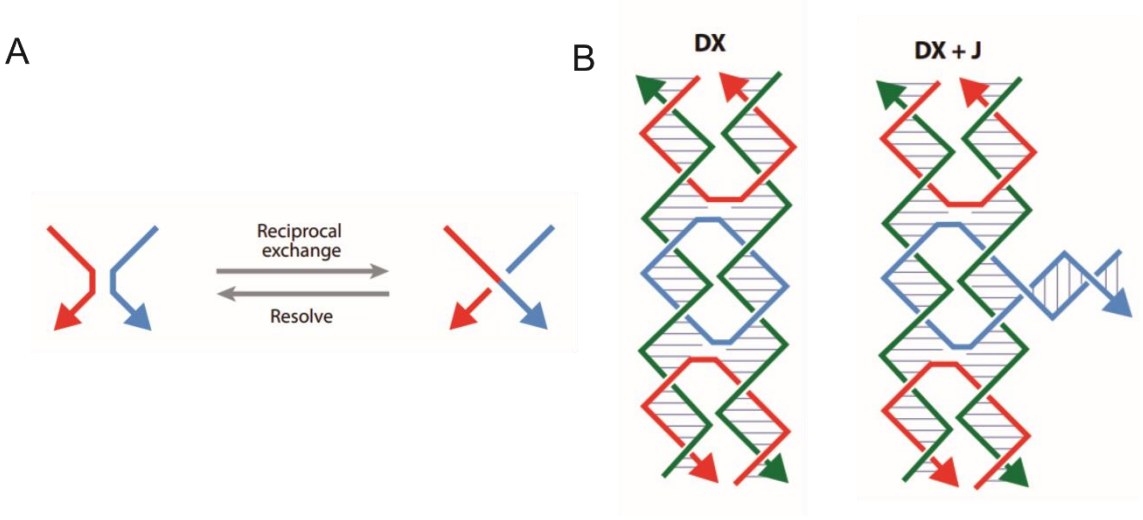

Figure 1:9 Motif generation by reciprocal exchange. A) A red strand and a blue strand becomes red-blue and blue-red strand as a result of reciprocal exchange operation. B) DX motif and DX + J motif. DX motif arises from two reciprocal exchange between DNA strands of different polarity. DX + J motif contain an additional domain which is perpendicular to the plane of the DX DNA helices (Adapted from [27]).

Using the principles described above, DNA can be used to construct nanostructures which are mostly characterised by their topologies. However, some structures have been characterised geometrically such as large constructs made from annealing of long scaffold strand with several helper strands, often called a DNA origami which is described in the next section. Earliest DNA nanostructures were described as topological species as structures like branched junctions were not robust, but rather floppy [42, 43]. The first two nanostructures produced were a cube [34] and a truncated tetrahedron [44] characterised topologically by denaturing gel electrophoresis. Other example is the assembly of DNA oligonucleotides to form a octahedron structure characterised by cryo-electron microscopy [45]. In this work, the three dimensional structure has 12 edges connected by 6 flexible joints . Five of the edges are DX motifs and seven are PX motifs. The PX molecule is formed by exchanges between strands of identical polarity at every possible position. The joints are four-way junctions that connect the core-layer double helices of each edge. The DNA folds successfully to form an octahedron of 22 nm (Figure 1:10).

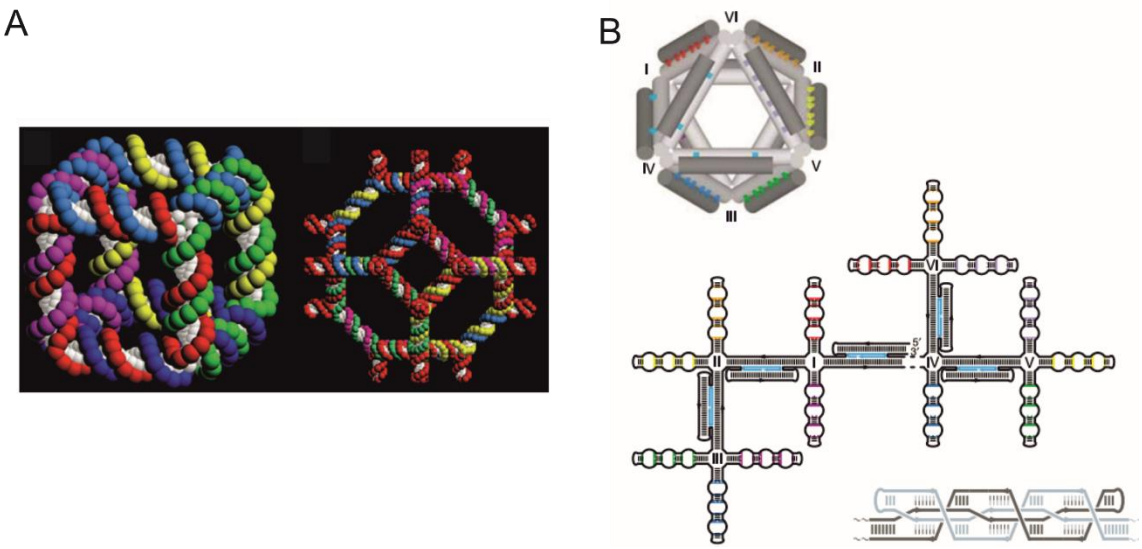

Figure 1:10 A) early topological structures built from DNA. A cube like molecule is shown on the left, each edge corresponds to two double helical turns of DNA. A DNA truncated octahedron is shown on the left. B) Design of DNA octahedron. Top: Three-dimensional structure involving twelve octahedron edges connected by six flexible joints (octahedron vertices). Five of the edges are DX motifs (cyan) and seven are PX motifs (rainbow colours). The joints are four-way junctions that connect the core-layer double helices of each edges. Middle: Secondary structure of the branched-tree folding intermediate. Bottom: Schematic of a PX edge (Adapted from [27] and [45]).

1.2 DNA origami

DNA origami technique involves the use of a scaffolding strand with helper strands to assemble into a nanostructure. The first example of the use of a scaffold strand in DNA nanotechnology was reported by Yan et al. to make a one-dimensional array [46]. The formation of octahedron by Shih et al. described in the previous section also utilised a long DNA strand annealed with five short helper strands [45]. However, a major impact of using a long DNA strand with short helper strands to form a nanostructure was put forward by Rothemund in 2006 [9]. The nanostructure called DNA origami was folded from single stranded M13 viral DNA and formed into a variety of shapes.

Paul Rothemund described the assembly of several designs including single layered and planar structures ranging from simple triangular, rectangular, star shapes to complex smiley shapes (Figure 1:12). A designated planar pattern was converted into an array of parallel cylinders, each representing a DNA double helix. To interconnect these helices, periodic crossovers were strategically incorporated, with a spacing of 1.5 helical turns (16 base pairs) along each helix. This arrangement enabled a single strand to weave through successive helices, serving as the scaffold. Rather than remaining intact, the complementary strand was fragmented into numerous shorter oligonucleotides, known as staple strands, typically ranging from 15 to 60 nucleotides in length, which traversed

between neighbouring helices via the crossovers. Instead of synthesizing a long single-stranded DNA chemically, a more cost-effective and practical approach is to use a naturally occurring viral genome as the scaffold. Viral genomes, often thousands of nucleotides in length, originate from bacteriophages with well-defined sequences, among which the M13mp18 genome is the most commonly used for assembling DNA origami structures. The sequences of the staple strands are dictated by the scaffold's routing pathway, the positions of the crossovers necessary for structural integrity, and the locations of nicks in the strand (Figure 1:11). The scaffold and staple strands are then combined in a salt-containing buffer and gradually annealed by cooling from 90°C to room temperature. This controlled annealing process allows each staple strand to hybridize at its designated position on the scaffold, ultimately forming the intended DNA origami structure [9].

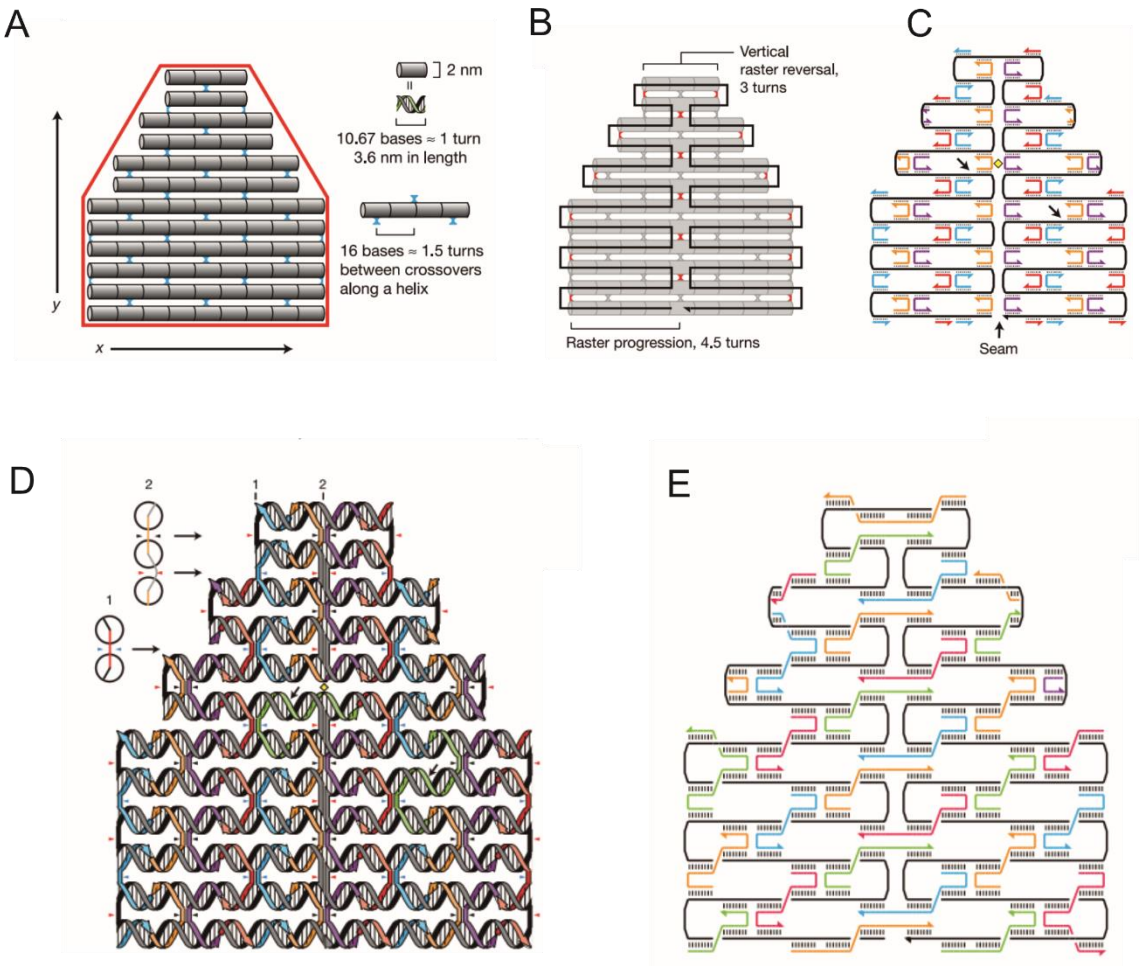

Figure 1:11 Illustration of DNA origami design. A) A red shape is approximated by parallel double helices that are interconnected through periodic crossovers, shown in blue. B) The scaffold, represented in black, weaves through each helix, forming additional crossovers highlighted in red. C) Initially, most staple strands bind two helices and are 16 nucleotides long. D) A similar representation to C displays strands as helices, where red triangles indicate scaffold crossovers, black triangles mark periodic crossovers with minor grooves on the top face, and blue triangles highlight periodic crossovers with minor grooves on the bottom. Cross-sectional views of the crossovers provide insights into backbone positions, represented by colored lines, while major and minor grooves are distinguished by large and small angles between them. In C, arrows point to nicks that are sealed to form continuous green strands, while yellow diamonds in C and D denote positions where staples can be cut and rejoined to bridge the seam. E) The final design, achieved after merging and rearranging along the seam, consists mainly of 32-nucleotide staples that span three helices (Adapted from [9]).

For folding a DNA origami structure, Rothemund's work utilized circular single-stranded genomic DNA from the M13mp18 phage, which consists of 7249 nucleotides, as the scaffold. A hundred-fold excess of 200-250 staple and supplementary strands were then mixed with the scaffold and annealed by gradually cooling from 95°C to 20°C in under two hours. The resulting DNA origami structures were characterized by depositing them on mica and imaging them with an atomic force microscope. Using this method, several

shapes of DNA origami was designed such as 26 helix square, rectangle, a five-pointed star, triangle and even a smiley [9].

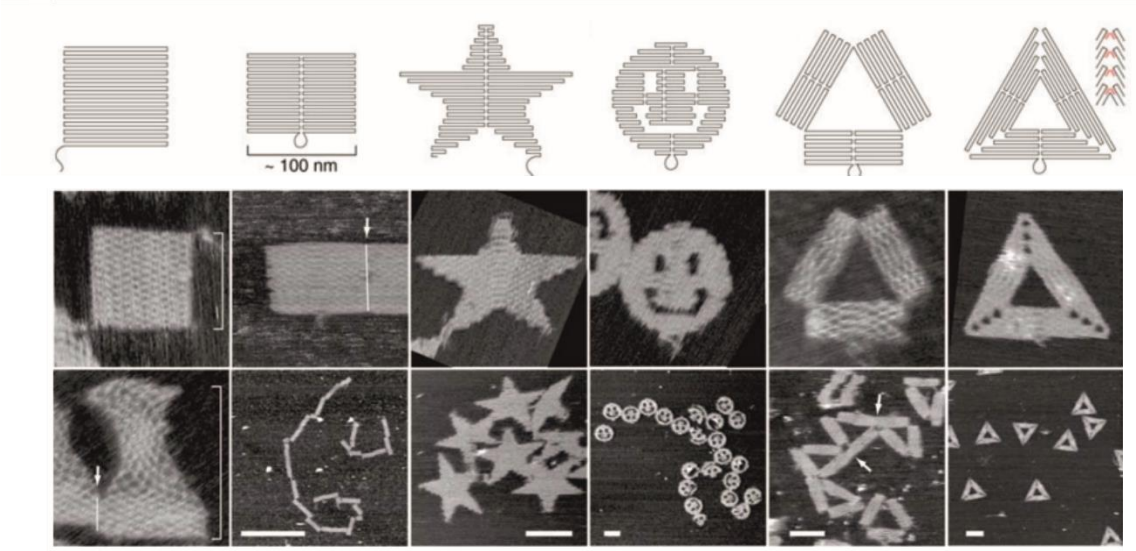

Figure 1:12 DNA origami shapes. Folding paths of DNA origami shapes; (from left to right) square, rectangle, star, smiley, triangle with rectangular domains, triangle with trapezoidal domains and bridges between them. Dangling curves and loops represent unfolded sequence. Middle and bottom rows represent AFM images. Scale bars in images without scale bars: 165 nm x 165 nm. Scale bars in bottom row; for rectangle 1 μm, remaining images in bottom row: 100 nm (Adapted from [9]).

1.2.1 DNA origami design and synthesis

Designing a DNA origami structure involves guiding the scaffold strand through the desired shape and generating complementary sequences to facilitate its assembly into the intended form. The first-generation DNA origami designing tools such as caDNAno were developed for designing 2D and 3D origami [47]. caDNAno remains the most robust software to design DNA origami while other software such as Tiamat, SARSE-DNA, Nanoengineer-1, GIDEON, Hex-tiles, K-router etc has been developed [48]. The first-generation software require manual scaffold routing and manual or semi-automatic scaffold and staples crossover. Second generation software offer more features such as it is user friendly and demand less technical knowledge when compared to first generation software. The most used second generation software is vHelix which integrates a simulation platform that can predict the folding of DNA origami in different buffers [49]. Other examples include DAEDALUS [50] and TALOS [51] for 3D origami and v-Helix-BSCOR [52], PERDIX [53] and METIS [51] for 2D origami. Another software which has been reported is ATHENA that combines the features from first and second generation [54]. DNA origami screening of large number is tedious using experimental method, therefore computational based methods to predict DNA origami structures have been developed. Molecular dynamic simulation can determine the structural, mechanical and ionic properties of DNA origami [55]. However, due to the larger size and dynamic

hybridisation and rehybridization of DNA origami, conventionally available structure prediction packages such as AMBER [56], NAMD [57], and GROMACS [56] are extremely computationally expensive. Coarse-graining packages such as canDO [57] and COSM [58] are available to predict the mechanical strain of DNA origami to minimise undesired folding. A versatile and practical approach to predict structural features in detail that is developed is called oxDNA which is a web-based server [59-61]. oxView which is the user interface in oxDNA offer *de novo* design of DNA nanostructure. MrDNA can perform an all-atom molecular dynamic simulation in 30 minutes offering high resolution and faster speed in simulating DNA origami [62].

For DNA origami assembly, the type of scaffold is chosen based on the size and complexity of the desired DNA origami. The most commonly used scaffold is the M13mp18 derived from the phage which is 7249 nucleotide long. Other commonly used scaffolds include p7308, p7560, p8064 which are also isolated from M13 and are of different lengths. The size of the DNA origami is dependent on the length of the scaffold hence custom size scaffold could potentially expand more design possibilities [63]. Research has been done for scaling up of DNA origami synthesis by employing longer scaffold strands [64, 65]. The yield of DNA origami is dependent on the cation concentration as the stability is sensitive to cation concentration. The assembly of DNA origami usually occurs at pH 8 in a Tris-acetate-EDTA buffers in the presence of Magnesium ions (5-20 mM). The concentration of Mg^{2+} ions varies with the complexity of the DNA origami design. For example, high concentration Mg^{2+} is required for 3D origami structures whereas low concentration is enough for wireframe structures. Closely packed DNA origami structures and wireframe structures can also fold under other cations such as Na^{+} [66]. The required NaCl concentration depends on the proportion of staple strands that form stable double-stranded regions with the scaffold. By minimizing weakly binding staples during design and adjusting sodium concentration accordingly, efficient folding comparable to magnesium-based conditions can be achieved. Folding of multi-layer DNA origami in sodium requires much higher salt concentrations (around 1.2–3.4 M NaCl) compared to magnesium, as proper assembly occurs only at these elevated levels where both folded and unstructured species may coexist. DNA origami structures are typically folded in one-pot, and involves the addition of 10-20x higher concentration of staples compared to scaffold strands to avoid the formation of non-specific aggregates [9, 67]. The folding involves the mixing of scaffold and staple strands under appropriate buffer condition followed by heating to near boiling point and then gradually cooling to enable spontaneous self-assembly of origami. This process is called as thermal annealing [9, 68]. The time taken for the folding depend upon the complexity of the structure, 2D structures need few hours whereas 3D origami requires days of folding.

1.2.2 DNA origami functionalisation

Functionalisation typically means attaching chemical moieties on DNA origami. There are two ways by which DNA origami are typically functionalised; Pre-assembly functionalisation and post-assembly functionalisation.

Pre-assembly functionalisation involves incorporating functionalised staples while folding of DNA origami (Figure 1:13). One advantage of this approach is that the number of attached molecules on the DNA nanostructure is precisely controlled, and each attachment site is fully occupied, as long as the staple strands are pure and correctly incorporated into the structure. They are most commonly used for incorporating fluorophores as they can be easily incorporated while solid phase synthesis of oligonucleotides [69, 70]. Such structures have been used as biosensor to investigate cellular uptake and silence genes in plants [71-73]. Pre-assembly functionalisation has been widely used to attach proteins, lipids [74, 75], aptamers [76-78], peptides [79, 80], and polymers [81] to DNA origami. Aptamers have been incorporated onto DNA origami scaffold and has been used for targeted cancer therapy [82]. However, some disadvantages with pre-assembly functionalisation is that it is incompatible with conjugates or functional molecules that are sensitive to high temperature and salt such as proteins that can denature and aggregate. Moreover, the functionalised staples need to be individually synthesised, purified and characterised.

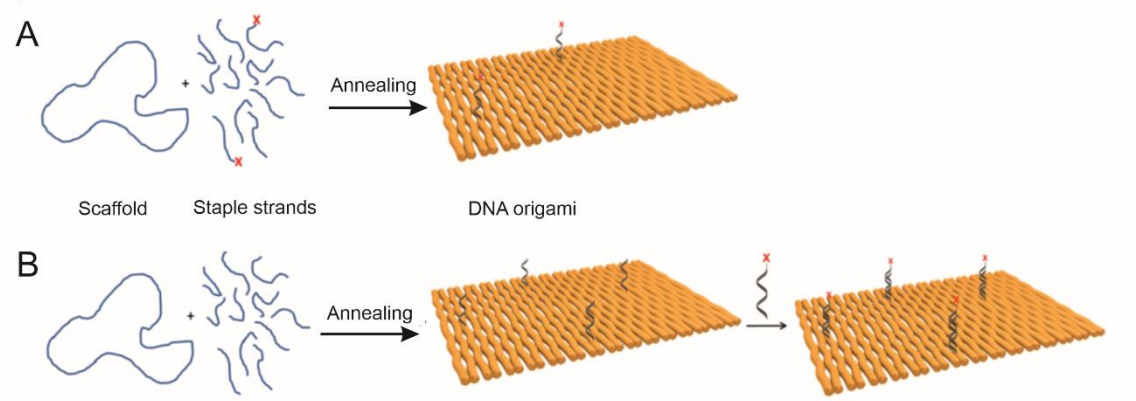

Figure 1:13 DNA origami functionalisation strategies. DNA origami is assembled by annealing scaffold strand with short staple strands. A) modified DNA oligonucleotides is added prior to folding in order to incorporate them during folding process. B) Modified oligo nucleotides are conjugated in a separate step after folding DNA origami (Adapted from [83]).

An alternative to this is post-assembly functionalisation where the functional molecule is attached in a separate step onto origami after folding, either through covalent or non-covalent approaches (Figure 1:13 B). Non-covalent modification involves DNA-DNA

hybridisation and the functional molecule chemically conjugated to a DNA strand is complimentarily attached to ssDNA overhangs protruding from DNA origami. The assembled DNA origami is incubated with functional molecule conjugated with DNA which complimentarily binds to the protruding overhang from the structure. This has been used for attaching functional molecules such as proteins [84-87], fluorophores [10, 88, 89], aptamers [13, 90-92], small interfering RNA [73, 93, 94], polymers [81], quantum dots [95], peptides [93, 94, 96] and lipids [97, 98]. This type of functionalisation has a risk of DNA-DNA dissociation and loss of conjugate molecule.

Another common strategy for functionalising DNA origami is DNA-X conjugation. This method involves using DNA handles such as peptide nucleic acids or DNA-binding proteins to attach to DNA overhangs.. The most common non-covalent interaction exploited for DNA origami functionalisation is high affinity biotin-streptavidin functionalisation. This method is adopted for its ease of biotinylating staples and engineering streptavidin systems hence used to attach proteins [74], peptides [99] and metal conjugates [100]. Such systems are also used to study chemical reactions observing successive cleavage and bond forming reactions on DNA origami [11]. This work explores three linkers in which one linker A involves covalent attachment, while other linkers are attached non-covalently. The reaction involves cleaving and bond formation resulting in detachment of streptavidin which is monitored by AFM technique.

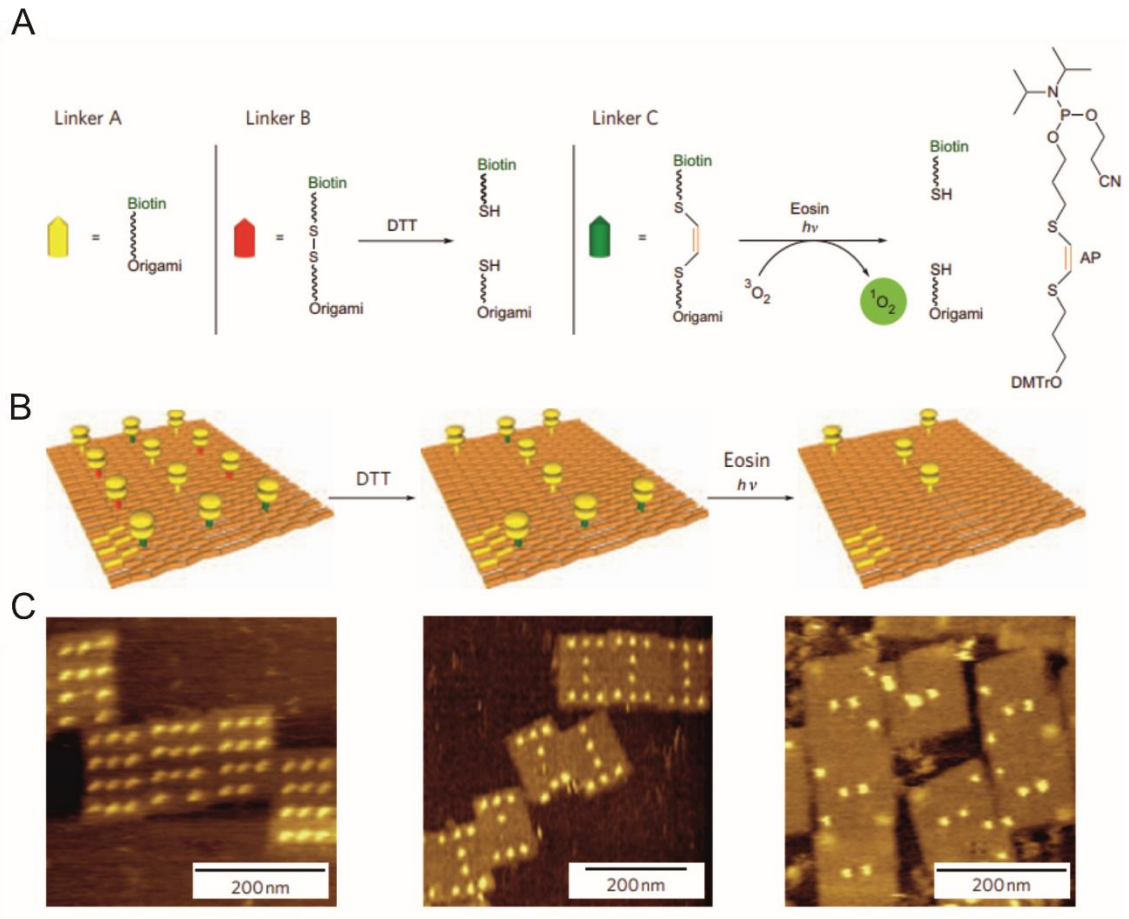

Figure 1:14 Chemical cleavage reactions on DNA origami. A) Linkers A, B and C used for immobilization of biotin. Linkers B and C are cleavable. Linker B is cleaved by DTT (10 mM) and linker C by photogenerated singlet oxygen (sensitizer, eosin 100 mM). AP is the phosphoramidite used for the synthesis of linker C. B) Schematic of the arrangement of the linker–biotin–streptavidin conjugates at the DNA origami. C) AFM images of origamis with streptavidin arranged as the letter 'I' after disulphide cleavage, and the letter 'Y' after subsequent photochemical cleavage. (Adapted from [11])

Covalent functionalisation involves chemically modifying DNA origami with functional groups enabling more stability and specificity compared to non-covalent hybridisation. One approach is to modify the staple strands with primary amines that can interact with N-hydroxy succinimide (NHS) esters on the functional molecule to form a stable amide bond. This method is used to functionalise proteins [101], metals [102] and small molecules on DNA origami. However, this approach offers poor functionalisation efficiency. Another covalent approach is to utilise the maleimide -thiol chemistry to conjugate functional molecules. DNA strand containing thiol groups (-SH) can be reacted with maleimide containing functional molecule to form a stable thiosuccinimide bond [103, 104].

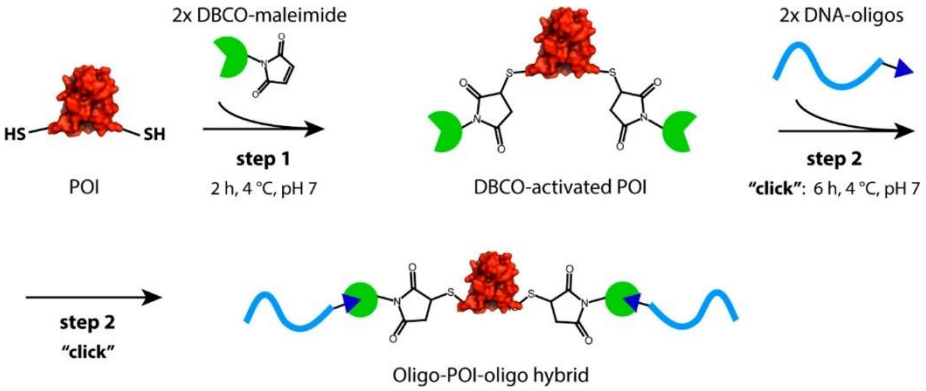

Figure 1:15 Cysteine-Bearing Protein of Interest (POI) is conjugated to the Azide-Modified Oligos by DBCO-Maleimide Cross-Linker via a Copper-Free 1,3-Dipolar Cycloaddition Reaction. (Adapted from [105]).

DNA-protein conjugation primarily relies on engineering single amino acid residues to enable site-specific functionalization while preserving protein activity. Single amino acid mutations or insertions are advantageous as they typically do not disrupt the functionality of the modified protein. Most binding or model proteins used in conjugation reactions lack naturally occurring cysteine or lysine residues, allowing these amino acids to be strategically introduced at desired sites [106]. Cysteine is less abundant than lysine, making it a preferred candidate for selective conjugation. However, the thiol (-SH) group in cysteine can form disulfide bonds, leading to protein multimerization [107]. To prevent this, a reducing agent must be used before conjugation. Cysteine-containing proteins can be conjugated to DNA through two main approaches. One method involves the direct attachment of cysteine to maleimide-modified oligonucleotides. An alternative strategy, developed by Mukhortava and Schlierf, follows a two-step process: first, cysteine is functionalized with DBCO-maleimide, and then it is conjugated to azide-modified oligonucleotides (Figure 1:15) [105]. This approach utilises a Strain-promoted azide-alkyne cycloaddition (SPAAC) which is a bioorthogonal click chemistry reaction that enables covalent conjugation without the need for a copper catalyst. Murphy et.al has demonstrated covalent attachment of urease enzyme to DNA origami using thiol maleimide chemistry. The enzyme has a thiol group which reacts with a maleimide on heterobifunctional crosslinker azido-PEG3-maleimide to form a stable thiosuccinimide bond. In a second step, DBCO-modified ssDNA strand complimentary to overhang on DNA origami is reacted with azide on urease enzyme using click-chemistry [108].

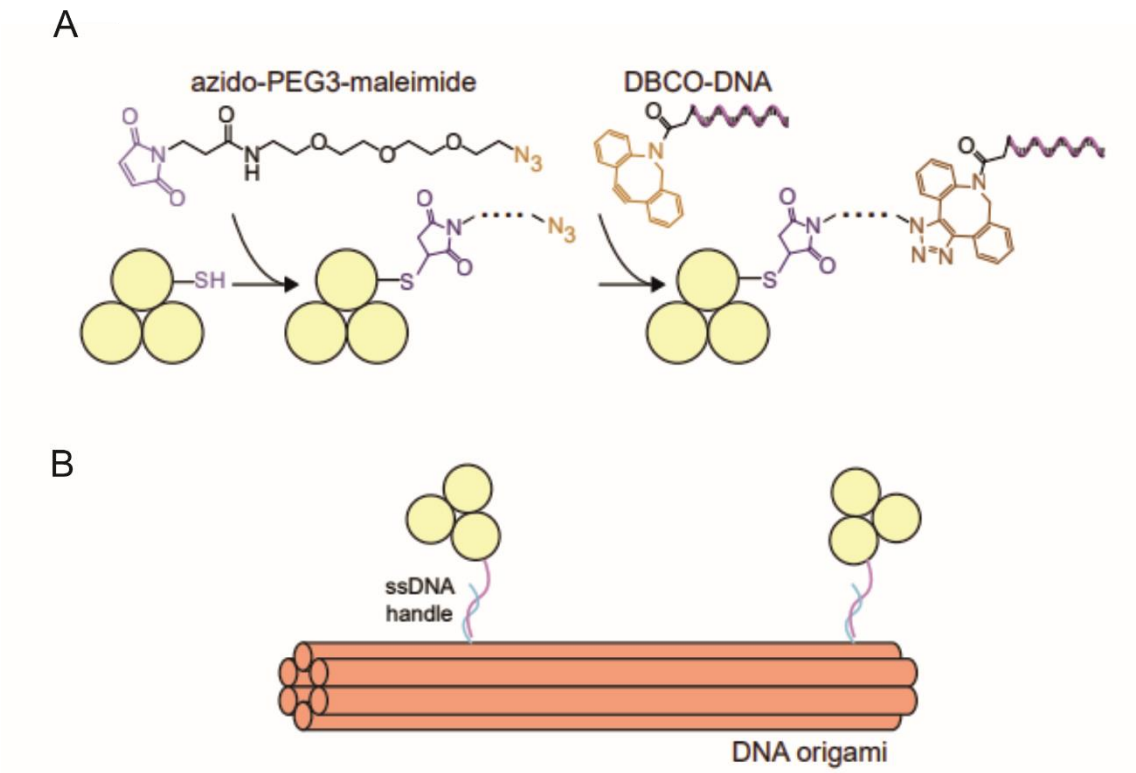

Figure 1:16 A) The heterobifunctional crosslinker azido-PEG3-maleimide is incubated with reduced urease, allowing the maleimide (purple) to react with the enzyme's thiol groups (-SH). A stable thiosuccinimide bond is formed between the maleimide and the thiol. In the second step, DBCO-modified single-stranded DNA is reacted with the urease-azide using "click" chemistry. B) Illustration showing DNA-conjugated urease binding to DNA origami via complementary DNA strands (single-stranded DNA handles shown in cyan and magenta). (Adapted from [108]).

1.2.3 DNA origami purification

The staple strands used for DNA origami assembly is added in excess to enable high efficiency of folding. Similarly, functional molecules are also added in excess to ensure high functionalisation efficiency on DNA origami in both pre-assembly and post-assembly functionalisation. Purification removes excess oligonucleotides, functional molecules, and mis-folded products. Same purification methods are used for purifying both unfunctionalized and functionalised origami though each method has its own merits and demerits. The main challenge with purifying DNA origami, especially functionalised DNA origami is that most methods damage the nanostructure or the functional molecule. Moreover, efficiency of purification reduces when large size proteins are used as functional molecules.

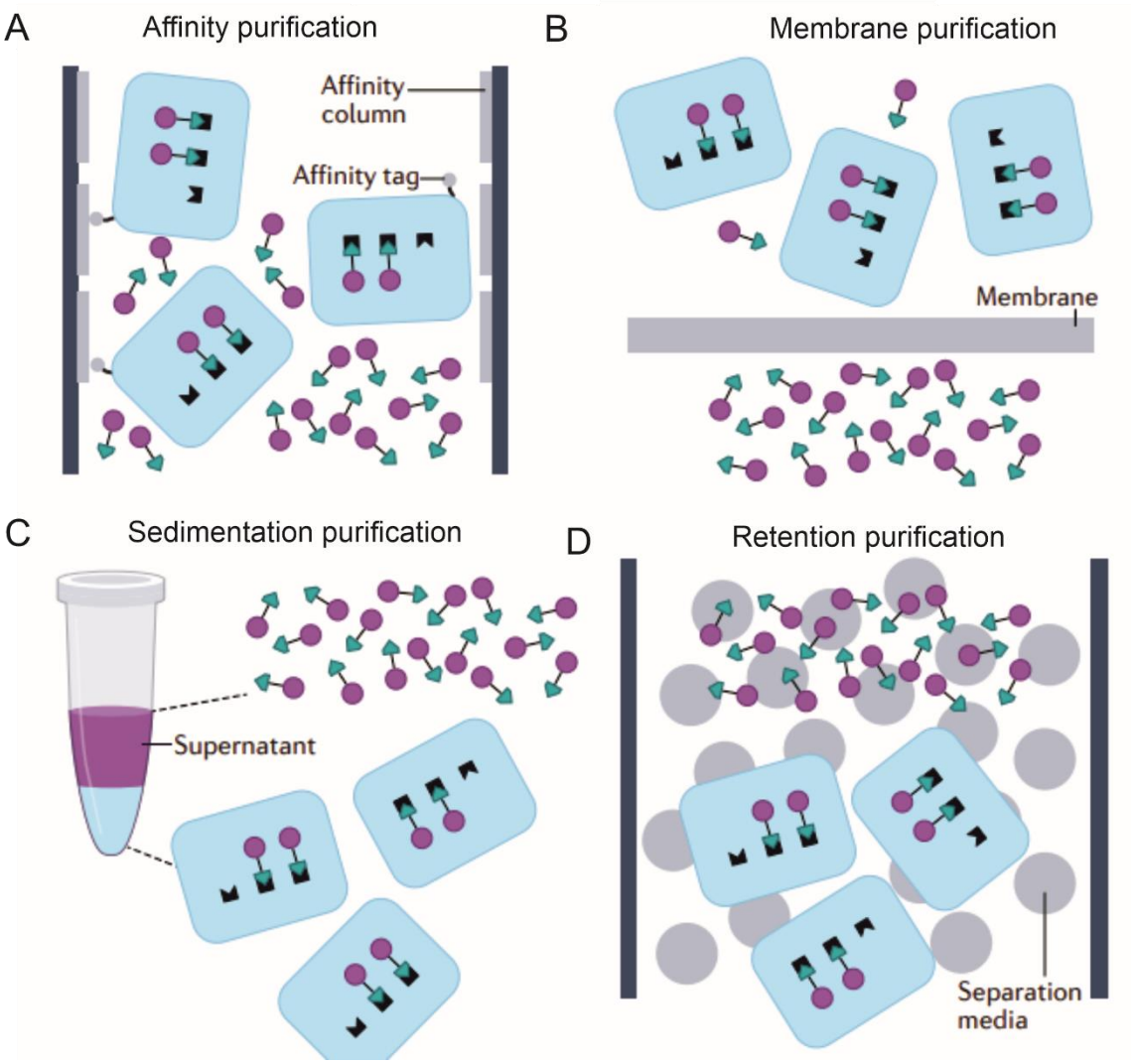

Figure 1:17 Illustration of methods to purify DNA origami. A) Affinity purification relies on affinity between a tag on DNA origami with an external material such as column surface or magnetic beads. B) membrane filtration uses a membrane to separate origami from excess material using size cut-off membrane. C) Sedimentation purification utilises the difference in density and size in separating heavy materials and light materials. D) Retetion purification depends on the difference in retention times of materials in different media such as agarose gels or size-exclusion chromatography beads. (Adapted from [109]).

1.2.3.1 Sedimentation purification

Sedimentation purification utilised centrifugation to remove excess materials from DNA origami and works on the principle of difference in size, density and shape between DNA origami and smaller functional molecule or oligonucleotides (Figure 1:17C). Centrifuging DNA origami sample in aqueous buffers results in retention of excess materials in the supernatant which can be discarded. However, centrifugation might result in losing samples, low molecular weight resolution and consuming time hence has limited applicability. An updated method includes using gradient of glycerol to purify DNA origami structures called rate zonal centrifugation [110]. This involves incubating the assembled or functionalised DNA origami samples with different gradients of glycerol

followed by centrifugation to result in separated fractions of product of interest and excess molecules. The DNA origami and the excess molecules sediment through the gradient at different rates enabling separation. This method struggles to produce high concentrations hence poses as disadvantage on conditions where DNA origami is needed in high concentrations such as structural studies. Another type of sedimentation purification is PEG precipitation which give high yield of origami structures after purification [111]. High-molecular-weight nanostructures are separated from low-molecular-weight conjugates due to the excluded volume effects of added PEG molecules. The nanostructures precipitate from solution as a result of PEG-induced crowding, and are then resuspended in a buffer of choice at the desired concentration. The main disadvantage of this method is it leaves residual PEG in the sample with origami which might interfere with the applications [48]. In general, centrifugation based method have limitations in scaling up and industrial applications.

1.2.3.2 Affinity purification

Affinity purification involves the attraction between an affinity tag on DNA origami to an external material (Figure 1:17A). For example, Histidine tagged DNA origami staples can be incorporated while origami assembly and can be purified by its affinity to a cobalt based metal affinity resin [80]. Magnetic beads could also be used for affinity purification. This approach involves incorporating biotinylated staples on DNA origami while folding followed by attachment to streptavidin coated magnetic beads. The origami can be pulled from the rest of the material by a magnet [112, 113]. Functionalised origami can then be detached from magnetic beads by competitive binding that displaces biotin-streptavidin bonding. This technique has been used for solid phase synthesis of DNA origami, the DNA origami is attached to a magnet by biotin-streptavidin linkage, then functionalised with protein followed by purifying excess proteins before being removed from magnetic beads [114].

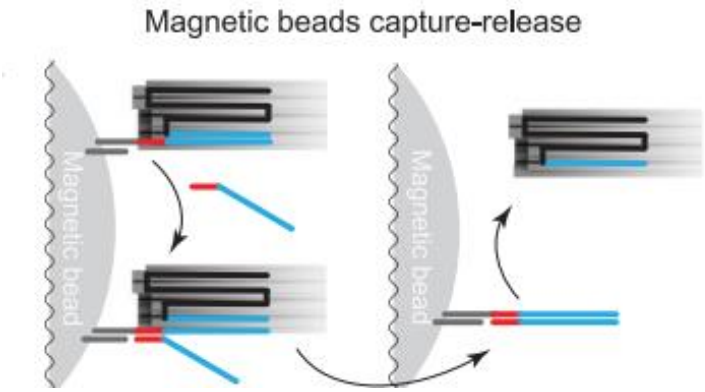

Figure 1:18 Magnetic beads modified with poly-T oligonucleotides (gray lines) were hybridized to linker oligonucleotides (the gray-red-blue line) on the DNA origami. After capture and removal of excess conjugates an invader (red-blue line) was added, binding to the red toehold region on the linker and displacing the blue sequence, releasing the origami. (Adapted from [114]).

1.2.3.3 Membrane purification

Membrane purification uses a membrane with a size cut-off which can separate large DNA origami structures from small staples or functional molecules (Figure 1:17B) [104, 115]. The speed of purification can be increased by coupling the membrane filters with centrifugation and is the most common method used for purification. This method is typically used to purify both non-functionalised and functionalised DNA origami, however the increase in size of the functional molecule needs repeated rounds of purification which often decreases the yield of purified origami. DNA origami samples are placed in a centrifugal unit with an appropriate molecular weight cut-off and centrifuged resulting in forcing excess staples and salt through the membrane while retaining DNA origami. The retained origami can be suspended in a buffer and collected [94].

1.2.3.4 Retention purification

Retention purification relies on the difference in retention time of materials in different media (Figure 1:17D). Size exclusion chromatography (SEC) is one of the type of retention purification which uses a column packed with porous beads through which the sample solution is passed through resulting in separation of component based on different size dependent retention times [84, 86, 116]. The separation is as a result of different path lengths during fluid passage through the resins. Smaller particles exhibit longer path length due to diffusion into the resin. SEC based purification can be scaled-up and used in industrial applications. SEC could be used to separate different types of DNA origami such as separating monomers, dimers, trimers and other higher order nanostructures. A related technique called fast protein liquid chromatography (FPLC)

using superose 6 column which uses low pressure and faster flow rate could separate DNA origami from excess staples, however could not distinguish between monomer and dimer origami [114]. Another type of retention purification is gel filtration which is similar to SEC, but uses centrifugation to send the samples through a column rather than pump-driven or gravity driven flow as in SEC [114, 117]. This method does not require complex chromatography instrumentation like SEC but the scalability is limited based on the volume capacity of gel column and centrifuge. Gel purification is the another approach which uses an applied electric field to push materials through a gel forming a band based on the material size and charge [75, 81, 118, 119]. The sample can be collected by excising the band followed by dissolving it and exchanging in buffer to yield a pure sample.

Work done by Hogberg et al. compared purification of three different functionalised origami using purification methods such as ultrafiltration, gel filtration, ultra centrifugation, PEG precipitation, gel extraction, magnetic bead capture and FPLC (Figure 1:19). Origami structures were modified with three types of functional molecules; Alexa 488 fluorophore representing smaller molecule, antibody fragment representing moderate sized molecule and ferritin representing large sized molecule. It was demonstrated that magnetic bead separation was superior to other methods in purity of purified structures and recovery yield. Additionally the purity was independent of the functional molecule attached establishing magnetic bead based method as a universal method for purification of DNA origami [114].

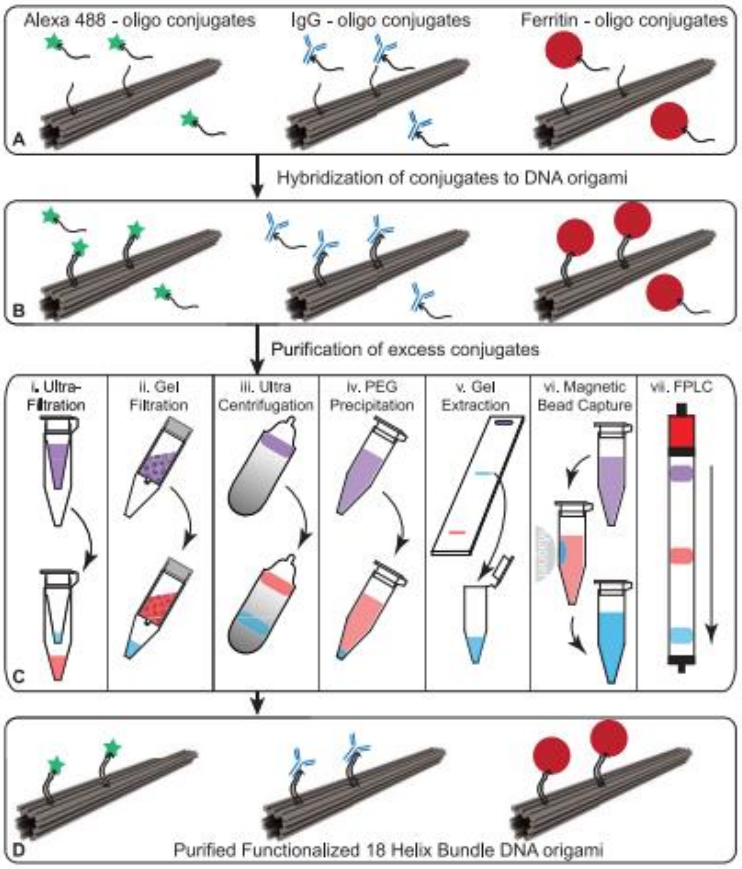

Figure 1:19 Assembly and purification of functionalised DNA nanostructures. A and B) conjugates were added to DNA origami, excess conjugates were still present in the sample. C) The samples were purified using the seven different methods compared in this study. Purple represents the mixture of excess conjugates with DNA origami, red denotes the fraction containing excess conjugates, and blue indicates the fraction with purified DNA origami. D) Excess conjugates were removed and purified origami obtained. (Adapted from [114]).

Thus, DNA origami structures provide precise spatial control at the nanometre scale, enabling the site-specific attachment of proteins. Advances in purification techniques to remove excess materials have improved the yield of functionalised DNA origami, enhancing its utility in single-molecule analysis. Recent research has explored the use of DNA origami as carriers for single-molecule detection in nanopore sensing, which is the focus of the following section. Before discussing this application, an overview of nanopores, their types, and their broader applications is presented.

Nanopores

Nanopores consist of a nanometre sized pore embedded within a membrane separating it into two compartments containing electrolyte solution such as NaCl, KCl, or LiCl. Electrodes (Ag/AgCl) fit within the two compartments and when a voltage is applied across the nanopore, ion flow freely through the pore producing an open current. The flow of ions is partially obstructed when a biomolecule translocates through the pore under the influence of the applied bias producing an ion current blockage. The current blockage is recorded as current vs time (Figure 1:20). This principle of working is called resistive pulse sensing and is widely used to detect size, shape and charge of biomolecules [120].

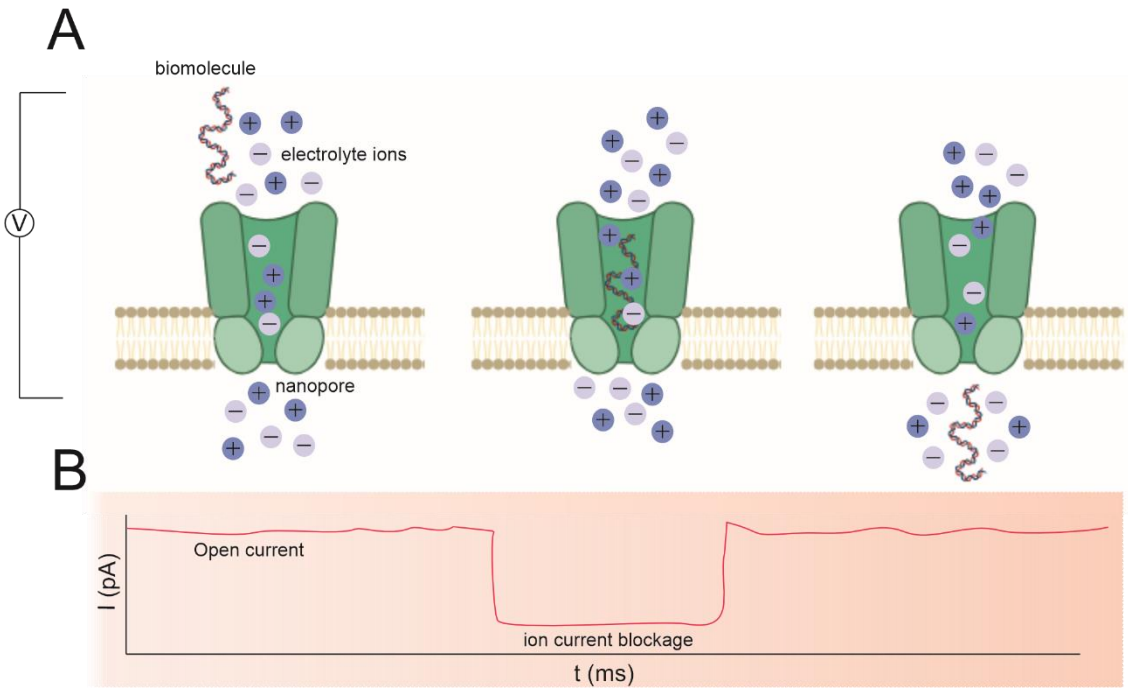

Figure 1:20 Illustration of nanopore set-up. A) nanopore inserted in a membrane separating two fluidic reservoirs. An open current is produced (B) when a voltage is applied across the compartments, whereas translocation of analyte (biomolecule) reduces the current producing an ion current blockage. The current returns to its baseline once the biomolecule exits the pore.

The nanopore sensor is set up in a Faraday cage to block electromagnetic fields. The sensor is connected to a head-stage which transduces the current to an amplifier. The amplifier amplifies and condition the signals before passing it to a digitizer, which converts the analog signal to digital format which is recorded by a computer (Figure 1:21). These signals or events are analysed to extract information about the translocating biomolecules based on the amplitude and dwell time of the event. These parameters can give information about the characteristics of the analyte molecules. For example, nanopore signals can provide information about the concentration of analyte in bulk

solution from the translocation rate [121], conformational changes and secondary structure of proteins through the event amplitude [122, 123], charge of analyte and diffusion coefficient through dwell time [124, 125], aggregation and unfolding kinetics of proteins through event amplitude and dwell time [126-128].

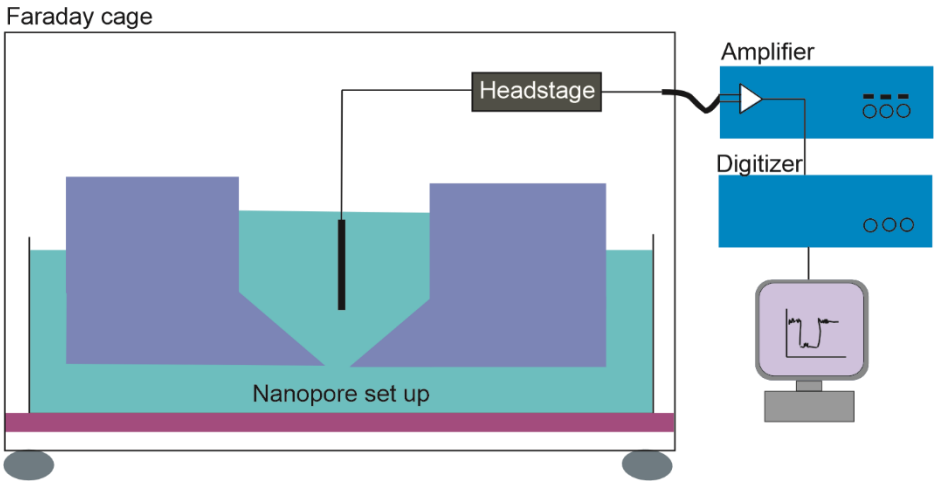

Figure 1:21 Illustration of nanopore set-up. The nanopore sensor is connected to head stage which transformed into an amplifier. Amplifier is connected with a digitizer that converts analog signals to digital signal read on a computer.

1.3 Types of nanopores

Nanopores can be classified based on the membrane on which the nanopore is located. The membrane can be of biological origin often called a biological nanopore or be inorganic called solid-state nanopores. Solid-state nanopores include 2D material nanopores and glass nanopores or nanopipettes based on the material from which it is fabricated (Figure 1:22). Further, biological and synthetic pores are combined to form hybrid nanopores.

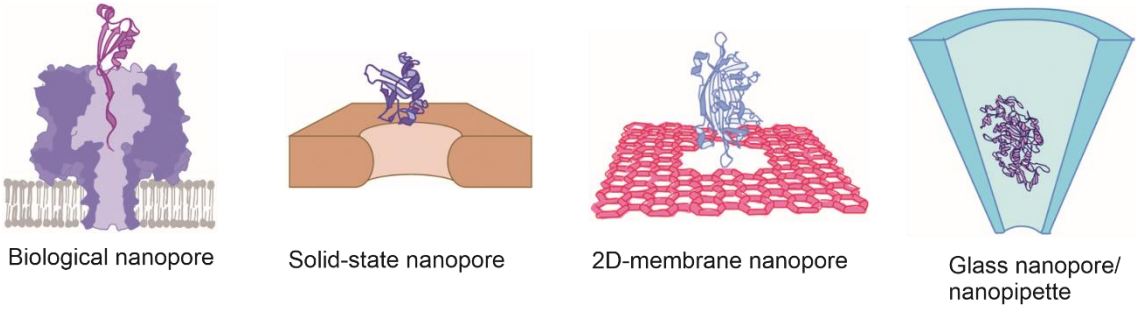

Figure 1:22 Illustration of types of nanopores. (Adapted from [4]).

1.3.1 Biological nanopores

Biological nanopores are membrane protein embedded within a lipid membrane usually synthesised by recombinant expression techniques. One such example is α-hemolysin (α-HL), purified from *Staphylococcus aureus* and characterised to have a pore diameter of 1.4 nm large enough to detect single stranded DNA and RNA molecules [129, 130]. The α-hemolysin monomers assemble into the lipid bilayer to form a heptameric structure and remain open for an extended period of time allowing ions to pass through the pore producing an open current [131]. The nanopore sensor would consist of a single membrane protein channel embedded within a lipid membrane. Over time, other protein pores were also isolated and used for single molecule detection of biomolecules such as cytolysin-A (Cly-A) from *Salmonella typhi* (pore diameter 3.8 nm) [122, 123, 132], aerolysin (pore diameter 1 nm) isolated from *Aeromonas hydrophila* [133, 134], MspA from *Mycolicibacterium smegmatis* [135], and FraC with pore size 1.6 nm from a sea anemone *Actinia fragacea* [136] (Figure 1:23). These nanopores are widely used for stochastic sensing of various analytes such as DNA [137-140], RNA [141], peptides [142, 143], proteins [128, 144-146], metabolites [147] and protein-DNA complexes [148] at single molecule level. The advantages of using a biological nanopore is its well defined sensing region typically about 2 nm and its capability for modification with precision by chemical methods or mutagenesis. Mutagenesis is widely used to engineer nanopores as it offers high degree of control and selectivity. One example is the modification of Cly-A pore in which a ring of glutamine residues were mutated to tryptophan residues in the inner channel to detect post-translational ubiquitination of proteins. The analyte used for this study was an enzyme (E2) isolated from *Saccharomyces cerevisiae* which could self-ubiquitinate. The mutation of the biological pore which increased the hydrophobicity of the nanopore lumen increased the dwell time of the E2 protein enabling real time detection of ubiquitination of the enzyme [122].

However, biological nanopores present certain challenges, such as restricted pore size (1-2 nm). Since they are membrane proteins of biological origin, they are prone to degradation and impose limitations on the size of detectable analytes due to their fixed pore dimensions unless specifically engineered. Consequently, the range of analytes that can be detected remains restricted [4, 149, 150].

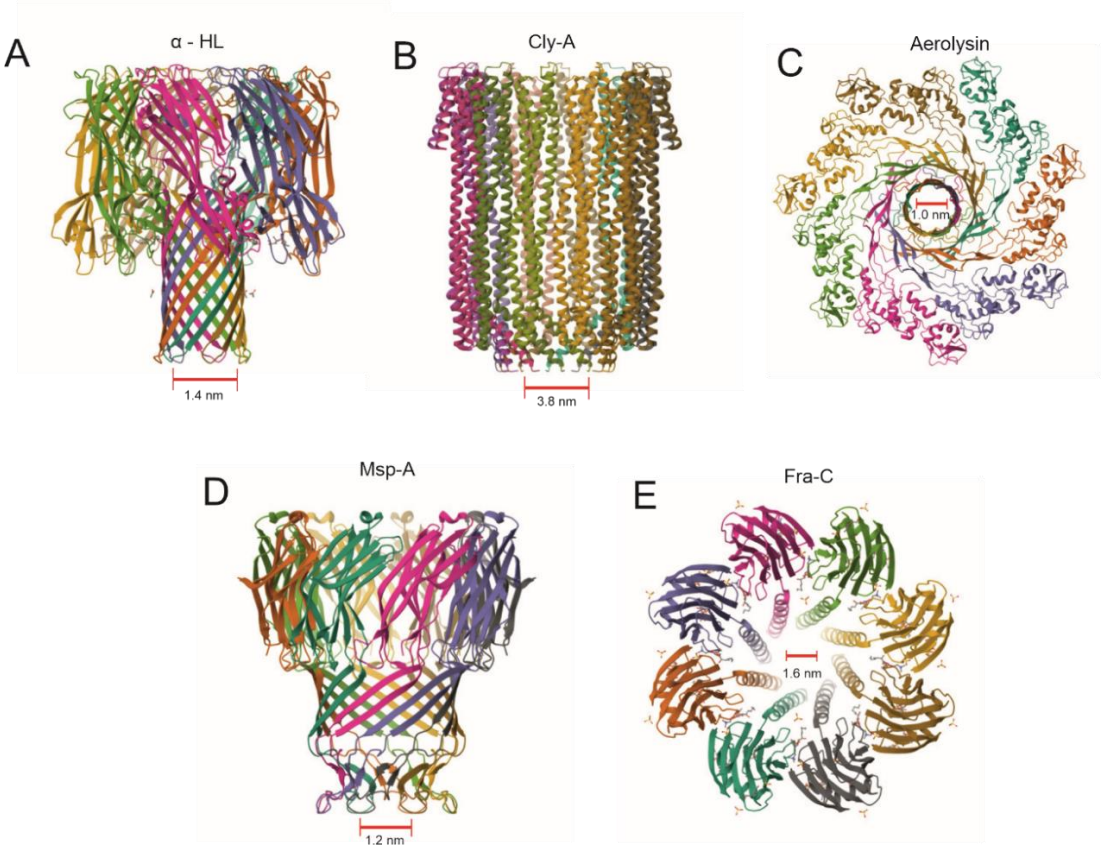

Figure 1:23 Biological nanopores: Structure of biological nanopore with their constricted pore size (marked in red). A) α-hemolysin (PDB: 3ANZ), B) Cytolysin-A (PDB: 2WCD), C) Aerolysin (PDB: 5JZT), D) MspA (PDB – 1UUN), and E) Fra-C (PDB: 4TSY).

1.3.2 Solid-state Nanopores

Solid-state nanopores are pores within inorganic or plastic materials fabricated by methods such as ion beam sculpting [151], laser drilling [152, 153], electron beam drilling [154] and dielectric breakdown of ultra-thin membranes [155, 156]. These nanopores are thermally and mechanically stable when compared to biological nanopores but has difficulty in controlling the shape of the pore. Solid state nanopores are fabricated from materials such as SiN_x [148, 157], Al_2O_3 [158, 159], ZnO [160], TiO_2 [161], graphene [162-164], MoS_2 [165-167], and HfO_2 [124, 168]. The inorganic or plastic membrane enables solid-state nanopores to have extended diameters of up to 100 nm or more, facilitating the translocation of large biomolecules. Electron beam drilling is the most common method used to fabricate sub-10 nm pores using materials such as Si or SiN. This method uses a high energy electron beam from a transmission electron microscope (TEM) to remove atoms from the membrane generating a nanopore which can be monitored real time (Figure 1:24). This method has been reported to produce pore size less than 0.13 nm [154, 169, 170]. Ion beam sculpting involves exposing a free standing Si_3N_4 containing a pre-drilled hole (formed with a focused ion beam machine) with ion

beam, typically Ar^+ ions controlling the size of the nanopore which allows optimising the size of nanopore and Li et.al has demonstrated they could reduce the initially drilled pore size from 60 nm to 1.8 nm and validated using TEM images. This method utilises a feed-back control ion sputtering system that counts the ion emitting through the nanopore ceasing the ion erosion at the appropriate time [151]. A freestanding SiN_x membrane can be etched by exposing it to a 488 nm blue laser etching the membrane to form a nanopore which can be precisely controlled. These laser etched nanopores were used to detect proteins and DNA to produce ion current blockages [152]. Fabrication methods for solid state nanopores utilises high cost and complex instruments such as TEM which is labour intensive and time consuming. However, a method called controlled di-electric breakdown (CBD) was introduced to solve this problem. In this method, a strong electric field with a dielectric strength similar to, but not high enough to break the membrane is applied across it producing a leakage current. This current creates tiny defects in the membrane, allowing more charge to pass through increasing the damage. Over time, these defects link together, forming a continuous path causing the membrane to breakdown. This increases the current at the spot removing the membrane material to form a nanopore with size ranging 1-20 nm (Figure 1:24) [156]. Another fabrication technique for solid state nanopore is atomic layer deposition (ALD) which involves depositing an ultra-thin membrane on a sacrificial layer which is then removed to yield a free-standing membrane with desired composition. Nanopores are generated on this membrane using focused electron beams or controlled di-electric breakdown and this is done on materials such as SiO_2 [171], TiO_2 [161], Al_2O_3 [158, 172], and HfO_2 [173, 174]. Advances in micro-nanofabrication enabled the fabrication of single atom layer nanopores from 2D materials such as graphene [162, 175-177], boron nitride (BN) [178, 179], tungsten disulphide (WS_2) [180], bismuth telluride (Bi_2Te_3) [181], molybdenum disulphide (MoS_2) [165, 182] and transition metal carbides (MXenes) [183] offering high sensitivity in detection. Nanopores are fabricated within these membranes typically by focused electron/ion beam. The next category of synthetic nanopores, glass nanopores or nanopipettes is discussed in detail in the next section as it has been extensively used in my thesis.

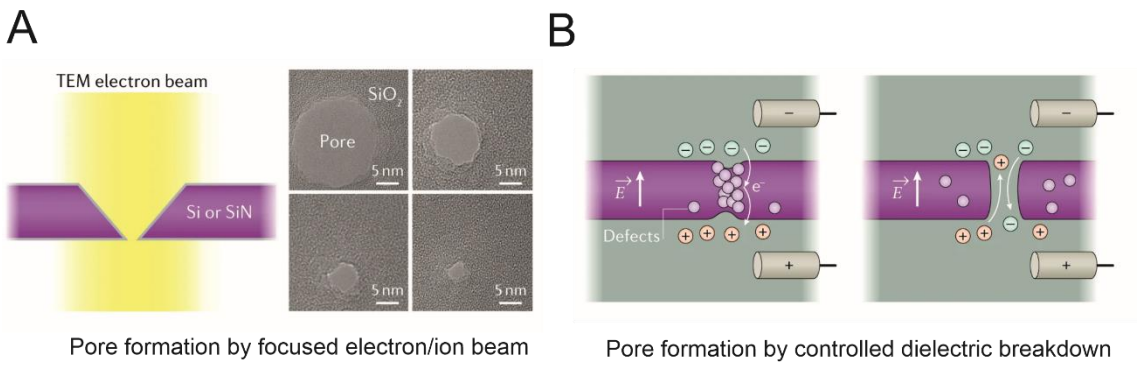

Figure 1:24 Fabrication of solid state nanopores A) Focused electron or ion beam is the common method used to fabricate sub-10 nm pores. The pore size and shape can be monitored real time during fabrication. TEM images (right) shows the formation of nanopore in silicon dioxide membrane. The electron irradiation leads to a gradual decrease in pore size to 3 nm. B) Controlled dielectric breakdown of membranes such as SiN, SiO_2, HfO_2. The membrane is immersed in an electrolyte such as KCl, LiCl or NaCl and exposed to electric field with dielectric constant comparable to the membrane resulting in breakdown of membrane forming nanopore. (Adapted from [184]).

Solid state nanopores are widely used for detection of analytes such as dsDNA [154, 185], ssDNA [182, 186], plasmid DNA [187], proteins [153, 188], polypeptides [161], miRNA [189], t-RNA [190] and dsDNA-protein complexes [171].

1.3.3 Hybrid nanopores

Hybrid nanopores involves the combination of biological and solid-state nanopores to enhance detection of biomolecules. The advantage is combining the sensitivity and reproducibility of biological nanopore with the robustness of solid state nanopores. The first hybrid nanopore was the electrophoretic insertion of α-HL tethered with DNA to 3.6 nm SiN pore to detect ss-DNA [191]. This work involved mutating an α-HL to add an additional amino acid loop containing a cysteine to which a thiol modified DNA oligomer with a complimentary single stranded end was attached through disulphide bond (Figure 1:25). The DNA oligomer acted as an attachment point for a dsDNA that guides the insertion of α-HL nanopore to SiN nanopore as a result of electrophoretic translocation. The observation of ion current blockades upon the addition of single-stranded oligonucleotides confirmed their translocation through the nanopore under applied voltage, thereby demonstrating the functional integrity of the nanopore. However, integration of biological nanopore to a solid state nanopore might lead to structural deformation of biological pore leading to loss of its inherent single nucleotide discrimination capability. Additionally, current leakage could be observed due to incomplete sealing between the biological and solid state nanopore. These factors could affect the overall performance and applicability of hybrid nanopores [150].

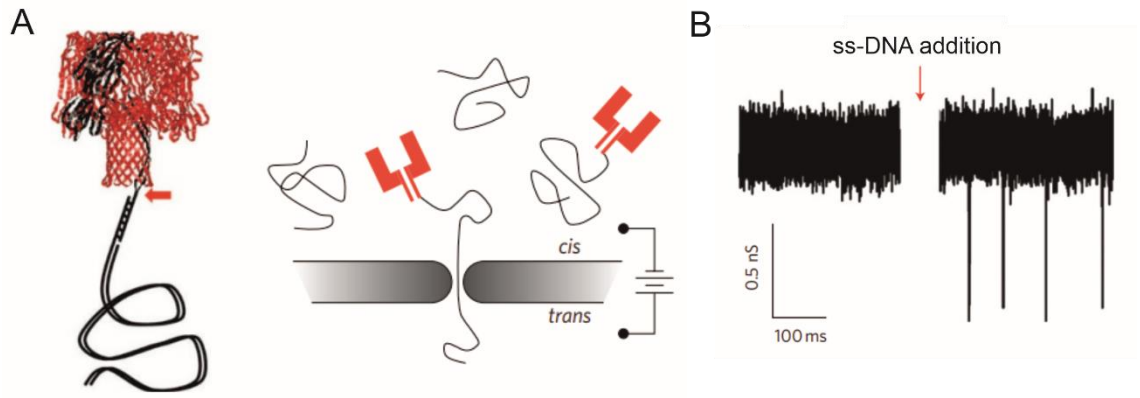

Figure 1:25 Illustration of hybrid nanopore set-up. A) α-HL nanopore a 3 kb ds DNA attached via a 12-nucleotide oligomer to one protein subunit. Arrow indicate the disulphide at connection point (left). Experimental set-up where protein conjugated dsDNA is electrophoretically translocated through solid state nanopore. B) Recorded ion current traces at -300 mV with baseline conductance after α-HL insertion and ion current peaks upon addition of ssDNA. (Adapted from [191]).

Other hybrid nanopores are formed by self-assembled nanostructures [192, 193] and viral proteins [194]. 3D DNA origami structures were designed to insert into solid state nanopore and was used to analyse λ-DNA molecules. For this, four layers of overlapping DNA skirts were designed one above the other to form a pore size of 7.5 nm followed by voltage-driven insertion into the solid state nanopore. The functionality of this hybrid nanopore as a resistive pulse sensor was demonstrated by DNA translocation events with λ-DNA [192]. Another interesting work was the design of self-assembled nanostructures inserted directly into lipid bilayer to act as a transmembrane channels (Figure 1:26 A). The DNA origami nanopore design consisted of a stem that penetrated and spanned the lipid membrane and a barrel shaped cap that adhered to the membrane via 26 cholesterol moieties. The nanopore demonstrated around 1 nS conductance and gating properties in single channel electrophysiological measurements. These nanopores are envisioned to be used as analytical sensors, antimicrobial agents and nanodevices [193]. Interestingly, viral DNA pore has been inserted into a larger silicon nitride nanopore to form a hybrid pore with low leaking and ability to discriminate and sense biomolecules. Portal protein in the viral capsid is electrokinetically inserted into the SiN pore and is used for detection of ssDNA, dsDNA, peptides and globular proteins. The portal protein was squeezed into the thin membrane as a result of applied voltage [194].

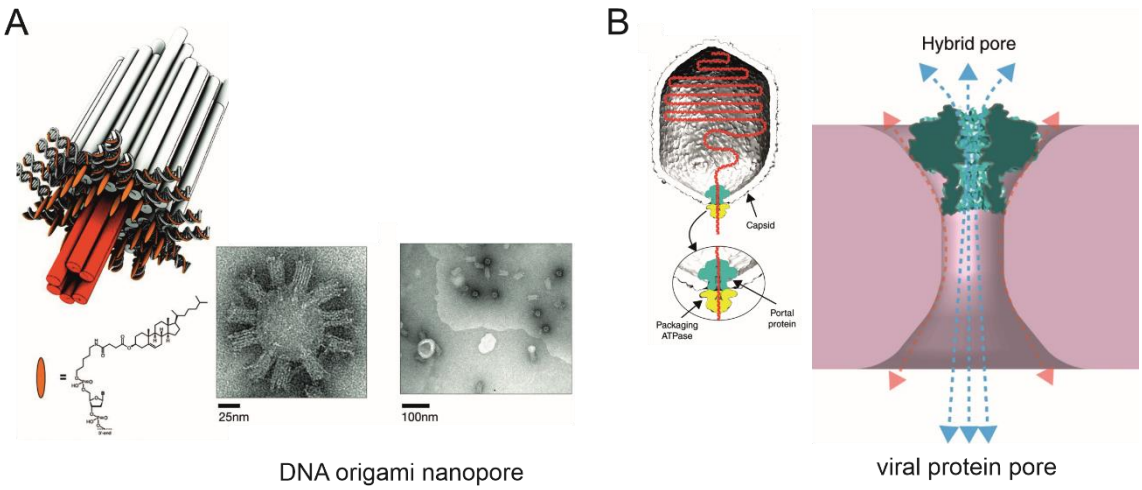

Figure 1:26 Hybrid nanopores. A) Schematic illustration of DNA origami pore formed from 54 helical bundles. Cylinder indicate double helical DNA domains. Orange ellipsoid indicate cholesterol modified oligonucleotides connected to adaptor strands. TEM images of origami channels adhering to liposomes (right). B) Left: Illustration of DNA packaging machine of dsDNA virus. Viral genomic DNA (red) is translocated into the viral capsid by the packaging ATPase (yellow) through the portal protein (aqua) embedded in viral capsid (grey). Right: Illustration of integration of viral portal protein into solid-state nanopore and application of voltage results in ion current (blue arrows). (Adapted from [194] and [193]).

1.3.4 Glass nanopores or Nanopipettes

Pipettes are designed to measure and dispense volumes of liquid. The origin of pipettes dates back to 1940s when Louis Pasteur developed Pasteur pipettes to transfer liquid for his experiments. This was further developed into micropipettes in the 1950s to transfer and measure small volumes. Albert Barber fabricated micropipettes from glass to detect bacteria followed by fabrication of glass pipettes with pore size above 0.5 µm by Ling and Gerard in 1949 which was extensively used to study cell physiology [195, 196]. The continuous evolution of pipette technology and advancement in fabrication methods lead to the development of nanopipettes which can manipulate extremely small liquid volumes at nanolitre scale. These advancements paved the way for development of fields such as single molecule analysis and nanotechnology allowing unprecedented precision in liquid handling at the nanoscale.

Nanopipettes are glass pipettes with pore size less than 200 nm . Nanopipettes are used as nanopores due to their ability to create a highly controlled nanoscale aperture enabling single molecule detection and electrochemical measurements. Nanopipettes enable resistive pulse sensing just like biological and solid-state nanopores hence are used to detect size, shape and conformation of biomolecules [197]. Nanopipettes are a powerful tool for single-molecule detection due to their simple, accurate, and cost-effective fabrication technique, which can be easily performed on a standard laboratory bench.

1.3.5 Properties of nanopipettes

The electrochemical behaviour of nanopipettes is largely dependent on the interaction of the solid surface of nanopipette with the electrolyte. The surface charge affect the ionic transport through the nanopipette and molecule sensing. The translocation of analytes through nanopipettes is affected by the electro-osmotic flow and electrophoretic forces, which is described in the next section.

1.3.5.1 Double diffuse layer (DDL)

When a solid surface such as that of a nanopipette is in contact with an electrolyte, it develops a surface charge due to ionisation or adsorption. Quartz (SiO_2) contain silanol groups on the surface, leading to a negative surface charge at neutral pH due to deprotonation of silanol groups. This attracts the oppositely charged ions called counter ions from the electrolyte solution to the nanopipette surface forming electric double layer (EDL) [198]. The negative charge on the surface attracts the positive cations to form a stern layer or stationary layer which is a tightly bound layer of counter ions. However, as these ions are surrounded by large water molecules, a residual amount of anions are still present which attract more cations to form a second layer called diffuse layer (cloud of counter ions) which is loosely ordered. The diffuse layer is extended to the bulk solution to form double diffuse layer (Figure 1:27). The thickness of the DDL is called the Debye length, typically in nanometre range and is dependent on the ionic strength of the solution. The potential generated at the boundary of stern layer and DDL is called stern potential. The potential difference can affect the acceleration or deceleration of the charged analyte translocating through the nanopipette [199]. For analytes with charge opposite to the surface charge, DDL can enhance the translocation by electrostatic attraction. By deliberatively introducing positive charges on the surface of nanopore, reduction in translocation speed of ssDNA was observed which demonstrates how DDL can affect the ion screening [200].

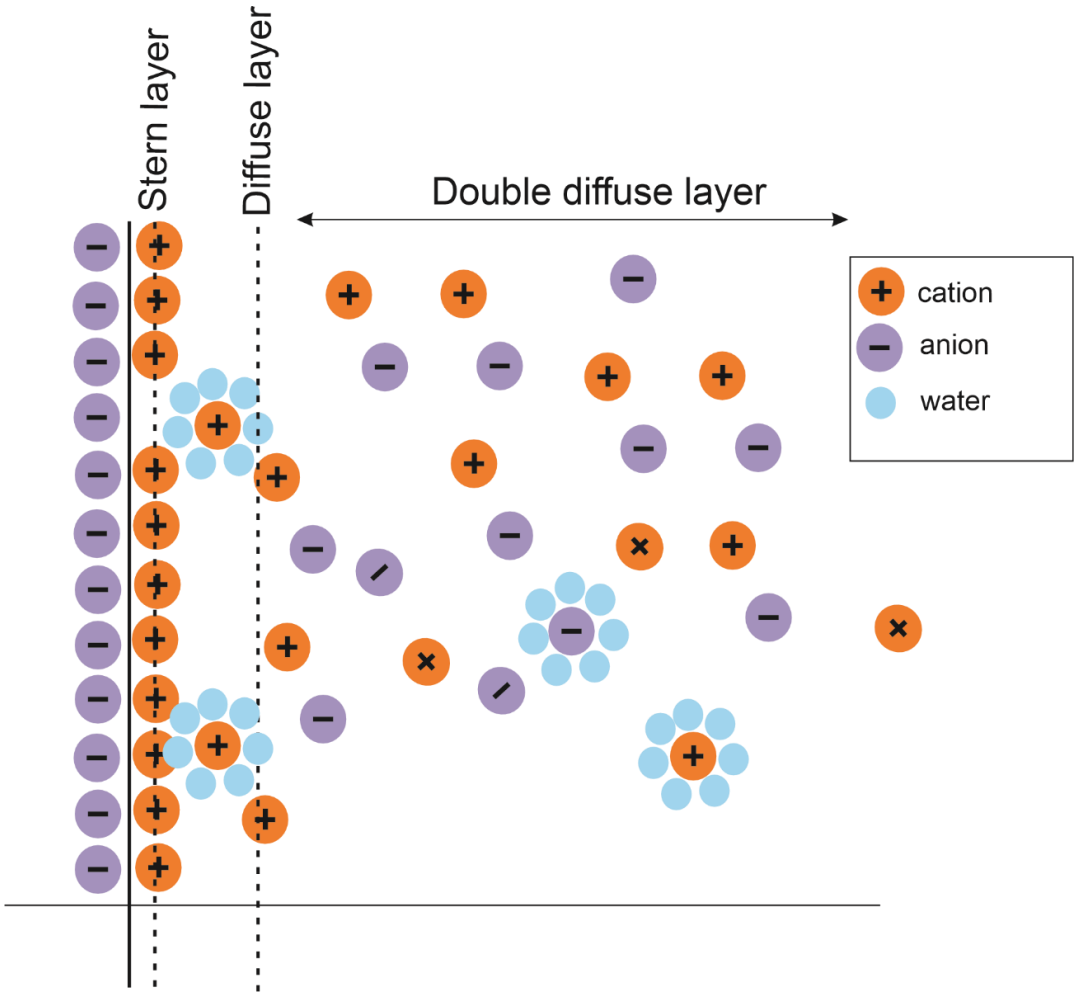

Figure 1:27 Schematic of electrical double layer.

1.3.5.2 Electrophoretic and electro-osmotic forces in nanopipette.

When a quartz nanopipette filled with an electrolyte (KCl) is immersed in an electrolyte bath and connected to counter and reference electrodes (Ag/AgCl), the application of a voltage across the system induces ion current flow through the nanopipette [201]. When a voltage is applied, a potential difference is generated in the electrolyte creating an electric field driving the motion of charged analyte called electrophoresis. An electrochemical reaction is facilitated at the anode and cathode where oxidation occurs at the anode and reduction occurs at the cathode, thus generating an electric field.

Anode: $Ag + Cl^- \rightarrow AgCl + e^-$

Cathode: $AgCl + e^- \rightarrow Ag^+ + Cl^-$

Electrophoretic transport involves the movement of charged analytes under the influence of an electric field. EDL will attract the counterions to the surface, hence for a negatively charged analyte, an attractive force is generated pushing analytes to the positive electrode.

Electroosmosis is referred to the motion of liquid induced by the electric field, and is generated due to the accumulation of ions in the surrounding electrolyte near the charged inner surface. Electroosmotic flow can influence the translocation dynamics of analytes depending on their charge. For analytes with charge opposite to that of the nanopipette surface, EOF can accelerate the movement of analyte towards the detection area enhancing detection speed [202]. Electrophoretic force is the primary force governing translocation of DNA [203] whereas for proteins with respect to the electrolyte parameters could be a combination of electrophoretic and electroosmotic forces [204].

1.3.5.3 Nanopipette fabrication

Nanopipettes are fabricated from glass most commonly quartz or borosilicate as the starting material. These glass capillaries are converted to nanopipettes by an instrument called laser puller. An example model of laser puller is the P2000 manufactured by Sutter instruments (Figure 1:28). A laser puller consists of a CO_2 laser to heat and soften the glass capillary followed by controlled pulling forces to create two nanopipettes with fine tips or apertures. The material to choose for nanopipette largely depends on the type of experiment. Borosilicate can be fabricated easily due to its soft nature and is cost effective but has a higher dielectric constant resulting in high noise during electrical measurements. They are often used for application in general microinjection or electrochemical measurements. However, quartz capillaries have low dielectric constant (3.8) and high resistivity reducing the noise in electrical recordings [205]. They are also stronger and flexible making sharper breakage resistant pores hence is suitable for single molecule detection [206]. The outer diameter and the inner diameter of the glass capillary is also an important factor to consider to choose the right size of nanopore as it determines the radius of the nanopore. The physical properties of the nanopipette is governed by five parameters which can be controlled in laser puller. They are heat, filament, velocity, delay, and pull. The steps involved in nanopipette fabrication is illustrated in Figure 1:28.

Heat – The heat parameter in a laser puller determines the intensity of CO_2 laser, which determines the extend of softening of glass capillary before pulling. This determines the tip diameter, taper shape and integrity of the nanopore.

Filament – This parameter controls how the CO_2 laser pattern is distributed across the glass capillary and determines the shape of the tip such as longer taper (large value) or shorter tip (small value).

Velocity – This controls the force with which the pull bar travels to each side. High velocity value means the pull will be sooner after glass softening.

Delay – Delay parameter controls the waiting time between the end of laser heating and the pulling of capillary determining the time for which the glass will be in molten state before being stretched.

Pull – This determines the force with which the pipettes are pulled.

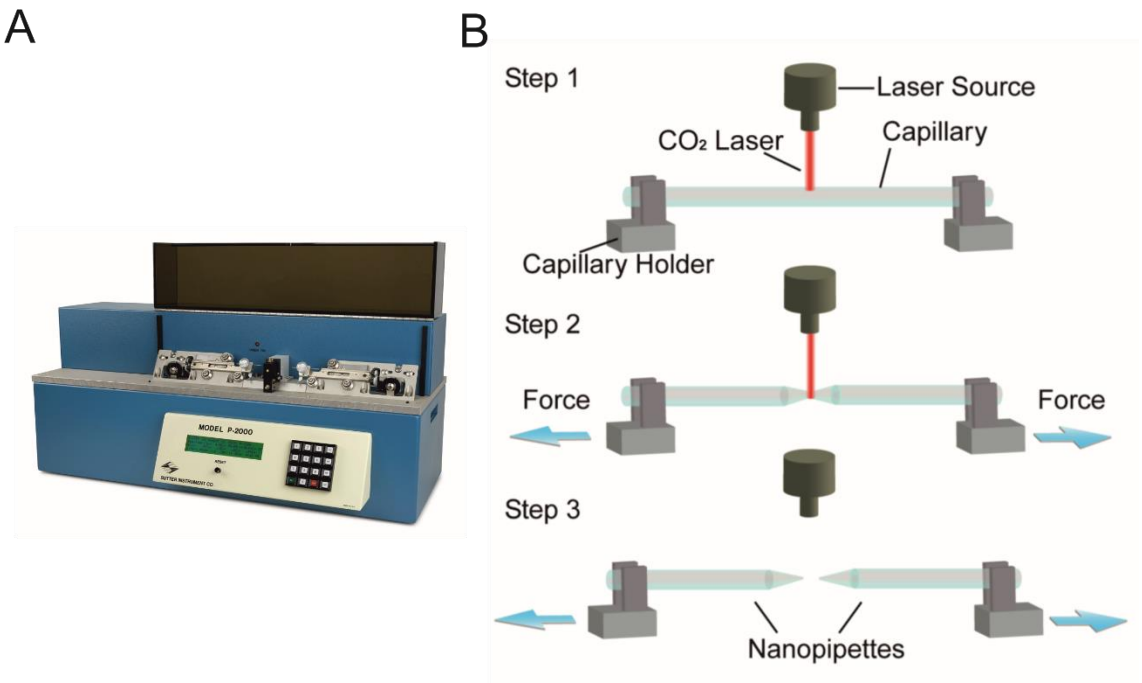

Figure 1:28 A) Image of a laser puller (Sutter Instruments). Illustration of steps involved in nanopipette fabrication using laser puller (Adapted from [207]).

1.3.5.4 Nanopipette morphological characterisation

Morphology of a nanopipette consist of the tip, a shank, shoulder and a stem as shown in Figure 1:29B. The stem is several centimetres in length and the shank in millimetres [201]. The morphology is characterised by optical or electron microscopes such as scanning electron microscopy (SEM) or transmission electron microscopy (TEM) (Figure 1:29). The morphological parameters influence the application of nanopipette in single molecule sensing. The taper is the region between the shoulder and the tip, the shape and length influence the biosensing application. Other morphological characters such as the tip diameter, material used for fabrication, outer and inner diameter also influence the nanopipette application [208].

A

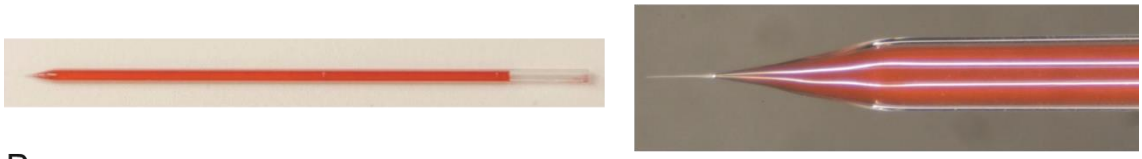

B

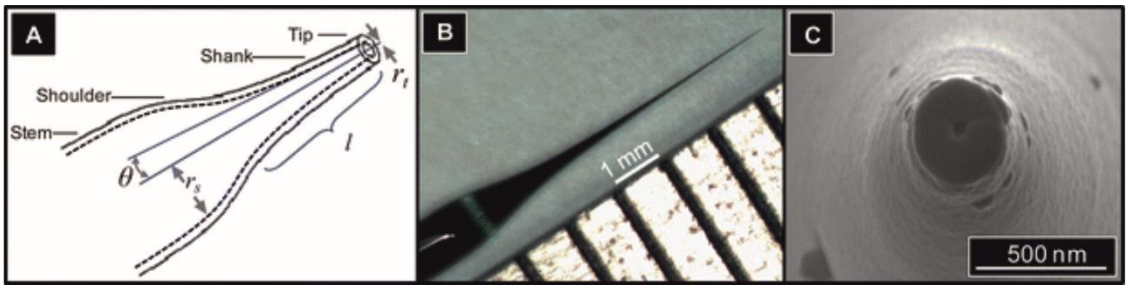

Figure 1:29 A) Image of a nanopipette filled with a red coloured solution (adapted from [209]). B) morphology of a nanopipette (left) and SEM micrographs of shoulder, shank and tip of nanopipette (centre) and orifice of nanopipette (right) (Adapted from [208]).

1.3.5.5 Nanopipette electrochemical characterisation

Electrochemical method is used to characterise nanopipettes as high resolution microscopy is tedious and expensive. For electrochemical characterisation, the pipette is filled with an electrolyte and immersed in the electrolyte bath. The Ag/AgCl electrode is inserted into the stem of the nanopipette and electrolyte and potential difference is applied across it to generate ionic current. By sweeping the voltage across the electrodes, pipettes current-voltage response can be measured and current-voltage plot can be used to determine the resistance of the nanopipette. This value can be used to determine the nanopore size as higher resistance value often indicates lower conductance, subsequently smaller pore. The resistance can be calculated from the equation [210, 211]:

$$R = \frac{\rho l}{\pi r_s^2} + \frac{\rho \cot\frac{\theta}{2}}{\pi}\left(\frac{1}{r_t} - \frac{1}{r_s}\right)$$

R is the resistance of the nanopipette pore, ρ is the resistivity of the electrolyte solution, l is the length of the nanopipette stem, r_s is the radius of the stem, r_t is the radius of the nanopipette tip and θ is the cone angle of the nanopipette.

1.4 Nanopipette in Biosensing

Nanopipettes are extensively used as sensors in analytical science and biomedical application for detection of biomolecules. Nanopipettes offer controlled nanoscale dimensions combined with sensitivity and surface modification enhancing specificity. The ease of fabrication and low cost makes nanopipette a potential tool for biosensing

application. Biomolecule sensing using nanopipettes, including surface modifications to enhance specific detection, with an emphasis on protein detection, is discussed below.

One method of sensing biomolecules using nanopipettes is by observing the changes in ion current rectification (ICR) when molecule translocate through the pore. ICR is a property observed in nanopipette where the ionic current flowing through the pipette exhibit a non-linear response to applied voltage, leading to asymmetric current-voltage characteristics [212]. The approach involves reversing the ion rectification of nanopipette by reversing the surface charge on pipettes. The silanol groups of quartz pipette lead to a negative surface charge at neutral pH and functionalisation of the nanopipette tip with positively charge polyelectrolytes such as poly-L-lysine can reverse the rectification. Therefore, the surface charges becomes positive, thus reversing ion selectivity to anions. This enables the fine tuning of the sensing properties of nanopores. The sensitivity and selectivity of the biomolecule detection can be enhanced by modifying the surface charge of nanopipette by chemical modifications. Nanoparticles [213], aptamers [214, 215] and proteins [216] has been used to modify nanopipettes and to enhance specificity in detection of target molecules. The approach involves functionalising quartz nanopipette with poly-L-lysine (PLL) or polyacrylic acid (PAA) followed by attachment of aptamer specific to the target. An aptamer encoded nanopipette is developed to detect proteins such as immunoglobins and ricin enabling single molecule detection [214]. Furthermore, thrombin protein is detected by aptamer modified nanopipette using STING technology. Signal transduction by ion nano-gating (STING) depends on an electrochemical read-out and enable label-free detection of proteins [215]. Interestingly biotin-streptavidin interaction is studied using nanopore by coating PLA/PAA functionalised nanopipette tip with biotinylated BSA followed by attachment of streptavidin causing a change in current amplitude [216]. Similarly, current rectification were also used to detect vascular endothelial growth factor protein (VEGF) using pipette modified with IgG.

Resistive pulse sensing is also demonstrated with nanopipette for detection of biomolecules. The principle as described earlier measures the ion current when a voltage is applied across the electrodes immersed in the stem of nanopipette and in electrolyte. The analytes when electrophoretically pulled through the nanopore generates ion current peaks characteristic of the analyte. The folding state of a 45 kbp double-stranded λ DNA strand is demonstrated at single molecule level using glass nanocapillaries combining it with microfluidics [217]. Raveendran et al. has demonstrated detection of different conformation of ribosome units using nanopipettes. In this work, a quartz nanopipette is used to discriminate between individual 80 s ribosome with that of polysome based on the difference in peak amplitude and dwell time of ion current peaks (Figure 1:30) [218].

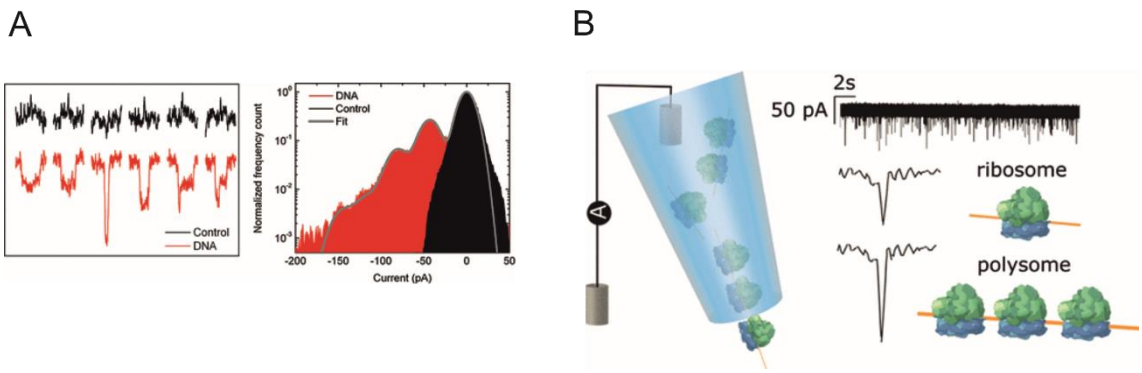

Figure 1:30 A) Control and DNA translocation experiments. No events are observed in control (black), whereas ion current blockages observed when DNA is translocated (adapted from [217]). B) Ribosome detection using nanopipette (illustration in the left). Single molecule event trace and events corresponding to individual ribosome and polysomes (right) (Adapted from [218]).

1.5 Carrier molecules in Biosensing

A biosensor converts the interaction between an analyte and a receptor molecule into a measurable signal. Depending on the analyte, the carrier molecule can be a biomolecule such as an antibody, enzyme, DNA, organelle, whole cell, or microorganism. In biosensing, a carrier molecule facilitates the transport, immobilization, or presentation of the analyte to the sensor surface, enhancing detection efficiency. It can help stabilize the target molecule, improve signal amplification, and ensure specificity in the interaction between the analyte and the biosensor. Carrier molecules are often used in signal transduction mechanisms, targeted delivery, or to bridge the interaction between the recognition element (e.g., antibody, aptamer) and the sensor platform. These interactions generate a unique fingerprint specific to the analyte. Antibodies are widely used as carrier molecules due to their high specificity, strong binding affinity, and ability to be functionalized for targeted delivery in diagnostics and therapeutics. One limitation of using antibodies in biosensing is their stability and regeneration capacity, which has led to the adoption of synthetic carrier molecules [219]. Whole cells, despite their potential as carriers, are less commonly used due to their lower specificity, higher detection limits, and longer response times. Interestingly, synthetic analogues can mimic biomolecules, offering greater stability and flexibility for modifications tailored to specific applications. Synthetic recognition elements include peptide aptamers-affimers, oligonucleotide aptamers, and nucleic acid analogues such as peptide nucleic acids (PNAs), locked nucleic acids (LNAs), glycol nucleic acids (GNAs), and threose nucleic acids (TNAs) [220]. PNAs consist of repetitive N-(2-aminoethyl) glycine units attached to nitrogenous bases, replacing the traditional sugar-phosphate backbone. LNAs, incorporating a 2'-oxygen and 4'-carbon in the ribose methylene unit, provide enhanced

stability, compatibility, and hybridization efficiency, making them valuable in clinical diagnostics. However, their sequence length and base composition can affect stability, limiting their broader application [221]. Oligonucleotide aptamers, typically 12–25 bases long, can bind proteins and serve as antibody alternatives. Their stability and shelf life can be enhanced by modifying the sugar-phosphate backbone, making them suitable for in vitro diagnostics, binding studies, and targeted therapy. However, these molecules are susceptible to nuclease degradation and may exhibit reduced binding efficiency in blood due to interactions with endogenous nucleic acid-binding proteins [222]. While antibodies have long been the gold standard for protein binding, their size and complexity limit their use in various biosensing applications. Affimers, present a promising alternative. These small, stable proteins feature high-affinity binding surfaces for target proteins and have successfully replaced antibodies in pathogen detection, protein sensing, and medical diagnostics [223].

1.5.1 Carrier molecules in nanopipette biosensing

Surface functionalisation of nanopipette has gained importance in the last decade. The selectivity stability and biocompatibility reduces any non-specific adsorption and enables specific molecular detection due to which it has applications in advanced biosensing, electrochemistry and intracellular probing [224]. However, surface modification is not always feasible for detection of multiple analytes from the same fluid. Also, there is no control over the exact location of the functional molecules on the nanopipette surface. Hence, advances are required for detection of target analyte from a complex fluid and for rare analyte which are at low concentration [225, 226]. One approach is to use a high band width amplifier (MHz) to capture even small molecules, however, they generate high noise. Small analytes such as proteins translocate very fast exceeding the bandwidth of modern amplifiers, furthermore the translocation event rate of such analytes are low. This would require a high concentration of protein molecules as analyte which is difficult in clinical detection studies [7].

An interesting approach to rectify this issue is to use molecular carriers. A carrier molecule contain a recognition element which can specifically bind to the target analyte. A difference in ion current signals is observed when the analyte is bound with molecular carrier vs empty carrier (Figure 1:31). The advantage of using a molecular carrier is that the nanopipette would not have to be modified keeping the sensor generic and constant for all the analytes. Another advantage is that smaller analytes such as proteins could be easily detected by employing a carrier. The high signal to noise ratio and resolution of ion current signals is highly dependent on the size of the analyte being comparable to the size of the nanopore. it is often difficult to fabricate nanopipette with pore size as small as that of protein. A widely used molecular carrier is DNA due to its uniform and

well-defined negative charge and the ability to be electrophoretically pulled through the nanopore. This might be of advantage for otherwise heterogenous analytes such as proteins to be easily transported through nanopipettes under applied voltage [227]. The carrier molecule could also slow down the transport of the target analyte enhancing the signal to noise ratio and enable multiplexing as multiple analytes could be attached to different regions of a molecular carrier [226, 228, 229]. Strategies of detection of target analyte using molecular carriers are illustrated below (Figure 1:31).

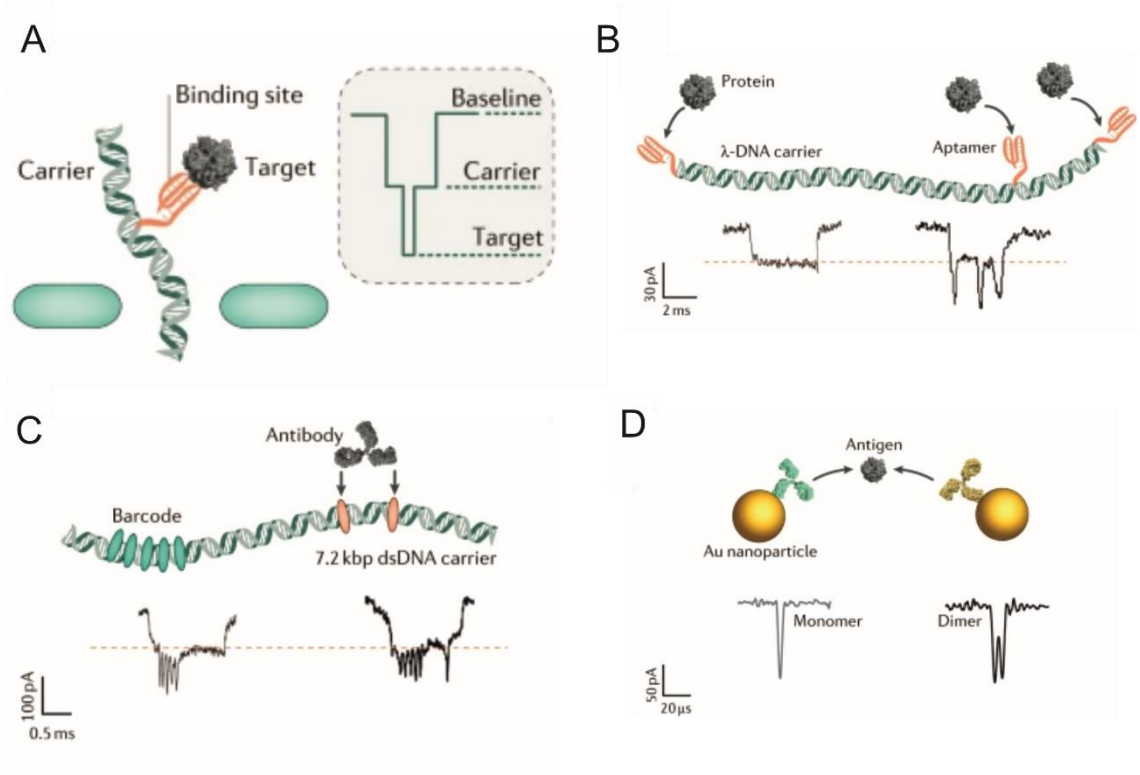

Figure 1:31 A) Illustration of molecular carriers used for target detection. B) attachment of multiple aptamers specific to different protein targets to enable multiplexed detection. C) Digitally encoded dsDNA carrier for detection of antibody. A 3-bit barcode is used to identify the DNA carrier. D) Antigen detection based on gold nanoparticle dimerization. (Adapted from review [184]).

Carriers can be of different types such as polymer based comprising of DNA and nanoparticle based. An example is the detection of single stranded thiol modified DNA conjugated to a 10 nm nanoparticle using a 50 nm nanopipette where ion current blockage is recorded against time [230]. A 10 nm nanoparticle is used as molecular carrier with quartz nanopipette to detect IgY antibody [231]. The functional group is a peptide which is conjugated to the nanoparticle which is complimentary to anti-peanut IgY antibody. Picomolar to nanomolar concentration of lysozyme is detected by specific aptamer conjugated to 5 nm nanoparticle using quartz pipette (Figure 1:32) [232].

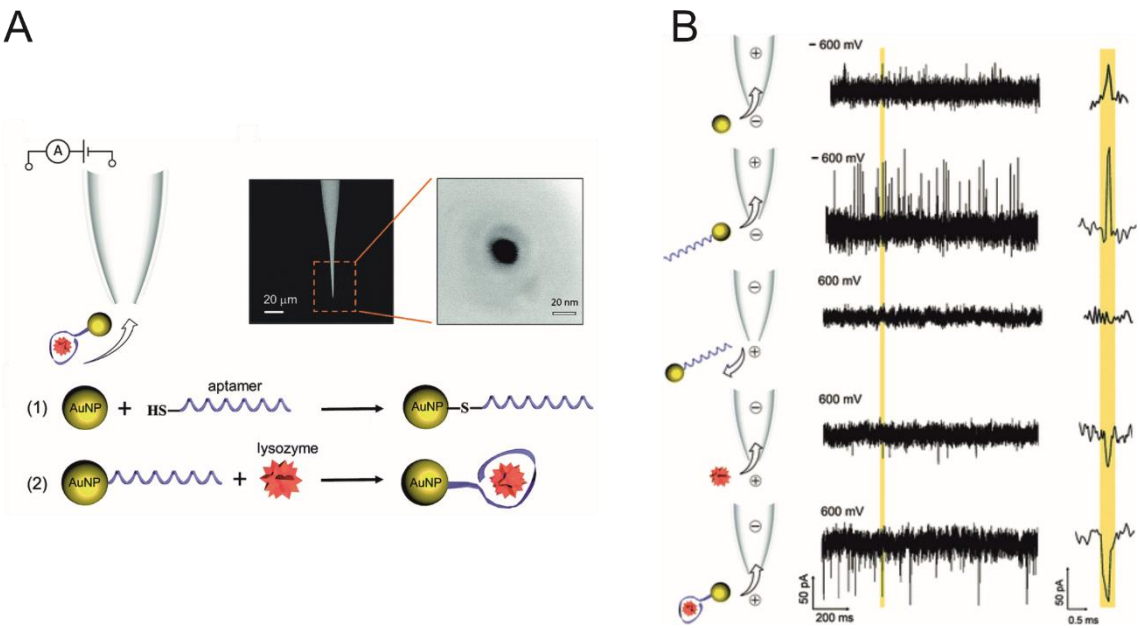

Figure 1:32 A) Working principle for single molecule detection of AuNP LBA/lysozyme complexes through a nanopipette. SEM images of a typical nanopipette (left) and nanopore (right) at the tip of the nanopipette. Schematic highlighting the strategy for detection of lysozyme using AuNPs functionalised with an (lysozyme binding aptamer) LBA aptamer. B) Current–time traces of top to bottom- AuNPs and AuNP-LBA ,AuNP-LBA, free lysozyme, and AuNP-LBA/ lysozyme complexes. AuNPs and AuNP-LBA exhibited current enhancement at negative while free lysozyme and AuNP-LBA/lysozyme complexes exhibited current blockade at positive voltages. Representative individual events are shown on the right-hand side of each trace (Adapted from [232].

DNA based carriers are more commonly used due to their fixed charge and uniformity. Several approaches are adopted to detect target molecules as showcased in Figure 1:33. Protein quantification is at nanomolar ranges are demonstrated by using DNA carriers and nanopipettes. A 7.2 kb M13mp18 strand is used as the DNA carrier to study the binding of biotin-streptavidin and digoxigenin-antidigoxigenin [233]. M13 mp18 strand is also used as a carrier in nanopipette system to detect streptavidin using biotin interaction but from a protein mixture [8]. This indicates that carrier molecule is potentially an effective label free system to detect protein molecules at single molecule level. Protein molecules in different size range is also analysed using 7.2 kp DNA carrier such as ATP, lysozyme and thrombin by using their specific aptamers [234]. This has demonstrated that this approach could be used for multiplexed detection of analyte molecules. Approaches have been developed to enhance the sensitivity and specificity of target detection, enabling the identification of single nucleotide polymorphisms at nanomolar concentrations by incorporating carrier molecules with a nanopipette (Figure 1:33) [235]. Similar methodology has been utilised for detecting small DNA fragments circulating as cell free DNA in bodily fluids such as blood plasma and saliva which has been identified as biomarkers for cancer and infectious diseases [236]. Multiplexed

detection of analytes are further explored by attaching dcas9 probes to create unique barcodes on DNA which can give unique nanopore readout [229]. Aptamer-modified DNA carriers are commonly employed for multiplexed detection, enabling the simultaneous identification of up to three proteins, such as acetylcholinesterase and thrombin, even in complex fluids like human serum [226].

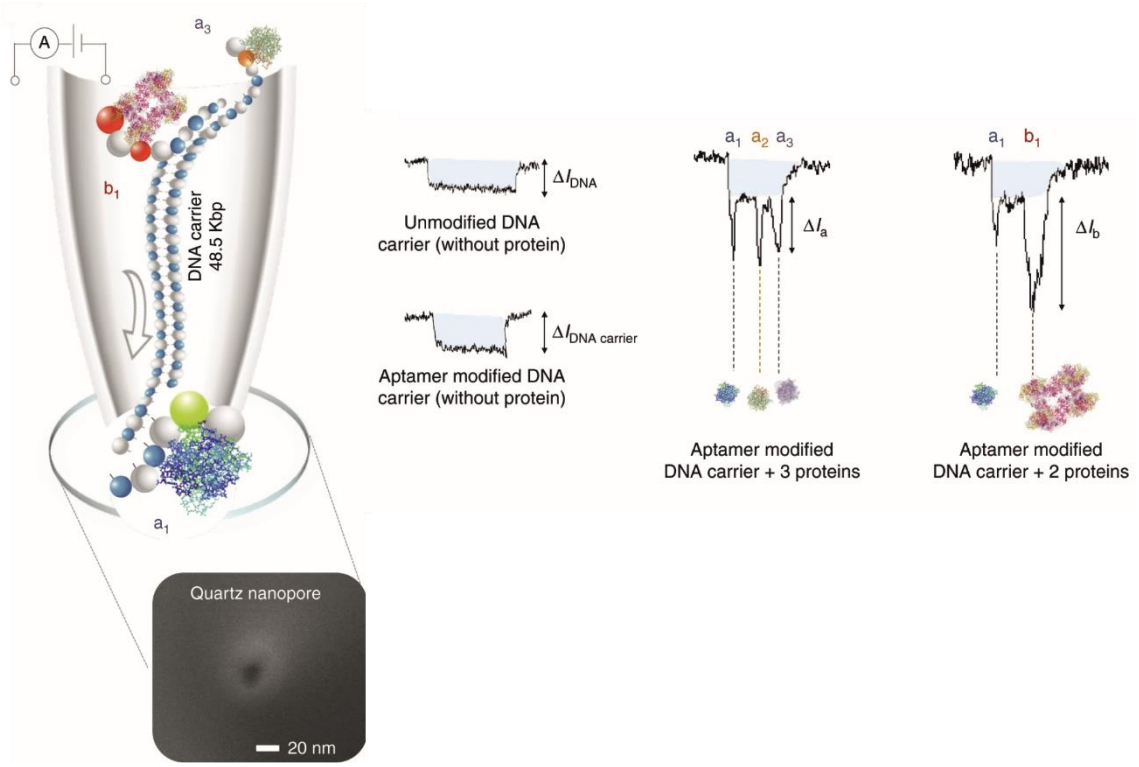

Figure 1:33 Schematic representation of a DNA carrier (48.5 kbp) engineered to contain aptamer sequences (a1, b1, a3) that bind to three proteins translocating through a nanopore driven by the electric field. Translocations take place from inside the nanopipette to the outside. As an example, a SEM is shown of a typical nanopipette tip used with a pore diameter of 16 nm. Examples of translocation events of unmodified and aptamer modified carriers are shown. Also shown are example translocations for the detection of 3 and 2 proteins bound to the aptamers on the DNA carrier. Importantly, the sub-levels can be used to differentiate between proteins both in terms of location and magnitude (Adapted from [235]).

Though linear DNA carriers are widely used as molecular carriers for biomolecule detection, translocation of long strands of DNA could result in knots and kinks resulting in false positives [217, 237]. Another limitation is the translocation of multiple carriers through the pore which could affect the single molecule detection [238]. To circumvent this issue, DNA origami is used as a carrier in nanopipettes for detection of proteins. Acetyl choline esterase protein is detected by an aptamer conjugated to a DNA origami tetrahedron [239]. DNA origami structure can enhance the signal to noise ratio and also form stable DNA carriers. Furthermore, Raveendran et al. has demonstrated detection of c-reactive protein biomarker using aptamer conjugated DNA origami (Figure 1:34).

The CRP protein was undetectable when translocated through the nanopore alone whereas attachment to DNA origami produced ion current signals and made the protein detectable [13]. This approach involves designing a DNA origami frame and inserting an aptamer specific to CRP protein enabling the capture of CRP protein at the centre of DNA origami. The unoccupied carrier and CRP occupied carrier can be discriminated based on ion current signals, specifically the peak amplitude and dwell time values. The CRP protein itself and when bound to the aptamer did not produce any ion current signals whereas attachment to DNA origami produced ion current signal with high S/N ratio. A shift in the values of peak amplitude and dwell time is also differentiated between CRP occupied and unoccupied carrier.

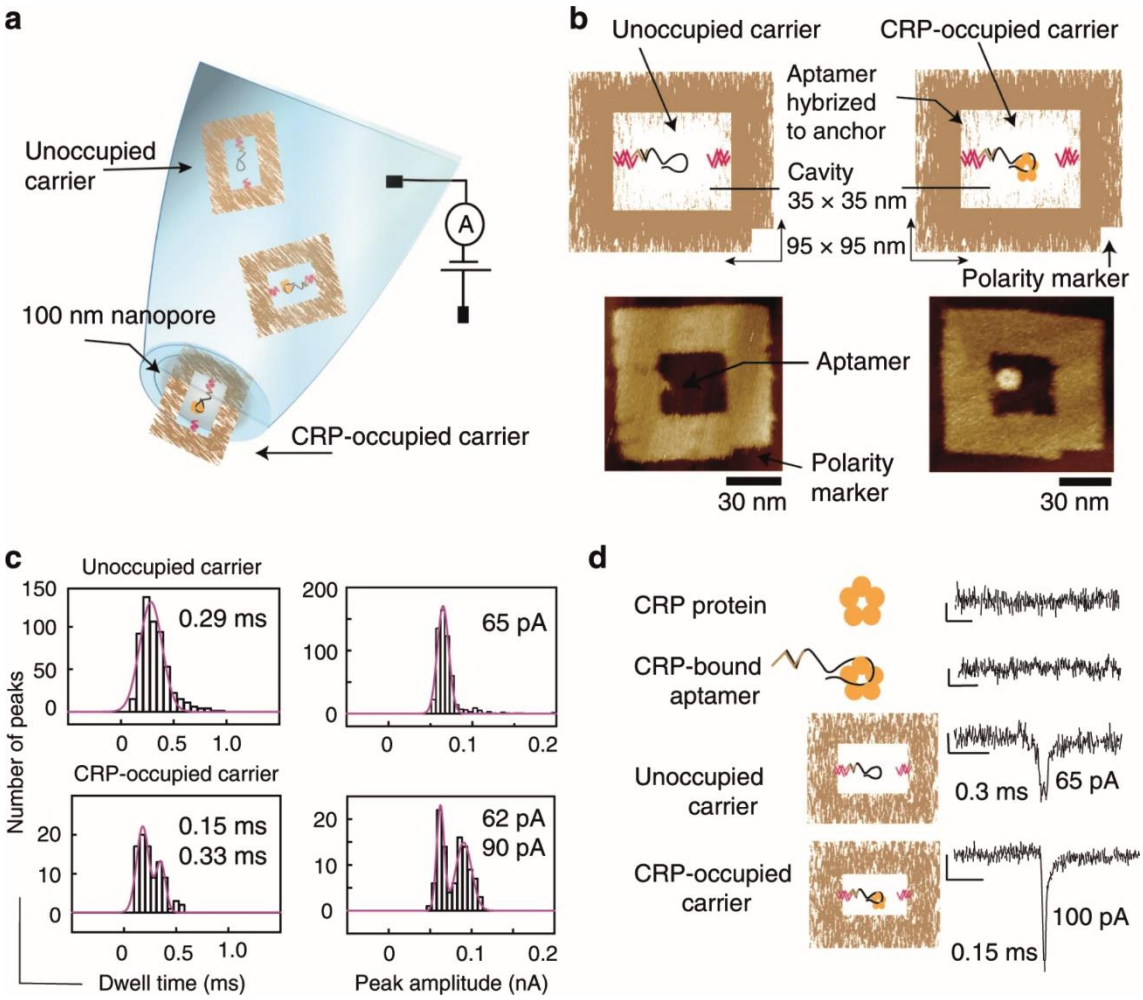

Figure 1:34 DNA origami carrier based biosensors. A) Schematic representation of translocation of unoccupied carrier and CRP occupied carrier. B) Schematic representation of the design and representative AFM micrographs of the unoccupied and occupied DNA origami carriers. The frame DNA nanostructure is ~95 nm × 95 nm in dimension with a 35 nm × 35 nm inner cavity. The DNA origami comprises small nucleotide 'anchors' that protrude into the cavity which facilitate the incorporation of the DNA aptamer via hybridisation. The DNA carrier also includes a polarity marker. c Peak amplitude and dwell time histograms of DNA nanostructure carriers (9 nM) and carriers incubated with CRP at 9 nM concentration, both measured at a final carrier concentration of 500 pM. d Typical ion current signatures upon translocation of CRP molecules, CRP–DNA aptamer complexes, unoccupied carriers and CRP-bound occupied carriers. The scale bars represent 20 pA and 1 ms, respectively. (Adapted from [13]).

DNA origami approach is effective, nevertheless, aptamers has several disadvantages as a binding molecule as discussed in the previous section when compared to protein binders. Hence, protein binders could be combined with the DNA origami carrier to improve the sensing system to detect proteins. Moreover, the DNA origami design used in [13] forms a ribbon like structure as seen in AFM images (Figure 1:35) hence the design could be improved to ensure single molecule events.

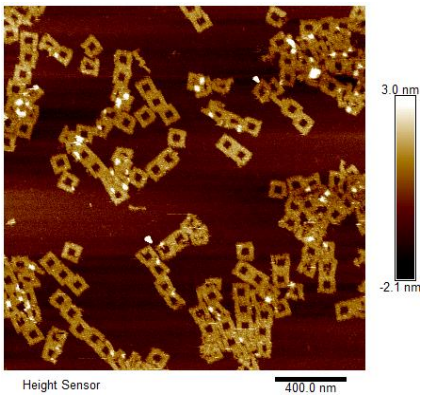

Figure 1:35 AFM image of DNA origami frame used in [13].

There is a rising need for the development of sensors for detecting small proteins as they are relevant in clinical diagnostics. They are crucial for biomarker discovery and disease diagnosis as many small proteins and peptides serve as important clinical biomarkers. This thesis is focused on improving the DNA origami nanopipette sensor by incorporating protein binders and emphasising on detection of small proteins.

1.6 Affimer proteins

Antibodies have been the most commonly used binding proteins in clinical diagnostics. However, their limitations, including large size, multimeric structure, high production costs, and time-consuming development have driven the search for alternative binding proteins [240]. Additionally, antibodies require glycosylation and disulfide bonds for activation, are sensitive to high temperatures, and cannot be efficiently expressed in bacterial systems. To overcome these challenges, several non-antibody protein scaffolds have been developed to display peptide sequences capable of binding specific target proteins. These include ankyrin repeat proteins, repebodies, anticalins, fibronectins, affibodies, and engineered Kunitz domains. These artificial binding proteins offer advantages such as small size, monomeric structure, stability, and ease of expression in *E. coli*. They can be engineered for various applications, including conjugation reactions, fluorescent labelling, and PEGylation for enhanced stability as these protein inherently lack cysteine residues (see 1.2.2). Affimers represent a novel class of binding proteins derived from a consensus sequence of plant-derived phytocystatins or human stefin proteins. These proteins, belonging to the family of protease inhibitors, are small, monomeric, stable, and devoid of disulfide bonds and glycosylation sites [241]. Structurally, affimers consist of a single α-helix and four antiparallel β-strands, with two variable regions (VR1 and VR2). VR1, composed of nine random amino acids, is located between the first and second β-strands, while VR2 is positioned between the third and fourth β-strands [242] (Figure 1:36). It is the variable regions that bind to the specific target molecules. Affimers are generated and screened using phage display, a technique that involves exposing complex phage libraries

displaying diverse binding sequences to immobilized target molecules. The target is typically immobilized either by adsorption onto solid surfaces or by chemical modification, such as biotinylation, followed by binding to a streptavidin-coated surface. After several rounds of selection, phages exhibiting strong target affinity are isolated, sequenced, and cloned into expression vectors [243]. Johnson et al. demonstrated the binding of CRP-affimers to CRP protein using techniques such as surface plasmon resonance (SPR), microarray experiments, and electrochemical impedance spectroscopy (EIS). Notably, one affimer-modified surface exhibited comparable target binding in EIS, whereas sterically bulky antibodies showed a lower response [244]. Additionally, the binding of CEA-affimers to their target protein, carcinoembryonic antigen (CEA), has been confirmed via SPR studies. These affimers have been shown to bind with high affinity (in the nanomolar range) to native glycosylated, partially glycosylated, and deglycosylated forms of the antigen.

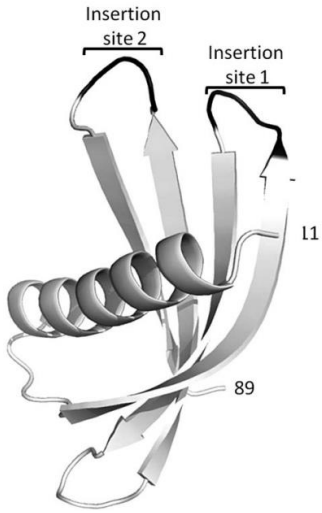

Figure 1:36 X-ray crystal structure of Adhiron92 scaffold (PDB ID no. 4N6T) at 1.75 A˚ resolution. The single alpha helix and the four anti-parallel β strands are shown in white with the insertion sites or variable regions shown in black. (Adapted from [241]).

1.7 Protein-oligonucleotide conjugation

Oligonucleotide-protein conjugation combines the molecular recognition capability of protein with the programmability and complementarity of DNA enabling its use in diagnostic, analytical and nanotechnology applications [245, 246]. Protein provides diverse functionalities such as acting as a specific receptor for ligand molecules while DNA can be used to position a molecule of interest with nanometre precision [247-249]. Such oligonucleotide-protein conjugates can be of diverse application in single molecule techniques which often require sophisticated experimental sample design. The complex sample design w.r.t oligonucleotide-protein conjugates comprises of factors such as high reaction yield, versatility across diverse proteins, and retention of biological activity of proteins. These conjugates have already been applied in single molecule techniques ensuring functionality and accurate assembly of biomolecules of interest [234, 250, 251]. They are widely used in ultrasensitive detection methods [252], DNA nanotechnology [253] and single molecule imaging [254].

Amino acids are the fundamental building blocks of a protein and amongst the naturally occurring amino acids, cysteine is distinguished by the presence of a thiol (-SH) functional group making it an excellent target for site-specific chemical modification. Cysteine is found in less abundance (1.5 %) in proteins hence easier to target a specific site without affecting other amino acids [255]. Moreover, the -SH group in cysteine is highly nucleophilic exhibiting high reactivity with electrophilic group like maleimides forming strong covalent bonds in conjugation reactions [256, 257].

1.8 DNA origami and nanopores in biosensing

One significant tool used for biosensing is nanopore sensing discussed in detail in next section. Although nanopore sensing is a powerful tool for biomolecular detection, the random translocation of proteins and DNA molecules through solid-state nanopores makes it challenging to interpret their spatial organization [258]. To address this, carrier molecules have been explored to facilitate controlled analyte translocation. Previously, stochastic sensing of unfolded proteins was achieved by incorporating protein-binding sites onto double-stranded DNA (dsDNA) carriers, which were then translocated through glass capillaries. This approach eliminated the need for nanopipette surface modification while allowing the DNA carrier to be tailored to specific analytes [251]. DNA carriers have primarily been used to study DNA-binding protein interactions, as demonstrated using silicon nitride (SiN) solid-state nanopores, where protein-bound and unbound DNA can

be distinguished based on current amplitude [259]. While DNA origami presents a promising carrier for escorting analytes through nanopores, understanding its own translocation dynamics is crucial. Studies by Keyser's research group have shown that adding neutral polymers to the electrolyte reduces electro-osmotic flow, facilitating the transport of large DNA structures through nanopores [260]. Recently, Ding et al. designed a ribbon-shaped DNA origami structure whose translocation was guided by surface modifications, such as ATP/aptamer binding (Figure 1:37). Their findings demonstrated that binding ATP or other target molecules altered the structural and electronic properties of the origami, influencing its passage through solid-state nanopores [261]. Additionally, DNA origami has been employed as a carrier in SiN nanopores to model the nucleoporin complex for studying intrinsically disordered proteins [262]. Further advancements include the use of DNA origami conjugated with aptamers for biomarker detection. A notable study demonstrated the detection of C-reactive protein (CRP) from human samples, where an aptamer specific to CRP was thermally annealed to the DNA origami and translocated through a nanopipette. The presence of CRP was identified based on peak shape, amplitude, and dwell time. This approach holds significant potential for multiplexed biomarker detection in clinical diagnostics.

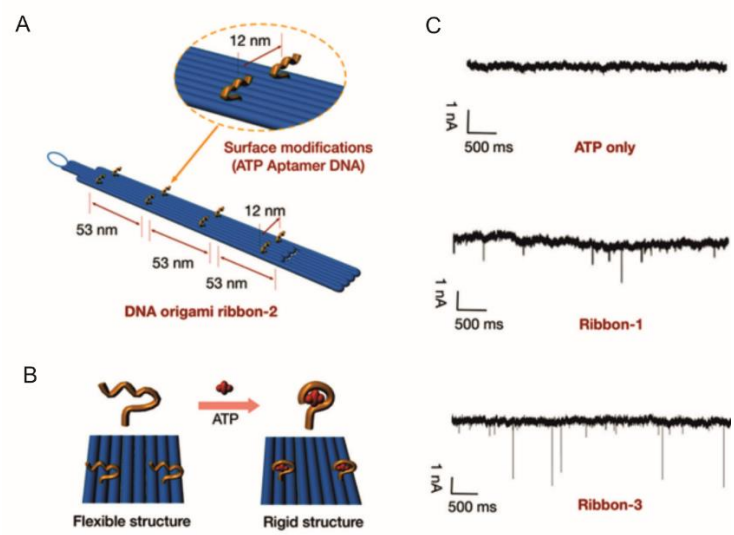

Figure 1:37 A) Design of DNA origami containing 8 aptamer sites for ATP binding. B) Schematic of structural changes induced by ATP binding. C) Current traces for origami translocation, ion current trace on top demonstrate signal for ATP translocation, middle trace is translocation of origami ribbon 1 which has no aptamer sites on it, bottom trace represents origami ribbon 3 which has 8 aptamer sites and saturated with ATP molecules to ensure complete binding (Adapted from [261]).

1.9 Conclusion

In this chapter, an introduction to protein sensing strategies and single-molecule techniques, particularly nanopores and DNA origami, is presented. A detailed review of DNA and DNA nanotechnology is included, covering DNA origami, its applications, and purification methods. Additionally, the chapter provides an in-depth overview of nanopores and their applications in protein sensing. An overview of carrier molecules used in biosensing is also discussed.

The first section introduces the chemical structure and biological function of DNA. The unique complementarity of DNA base pairing is a key feature exploited for the construction of DNA nanostructures. From Seeman's pioneering concept of DNA self-assembly to the development of complex DNA origami designs, the field of DNA nanotechnology has grown substantially, with wide-ranging applications in biosensing, drug delivery, and vaccine development. The applications of DNA origami are enabled by functionalization with DNA strands, proteins, and other biomolecules, which is discussed in this chapter. Furthermore, the use of carrier molecules such as short oligonucleotide binders (e.g., aptamers) and protein-based binders (e.g., affimers) offers distinct advantages for DNA origami functionalization. For applications in areas like vaccine development and drug delivery, robust purification of DNA origami is essential; therefore, different purification techniques are reviewed in this chapter.

The following section focuses on nanopore biosensors. Nanopores have an established role in analytical science and have emerged as powerful platforms for single-molecule detection, enabling real-time analysis of biomolecules through ionic current recordings. Various types of nanopores and their fabrication strategies are described in detail. This chapter also provides an overview of research on nanopores as biosensors. Within this field, nanopipettes have attracted interest due to their low cost, ease of fabrication, and stability. Key properties of nanopipettes—including electrochemical characterization, double-layer effects, resistive pulse sensing, and surface charge—are critical for understanding their single-molecule detection capabilities and are discussed in detail.

Together, this chapter provides a comprehensive foundation for the research presented in this thesis.

Chapter 2 Materials and Methods

All chemicals are acquired through commercial suppliers Merck or Fisher at high purity grade unless otherwise stated. All graphs are generated either through Origin2024b, or python unless otherwise stated.

2.1 DNA origami production

All DNA strands used throughout this study were ordered from Integrated DNA Technologies (IDT-DNA) with standard desalting service. The caDNAno (2.4.7) software was used to design the DNA origami structures [47]. All origamis were folded using the 7249 nt M13mp18 circular single-stranded DNA scaffold (N4040S; NEB). All folded origamis were stored at 4°C or immediately purified.

The caDNAno files of all the origami designs are publicly accessible on the repository: https://archive.researchdata.leeds.ac.uk/1190/

2.1.1 4-Fold Symmetrical Tile and the biotinylated tile origami

The design of the 4-Fold Symmetrical Tile (4FST) DNA origami used here follows the design published by Tikhomirov et al. [263]. The 4FST DNA origami staples are categorized into 4 staple mixtures: interior, bridge, edge and negation, each mixture is a mixture of all relevant staples.

To fold 40µl of the 4FST DNA origami, the folding mixture contained: 10nM M13mp18 scaffold, 12.5mM magnesium acetate, 75nM bridge mixture, 75nM bridge mixture, 75nM edge mixture, and diluted in 10mM tris-HCl, 1mM Ethylenediaminetetraacetic acid (EDTA) at pH 8.0 (1X TE buffer) (93283; Sigma-Aldrich). The folding of the 4FST DNA origami was carried out with a thermal cycler by heating the folding mixture to 90°C for 2 minutes, followed by a gradual temperature decrease from 90°C to 20°C at the rate of 1°C per minute. The temperature was then further decreased down to 4°C until use.

For the biotinylated 4FST DNA origami, one of the standard edge staples (Edg-T1R10C7-DHP) in the edge staple mixture was replaced with a 5’ biotinylated version of the same staple. To fold the biotinylated 4FST, the same procedure as the standard 4FST was used. After the purification of the biotinylated 4FST origami, a total of 20nM streptavidin (434301; Thermo Fisher) was added to the 4FST origami and incubated for 10 minutes at room temperature, then the biotinylated 4FST and streptavidin mixture was subjected to purification again.

2.1.1.1 Dimeric 4-Fold Symmetrical Tile

To generate the dimer 4FST, the edge was replaced with a different set of edge staples that allows the hybridisation between two 4FST. After the folding of the two separate 4FST origamis, the two samples were mixed at 1:1 volume (including all excess staples). The mixture was then heated to 55°C and the temperature was then gradually decreased to 20°C at a 1°C/min rate. The temperature was then further decreased down to 4°C until use or storage at 4°C inside a fridge.

2.1.1.2 4-Fold Symmetrical Frame origami

The basic design principle of the 4-Fold Symmetrical Frame (4FSF) follows the 4FST, thus the folding mixture components and the steps were the same as 4FST except for the differences in staple sequences. For differences in structure, check the staple sequences in the public repository mentioned in 2.1.

2.1.1.3 Frame origami

The design of the frame origami used here followed previously published design by Raveendran et al. [13]. All the staples were pooled together into the staple mixture. The origami folding mixture contains 10nM M13mp18 scaffold, 50nM staple mixture, 5mM tris acetate (pH 7.4), 5mM magnesium acetate and 0.5mM EDTA. The folding of the frame origami was carried out by heating the mixture to 95°C for 5 minutes followed by gradual temperature decrease to 20°C. The temperature was then further decreased down to 4°C until use.

2.1.2 DNA origami purification

All purified DNA origamis were stored in the DNA origami storage buffer composed of 10mM tris acetate, 10mM magnesium acetate, 1mM EDTA unless otherwise stated. All origamis were stored at 4°C and analysed within 2 weeks. All purification procedures were performed in 1.5ml centrifuge tubes unless otherwise specified.

2.1.2.1 SPRI beads selection

HighPrep™ PCR Clean-up System (AC-60050; Magbio) was used for SPRI bead purification of DNA origami. Prior to purification, the bead solution was set on the bench at room temperature for 15 minutes. The beads solution was then vortexed for 30 seconds until a homogenous colour was observed. The 40µl folded DNA origami after the folding reaction was mixed with 32µL of the SPRI beads to achieve the 0.8X volume ratio. The volume for rest of the volume ratio is mentioned in the table below (Table 2-1). The solution was mixed until a homogenous colour via flicking on the tube or pipette mixing, followed by 10 minutes incubation at room temperature on the bench. The tube

was then placed on a magnetic separation rack (commercially available or homemade with 3D printer) for 5 minutes, the magnet pulled the SPRI beads from the solution to form a pellet at the corner of the tube. The clear supernatant was then isolated and discarded by pipette without disturbing the beads pellet. Then, two washes with 500µl of 80% (v/v) were performed and all excess ethanol from the tube was then carefully removed with a P10 pipette. The tube with the beads pellet was removed from the magnetic separation rack and sat on bench for 5 minutes to air dry. The dry pellet was then resuspended in 40µl of the DNA origami storage buffer through pipette mixing to elute the DNA origami from the SPRI beads, followed by 5 minutes of incubation time. The tube was placed back on the magnetic separation rack and the magnet caused the beads to pellet at the corner of the centrifuge tube, a pipette was used to aspirate the supernatant and transferred to a PCR tube. The purified DNA origami would need to undergo a thermal de-clumping procedure (refer to main text for further information about the process). The PCR tube was heated to 50°C using a thermal cycler for 2 mins, followed by a gradual decrease of the temperature to 20°C at the rate of 3°C/min. The temperature was then further decreased down to 4°C until use.

SPRI volume ratio	Volume of origami (µL)	Volume of SPRI beads (µL)
0.4X	40	16
0.6X	40	24
0.8X	40	32
1X	40	40
2X	40	80
3X	40	120
4X	40	160

Table 2-1 SPRI volume ratio for DNA origami purification.

2.1.2.2 S-400 HR spin column filtration

The Microspin™ S-400 HR spin columns (27-5140-01; Cytiva) was used to purify the DNA origami. The spin column was set-up according to the manufacturer instructions. After the removal of the storage solution from the column by centrifugation at 750xg for 1 minute, the spin column was equilibrated with DNA origami storage buffer by adding 200µL to the column followed by centrifugation at 750xg for 1 minute. The equilibration

step was repeated for 2 more times, all the eluates collected up were discarded. The column was then transferred and inserted into a clean centrifuge tube, then 40µl of the folded DNA origami was added to the column and spun down at 750xg for 1 minute. The eluate from the column was collected which contained the purified DNA origami. The volume of the purified DNA origami was checked with a pipette, if the volume was less than 40µl, additional DNA origami storage buffer was added to bring the volume to 40µl.

2.1.3 DNA origami yield measurement

2.1.3.1 Absorption spectroscopy

The concentration of the purified DNA origami was measured via absorption spectroscopy using a NanoDrop™ 2000c Spectrophotometer (Thermo Fisher). The machine was blanked with the DNA origami storage buffer, 2µl of the sample was dotted onto the measurement platform, measurement was performed using an extinction coefficient of 33 mg/ml for A_{260} = 1.

2.1.4 Agarose Gel analysis

For the agarose gel analysis of the DNA origami, a 0.8% agarose gel was used. The high purity agarose (16500500; Thermo Fisher) was mixed with 0.5X TBE, 10mM $MgCl_2$ buffer in an Erlenmeyer flask, the agarose was melted via microwave at full power for 45 seconds, and immediately poured into the casting module of the agarose gel electrophoresis system (Mini-Sub Cell GT Systems; Bio-Rad). Either a fixed mass (25 ng) of the purified DNA origami or a fixed volume (4 µl) of the purified DNA origami was used. The purified DNA origami was mixed with 2µl of the loading dye (B7025S; NEB) and the volume was brought up to a total of 8µl with DNA origami storage buffer. The M13mp18 ssDNA scaffold was prepared in the same way with a fixed mass of 25 ng for gel analysis. The gel was submerged in the 0.5X TBE, 10mM $MgCl_2$ buffer inside a cold room (4°C), the samples were loaded with pipette, 70V was applied for 90 minutes. After the agarose gel has finished running, the gel was transferred to a foil covered container with 30ml of 1X TAE buffer inside, then 10µl of the Diamond nucleic acid dye (H1181; Promega) was used and stained the gel for at least 30 minutes.

For the gel analysis of the DNA ladder, a 0.8% agarose gel was used. The agarose was mixed with 1X TAE, melted with microwave at full power for 45 seconds, and casted with the gel casting module as described above. The samples were prepared similarly to DNA origami but with a different loading dye (B7024S; NEB). The gel was ran at 60V for 60 minutes, followed by gel staining with Diamond nucleic acid dye as described above. The gel imaging was carried out with the InGenius LHR Gel Doc System (Syngene). Further analysis of the gel such as densitometry analysis was done using python script.

2.1.5 Origami-protein mixture clean up

DNA origami purification from excess functional molecules: Folded origami structures were purified using SPRI beads as described earlier. The concentration of origami solution was checked with absorption spectroscopy. 24 nM of C-reactive proteins (CRP; 140-11R; Lee-Bio) was added to 12 nM of purified 4FST origami. The clean-up of the mixture follows the procedure described above.

2.1.5.1 SDS-PAGE analysis

A gradient Sodium dodecyl sulphate polyacrylamide gel electrophoresis (SDS-PAGE) gel was prepared by first preparing a 4% and 20% polyacrylamide gel by mixing 1M Tris-base, 0.3% SDS, pH adjusted with HCl to 8.45 buffer with 30% acrylamide/bis-acrylamide (29:1), 1% ammonium persulfate and 0.1% Tetramethylethylenediamine (TEMED).

For the preparation of the gradient gel, 1 volume portion of the 4% gel mixture was aspirated with a 10 ml serological pipette with an electronic pipette controller, then the same pipette was used to aspirate 1 volume portion of the 20% gel mixture. The serological pipette was withdrawn from the gel buffer tube, an air bubble was then generated by gently pressing the aspiration button from the controller, the air bubble was allowed to raise. After the air bubble disappeared, the gradient gel mixture was dispensed to the narrow gap in the sandwiched 1.0 mm glass plates. 1 mm size comb was inserted, and the gel was allowed to solidify. 15 µl of samples were mixed with 6 µl of 3X sample loading dye (187.5 mM Tris-HCl, 6% SDS, 30% glycerol, pH 6.8) so that the final mixture contains a 1X loading dye buffer and 12 ng of materials. 1X cathode (0.1M Tris base, 0.1M Tricine, 0.1% SDS, pH 8.3; J60992.K2; Alfa Aesar) and 1X anode buffer (0.2M Tris-HCl, pH 8.9) were used for running the gel. 20 µl of sample was loaded into the wells after the gel was solidified. The gel was then run at 200 V for 30 minutes. Staining of the gel was done by silver staining kit (24641; Thermo scientific) following the manufacturer's instruction. The silver stained all organic components including proteins and DNA. The stained gel was visualised and imaged using InGenius LHR Gel Doc System (Syngene).

2.1.6 Intact origami percentage calculation

To calculate the percentage of the intact origamis from AFM images, the following rules were used.

- Structures having at least three sides 80 nm considered as origami tile.
- Structures with at least half of one triangle or all combined missing is considered as a deformed tile.
- Only structures fully in AFM image frame is considered.
- Shape of a square as outline of structure only considered intact.
- The structure should have two parallel lines meeting at a right angle to be considered intact.

2.1.7 Protein functionalised origami percentage calculation

To calculate the percentage of the streptavidin functionalised origami from AFM images, the following rules were used.

- Structures having at least one side 80 nm considered as origami tile.
- Only structures fully in AFM image frame is considered.
- Protein on deformed origami is not considered.
- If two origami structures are linked with one protein, it is counted as one.

2.2 Affimer purification

2.2.1 Expression of CRP affimer in E.coli

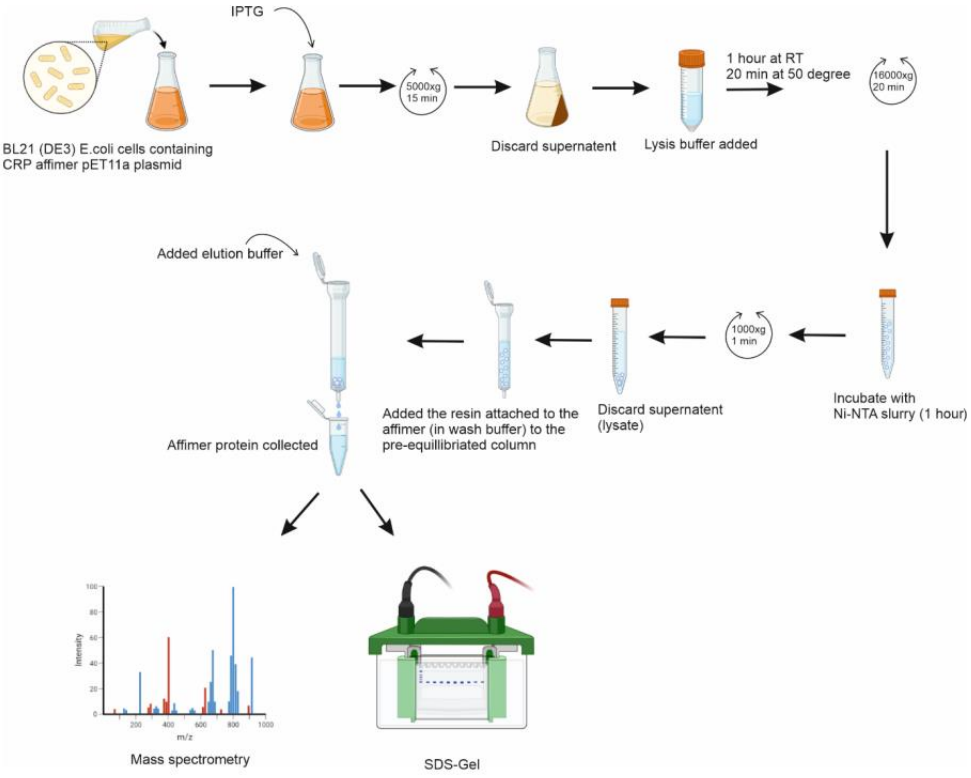

Figure 2:1 Illustration of protocol used for Affimer expression, purification and characterisation.

2.2.2 Transformation

T7 RNA polymerase under control of lacUV5 promoter was used to express C-Reactive protein (CRP) specific affimer protein. The competent BL21 (DE3) E coli cells were thawed on ice. 10 ul of competent cells were added to carbenicillin resistant plasmid containing CRP affimer sequence. The cells with the plasmid were incubated on ice for 30 seconds, followed by heat shock at 42^{o}C in a water bath. This was then incubated on ice for 2 minutes and 200 ul of 19 autoclaved 2YT media (16g tryptone, 10 g yeast extract, 5 g NaCl, 1L) was added, followed by inoculation at 37^{o}C for 1 hour at 230 rpm. 100 ul of the grown bacteria was plated on a LB agar plate (40g LB agar in 1L, autoclaved) containing 100 ug/ml carbenicillin and incubated at 37^{o}C overnight. The mixture (100 µL) was spread onto an LB agar plate supplemented with 100 µg/mL carbenicillin and incubated at 37^{o}C overnight.

2.2.3 Selection, growth and storage

A single colony was picked from the overnight cultured LB agar plate and added to 7 ml of LB broth (LB broth powder, 20g in 1L, autoclaved) containing 100 ug/ml carbenicillin. This was grown overnight at 37^{o}C at 230 rpm. 5 ml of overnight culture was added to 400 ml of LB broth containing 100 ug/ml carbenicillin and grown until it reaches 0.8 at OD600 measured by a UV-Vis spectrophotometer.

Protein production by induction with IPTG was used to initiate the production of the CRP affimers. The culture with OD_{600} 0.8 was induced with 0.1 mM of Isopropyl β-D-1-thiogalactopyranoside (IPTG) and inoculated for 6 hours at 25^{o}C, 150 rpm. The cells were harvested by centrifugation at 4816xg for 15 minutes.

2.2.4 CRP affimer extraction and purification

The bacterial pellet was resuspended with 7.8 ml of lysis buffer (50 mM monobasic sodium phosphate, 300 mM NaCl, 30 mM imidazole, 10% glycerol, 1% triton-X-100, pH 7.4), 80 ul of 10 mg/ml lysozyme, 3.2 ul of 25 U/ul Benzonase nuclease 99%, 80 ul of 100X Halt protease inhibitor, 80 ul of 0.5 M TCEP and incubated on a rotator (Stuart SB2 fixed speed rotator) at room temperature for 1 hour. This was then incubated in a 50^{o}C in a water bath for 20 minutes. The samples were centrifuged at 16000xg for 20 minutes to pellet the cell debris The supernatant was transferred to a tube and centrifuges at 12000xg to pellet the remaining cell debris and insoluble proteins.

Purification of His-tagged affimer 800 ul of Ni-NTA slurry (400 ul resin) (Ni-NTA affinity resin-Amintra;Abcam) was resuspended in 5 ml of wash buffer (50 mM monobasic sodium phosphate, 500 mM NaCl, 30 mM Imidazole, 5 mM TCEP, pH 7.4). This mixture was centrifuged at 1000xg to sediment the resin and aspirated the buffer. The supernatant after lysis was added to the washed Ni-NTA resin and incubated at room temperature on a rotator (Stuart SB2 fixed rotator) for 1 to 2 hours. This mixture was then centrifuged at 1000xg for 1 minute, the supernatant was aspirated and stored to load in SDS PAGE gel. A 5 ml centrifuge column (Thermo Fisher Scientific) was equilibrated by adding wash buffer and allowing it to flow through the column by gravity. The resin containing the attached affimers were resuspended in wash buffer and added to the equilibrated centrifuge column and allowed it to be emptied by gravity flow. 1 ml of wash buffer was added to the column and allowed to pass through the column by gravity. This process was repeated until the absorbance of wash buffer was consistently <0.09. The resin in the column was resuspended with 1 ml elution buffer (50 mM monosodium phosphate, 500 mM NaCl, 300 mM imidazole, 20% glycerol, 5 mM TCEP, pH 7.4). The eluate containing the affimer was collected in a tube. The process was repeated several

times until no more protein was eluted as monitored by A280 reading on a spectrophotometer.

2.2.5 Sodium dodecyl Sulphate-Polyacrylamide Gel electrophoresis

15% polyacrylamide gel was prepared for confirming the size of the proteins. Ammonium persulfate was added immediately before casting the gel and around 6 ml of resolving gel was poured in between two gel plates separated by 1.0 mm spacer. 1 ml of propan-2-ol was added to level the resolving gel. Once resolving gel was solidified, propan-2-ol was removed and stacking gel was poured on top of resolving gel, immediately followed by the insertion of the 1.0 mm gel comb, the gel was allowed to set.

Solution component	**Resolving gel (ml)**	**Stacking gel (ml)**
30% (w/v) Acryamide 0.8 % (w/v) bis-acrylamide	7.5	0.83
3X - Gel buffer (0.3 % (w/v) SDS, 3M Tris-HCl, pH 8.45)	5	1.55
dd H_2O	2.4	3.72
10 % (w/v) ammonium persulfate (APS)	0.10	0.10
Tetramethylethylenediamine (TEMED)	0.01	0.01

Table 2-2: composition of SDS gel

3X Reducing blue protein loading dye (New England Biolabs) was diluted to 1X using protein samples and incubated at 95^{O}C for 5 minutes. The samples were then centrifuged for 1500xg for 2 minutes. The gel cassettes were assembled according to manufacturer guideline and inserted into the gel electrophoresis chamber, the respective reservoirs were filled with cathode buffer (100 mM Tricine, 0.1 % (w/v) SDS, 100 mM Tris-HCl, pH 8.3) and anode buffer (400 mM Tris-HCl, pH 8.8). Precision plus protein dual colour standards (Bio-Rad) marker was loaded into one of the wells and other wells were loaded with respective protein samples. The gels were run at 50 V until the samples entered resolving gel, and then at 100 V until the end. The gels were run until the blue dye reached the bottom of the gel. The gels were then stained with InstantBlue Protein stain for 15 minutes and photographed using GeneSnap software.

2.3 Mass spectrometry

Mass spectrometric analysis was conducted at the University of Leeds, School of Chemistry Mass Spectrometry Service with Dr. Martin Walko. The analysis was performed using a Bruker impact II Q-TOF mass spectrometer equipped with a VIP-HESI source, operating in positive ion mode. Data acquisition was carried out with the scan range set between 50 and 2000 m/z.

2.4 Surface Plasmon resonance

Protein-maleimide conjugation was performed using thiol–maleimide click chemistry to covalently link purified cysteine-containing affimers (or other proteins, ~12 kDa) to biotin-PEG2-maleimide (Thermo Fisher Scientific, A39261). Each 2 mg No-Weigh™ aliquot of biotin-PEG2-maleimide was dissolved in 30 µl of anhydrous DMF (120 mM stock solution). A freshly prepared buffer of 1×PBS with 5 mM TCEP and 3 mM EDTA at pH 7.5 was used throughout. This buffer was generated by mixing 1 ml of 10×PBS, 100 µl of 0.5 M TCEP (prepared by dissolving 0.285 g TCEP in 2 ml ddH_2O, pH adjusted to 7.0 with NaOH), 60 µl of 500 mM EDTA stock, and 8.6 ml of ddH_2O, followed by pH adjustment with concentrated HCl if necessary. Zeba Spin Desalting Columns (7K MWCO, 0.5 ml resin volume, Thermo Fisher Scientific, 89882) were used for buffer exchange. Columns were pre-washed by removing the bottom cap, placing the column in a 1.5 ml Eppendorf tube, centrifuging at 1,000 ×g, discarding the flowthrough, and washing twice with 300 µl of the prepared PBS/TCEP/EDTA buffer, centrifuging each time at 1,000 ×g. Approximately 50 µl of synthesized affimer protein (~3–4 mg/ml, ~300 µM) was diluted with 50 µl of 1×PBS with 10% glycerol or the native buffer. The 100 µl protein solution was added to the equilibrated Zeba column resin, followed by a 15 µl droplet of ddH_2O to ensure elution, and centrifuged at 1,000 ×g for 2 minutes, yielding ~115 µl of buffer-exchanged protein in 1×PBS with 5 mM TCEP and 3 mM EDTA. This solution was incubated for 45 minutes at 4°C on a tube rotator (1.5 ml tubes placed inside a 50 ml Falcon tube). For conjugation, a fresh Zeba column was washed as before but held before protein loading. In a new 1.5 ml Eppendorf tube, 10 µl of 120 mM biotin-PEG2-maleimide (in DMF) was added. The Zeba column was then placed on top of this tube, and the protein was eluted directly into the 10 µl maleimide-containing solution, starting the conjugation reaction immediately. This gave a final linker concentration of approximately 10 mM, in more than 20-fold molar excess over the protein (~500 µM). The reaction mixture was incubated overnight (>12 hours) at 4°C with rotation. The resulting mixture contained protein-PEG2-biotin conjugates and excess biotin-PEG2-maleimide. To remove the excess linker, another Zeba spin column (7K MWCO, Thermo

Fisher Scientific, 89882) was used to buffer exchange into 1×PBS with 10% glycerol. For this step, columns required 2 minutes of centrifugation instead of 1 minute during the initial wash step due to the glycerol content. The final protein solution was collected, and concentration was measured using absorbance at 280 nm (A280), assuming the molar extinction coefficient of the native protein without linker interference. For affinity characterization, surface plasmon resonance (SPR) was performed on a Biacore T200 system (Cytiva) by Dr. Iain Manfield in the Faculty of Biological Sciences of University of Leeds. The SA sensor chip (Streptavidin surface, 4-channel) was used, with flow cell 1 reserved as the reference. The running and start-up buffer consisted of 1×PBS with 0.05% (v/v) Tween-20, and all samples were diluted into this buffer. Ligand proteins were manually injected at 100 pM concentration to achieve an immobilization level of ~15 response units (RU), ensuring low surface density for accurate binding kinetics. In the case of multivalent targets like CRP (C-reactive protein, a pentamer of 115 kDa), surface density was adjusted to reflect a binding stoichiometry of 5:1 (analyte: ligand), ideally targeting an RU increase of 16 for optimal kinetic fitting. SPR injection settings included 3 buffer washes before analysis, sampling at 10 Hz, detection across all flow cells, and analyte injection for 3 minutes followed by a 30-second dissociation phase at a flow rate of 13 µl/min. After each analyte cycle, dissociation was enhanced using 0.1 M sodium carbonate as the regeneration buffer, followed by extra washes with running buffer and stabilization before subsequent injections. Serial dilutions of analyte were prepared from a top concentration of 400 nM down to the low nM range using 2-fold dilution steps in 12–15 tubes. Data were fit using the Langmuir isotherm model to determine the affinity [13].

2.5 CRP functionalisation on DNA origami

The 4FSF origami frame was folded using protocol discussed earlier in materials and method for Chapter 3. The universal strand for bio-functionalisation (USB) was designed to functionalise the DNA origami. The USB included 2 strands, one is termed as the socket or binding point which is complimentary to the internal strand in DNA origami. The other one is called a plug which is attached with the binding protein of interest (biotin or affimer). The plug is complimentary to the socket. The sequence of the strands used as USB are as follows:

Sequence Name	Sequence
4FSF_25_2b:IEdg-T1L1R13C2-USB-Uni_Socket	ACCAACTTTGAAAGAGGACAGAATAAAACGAACTAACGGAACATTTATCACCCGCCATAGTAGA
4FSF_25_2b:IEdg-T2L1R13C2-USB-Uni_Socket	AAAGAACTGGCATGATTAAGACAGTAGCACCATTACCATTAGATTTATCACCCGCCATAGTAGA
4FSF_25_2b:IEdg-T3L1R13C2-USB-Uni_Socket	TTTACAAACAATTCGACAACTTACAGTAACAGTACCTTTTACATTTATCACCCGCCATAGTAGA
4FSF_25_2b:IEdg-T4L1R13C2-USB-Uni_Socket	CAGCTTTCCGGCACCGCTTCTTGTGAAATTGTTATCCGCTCAATTTATCACCCGCCATAGTAGA

Table 2-3 Universal binding strands for DNA origami functionalisation

The sequence marked in red are complimentary to each other. The plugs designed for binding to the USB are:

Sequence Name	Sequence
Affimer plug	Maleimide-TCTACTATGGCGGGTGATAAAT

Table 2-4 Sequence of affimer plug.

4FSF with oligo attachment points

The number of sockets can be increased to 12 total inside the square cavity. The interior binding sockets have expanded beyond the table above, allowing all 12 positions to be turned into socket. These were pre-mixed into specific interior staples mixture at 1.2 µM, simply add 5 µl into the folding mixture. The resultant 4FSF will have different number of binding points (BP).

For attaching different combinations of binding points 5 µL of these interior oligo is added while preparing DNA origami.

Tile	1 BP	2 BP	4 BP	6 BP	8 BP	10 BP	12 BP
T1	R13	R13	R13	R13	R9, R15	R9, R13, R15	R9, R13, R15
T2		R13	R13	R9, R15	R9, R15	R9, R15	R9, R13, R15
T3			R13	R13	R9, R15	R9, R13, R15	R9, R13, R15
T4			R13	R9, R15	R9, R15	R9, R15	R9, R13, R15
Make up TE buffer to the reaction volume of 80 uL							
	15.0 µl	10.0 µl	0.0 µl	0.0 µl	0.0 µl	0.0 µl	0.0 µl

Table 2-5 Combination of binding points for achieving multiple points of functionalisation on DNA origami.

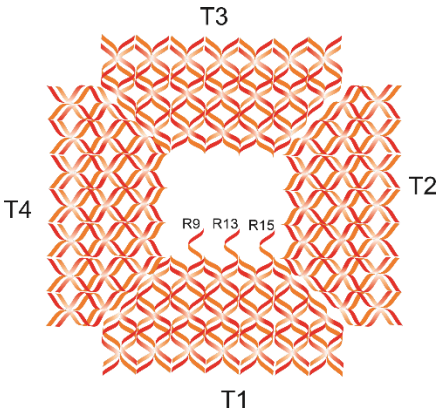

Figure 2:2 Illustration of DNA origami frame 4FSF demonstrating the binding points. R9, R13, R15 could also be placed at T2, T3 and T4.

The USBs are incorporated onto the DNA origami by adding it together with the staple mix during the standard folding. The affimer plug is added in a separate step after the folding of origami. The folded origami structures were purified using 0.8X SPRI method.

The thermal declumping at 50°C was coupled with attachment of oligo-affimer conjugate. The attachment of oligo-affimer to DNA origami was done using a Thermocycler. 5 ul from 2.5 µM oligo-affimer stock was added to 80 ul origami sample to yield a final concentration of 140 nM and heated to 50°C for 2 minutes, followed by gradual decrease to 20°C at the rate of 0.5°C per minute. The temperature was then further decreased to 4°C until use. After the attachment of oligo-affimer to DNA origami, it was incubated with 280 nM of CRP protein for one hour to facilitate binding of CRP to affimer. The sample was further purified using 0.8 X SPRI method to remove excess of CRP molecules. The attachment of CRP protein to DNA origami was confirmed by Atomic Force Microscopy.

2.6 Atomic Force Microscopy (AFM)

The freshly cleaved mica discs were pre-treated with 5µl of 10mM $NiCl_2$, then immediately 5µl of the DNA origami samples were deposited onto the mica by pipetting directly into the $NiCl_2$ solution and left on bench for 5 mins, the samples were topped up with 100µl of DNA origami storage buffer. The DNA origami samples were imaged using a Bruker Dimension Fastscan (Santa Barbara, CA, USA) with Fastscan-D-ss, Fastscan-D or ScanAsyst-Fluid+ cantilevers containing a Si tip. The imaging was carried out via PeakForce tapping with ScanAsyst™ liquid imaging mode via Nanoscope software. All images acquired have a pixel resolution of 1024 X 1024, images were analysed with Nanoscope analysis 1.9.

2.7 Nanopore fabrication

The nanopipettes was fabricated using glass capillaries of outer diameter 1.0 mm and inner diameter 0.5 mm (QF 100-50-7.5; Sutter instrument Co) using laser Puller (SU-P2000 Laser puller; World Precision Instruments, UK).

2.7.1 Nanopore detection of origami monomer and tetramer

The nanopipettes with pore diameter of approximately 100 nm was used of these measurements. Nanopipettes were pulled using a two-line parameter as shown below

Heat	**filament**	**Velocity**	**Delay**	**Pull**
750	4	30	150	80
510	3	40	135	150

Table 2-6 Table with parameters for pulling nanopipettes.

For translocation experiments, the nanopipette was filled 0.5 nM origami structures in translocation buffer (100 mM KCl, 0.005 % Tween 20, 5 mM Tris acetate, 5 mM Magnesium acetate, 0.5 mM EDTA). The origami structures were first diluted to 1 nM

concentration using origami folding buffer (10 mM Tris-acetate, 10 mM Magnesium acetate, 1 mM EDTA pH 7.4). This was then diluted to 0.5 nM concentration for translocation using equal volume of 200 mM KCl, 0.01 % tween 20. The nanopipette with the sample was immersed in an electrolyte bath containing 100 mM KCl. For measurement with PEG, the electrolyte bath was prepared containing 50 % (w/v) 35K polyethylene glycol (94646; Sigma-Aldrich) in 100 mM KCl. The nanopipette was inserted with an Ag/AgCl wire (0.25 mm diameter, Goodfellow UK) which acted as a working electrode and another Ag/AgCl wire was immersed in electrolyte bath which acted as reference/ground electrode. The origami structures were translocated by applying a negative potential to the working electrode placed inside the nanopipette with respect to the reference electrode in the electrolyte bath. The ion current was measured using a MultiClamp 700B patch clamp amplifier (Molecular Devices). The signal was filtered using a low-pass Bessel filter at 20 KHz and digitized with Digidata 1550B. The data was recorded using the pClamp10 software (Molecular Devices). The ion current signals were analysed using a MATLAB script generously provided by Prof Joshua Edel of Imperial College London. The events obtained were further analysed and plotted using Origin 2019b. All the illustration figures were prepared using Coreldraw 2020.

2.7.2 Nanopore detection of functionalised origami

The nanopipette with a pore diameter of 90 nm was used for these experiments and the program used in laser puller is as follows:

Heat	**filament**	**Velocity**	**Delay**	**Pull**
750	4	30	150	80
650	3	40	135	149

Table 2-7 Parameters for pulling nanopipettes

All experiments in this section were performed with 35K 50% PEG in 100 mM KCl as electrolyte in which nanopipettes were performed. All functionalised DNA origami structures were first diluted to 1 nM using origami folding buffer (10 mM Tris-acetate, 10 mM Magnesium acetate, and 1 mM EDTA). This was then diluted to 0.5 nM for translocation experiments using 200 mM KCl, 0.01% tween 20 and filled in the nanopipette. The instrument set-up was the same as used in the previous section (2.7.1).

For investigating whether the yield of protein binding affect the detected change in ion current peaks, DNA origami frame (4FSF) with one binding site was made into 2 nM. Then oligo-affimer construct was added to the origami at 5x, 10x, 50x and 100x excess

by adding 10 nM, 20 nM, 100 nM and 200 nM oligo-affimer construct in a total volume of 40 uL. Similarly, origami structures with 10 binding points were treated with affimer-oligo concentrations of 2.5x, 5x, 10x, 50x, and 100x to further evaluate yield dependency. 2 nM origami was added with 5 nM, 10 nM, 20 nM, 100 nM, and 200 nM affimer-oligo construct in a total volume of 40 uL. To validate that the observed ion current changes were not due to random non-specific interaction of affimer, DNA origami 4FSF was mixed with 10-fold excess of affimer proteins. Affimer proteins were first diluted to 2 μM followed by addition of 2 uL from it to 80 uL of 5 nM DNA origami 4FSF sample.

2.7.3 Event Data Analysis

In this study, I implemented a bootstrap-based statistical analysis to evaluate range-specific characteristics across multiple datasets for all the functional DNA origami analysis. The method was further developed and modified by Dr. Chalmers Chau based on a publicly accessible script (https://github.com/chalmers4c/Bootstrap_analysis).

The analysis began by generating 1,000 bootstrap samples for each dataset through random sampling with replacement, maintaining a consistent sample size of 500 observations. This resampling approach allowed us to estimate the variability of key statistical metrics without relying on parametric assumptions. After generating the bootstrap samples, we categorized the data into predefined value ranges derived from the distributional properties of each dataset, enabling stratified analysis across distinct intervals. These ranges, typically defined as 2, 3, or 4 segments, were determined based on the underlying distribution and used to isolate data characteristics within specific intervals. For each range and dataset, we computed summary statistics, including the mean, median, and effect size. The effect size was measured as the difference between the central tendency (typically the median) of each dataset and that of a designated reference dataset, allowing for a relative comparison of distributions. Confidence intervals for the effect sizes were constructed using the 2.5th and 97.5th percentiles of the bootstrap distributions, providing a measure of statistical uncertainty. Additionally, we calculated the proportion of data points falling within each range, referred to as the population ratio, to understand the distributional spread of the data across segments. To facilitate condition-specific interpretations, we further segmented the results based on unique experimental or observational conditions. This comprehensive, non-parametric approach allowed for robust statistical inference and meaningful comparison of data subsets, particularly valuable in contexts where traditional distributional assumptions may not hold.

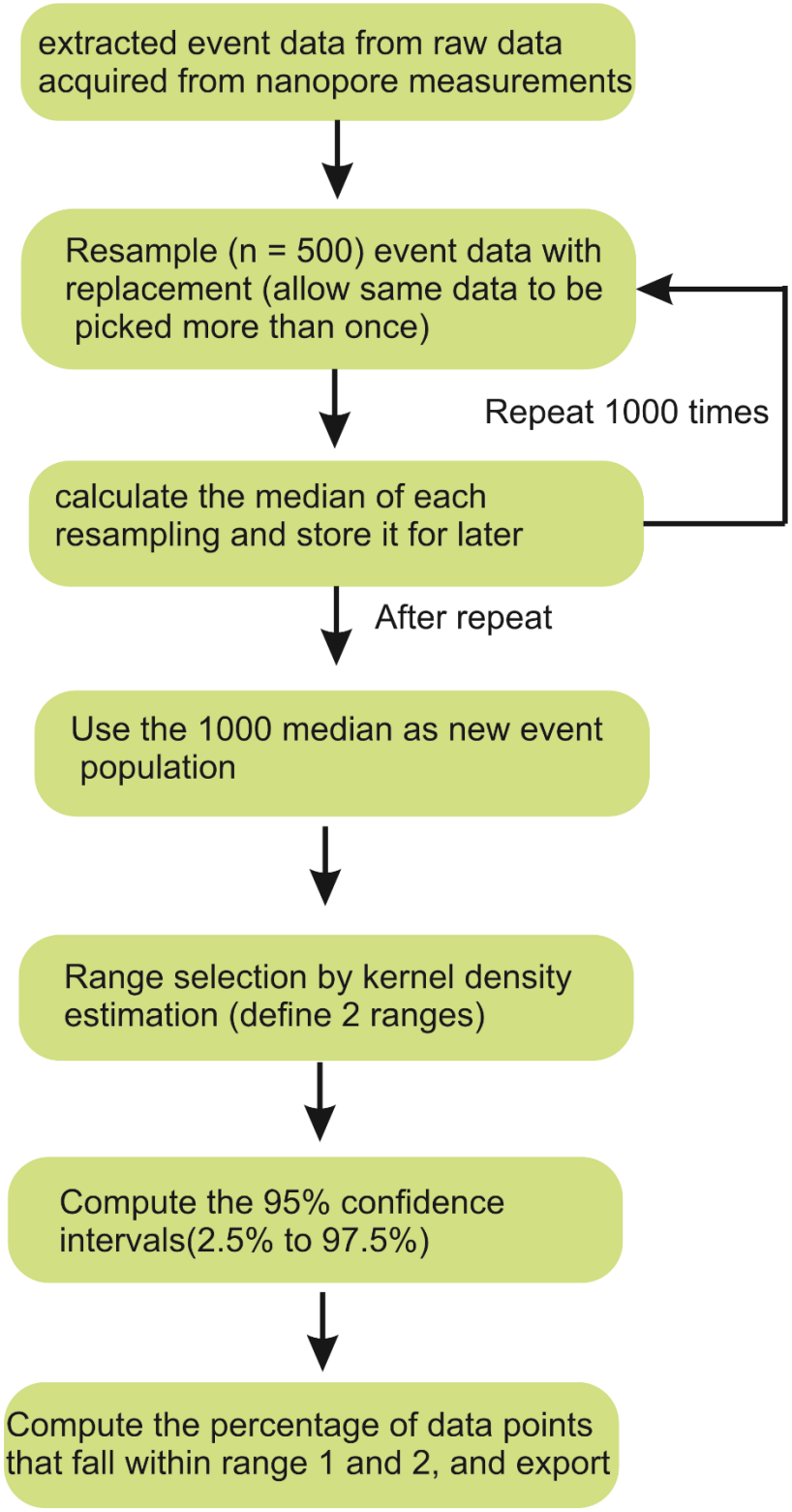

Figure 2:3 Flow chart representing the step-wise process of bootstrapping.

Chapter 3 DNA origami purification using Solid phase reversible immobilisation beads (SPRI).

Introduction

While the assembly and functionalisation of DNA origami are well established, the purification of desired structures from excess staples and functional molecules remains challenging [48]. Although several methods have been developed to remove excess staples and background proteins, an approach that achieves high purification efficiency without compromising protein functionality is still lacking.

A wide range of DNA origami purification techniques are established and are routinely used as described in detail in introduction section (1.2.3). These methods include agarose gel electrophoresis [264], poly (ethylene) glycol (PEG) precipitation [111], molecular weight cut-off (MWCO) membrane filtration and spin-column based filtration method [48, 109, 111]. These methods are not suitable for large volume purifications and require manual operations [48]. Furthermore, when attaching functional molecules, particularly large proteins, to DNA origami, it is often challenging to remove excess proteins, and these proteins can interfere with downstream analytical techniques [114]. In this chapter, I demonstrate the use of Solid phase reverse immobilisation beads (SPRI) to purify DNA origami from excess oligonucleotides as well as background proteins (Figure 3:1). The SPRI beads are paramagnetic microparticles modified with carboxyl functional group on its surface which can reversibly and non-specifically bind to DNA [265]. These beads are widely used in next generation sequencing to select DNA fragments of particular size prior to sequencing [266, 267]. In this chapter, DNA origami purification using SPRI beads is discussed in detail. The aim of the chapter is to employ SPRI magnetic bead-based purification to remove excess oligonucleotides from DNA origami as well as excess proteins and validate the efficiency of purification.

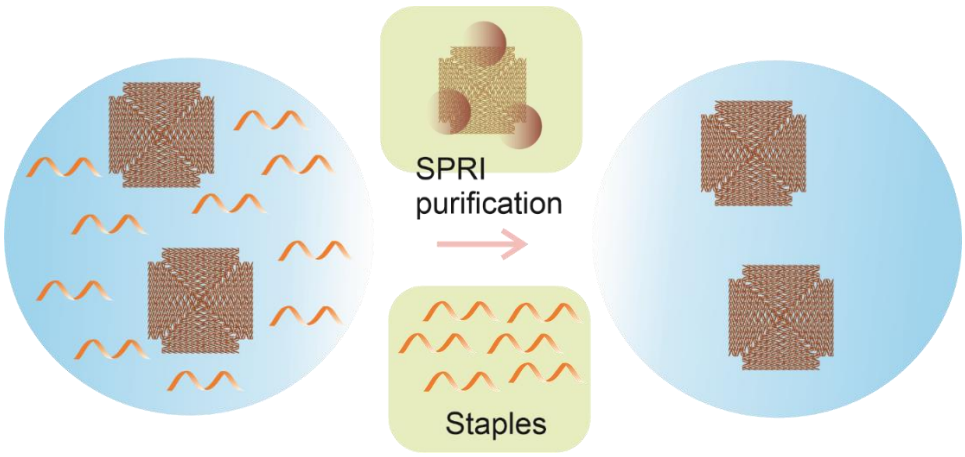

Figure 3:1 Illustration of DNA origami with excess oligonucleotides (on left) and removal of oligonucleotides by SPRI bead purification to obtain purified DNA origami (left). The pink colour square tile structures are DNA origami, small pink comma shaped structures are free oligonucleotides.

Result and Discussion

3.1 DNA origami folding and purification using SPRI beads.

In this section, I demonstrate the use of SPRI clean-up as an effective method to purify DNA nanostructures from excess oligonucleotides. The SPRI beads are suspended in a buffer composed of an alkali halide salt such as NaCl and high molecular weight PEG at certain w/v percentage. The size selectivity of the beads can be adjusted by varying the concentrations of these components [268]. Stortchevoi demonstrated that the traditional size selection range of 150-800 bp can be shifted to 1.5-7 Kbp by changing the concentration of NaCl. Mixing the SPRI beads with DNA will cause the DNA to precipitate onto the carboxyl coated beads through Ψ condensation and subsequently isolated using a magnet [269, 270]. An 88 nm × 88 nm 4-fold symmetrical tile (4FST) DNA origami [263] was selected and used throughout this chapter as the model DNA origami for the validation of the SPRI clean-up (Appendix A - .1). The DNA origami tile was folded from 7249 nt M13mp18 scaffold in the presence of >200 oligonucleotide (Figure 3:2).

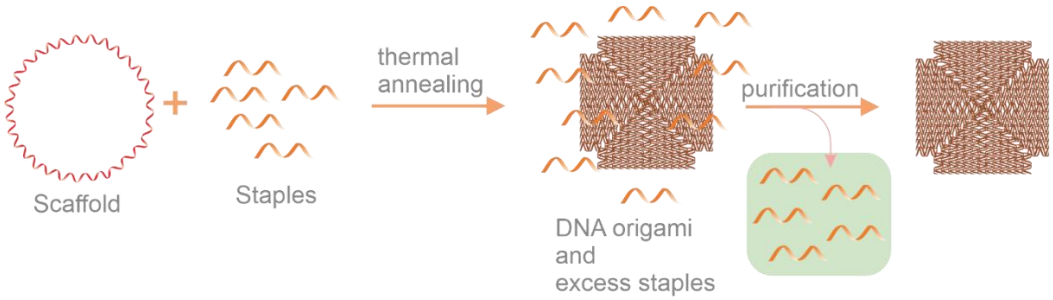

Figure 3:2 Illustration of DNA origami folding from single stranded scaffold DNA (M13mp18) and short oligonucleotides (staples) followed by purification.

The purification procedure involves mixing the unpurified folded DNA origami with SPRI beads and utilise the paramagnetic property of the SPRI beads [271] to enable magnetic separation. The supernatant containing the excess oligo is discarded, followed by washing the beads in ethanol and eluting in origami elution buffer containing Tris-acetate, EDTA and Magnesium acetate (Figure 3:3). The principle of this technique is based on the ability of polyethylene glycol (PEG) to induce a coil-to-globule transition in DNA molecules. This structural compaction increases the exposure of negatively charged phosphate groups along the DNA backbone, promoting interactions with the negatively charged carboxyl-functionalized surfaces of the paramagnetic polymer beads [272]. The salt in the buffer provide ion bridging of negatively charged molecules, allowing the exposed phosphate groups of DNA to bind to carboxyl group of beads [273]. The small excess oligonucleotides (unincorporated staple strands) remain in solution because the conditions are optimised to exclude molecules below a certain size or molecular weight. Therefore, when a magnet is applied, the beads, along with the bound origami, are pulled to the side of the tube, and the supernatant containing the short oligonucleotides are discarded. The beads are washed in 70% ethanol to help remove the residual salts, PEG and other contaminants if any while keeping the origami structures bound to the beads, as ethanol maintains the DNA-bead interaction but prevents solubilisation of DNA [274]. In the next step, ethanol is replaced by an aqueous buffer that restores the hydration and weakens the hydrophilic interaction between the DNA origami and beads [265]. As a result, the DNA origami structure detaches from the bead surface and redissolve in the DNA origami elution buffer.

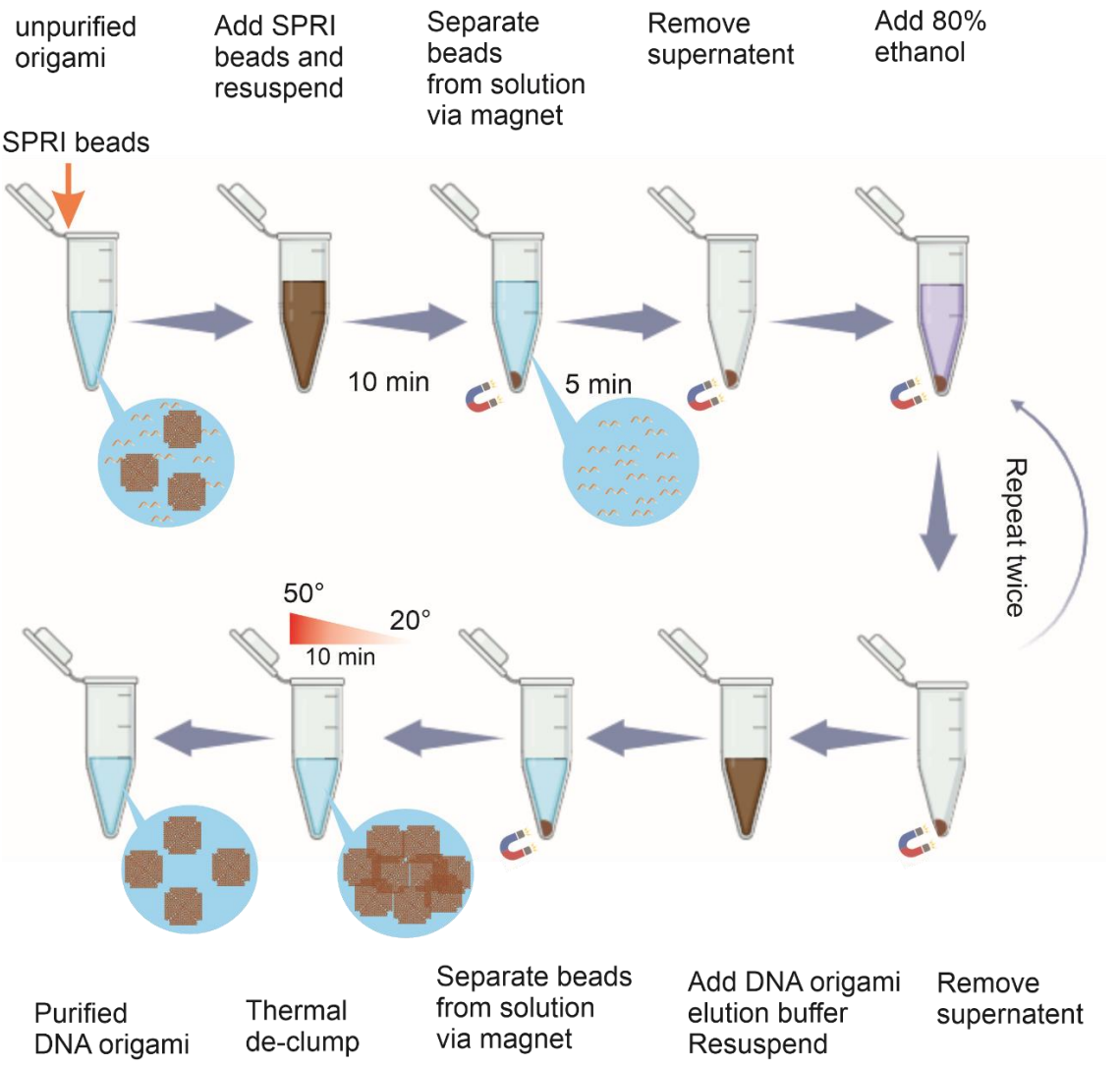

Figure 3:3 The schematic illustration of the SPRI DNA origami purification routine. The folded DNA origami after the folding reaction is then mixed with SPRI beads at a specific ratio, the SPRI beads with the DNA origami together form a beads pellet with the aid of a magnet, the excess staples in the supernatant are removed from the mixture. The beads pellet is washed with 80% ethanol twice to remove excess salt contamination from the SPRI beads buffer and the folding reaction buffer. The purified DNA origami can then be eluted in any buffer of choice (10 mM tris acetate, 10 mM magnesium acetate, 1 mM EDTA), the eluted DNA origami is subject to thermal de-clump procedure prior to finish.

To achieve high quality purification, it is important to optimize the volume ratio between sample and the SPRI beads solution [265, 268]. The volume ratio refers to the proportion of SPRI bead solution relative to the origami volume. For example, a volume ratio of 0.4X means adding 0.4 times the volume of DNA origami sample in SPRI beads. Specifically, for an 80 µL DNA origami sample, 0.4X ratio corresponds to adding 32 µL of SPRI beads. Volume ratios between 0.4X and 4.0X were investigated using agarose gel electrophoresis, the optimal volume ratio is identified as the efficient removal of excess staples from the DNA origami assembly mixture. The folded 4FST origami band migrated slower compared to the scaffold and can clearly be observed as a prominent band in the

gel. As shown in the gel, the excess staples from the folding reaction could be found in the supernatant, suggesting that the SPRI beads efficiently retained the DNA origami and excluded the staples into the supernatant. For the analysis of the supernatant, a fixed volume of sample was added instead of fixed DNA mass. The stronger bands on the lower ratio indicate more staples, due to the mixing of the SPRI beads and folded DNA origami solution, the concentration of materials on the higher ratio size would be more diluted (e.g. 180 µL with 4.0X versus 56 µL with 0.4X), thus it was expected to observe more staples on the lower end due to a fixed volume of samples were loaded.

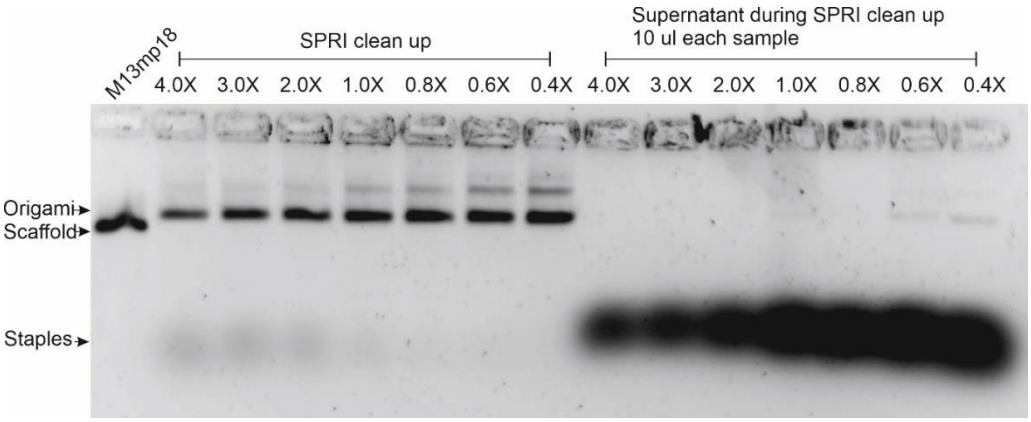

Figure 3:4 Purification of DNA origami using different ratio of SPRI beads, Agarose gel of 4FST origamis after SPRI purification at different volume ratio. During the SPRI purification step, the supernatant was kept and analysed through agarose gel electrophoresis (Figure adapted from [275]).

Gel electrophoresis confirmed that volume ratios higher than 1X resulted in incomplete purification, as indicated by the presence of excess staples after purification (Figure 3:4). A ratio of 1X or lower generated the purest origami as no excess staples were observed in the gel electropherogram. The total mass of origami ranged from ~700 ng to ~1200 ng in a 40 µL reaction and although 4.0X had the highest yield, it could be seen from the gel that it was contaminated by the excess staples in the solution (Figure 3:5). A second band, migrating slower than the origami structures, was consistently observed in all wells. This is likely due to base stacking at helix ends or reduced electrostatic repulsion between the negatively charged DNA backbones, particularly in the presence of Mg^{2+} ions, which can promote the formation of dimers or higher-order aggregates on gels [276].

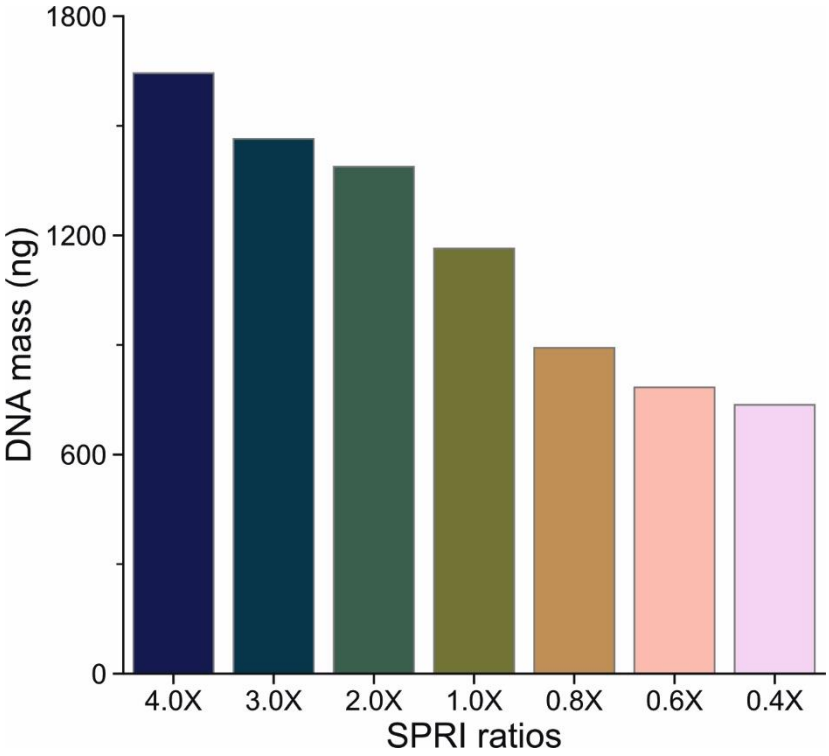

Figure 3:5 The yield of the DNA origami measured by absorbance at A_{260}.

I checked the integrity of the origamis for all ratios using atomic force microscopy (AFM) to demonstrate that the SPRI bead purification did not compromise the DNA origami structures. I observed intact 4FST origami tiles in AFM images for the 4X, 0.8X, and 0.4X ratios, as shown in Figure 3:6

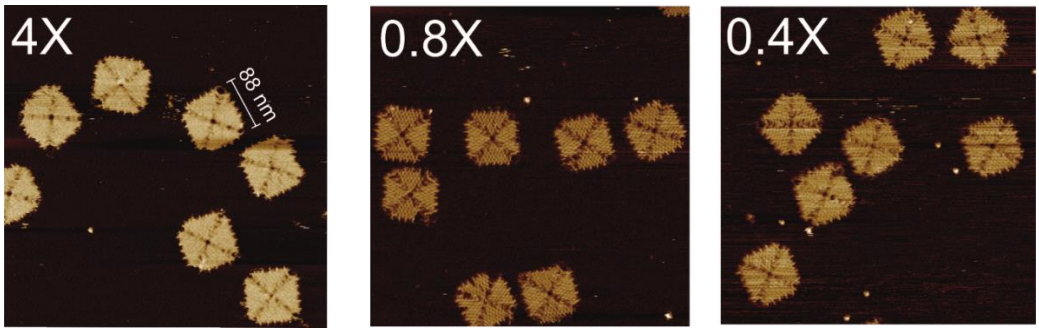

Figure 3:6 500 nm scan size AFM images of 4FST origami tiles purified using 4X, 0.8X and 0.4X ratio of SPRI beads to DNA origami.

AFM images were also acquired for other volume ratios, including 0.6X, 1X, 2X, and 3X. Additionally, for the 0.4X, 0.8X, and 4X ratios, further AFM imaging was performed at multiple scan sizes to assess structural integrity.

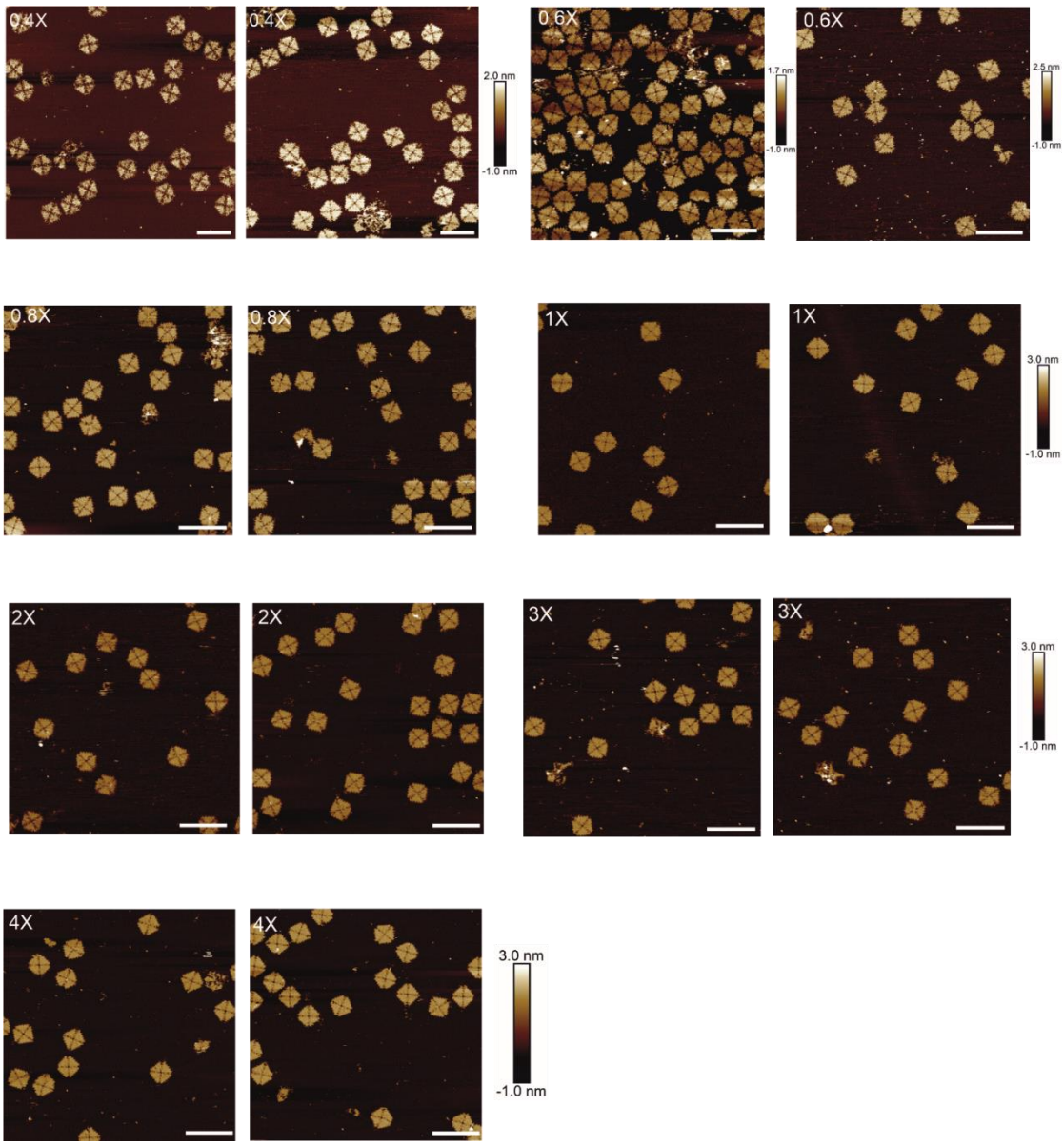

Figure 3:7 AFM images of 4FST origami structures at 0.4X, 0.6X, 0.8X, 1X, 2X, 3X, and 4X ratio of SPRI beads to DNA origami volume. (Scale bar: 200 nm).

While AFM images qualitatively confirmed that the purified DNA origami structures remained intact, their structural integrity was further assessed quantitatively based on the criteria described in Chapter 2 (2.1.6) (Appendix A - .2). A bar graph was plotted with the percentage of intact origami structures following purification using different volume ratios of SPRI beads to origami, ranging from 0.4X to 4X. A high proportion of 90% and above intact structures was maintained across all ratios indicating SPRI purification is an efficient purification technique in terms of retaining the structural integrity of DNA origami. The percentage of intact origami structures were estimated by counting an average of 130 DNA origami structures in AFM images.

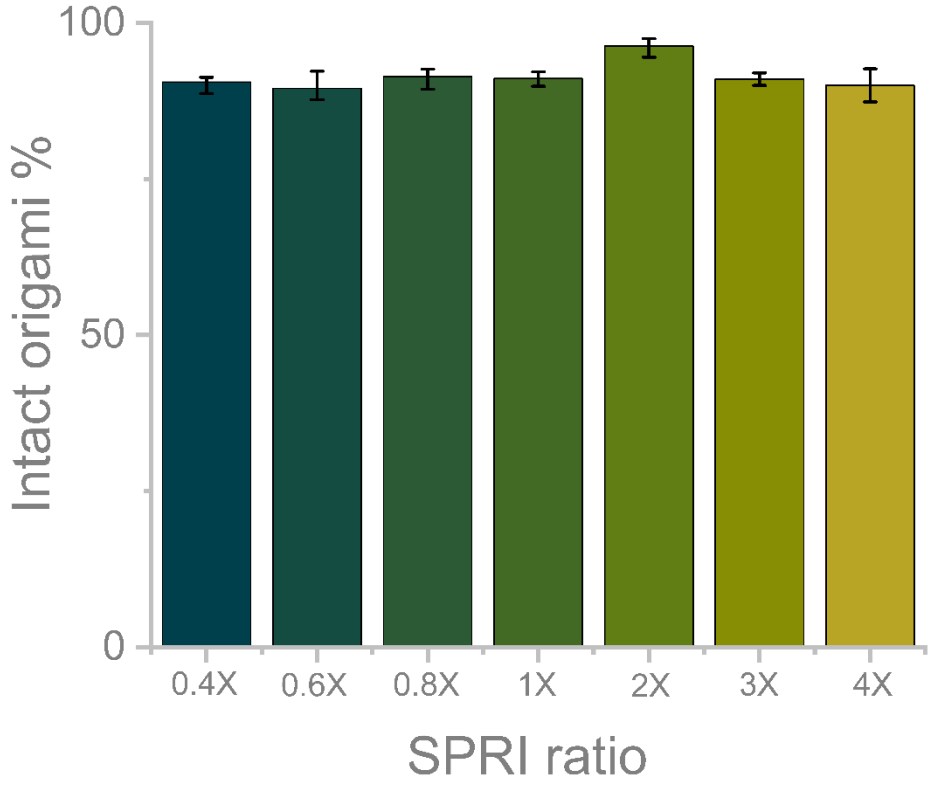

Figure 3:8 Bar graph indicating the percentage of intact origami for different volume ratios of SPRI ranging from 0.4X to 4X ratio. Number of origamis considered for the analysis were 0.4X: 269, 0.6X: 153, 0.8X: 117, 1X: 60, 2X: 141, 3X: 111, 4X: 50. Error bars indicate standard deviation plotted from three repeats.

SPRI ratio	No of intact origami	Total origami counted	% of intact origami
0.4X	241	269	89.5
0.6X	140	153	91.5
0.8X	109	117	93.1
1X	60	65	92.3
2X	141	144	97.9
3X	111	122	90.9
4X	47	50	94

Table 3-1 Table indicating the percentage of intact origami for different volume ratio of SPRI beads.

I chose the 0.8X ratio for all downstream testing. 0.8X ratio was selected due to the absence of excess staples after SPRI purification as observed from the gel electrogram in Figure 3:4. As noticed in the gel, ratios lower than 0.8X could also be utilised for efficient purification. To establish the universal application of SPRI beads in origami purification, I further carried out purification of three different origami designs (dimer 4FST, four-fold symmetrical frame (4FSF), and a frame) using 0.8X volume ratio. All these origami structures were assembled from 7249 nt long M13mp18 scaffold DNA. The 4FST dimerise when specific complimentary strands are added at the edge of the 4FSTs to form a dimer. 4FSF and other frame has a central cavity but are of different dimensions. I tested different designs of DNA origami using 0.8X volume ratio of SPRI beads to validate the effectiveness of SPRI bead purification in removing excess oligonucleotides regardless of origami design. The successful purification was tested using agarose gel electrophoresis and atomic force microscopy. It was observed that all the origami structures migrated to respective position in the gel (Figure 3:9A). Bands with a higher molecular weight than the origami was observed in each well suggesting base stacking of DNA helices and the formation of higher-order structures. The structural integrity of structures was quantitatively confirmed by calculating the percentage of intact origami structures after SPRI purification as validated from atomic force microscopy images. The percentage of intact origami observed for 4FST origami, dimer 4FST, 4FSF frame and frame origami were 93%, 83%, 89% and 77% (Figure 3:9B), respectively. The assembly and purification of the origami structures were also qualitatively checked from AFM micrographs (Figure 3:9 C-F). The high percentage of intact origami structures after SPRI purification confirmed the universal application of SPRI beads for purification of DNA origami structures from excess oligonucleotides.

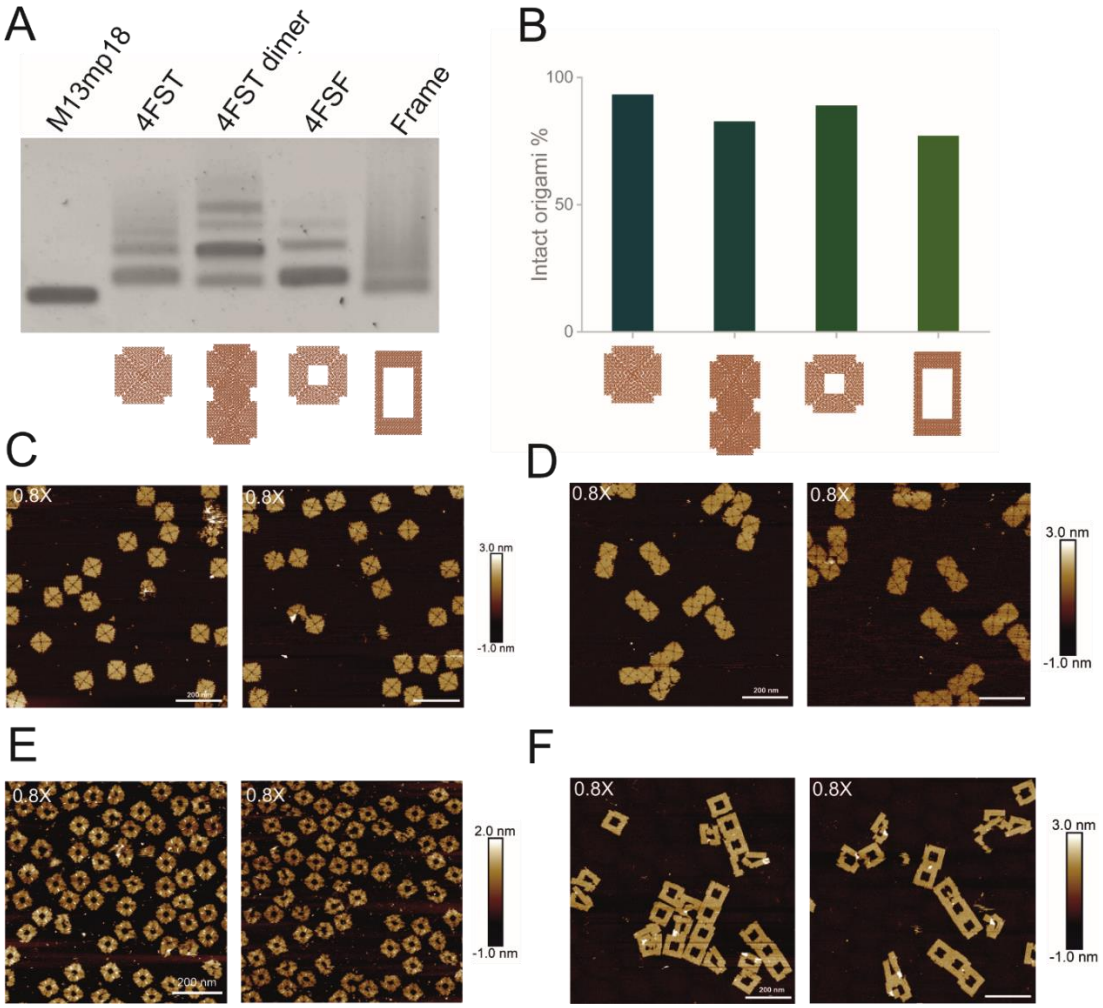

Figure 3:9 A) Agarose gel of origami structures loaded after SPRI purification at 0.8X volume ratio. The wells are loaded with M13mp18, 4FST origami, 4FST dimer origami, 4FSF frame origami and another frame origami. B) Bar graph indicating percentage of intact origami for 4FST, 4FST dimer, 4FSF and frame after 0.8X volume ratio purification. The counting analysis was done from a total number of 117, 23, 109 and 81 origamis from AFM micrographs imaged for 4FST origami tile, dimer 4FST, 4FSF frame and frame origami. C-F) AFM micrographs of 4FST origami, dimer 4FST, 4FSF frame origami and frame origami structures. (Scale bar: 200 nm).

	No of intact origami	**Total origami counted**	**% of intact origami**
4FST tile	109	117	93.1
Dimer 4FST	19	23	82.6
4FSF Frame	63	81	88.9
Frame origami	97	109	77.7

Table 3-2 Table indicating the percentage of intact origami for different designs after 0.8X SPRI bead purification.

While the purification yield was excellent, I observed that the SPRI bead-purified origami clumped together into a cluster (Figure 3:10). I hypothesised that the formation of aggregates was the result of the dehydration caused by the ethanol wash during the purification, as previous studies reported that high percentages of alcohol led to the condensation and precipitation of DNA due to electrostatic interaction [277-279]. Therefore, a thermal de-clumping step was introduced, which allowed the origami aggregates to be dispersed successfully as evidenced in the agarose gel and AFM images (Figure 3:10). This was performed by heating the origami after eluting in the Tris-acetate, EDTA, and Magnesium acetate buffer to 50^{o} followed by cooling down to 4^{o} at 0.5^{o} per minute. The thermal de-clumping step likely facilitated the dispersion of aggregated DNA origami structures by reversing weak inter-origami interactions that formed during the ethanol wash. Baptist et al*.* recently observed similar aggregation after purifying origamis via PEG precipitation [111], which they attributed to stacking interactions between origamis after prolonged centrifugation [280]. Although no centrifugation was involved with our SPRI clean-up method, stacking interactions could also have been enhanced during the ethanol wash step in our method, leading to the aggregation of origamis. The presence of ethanol could induce dehydration of the DNA molecules. Ethanol can reduce the dielectric constant of the solution wakening the electrostatic repulsion between negatively charged DNA backbone. This can favour base stacking and hydrophobic interactions between DNA potentially causing aggregation [281]. In addition to this, DNA origami structures are already condensed on to the paramagnetic beads via PEG and salt mediated interactions. This localisation of origami structures on the beads could mimic the crowding effect that occurs during centrifugation-based pelleting [268]. Importantly, the thermal de-clumping does not lead to degradation of the origami as evidenced by the AFM images in Figure 3:6.

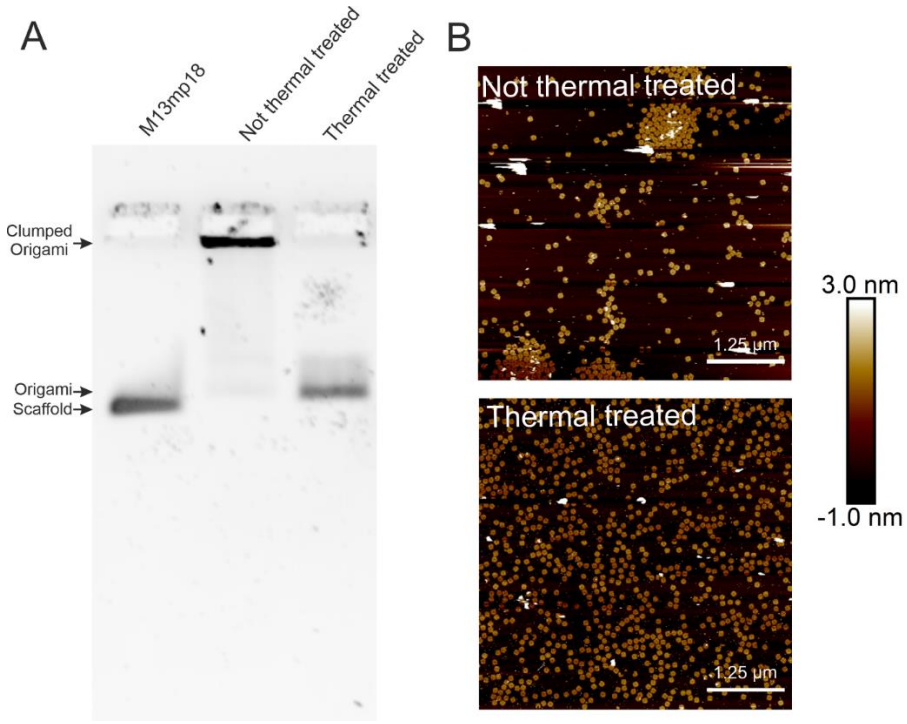

Figure 3:10 The impacts of thermal de-clumping step in the SPRI beads-based DNA origami purification method. (A) The agarose gel shows that without the thermal de-clumping treatment step, the 4FST DNA origamis were not able to migrate through the agarose, suggesting aggregation of the materials. In contrast, the thermal de-clumping treatment of the same sample leads to the 4FST DNA origami to enter the agarose gel and migrate to the expected position. (B) AFM images of the thermal and not thermal treated 4FST DNA origami, as could be seen from AFM, the origami clumped together on the mica for the not thermally treated sample, the thermally treated origami dispersed evenly across the mica surface (adapted from [275]).

3.2 SPRI purification of protein-functionalised DNA origami

For a wide range of applications, DNA origami must be functionalised with fluorophores, proteins, and nanoparticles, *inter alia* [109, 282, 283]. Various approaches for functionalisation of DNA origami and its application are discussed in detail in the introduction section in Chapter 1 (1.2.2). To achieve high functionalisation yields, a significant excess of functional molecules is added. This is essential because the excess functional molecules drive the functionalisation reaction towards completion ensuring that the majority of reaction sites on DNA origami are occupied. This is particularly important if some binding sites on the origami are sterically hindered or less accessible due to the complex architecture of DNA origami. Additionally, excess functional molecules compensate for any loss of molecules attached to origami due to hydrolysis or degradation. High concentration of functional molecules could improve the reaction kinetics allowing reaction to proceed faster and efficiently. However, large excess of unreacted molecules must be removed after functionalisation as their presence can interfere with downstream applications by contributing to background signals, non-

specific interactions and unwanted aggregates while retaining the functionalised DNA origami [13]. Similar approaches, where 5-fold and 10-fold molar excesses of biotinylated oligonucleotides and proteins were used for functionalisation of DNA origami, have been reported and required subsequent purification using different methods [104]. Here I used C-reactive protein (CRP) as a model system to demonstrate the effectiveness of the SPRI bead purification as it has a considerable size (125 kDa) which proves challenging for conventional purification methods such as membrane purification [13, 109]. Moreover, CRP protein is of research interest in diagnostic areas due to its role as a biomarker of inflammation and infection [284, 285]. CRP is an acute phase protein produced by the liver in response to inflammation, tissue injury, or infection [286]. In the following chapters, I will be developing an origami-based carrier functionalised with CRP to develop protein biosensor. CRP was added to the SPRI bead purified 4FST origami at a 2-fold excess, 10 nM of CRP protein is added to ~5 nM of DNA origami structures for maximising the functionalisation. The mixture was then cleaned using the same volume ratio of 0.8X of SPRI beads as for removing the staples after the origami assembly (Figure 3:11).

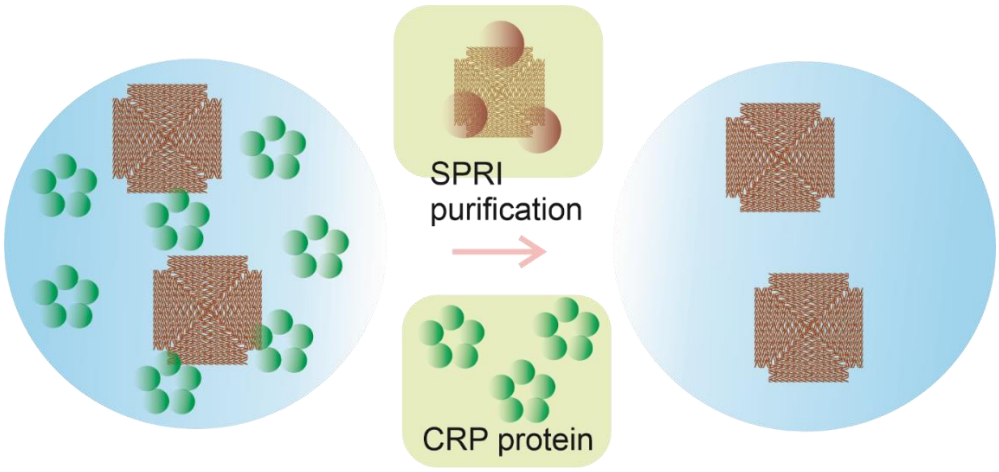

Figure 3:11 Schematic illustration of removal of excess protein from DNA origami using SPRI method.

The DNA origami-CRP mixture was purified using SPRI beads multiple times in succession to ensure the complete removal of CRP as well as to investigate the effect of successive purification rounds. This was to ensure sufficient intact DNA origami structures could be recovered even after multiple rounds of purification. Typically, functionalization of DNA origami, particularly with proteins, requires multiple rounds of purification to ensure complete removal of unbound proteins [114]. Therefore, protein purification was tested over three consecutive rounds. Surprisingly, I observed that CRP was completely removed during the first cleaning step as can be seen by SDS-PAGE gel in Figure 3:12, where the band corresponding to CRP disappeared. DNA origami

denatures under SDS-PAGE due to the presence of SDS, heat, and the absence of stabilizing magnesium ions, which disrupt electrostatic interactions essential for maintaining its structure. These denaturing conditions cause the origami to lose its folded architecture, appearing as a collapsed or smeared band on the gel [249]. 4FST DNA origami tile and CRP protein were loaded as controls for comparison. The 4FST + CRP sample showed a strong band corresponding to CRP control, confirming its presence. A band appearing at the same position as the 4FST origami tile control verified the presence of the 4FST DNA origami tile. I performed three rounds of SPRI cleaning and confirmed the removal of CRP after the first round by the absence of the CRP band.

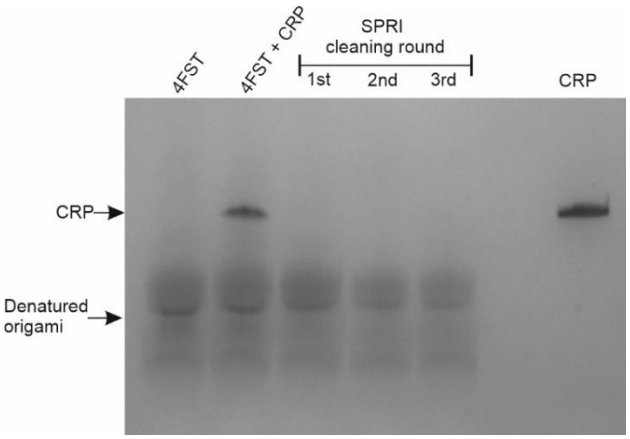

Figure 3:12 Silver-stained SDS-PAGE gel of 1st, 2nd and 3rd round cleaned and uncleaned origami, CRP as loading control.

This effective purification was confirmed by AFM, where the image is dominated by CRP in the background before the SPRI bead clean-up (Figure 3:13, left). Despite applying the same volume of sample onto the mica surface for imaging, the background appears clean after purification (Figure 3:13, right), and the DNA origami structures are predominantly intact.

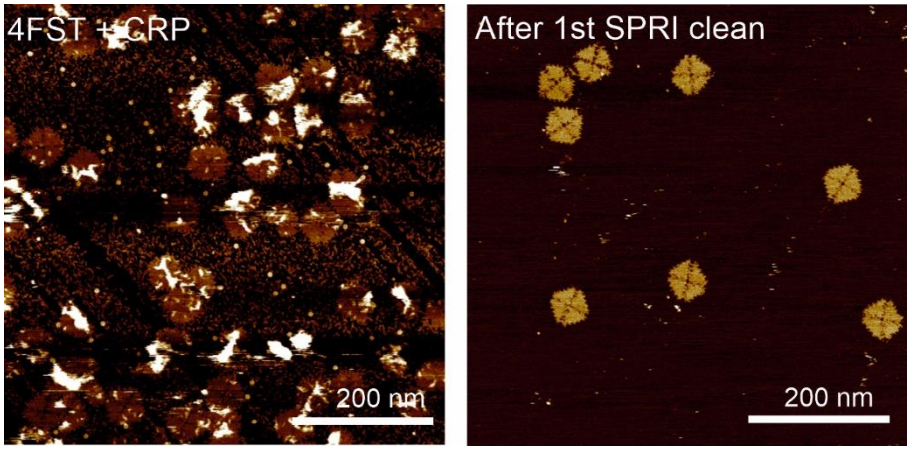

Figure 3:13 AFM images of CRP-DNA origami sample before (left) cleaning and after 1st round of SPRI bead cleaning (right). (Scale bar - 200 nm).

AFM images further confirmed the removal of CRP in all rounds of purification and predominantly intact origamis were observed after each round of clean-up (Figure 3:14). This indicated that SPRI bead technique could be used as an efficient tool for removing larger proteins like pentameric CRP (125 kDa). It is reported that removal of excess of larger proteins from DNA origami are considered challenging. Larger proteins can cluster and form non-specific hydrophobic interactions with DNA origami structures complicating their removal [114]. Although methods like gel electrophoresis and rate-zonal centrifugation is developed to remove excess proteins, they are time-consuming and not scalable [110].

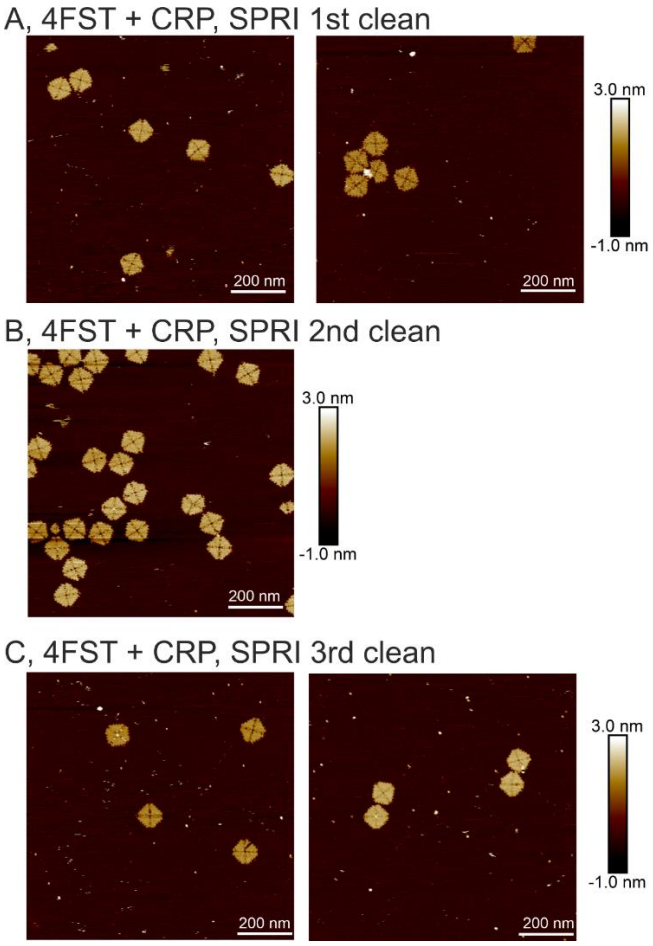

Figure 3:14 AFM images of the SPRI beads purification of the 4FST to remove background CRPs. (A) The 1st round of purification. (B) The 2nd round of purification. (C) The 3rd round of purification.

Next, the structural integrity of the DNA origami structures was quantified from the AFM images and was found to be 92%, 94%, and 88% after first, second and third round, repectively, of SPRI cleaning. The quantification was done by counting the intact and broken structures as per the rules outlined in Chapter 2 (2.1.6) and calculating the percentage of intact origamis (Figure 3:15).

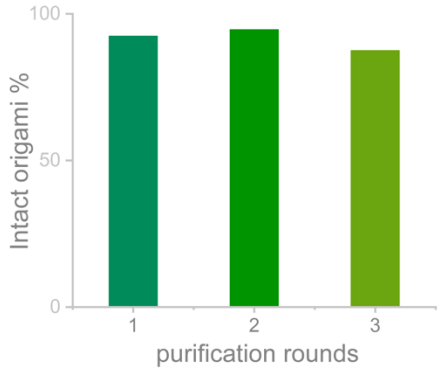

Figure 3:15 Bar graph depicting the percentage of intact origamis after multiple rounds of SPRI purification of excess CRP protein from 4FST origami tiles. The counting analysis was done from a total number of 132, 297, 100 origami structures from AFM micrographs.

Then, I assessed the performance of the successive SPRI bead purifications in terms of retaining DNA origami at different SPRI bead volume ratio and using S-400 HR spin column purification for comparison (Figure 3:16). In general, when DNA origami is used for functionalization, particularly with larger proteins, it often requires multiple cleaning rounds to remove excess functional molecules [114]. In literature, multiple methods are compared for removing excess functional molecules from DNA origami structures, for example, Shaw et al. utilised ultrafiltration and gel extraction to remove large protein like ferritin, however attained limited separation. Though they demonstrated high recovery with a magnetic bead approach, it requires an additional step of invader strand addition for elution and additional biotinylated oligonucleotides [114, 287].

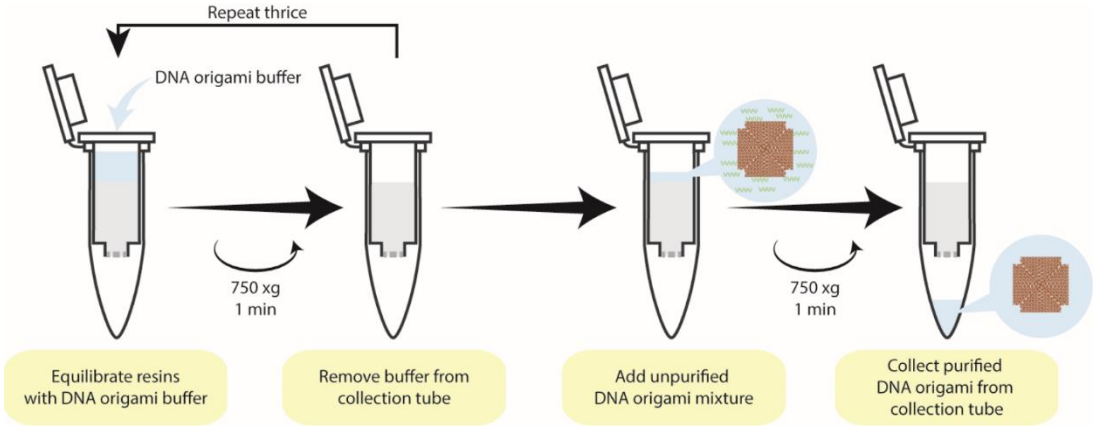

Figure 3:16 Illustration of DNA origami purification using S-400 filtration columns. The resins are equilibrated in DNA origami folding buffer by centrifugation and repeated thrice. The unpurified DNA origami mixture with folded origami and excess oligonucleotides are added to the column and centrifuges to collect the DNA origami in the collection tube (Adapted from [275]).

I folded 4FST origami tiles and did the purification as detailed earlier by using 0.8 X ratio volume of SPRI beads and using S-400 which is an established published method for DNA origami purification [13]. Then, I quantified the masses of DNA at different rounds of purification and used the same reaction volume for the analysis. Although there was a gradual decline in DNA mass after successive rounds of purification, the overall DNA mass at each round remained higher with the SPRI bead method compared to the S-400 columns. I found that SPRI bead purification retained a high proportion of DNA origami structures as quantified by absorbance at 260 nm even after multiple rounds of clean-up with ~500 ng left after three rounds, in contrast to only ~200 ng left after three rounds of S-400 HR spin column purification (Figure 3:17).

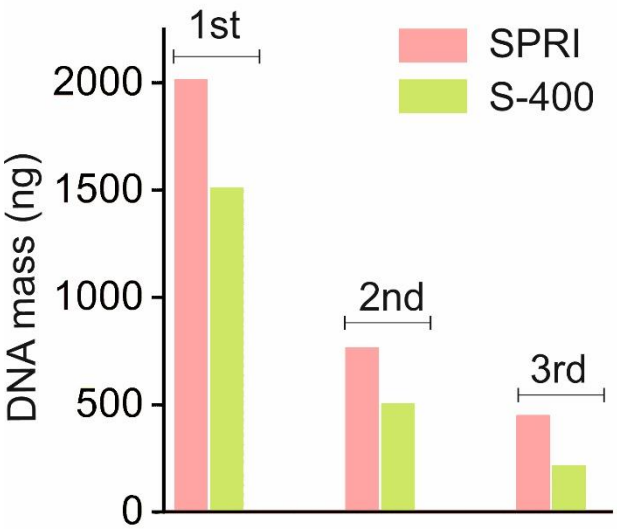

Figure 3:17 Yield of DNA mass of origamis after three rounds of purification using 0.8X ratio beads and S-400 columns.

The amount of DNA origami after successive rounds of purification was also confirmed by AFM, where after 3 rounds of S-400 HR cleaned up, the counts of the DNA origami dropped significantly, and origamis were hard to find through AFM (Figure 3:18). 5 ng/μL of samples are deposited on mica and 10 μm size scans at multiple positions were analysed for spotting DNA origami structures. Counts of 1 origami per image was observed in a 1 μm scan of S-400 purified AFM images in contrast to 4 origami per image for SPRI purified images (Figure 3:18). These findings clearly demonstrate the power of the SPRI bead purification to effectively remove excess functionalisation material from DNA origami with relatively high yield and little structural impact to the DNA origami.

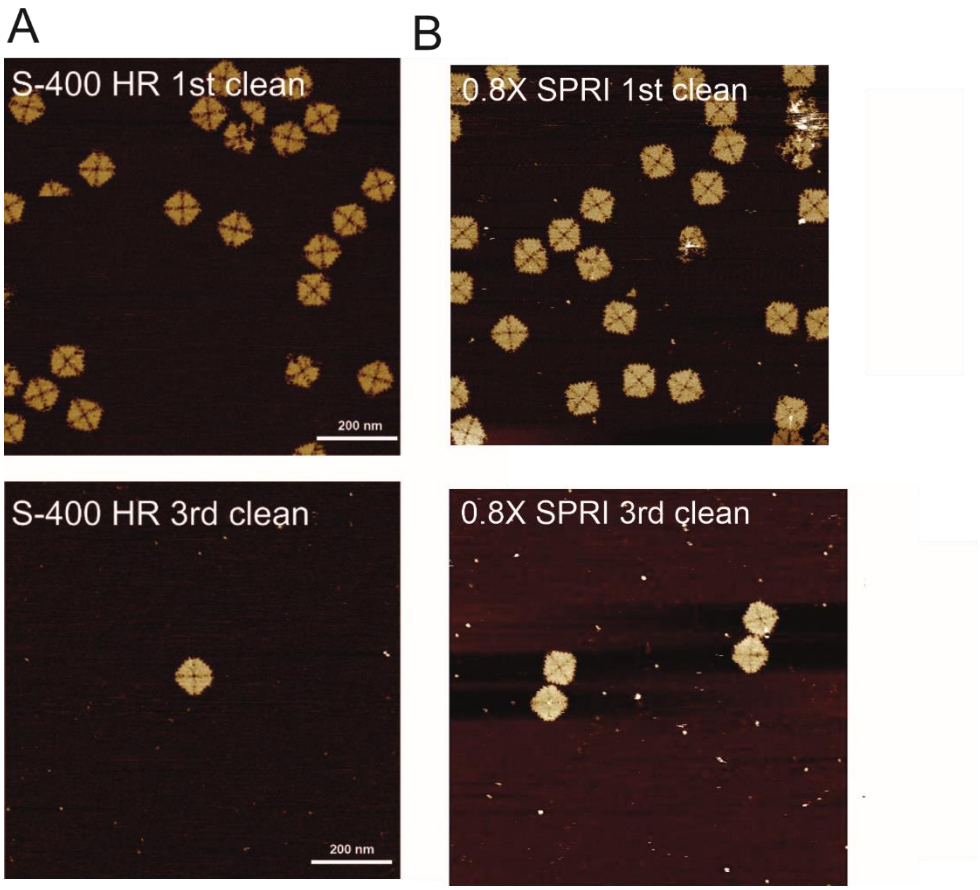

Figure 3:18 AFM micrographs of 4FST origami tiles purified using S-400 and SPRI bead technique.

As mentioned before, DNA origamis are routinely functionalised for different purposes such as in biosensing and diagnostics. Functional biomolecules such as nucleic acids, proteins and fluorophores can be attached to DNA origami to enable specific binding interactions [13, 78, 92, 288, 289]. In scenarios where excess materials are used to functionalise the DNA origami, it's important that the purification method does not interfere with or reverse the functionalisation. Previously, Shah et al. has utilised size exclusion chromatography columns to purify functionalised DNA origami structures, although the method is highly refined, the procedure is long, tedious and results in low yield of functionalised DNA origami. Several other methods such as ultracentrifugation, gel electrophoresis, and PEG precipitation are also utilised, however, the final yield is observed to be low or might contain contaminants from the purification procedure [110, 111, 114, 287]. The SPRI bead purification method could serve as a gentle yet high yield method which do not interfere or reverse the functionalisation from results obtained in the previous section. To test this, the functionalisation of DNA origami 4FST tile with streptavidin through interaction with a biotinylated staple strand was investigated. Biotin-streptavidin interaction is widely used as a model system due to their strong binding affinity (Figure 3:19) [109, 290]. The biotin-streptavidin interaction is considered to be

one of the strongest known non-covalent biological interaction ensuring stable binding [291]. Streptavidin is a tetramer protein comprising of four binding pockets forming a ring like structure. Each of the four identical subunit is capable of binding to one biotin molecule [292]. The biotinylated oligonucleotide is incorporated on one of the edges of the DNA origami as edge modification is much easier compared to modifying the internal structure of origami. The edge sites are more accessible allowing efficient hybridisation and functionalisation without disrupting the folding. The biotinylated oligonucleotide is incorporated during the folding of DNA origami 4FST tile followed by incubation with streptavidin. The origami-streptavidin mixture was purified using 0.8X volume ratio of SPRI beads. The functionalisation of streptavidin was confirmed from AFM images which showcased a bright spot at the one of the edges of the DNA origami indicating streptavidin attachment (Figure 3:19).

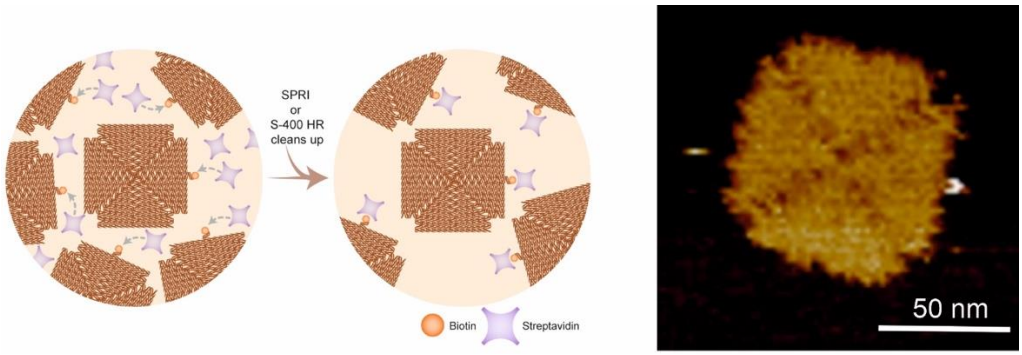

Figure 3:19 Illustration of streptavidin functionalisation to DNA origami via biotinylated oligonucleotide and its purification (left). AFM micrograph of streptavidin functionalised on DNA origami 4FST tile (Scale bar: 50 nm).

SPRI bead clean-up procedure was employed alongside the S-400 HR spin column filtration on the origami after incubating the biotinylated origami with streptavidin at 2:1 molar ratio. 20 nM of streptavidin was incubated with biotinylated 4FST DNA origami structure and the functionalisation efficiency were analysed from AFM images. The presence of streptavidin was qualitatively assessed first by spotting the bright spot at one of the edges of the 4FST DNA origami tile. Interestingly, I found two 4FST tile origami linked together as a dimer through a streptavidin molecule (Figure 3:20B). This is because of the tetrameric structure of the streptavidin with each binding pocket specific to a biotin. I assume that the biotin of two 4FST tile might have linked together through two different binding pockets of streptavidin. Next, I quantified the streptavidin functionalised origami from the AFM images based on the rules established in Chapter 2 (2.1.7). As per the rules, the two origami structures linked with a streptavidin is counted as one. The percentage of intact streptavidin functionalised origamis, defined as the percentage of origami that retained the streptavidin, was quantified by AFM after

purification with SPRI bead and S-400 method(Table 3-3). I found that SPRI purification led to a high percentage (85%) of streptavidin functionalised origami, compared to S-400 HR filtration where only about half (46.6%) of the origami had streptavidin bound after the clean-up, demonstrating the excellent performance and advantage of SPRI bead purification for applications where functionalised origami are required (Figure 3:20 A). This type of quantification is reported previously by Shaw et al. where they used a magnetic bead capture method for purification of DNA origami bundle from excess biomolecules like Alexa488, IgG and ferritin and observed a recovery yield of 70%, 57% and 30%. I have observed better recovery yield (85%) using SPRI bead method for the 4FST origami tile purification from excess streptavidin, though it needs to be investigated if a larger protein functionalised through more complex conjugation strategy would affect the yield recovery of functionalised origami.

A

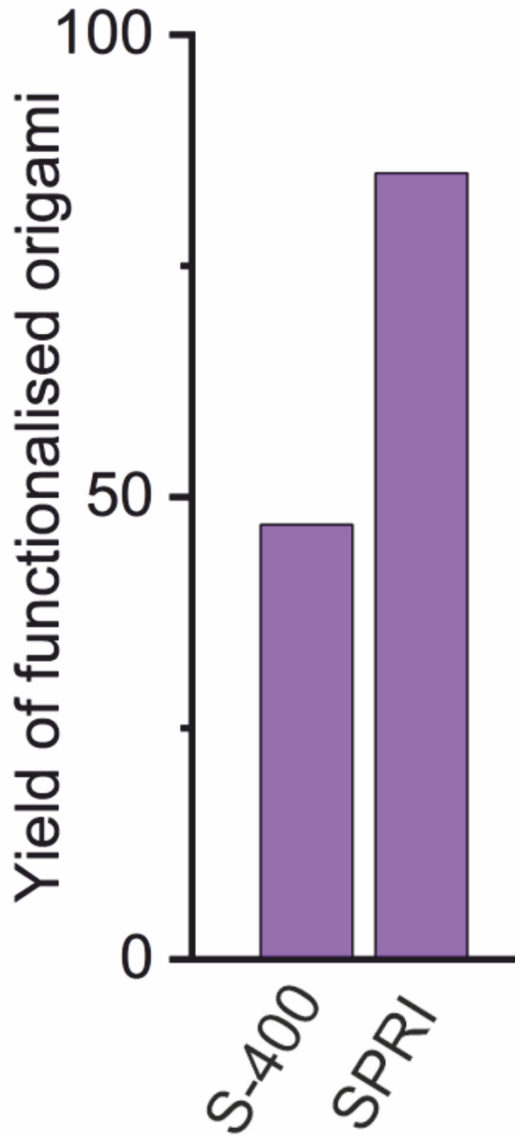

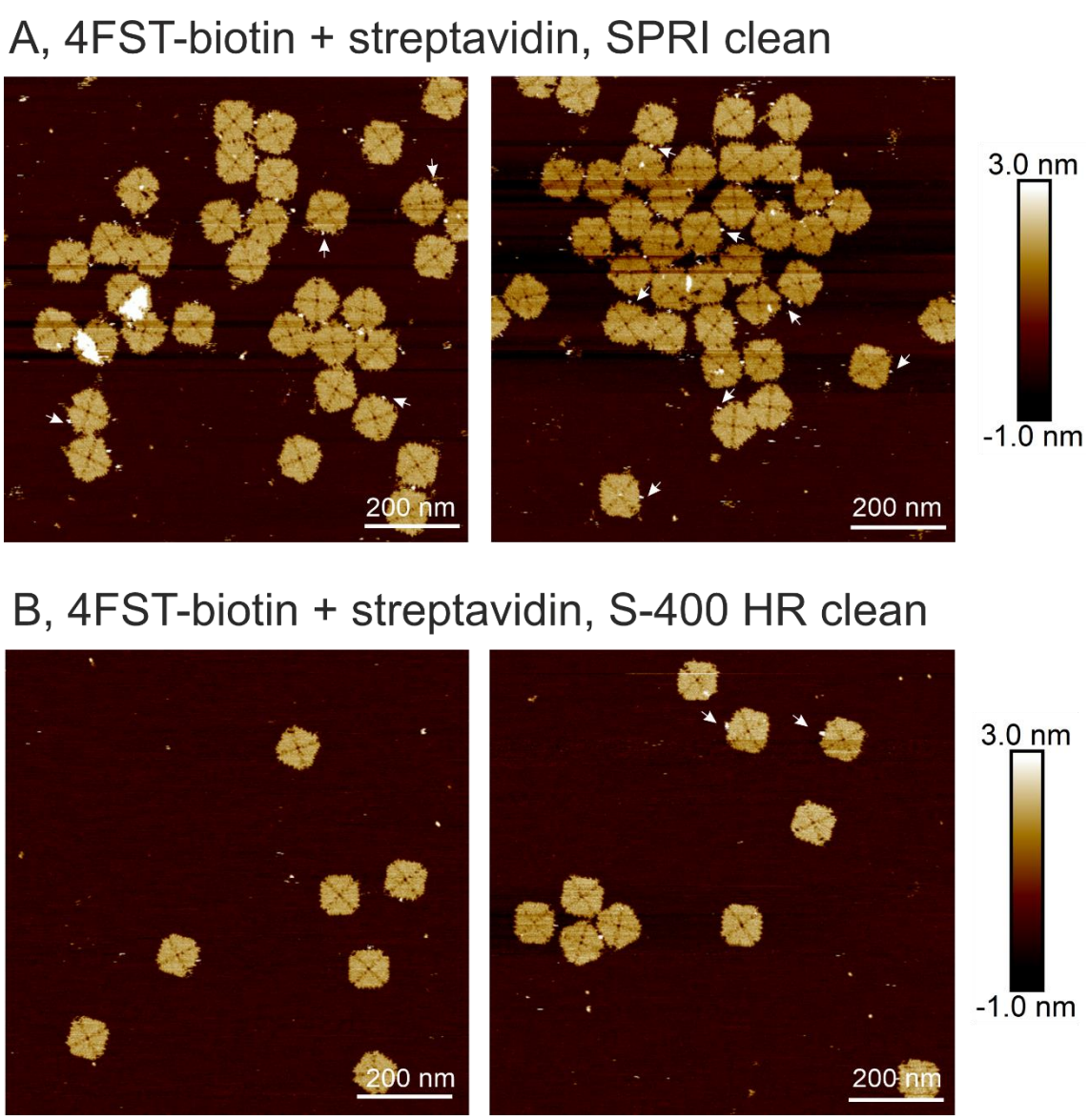

Figure 3:20 A) Bar graph indicating total yield of streptavidin functionalised 4FST origami tiles purified using S-400 columns and 0.8X volume ratio SPRI beads. B) Comparison between the SPRI and S-400 HR spin columns on the streptavidin functionalised biotinylated 4FST DNA origami. The white arrows indicate the streptavidin binding.

Method name	Streptavidin-functionalised origami	Total origami counted	% of functionalised origami
0.8X SPRI	102	120	85
S-400	49	105	46.6

Table 3-3 The quantification of streptavidin functionalised origami from AFM images for S-400 filtration and 0.8X SPRI method.

Conclusion

In this chapter, I have successfully demonstrated the use of SPRI beads in purifying nanostructures not only from excess staples, but also from excess functional molecules particularly proteins. I analysed the optimum volume ratio of beads to use for efficient purification of DNA origami and optimised that the ratio volume from 0.4X to 1X perform well for purification. Magnetic bead purification is reported previously to purify DNA origami from excess biomolecules. This method utilises DNA strand invasion for purification thus needs an additional invader strand for release of purified structures [114]. Similar magnetic bead purification needs magnetic beads to be modified and involves folding of origami on the beads followed by strand invasion. [287, 293]. The main advantage of the SPRI method I have developed is that it is universal and does not require any additional chemical coupling of DNA origami to the surface of beads. I tested this by applying the SPRI bead technique on multiple designs of DNA origami and recovering high yield for all the designs of purified origami. Compared to other methods, the SPRI technique does not require centrifugation [111], additional chemical modifications of the origami [287], and is suitable for multiple rounds of purification without losing the yield. Though centrifugation is routinely used for purification in the form of PEG precipitation [111] or ultracentrifugation [110], it is often tedious and require large instruments.

Importantly, I checked the efficacy of SPRI method for removing excess functional materials from DNA origami. By mixing CRP protein, which is a large protein typically used for developing diagnostic sensor with DNA origami and employing SPRI purification, I was successful in proving that CRP protein could be removed after the first round itself. I tested the efficiency of SPRI bead purification on multiple rounds and was able to recover good yield even after three rounds of purification. Multiple rounds of purification is relevant while purifying complex large proteins which are always added in excess amount for functionalisation to enable maximum binding efficiency [114]. Furthermore, I checked whether the method could retain biofunctionalized molecules on DNA origami without reversing the functionalisation. For this, DNA origami was incorporated with biotinylated staples and conjugated with streptavidin. The streptavidin-origami purification using SPRI was compared with S-400 filtration method and proved that SPRI method perform better especially when multiple rounds of purification are involved. Testing with large proteins was done in this chapter only mixing the protein (CRP) with DNA origami, therefore it needs to be further investigated if complex conjugation strategies and design of DNA origami would perform different than what was performed here. This will be validated in the Chapter 5 with the 4FSF frame origami

described earlier in this chapter where a DNA origami carrier is developed for specific attachment for CRP using affimer proteins.

SPRI technique only requires basic laboratory instruments, tubes, pipette and magnet thus can be coupled to a robot for automation and scaled up expanding its application in industry sectors. This is implemented successfully in Mohanan et al., where SPRI bead purification discussed in this chapter is performed on a robot and found to recover high yield of purified origami structures [275]. This could be of relevance in research involving handling high volumes of DNA origami and parallel purification such as in DNA origami related drug delivery and vaccine development [10, 96].

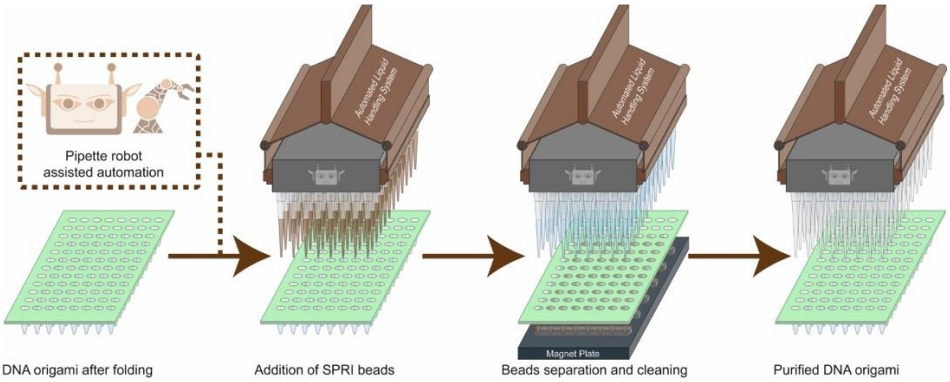

Figure 3:21 Schematic illustration of coupling SPRI bead purification with liquid handling robot. (Adapted from [275]).

SPRI method is utilised for purification of CRP functionalised DNA origami structures in Chapter 5 which will be discussed there. This functionalised origami structures are then used in Chapter 6 for developing a nanopipette based biosensor. Therefore, SPRI method could have application involving DNA origami functionalisation and purification and can be utilised as an established procedure while developing diagnostic biosensors. This chapter discussed the validation of SPRI method in terms of optimising the correct conditions, efficiency of the method, application of the method and comparison to other available purification method.

Chapter 4 Conjugation and Purification of Oligonucleotide-Protein Complexes.

Introduction

Covalent attachment of proteins to oligonucleotide is a commonly used strategy allowing controlled conjugation at specific sites with accurate stoichiometry. Among this, thiol-maleimide chemistry is widely used due to its high selectivity, rapid kinetics under mild conditions, and formation of a stable, irreversible thioether bond between cysteine residue and maleimide [294]. The reaction between a thiol (-SH group) and a maleimide generate a thiosuccinimide product and is generally called as a click chemistry reaction (Figure 4:1) [295]. The reaction proceeds via a Michael addition where the thiol acts as a nucleophile and attacks the electrophilic double bond of maleimide ring releasing a proton (H^+) as a by-product resulting in the formation of a thioether bond between thiol and maleimide (Figure 4:2 - inset).

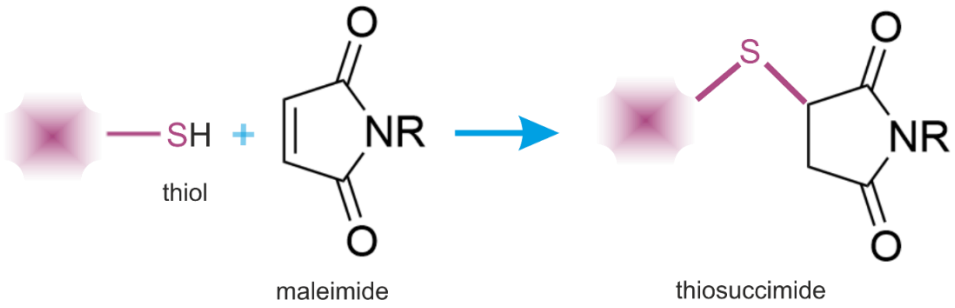

Figure 4:1 Illustration of reaction between a free thiol (-SH) and maleimide producing thiosuccinimide.

The aim of this chapter is to develop a stable oligonucleotide-protein conjugate comprising of cysteine labelled affimer protein specific to C-reactive protein (CRP) and maleimide labelled oligonucleotide (Figure 4:2). Affimers are small, engineered monomeric binder proteins (12 kDa) that bind to specific targets with high affinity and specificity using their variable loops (Figure 4:2) [241, 296]. They are thermally stable, lack glycosylation sites and disulfide bonds, easily produced in systems like *E.coli* and are widely used in diagnostics and research applications [240]. The functionality of the affimer is validated in this chapter using an SPR assay. Affimers are discussed in detail in the introduction section of this thesis. The CRP protein is a pentameric infection biomarker produced by the liver in response to inflammation and is used in this study as a target against affimer [297]. The oligonucleotide-affimer conjugate is used for functionalisation of CRP protein to a DNA origami described in the next chapter.

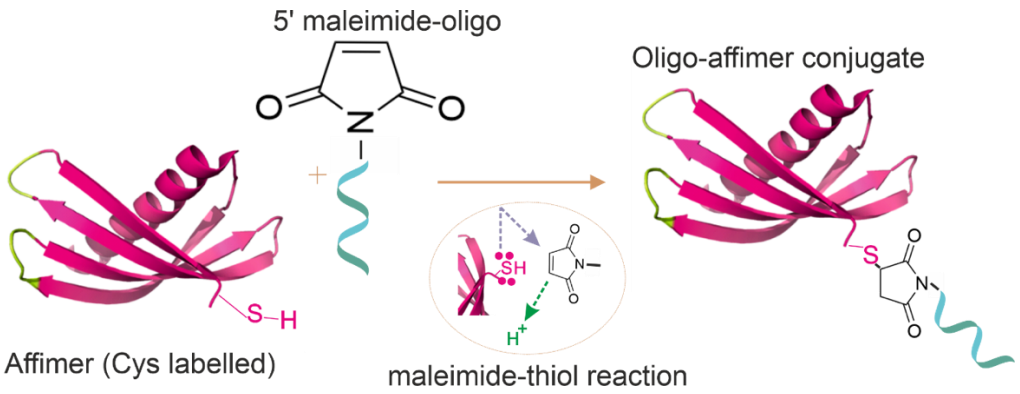

Figure 4:2 Illustration of oligonucleotide-affimer conjugation using maleimide chemistry. Maleimide at 5' end of the oligo is conjugated with cysteine labelled affimer to yield a conjugate. The yellow region in the affimer structure indicates the two variable loops. Affimer scaffold adapted from protein data bank (4N6T).

Results and Discussion

4.1 Affimer purification

The CRP affimer modified with a cysteine was purified as explained in Chapter 2 (2.2). The preparation was carried out under a reducing environment through the addition of reducing agent tris-(2 carboxy ethyl) phosphine (TCEP). Here I will demonstrate the purification of CRP affimer validated by SDS-PAGE analysis and mass spectrometry.

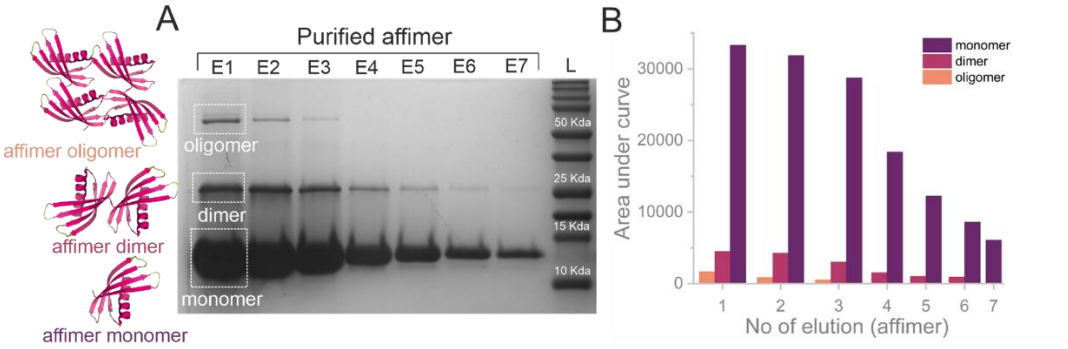

Figure 4:3 A) SDS-PAGE analysis of affimer. The affimer was purified and seven elutions were collected from the purification columns and run on SDS-PAGE gel as indicated by E1 to E7 in the image of gel. A band is observed between 10 kDa and 15 kDa which is representative of the affimer monomer as per the theoretical reported mass of affimer [240]. More than one band was observed in lanes with the band ~25 kDa represented the dimer population, and higher than that represented the oligomer. L represents the ladder. B) Column graph demonstrating the gel densitometry analysis. Dark magenta represents the monomer affimer, the pink shade represents the affimer dimer and orange shade represents the oligomer.

The first elution from the purification column yielded a concentration of 2 mg/ml as estimated from UV-Vis spectrophotometer and observed a band in SDS-PAGE electrophoresis gel between 10 kDa and 15 kDa (Figure 4:3). Two other bands were observed in the first elution, one corresponding to a mass of ~25 kDa when compared with the ladder, and other to ~50 kDa band. This observation qualitatively suggests that the extra bands correspond to dimers or tetramers of the affimer proteins based on their molecular masses. Since the affimers are His-tagged, the Ni-NTA columns specifically purify only the affimer proteins, effectively ruling out the possibility of non-specific protein binding. The densitometry analysis of the gel revealed that the area under the intensity profile curve corresponding to the dimeric and oligomeric forms of affimer was significantly smaller than that of monomeric band. The monomeric band had an integrated area of 33308 a.u. while the dimer and oligomer band had areas of 4477 a.u. and 1661 a.u. These values represent 84.4%, 11.3% and 4.2% of the total protein signal in the lane. The reduced area suggests that the dimers and oligomers are present in lower abundance compared to the monomer. A decreasing trend in total protein abundance was observed across successive elution fractions, as indicated by progressively lower band areas. Despite this reduction in total intensity, the monomer remained the dominant species in each fraction, indicating the stability and monodispersity of the protein following purification. The higher concentration of monomer when compared to other forms might be due to the reducing conditions under which the affimer purification was performed. TCEP was incorporated in the affimer purification to break the disulfide bond, both to maintain higher amount of monomer and to increase the accessibility of cysteines for conjugation to oligonucleotide described in the next section [298].The presence of cysteine residues in the affimer protein may facilitate the formation of disulfide linked dimers and oligomers despite the presence of TCEP suggesting the reduction may not have been 100%. Factors such as the protein concentration, oxidation state, incubation time, and buffer composition could influence the effectiveness [299]. Disulfide bond formation occurs between the thiol (-SH) groups of cysteine residues and results in covalent linkage between monomeric units leading to formation of dimers. The same effect is observed for CEA affimer during LC-MS analysis as reported by Shamsuddin et al. [300].

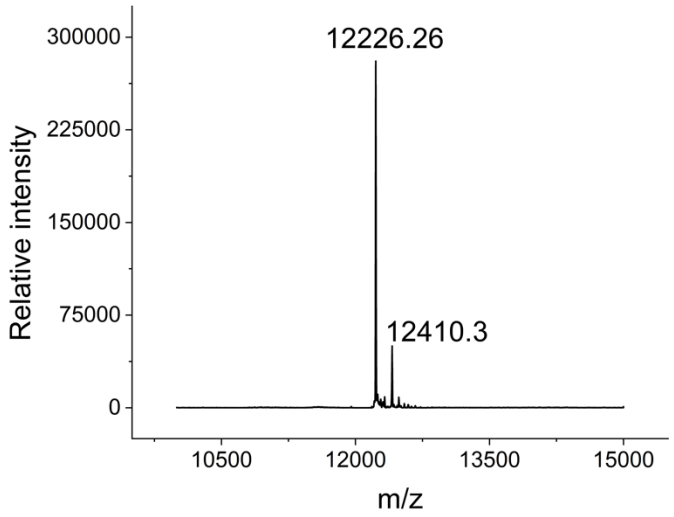

Figure 4:4 The mass spectra of purified CRP affimer displaying monomer peaks at mass 12,226.26 Da. A peak with 12,410.3 is observed at low intensity suggesting the presence of non-covalent adducts.

The theoretical mass observed using ProtParam software was 12,069.70 Da and indicated that the theoretical pI value of the affimer were within the neutral range (pI ~6.8) based on the sequence of the affimer (Table 4-1). The purity and molecular mass of affimer was further determined using electrospray ionisation mass spectrometry and the deconvoluted mass spectrum showed a primary peak at 12,226.26 corresponding to a mass increase of ~157 Da relative to the expected theoretical mass. A secondary, less intense peak was observed at 12,410.3 representing a further increase of 331 Da (Figure 4:4). These mass discrepancies suggest the presence of non-covalent adducts since the affimer was in buffer containing non-volatile components and reducing agents. The affimer was buffer exchanged to tris-acetate, EDTA and added with TCEP, and it is likely that weak, non-covalent interactions between protein and buffer components remained during ionisation, resulting in mass increases [301].

No of amino acids	Molecular weight (g/mol)	Theoretical pI	Molar extinction coefficient (L mol^{-1} cm^{-1})
103	12,069.70	6.87	12950

Table 4-1 Computed theoretical parameters for CRP affimer using Expasy ProtParam [302].

4.2 Affimer binding affinity

Surface plasmon resonance (SPR) analysis was performed to characterise the binding kinetics of affimer to its target, c-reactive protein (CRP) using a series of concentrations injected over the affimer-functionalised gold sensor chip. The detailed protocol for SPR method is described in the materials and method section and illustrated in Figure 4:5A. The binding responses were plotted against time to observe a concentration dependent association and dissociation of CRP molecules. As expected, a higher concentration of CRP led to an increase in the response unit indicating concentration dependent binding of CRP to affimer. The sensogram demonstrates that the response unit before CRP addition is low, near to the baseline whereas, during the injection (association phase), the response unit increases due to interaction of CRP with affimer. This is followed by a decline in the response unit indicating a dissociation phase corresponding to detachment of CRP from affimer molecules.

Varying concentration of CRP ranging from 25 to 0.78 nM was screened by performing a series of 2-fold dilutions, the response unit near the plateau phase was extracted (at 160s). The concentration of the CRP was plotted against the response unit, then the Langmuir isotherm model was used to fit the response unit and the obtain the affinity, the affinity was determined to be 8.52 nM for the CRP. The binding affinity is observed to be approximately 4 times higher compared to that reported for CEA (carcinoembryonic antigen) affimer binding to CEA protein (34.4 nM) [300]. The higher binding affinity could be due to the structural advantage of the CRP target including greater epitope exposure and better charge complementarity in the affimer variable loops [303]. This analysis confirmed the functionality of the affimer used in the study demonstrating its high specificity towards the target protein, C-reactive protein (CRP).

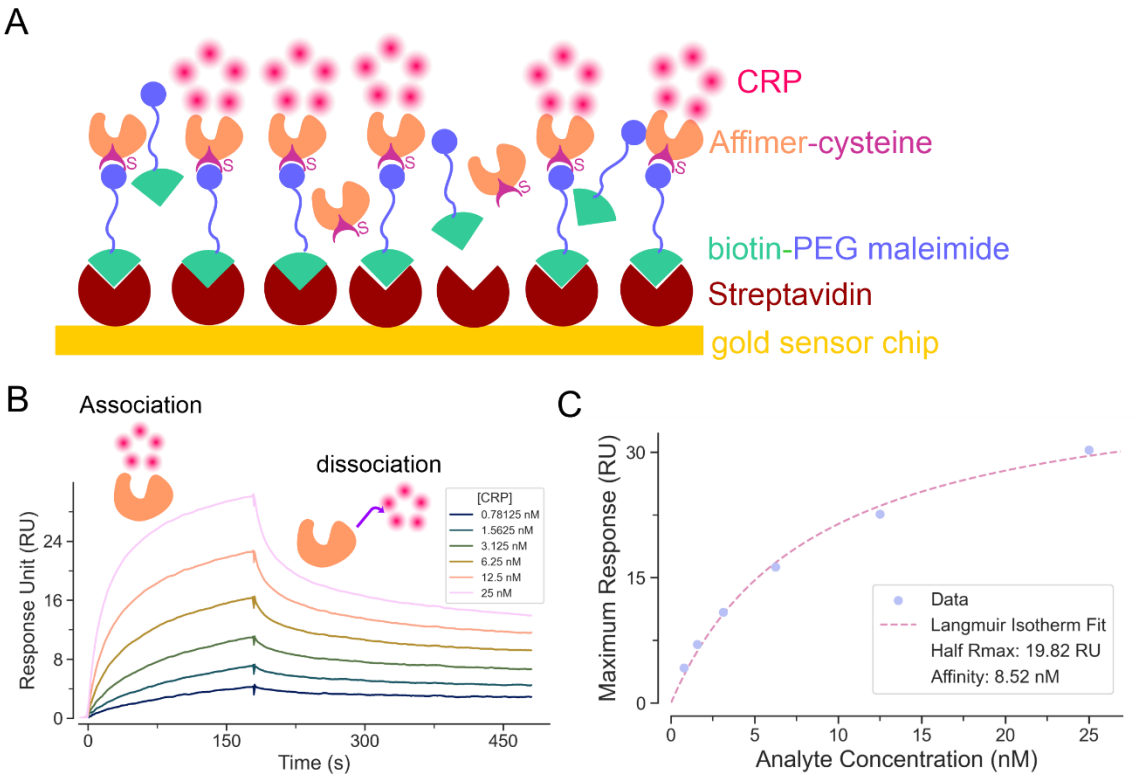

Figure 4:5 SPR Analysis. A) Illustration of the SPR set-up. The streptavidin coated gold sensor chip is bound with biotin-PEG-maleimide which further reacts with an SH group of cysteine on the affimer. The target protein CRP binds to the affimer via the variable loops. B) Sensogram representing the response (RU) vs time for CRP interaction with its affimer. C) Maximum response unit from the sensogram at 160s for each concentration was extracted and plotted against the CRP concentration, then Langmuir isotherm model was used to fit the data, the affinity is extracted when the response unit reaches half of its maximum. (Analysis performed by Dr. Chau)

4.3 Affimer-oligonucleotide conjugation

The purified affimer was conjugated with the oligonucleotide to develop a stable conjugate as described in this section (Figure 4:2). 38 µM of the affimer was conjugated with 95 µM of the oligonucleotide to maintain a 1:2.5 ratio between the two reagents. The confirmation of bioconjugation was validated by electrospray ionisation mass spectrometry. The mass spectra of affimer were first recorded using the instrument followed by the addition of the oligonucleotide and the spectra were collected at different time points to monitor the conjugation real time.

Conjugation was performed using different buffer compositions to optimise the conditions for affimer-oligonucleotide conjugation.

Firstly, maleimide conjugated oligonucleotides with 16 bases were purchased from commercial supplier Biomers where maleimide was attached at the 5’ end of the oligonucleotide. The maleimide containing oligonucleotides prepared in DMSO was mixed with affimer prepared in PBS to carry out the conjugation reaction. When maleimide at the 5’ end of the oligonucleotide (hereafter referred to as 5’-maleimide

oligonucleotide) was conjugated with affimer and the reaction monitored using mass spectrometry, a peak was observed after one hour corresponding to 17,525 Da (Figure 4:6).

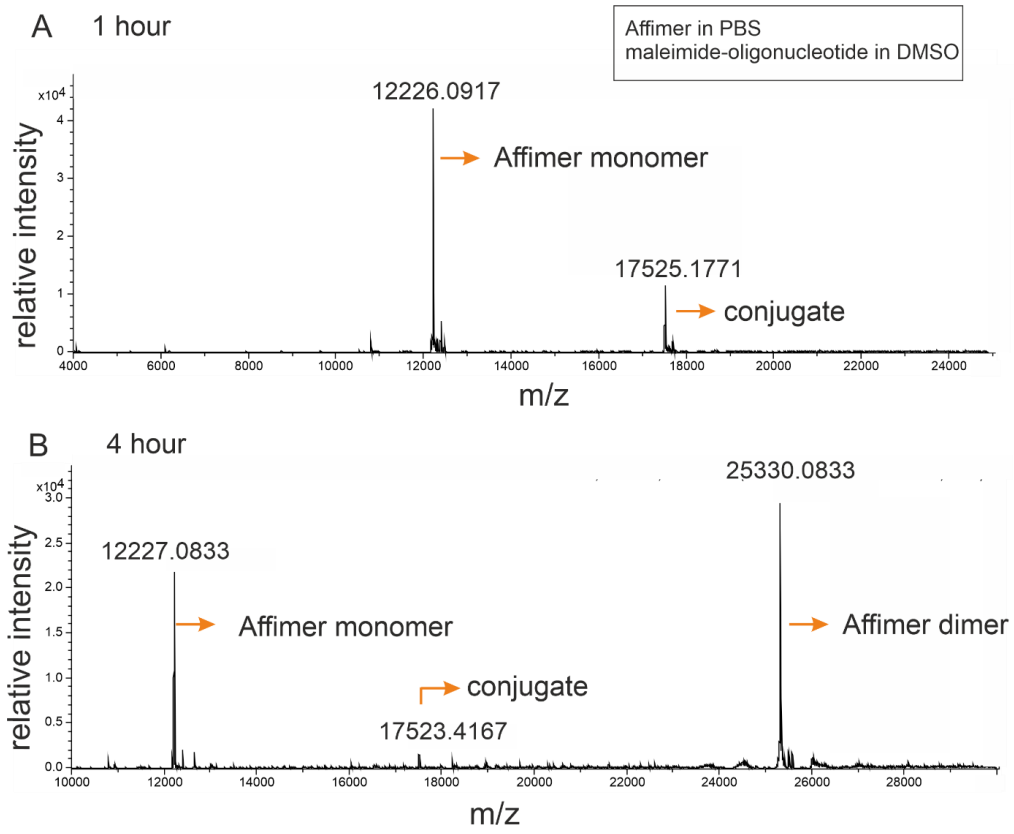

Figure 4:6 Mass spectra of affimer conjugated with 5'maleimide oligonucleotide. The affimer was prepared in PBS buffer and maleimide-oligonucleotide prepared in DMSO. A) Mass spectra of conjugation reaction between affimer and 5' maleimide oligonucleotide recorded at 1 hour of reaction. B) Mass spectra of conjugation reaction between affimer and 5' maleimide oligonucleotide recorded at 4 hour of reaction.

The 5'-maleimide oligonucleotide had a calculated mass of 5007 Da and affimer had a mass of 12,069.70 Da resulting in a combined theoretical mass of 17,076.7 Da. The observed mass of the affimer-oligonucleotide conjugate was 17,525 Da.

As the conjugation reaction progressed, the conjugation products degraded and affimer started dimerising as observed by a peak corresponding to 25,330 from the mass spectra after 4 hours. This peak is consistent with the disulfide linked dimerization, a known reaction in thiol containing proteins under oxidising conditions [300]. The buffer used for the conjugation reaction contained DMSO which although primarily acting as a solvent, also exhibit mild oxidising properties. Previous studies have demonstrated that DMSO can oxidise thiols to disulfides under prolonged incubation and higher temperatures [304]. A similar oxidative pathway is likely to be happened here, where prolonged incubation allowed DMSO to promote the formation of inter-affimer disulfide bonds,

leading to dimerization. To prevent this, the reducing agent TCEP is incorporated to maintain the affimer thiols in a reduced state favouring monomeric affimer and efficient conjugation with the maleimide oligonucleotide. However, TCEPs effect diminishes over time due to gradual oxidation and consumption [305]. As TCEP becomes depleted, DMSO continues to exert its oxidising effect, shifting the equilibrium in the favour of affimer dimerization over monomerization and labelling. The interplay between the TCEP depletion and persistent DMSO mediated oxidation likely contributes to the observed degradation of the conjugated product over time, as dimer formation competes with the productive labelling.

In addition to the redox environment, the maleimide thiol conjugation is highly pH dependent. For efficient and selective labelling, the thiol group must be partially deprotonated to act as a nucleophile which typically occurs at pH 7-7.5 (Figure 4:1). At lower pH values (below 6), thiol groups remain largely protonated significantly slowing or halting the reaction [294, 306]. Maintaining this pH balance is further hindered by other components in the reaction. DNA being highly polyanionic due to its phosphate backbone, can lower the effective pH of the sample solution [307]. Similarly, TCEP used as a reducing agent in the reaction is composed of three carboxylic acid groups, thus a 5 mM TCEP introduces approximately 15 mM equivalent acid into the buffer system contributing to acidification over time. [308]. The cumulative acid load from oligonucleotide (DNA) and TCEP can subtly shift the pH downward during the reaction, especially under prolonged incubation which is the condition I used in the experiment. A decrease in the pH below the optimal range would not only reduce thiol nucleophilicity, hindering conjugation, but also could limit the effectiveness of TCEP itself, which functions best at near neutral to slightly acidic pH [309].

Next, the conjugation of affimer with 5’ maleimide oligonucleotide was performed in Tris-EDTA buffer and validated using mass spectrometry. The affimer buffer exchanged to TE buffer was conjugated with 5’ maleimide oligonucleotide, also dissolved in TE buffer. A solution I implemented here to minimise the acidification from TCEP was to make the pH of TCEP solution neutral. The stability and purity of the affimer was first determined by examining the mass spectra and observed a peak at 12,226.25 which was comparable to the theoretical mass. A peak at 10,812.5 was observed which showed a 13-fold decrease in intensity compared to the peak corresponding to affimer. This could represent a truncated or degraded form of the affimer, potentially arising from partial proteolysis, fragmentation, or loss of a terminal tag or flexible linker region during sample preparation or mass spectrometry analysis, such degradation artefacts has been reported in mass spectrometry analysis [310, 311].

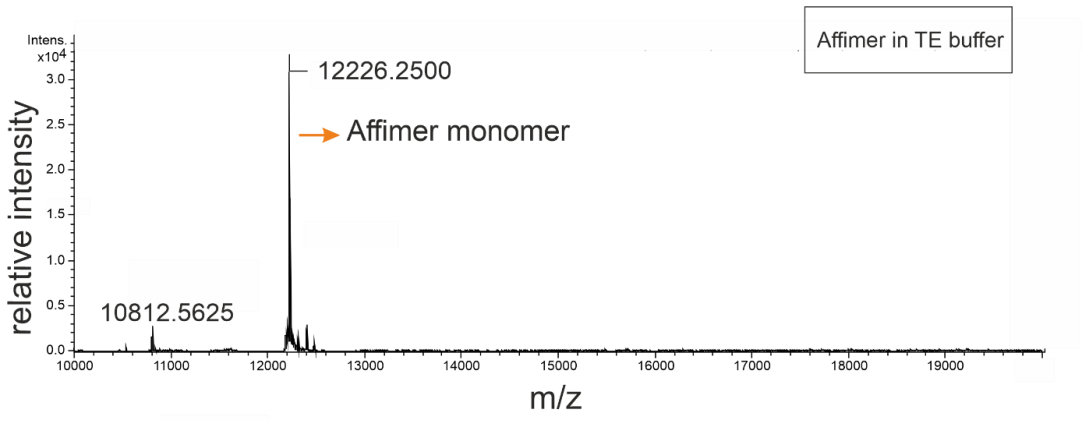

Figure 4:7 Mass spectra of affimer in TE buffer showing a major peak at 12,226.25 Da which is comparable to the theoretical mass and a secondary one at 10,812. 57 Da possibly indicating the presence of degraded or truncated affimers.

The affimer conjugated with 5'-maleimide oligonucleotide was then analysed using mass spectrometry. The spectra were recorded at 20 minute and re-checked after 100 minutes allowing real-time observation of the conjugation reaction. A peak at 12,227.3 was observed corresponding to the unmodified affimer and while an additional peak at 17525.4 was consistent with the theoretical mass of the affimer-oligonucleotide conjugate. The conjugate peak persisted even after 100 minutes of reaction although its intensity showed a slight decrease of approximately 1.2-fold. Therefore, conjugate formation of affimer with 5'-maleimide oligonucleotide was validated in TE buffer. Importantly, TE buffer is a suitable and preferred buffer for DNA stability, and as described in the introduction section, the preparation of DNA origami structures is widely done in TE buffer [312, 313]. The affimer-oligonucleotide is attached to a DNA origami structure for further studies as described in the following chapters.

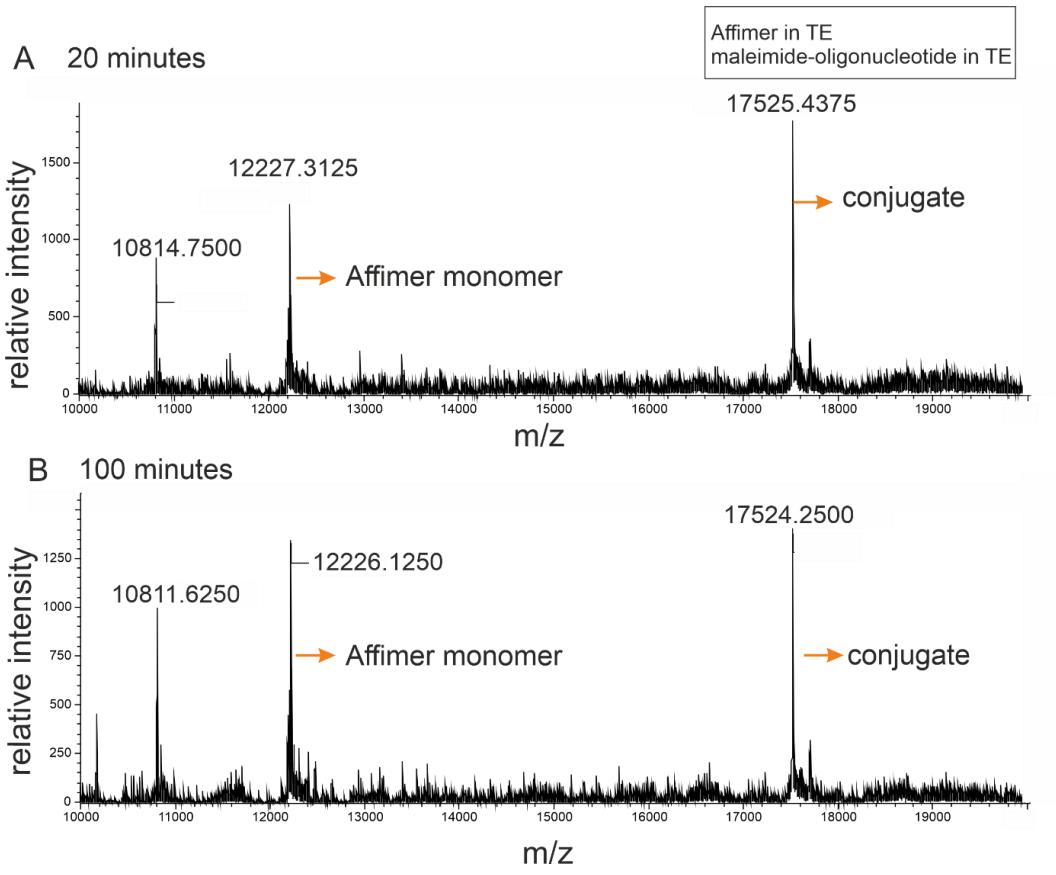

Figure 4:8 Mass spectra of affimer-5'-maleimide oligonucleotide conjugate in TE buffer. A) Mass spectra recorded after 20 minutes of affimer-oligonucleotide conjugation reaction. B) Mass spectra recorded after 100 minutes of affimer-oligonucleotide conjugation reaction.

In addition to the 5'-maleimide oligonucleotide, maleimide modified at the 3' end of oligonucleotide was also evaluated for its conjugation with affimer.

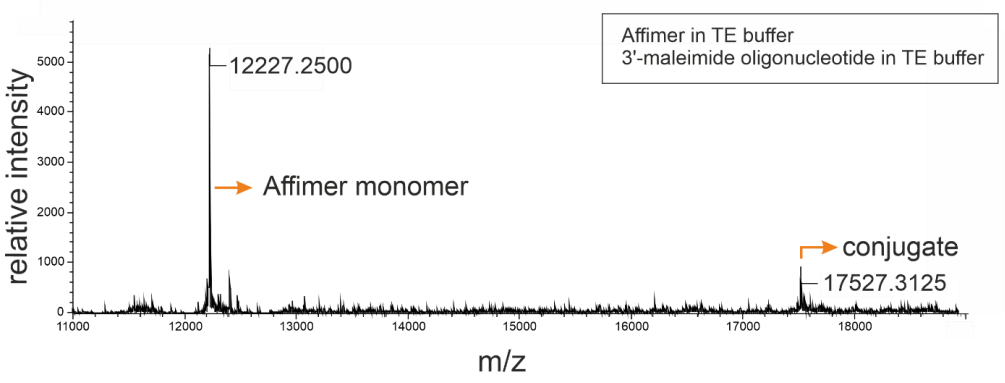

Figure 4:9 Mass spectra of affimer conjugated with 3'-maleimide oligonucleotide in TE buffer.

In conclusion, three conditions were tested for confirming the conjugation efficiency of affimer-oligonucleotide; 1) conjugation with affimer in 1x PBS buffer and 5' maleimide-oligonucleotide prepared in DMSO, 2) conjugation with affimer and 5' maleimide-oligonucleotide prepared in 1x TE buffer, 3) affimer conjugation with 3' maleimide-oligonucleotide in 1x TE buffer. To assess the conjugation efficiency, I compared the

relative intensity of the peak corresponding to the monomer and conjugate in each spectrum. As all conjugation reactions were performed under identical conditions except for the differences in buffer, the differences in the relative intensity on the y axis of the mass spectra qualitatively reflecting the abundance of each ion species was comparable. The mass spectra were analysed based on the relative intensity, where peak with highest intensity in each spectrum was set to 100 %, and intensity of all other peaks were scaled relative to this maximum. The normalisation allowed the comparison species within the same spectra and I assess the extent of conjugation by comparing the relative intensity of the conjugate peak with the affimer monomer peak within each condition. In PBS, the most intense peak corresponded to the affimer dimer at 25,530.08 m/z indicating significant dimer formation, the relative intensity of monomer was observed to be ~50 % whereas the conjugate intensity was only 12% confirming a reduction in conjugate yield (Figure 4:10A). When conjugation was performed in TE buffer, the highest intensity peak was for the conjugate at 17,524.25 m/z indicating the efficient conjugation of affimer with 5' maleimide oligonucleotide in TE buffer (Figure 4:10B) The affimer monomer peak remained intact but at 25% less than the conjugate suggesting a significant portion of affimer conjugated with the maleimide-oligonucleotide. A peak at 10,811.62 was also observed in this condition indicating the formation of truncated species or degraded products, which could be a result of batch-to-batch variability between the samples, as it was not observed when 3' maleimide oligonucleotide was conjugated with affimer in TE buffer. When 3' maleimide oligo nucleotide was conjugated with affimer in TE buffer, the highest intensity was observed for affimer monomer compared to 29% relative intensity for conjugate, indicating a significant portion of the affimer did not participate in the conjugation reaction (Figure 4:10C).

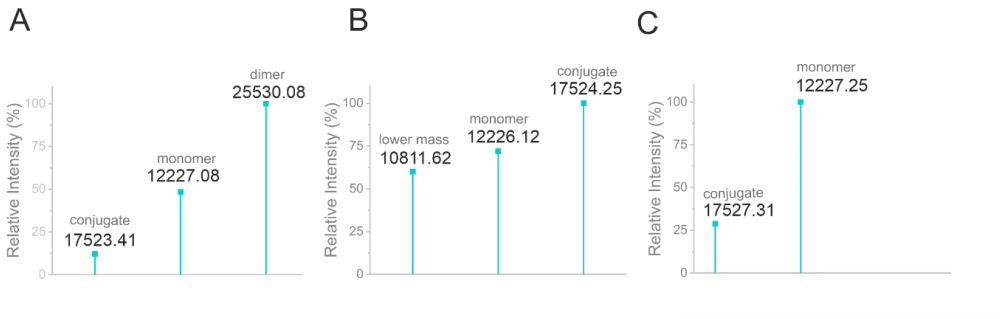

Figure 4:10 Relative intensity in percentage for affimer and affimer-oligonucleotide conjugate estimated from mass spectra in different buffer conditions, A) Affimer in PBS, 5'-maleimide oligonucleotide in DMSO, B) Affimer and 5'-maleimide oligonucleotide in TE buffer, C) Affimer and 3'-maleimide oligonucleotide in TE buffer.

Once the buffer condition for conjugation was optimised, the conjugation reaction was carried out using a 22 bases long oligonucleotide bearing a 5' maleimide group (molecular weight 7175 g/mol) and an affimer engineered with cysteine residue for site-specific conjugation. 38 µM of the affimer was conjugated with 95 µM of the oligonucleotide to maintain a 1:2.5 ratio between the two reagents. The confirmation of bioconjugation was validated by electrospray ionisation mass spectrometry real time as mentioned in the previous section. The relative intensity of the mass spectra peak was monitored for confirming the formation of conjugate and a peak was observed corresponding to a mass of 19,401.57 which is comparable with the theoretical mass of 19,244.7 g/mol (Figure 4:11). The peak at 19,401.57 exhibited the highest intensity hence was considered at 100% for normalisation. The peak at m/z 12,315.30 corresponding to the mass of affimer monomer showed an intensity of approximately 230, translating to a relative intensity percentage of 9%. This indicates that the conjugate species are in high abundance compared to the affimer species and majority of the affimer species reacted with the maleimide-oligonucleotide for conjugate formation.

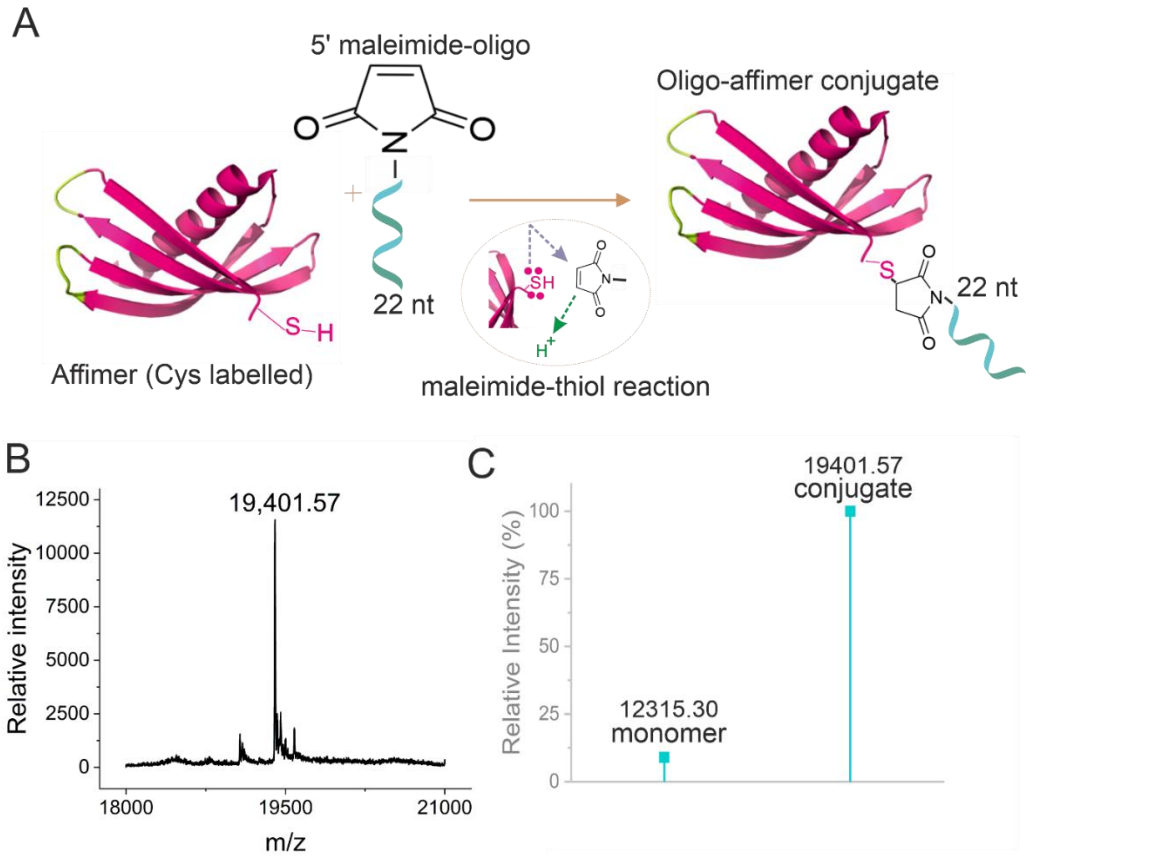

Figure 4:11 Mass spectra of conjugation of 22 nt long 5' maleimide oligonucleotide with cys labelled affimer. A) Illustration of maleimide-thiol conjugation reaction between affimer and maleimide-oligonucleotide via Micheal addition. B) Mass spectra showing relative intensity of affimer-oligonucleotide conjugate at 19,401.57. C) Relative intensity in percentage for affimer and affimer-oligonucleotide conjugate.

The conjugate formation was further confirmed using gel electrophoresis and a band was observed between 15 KDa and 20 KDa indicating the presence of the conjugate (Figure 4:12A). The same sample used for running mass spectrometry was used for loading the wells in SDS-PAGE which further confirms the results obtained in mass spectra. A control well was loaded with affimer alone to compare the mass. Bands corresponding to the affimer-dimer and affimer-monomer were also observed in the well loaded with conjugate, however the intensity as qualitatively estimated is significantly lower compared to the conjugate band. The sample collected after mass spectrometry is expected to contain four different populations - unreacted monomer, affimer dimer, affimer-oligonucleotide conjugate, and unreacted oligonucleotide. The affimer is His-tagged and the affimer-oligonucleotide conjugate was purified using Ni-NTA affinity chromatography to remove the excess oligonucleotide in the mixture. The resulting product was further validated by SDS-PAGE analysis where multiple elution fractions were examined for presence of band between 15 KDa and 20 KDa. The washes during the purification which are removed as supernatant were also analysed in gel, however no bands were observed indicating no conjugate was lost during the purification. The presence of the band at the expected mass indicated the presence of affimer-oligonucleotide conjugate after purification (Figure 4:12, Appendix A .2).

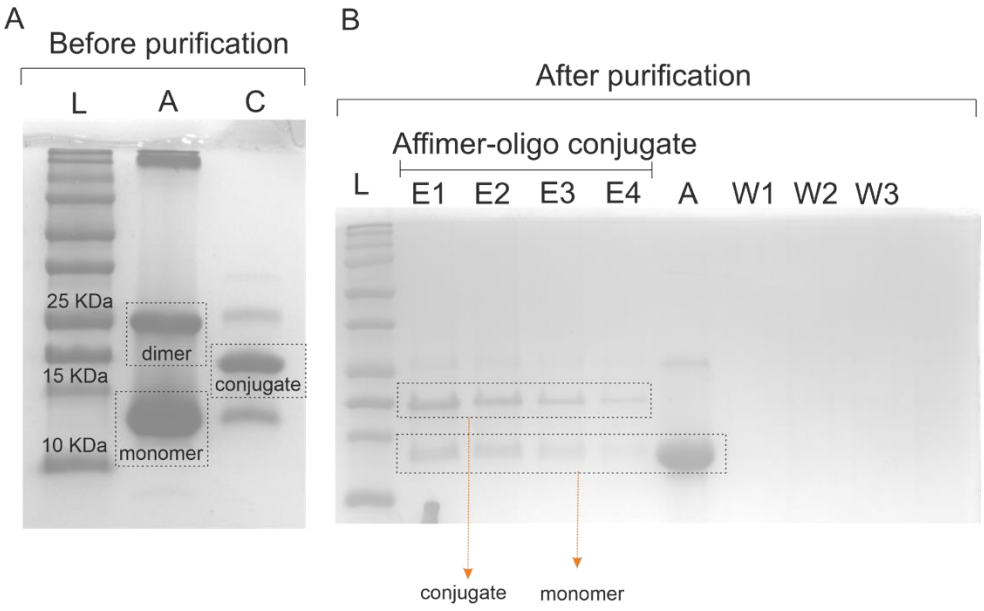

Figure 4:12 SDS-PAGE gel for confirmation of conjugate formation. A) Gel indicating the successful formation of conjugate as confirmed by a band between 15 KDa and 20 KDa. Wells annotation - L: Ladder, A: Affimer, C: conjugate. These samples were loaded in the well after conjugation before doing any purification. B) Gel indicating the presence of conjugate after purification using Ni-NTA affinity columns. Wells annotation – L: Ladder, E1, E2, E3, E4: multiple rounds of elution collected during purification, A: Affimer, W1, W2, W3: washes or supernatant removed during the purification.

The elution fractions were combined and were buffer exchanged to TE buffer. A strong band was observed corresponding to affimer-oligonucleotide conjugate between 15 KDa and 20 KDa indicating the presence of affimer-oligonucleotide conjugate. Furthermore, densitometry analysis of conjugate lane was estimated and the area under curve for conjugate was calculated to 4726 a.u., in contrast to 2205 a.u. for affimer monomer and 1856 a.u. for affimer dimer species (Figure 4:13C). This indicates that around 54% of the sample contains conjugated species whereas 46% comprises of unconjugated species. The concentration of the sample (after purification and buffer exchange to TE buffer) was estimated to be 3 µM from absorbance at 260 nm.

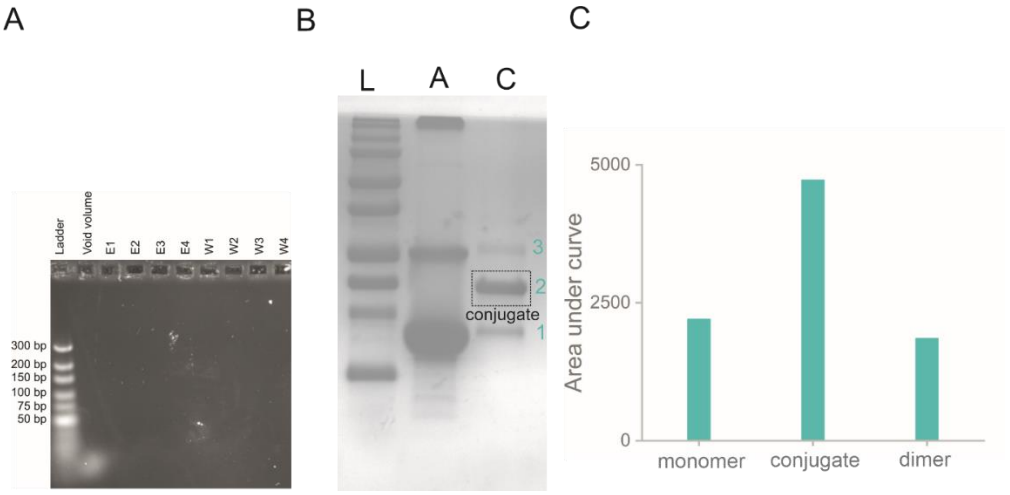

Figure 4:13 A) Agarose gel electrophoresis of 20-nt oligo nucleotide after Ni-NTA purification. Well annotation – Ladder, void volume (supernatant after Ni-NTA incubation), E1-E4: Four consecutive elutions during Ni-NTA purification, W1-W4: four consecutive washes during Ni-NTA purification. B) SDS-PAGE analysis of four elutions combined for affimer-oligonucleotide conjugation. Well annotation – L: Ladder, A: Affimer, C: conjugate. Cyan coloured numbers represent – 1) monomer 2) conjugate, 3) dimer in Figure C. C) area under the curve calculated from lane 3 (conjugate) in Figure B.

While the binding of the His-tagged affimer-oligonucleotide to the Ni-NTA resin and its successful purification was confirmed by SDS-PAGE (Figure 4:12B), a control experiment was performed to verify the oligonucleotide itself do not non-specifically bind to the Ni-NTA resin. For this, a 20-nt long oligonucleotide was incubated with the resin under identical conditions used for affimer-oligonucleotide conjugate purification.

The agarose gel analysis of different fractions is shown in Figure 4:13A. A strong band is observed in void volume lane (supernatant collected after incubation of 20-nt oligonucleotide with Ni-NTA resins), corresponding to the expected size of the oligonucleotide, indicating that majority of the oligo did not bind to the Ni-NTA resins and was recovered in the flow-through. In contrast, no bands were observed in the elution fractions (E1-E4), confirming that the oligo was not retained on the Ni-NTA resin.

The wash fractions (W1-W3) were also clear, further indicating the oligonucleotide was effectively removed during the initial flowthrough and did not remain bound to the resin. This result confirms the successful removal of oligonucleotide from the affimer-oligonucleotide conjugate sample after Ni-NTA purification.

Conclusions

In this chapter, a strategy for conjugation of cysteine engineered affimer with oligonucleotide is discussed. The reaction conditions were optimised, and conjugation performed in TE buffer was found to be effective compared to other conditions. Therefore, the conjugation was carried out between a 22-nucleotide oligonucleotide, functionalized with a maleimide group at the 5’ end, and an affimer containing a thiol group from an engineered cysteine residue in TE buffer. The conjugation efficiency was subsequently assessed using mass spectrometry and SDS-PAGE analysis. The results indicate the successful formation of the conjugate. The final conjugate sample was estimated to contain 54% affimer-oligonucleotide conjugate, while the remaining 46% comprised unconjugated species, including affimer monomers and dimers. This proves that maleimide-thiol reaction is a well-established method to conjugate affimer with oligonucleotide and with optimisation of reaction conditions, optimal conjugation efficiency can be attained. Such conjugation reaction can be of relevance in functionalisation of biomolecules to nanostructures and utilised for nanotechnology applications [104, 106].

The affimer used in this study is specific to the CRP protein and was conjugated with a 22-nucleotide oligonucleotide. This conjugate is subsequently utilised in the following chapter for functionalising CRP protein onto DNA origami structures.

Chapter 5 Functionalisation of DNA origami with CRP using affimer.

Introduction

Functionalisation of DNA origami plays a pivotal role in expanding its utility beyond structural nanotechnology into functional nanodevices, biosensing, and molecular engineering. DNA origami serves as an excellent tool for positioning biomolecules at specific sites at sub-nanometre precision. Functionalisation is the deliberate modification or decoration of origami with specific molecules such as nucleic acids, proteins, fluorophores or other chemical molecules to impart new functionalities or recognition capabilities. Functionalisation in this chapter is defined as the attachment of biomolecule to the DNA origami frame (4FSF). Previously, Raveendran et al. have demonstrated the capturing and detection of CRP protein using a DNA origami frame with 95 x 95 nm outer diameter and 25 x 25 nm size cavity. The frame had two overhangs and one of it was anchored with a DNA aptamer molecule specific to CRP enabling capture of CRP in the centre cavity which was characterised by AFM. The development of this DNA origami carrier enabled the detection of CRP protein from serum, functioning as a biosensor when integrated with a nanopore platform [13]. The design used in this work tend to form ribbon like structure as observed from the AFM image below (Figure 5:1). I envision on developing a stable origami frame that has inert edges and thus not attach to each other.

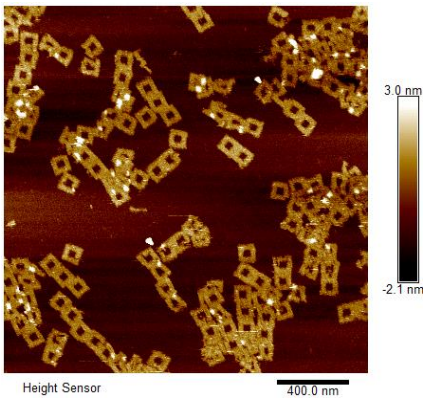

Figure 5:1 AFM image of origami frame used in [13].

In this chapter, I hypothesize that a DNA origami structure functionalized with affimers can serve as an effective platform for the selective capture of target proteins. Affimers, owing to their high binding affinity, specificity, stability, and reproducibility, are expected to function as efficient binding reagents when integrated into DNA nanostructures. To

test this hypothesis, C-reactive protein (CRP) is used as a model target due to its well-established role in sensing applications [13, 285].

I have developed an oligonucleotide-affimer conjugate using a thiol-maleimide coupling strategy (as detailed in Chapter 4). In this study, the affimer conjugates will be incorporated into a DNA origami frame, specifically, the four-fold symmetry tile previously discussed in the SPRI purification studies (Chapter 3). I propose that the DNA origami will successfully capture CRP within its central pocket (Figure 5:2), enabling visualization and confirmation of binding through atomic force microscopy (AFM).

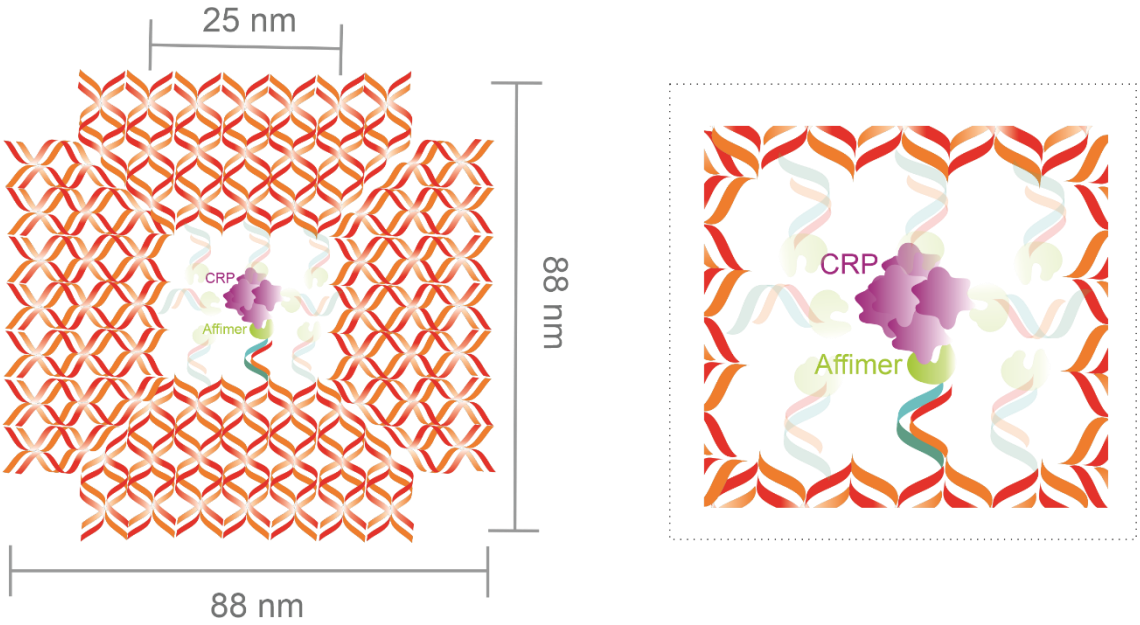

Figure 5:2 Illustration of functionalised origami in this study. The origami is a four-fold symmetry frame with a height x width of 88 x 88 nm. The cavity in the centre is 25 x 25 nm. The purple structure in the centre indicates CRP protein which is bound with affimer protein (green). The affimer is held with an oligonucleotide (cyan) which is complimentary to a binding point (oligo - orange) on the origami. The transparent affimer-oligonucleotide structures indicate that affimers can be positioned at more than one positions within the cavity of DNA origami. Inset on the right show the zoomed in image of the central pocket of DNA origami.

Result and Discussion

5.1 Origami design

The design of the DNA origami tile (4FST) discussed in Chapter 3 for purification is modified to generate a frame structure (4FSF) (see Chapter 2 (2.1.1.2), Appendix A .1). The frame structure has an outer dimension of 88 nm x 88 nm and an inner diameter of 25 nm x 25 nm. The origami is folded in 10 mM tris-acetate, 1 mM EDTA, 10 mM Magnesium acetate buffer and characterised using atomic force microscopy. The scaffold folded into a frame shape as shown in the Figure 5:3, however, failed to fold in PBS buffer. PBS buffer was evaluated for DNA origami folding, as proteins are generally stable in PBS, and the use of CRP and affimers for origami functionalisation indicated that PBS would be an appropriate choice. This demonstrates the importance of buffer for folding of origami and Tris-acetate, EDTA and Magnesium containing buffer proved to be the optimal. Millimolar concentration of magnesium are reported to be essential for DNA origami folding to neutralise the electrostatic repulsion between densely packed negatively charged DNA strands. This charge screening enables the precise folding and compaction of DNA scaffold and staple strands into defined architecture of origami nanostructures [314]. In the absence of Mg^{2+} as seen in buffers like PBS, the unscreened negative charges cause the structure to destabilise leading to destabilisation, incomplete or partial folding.

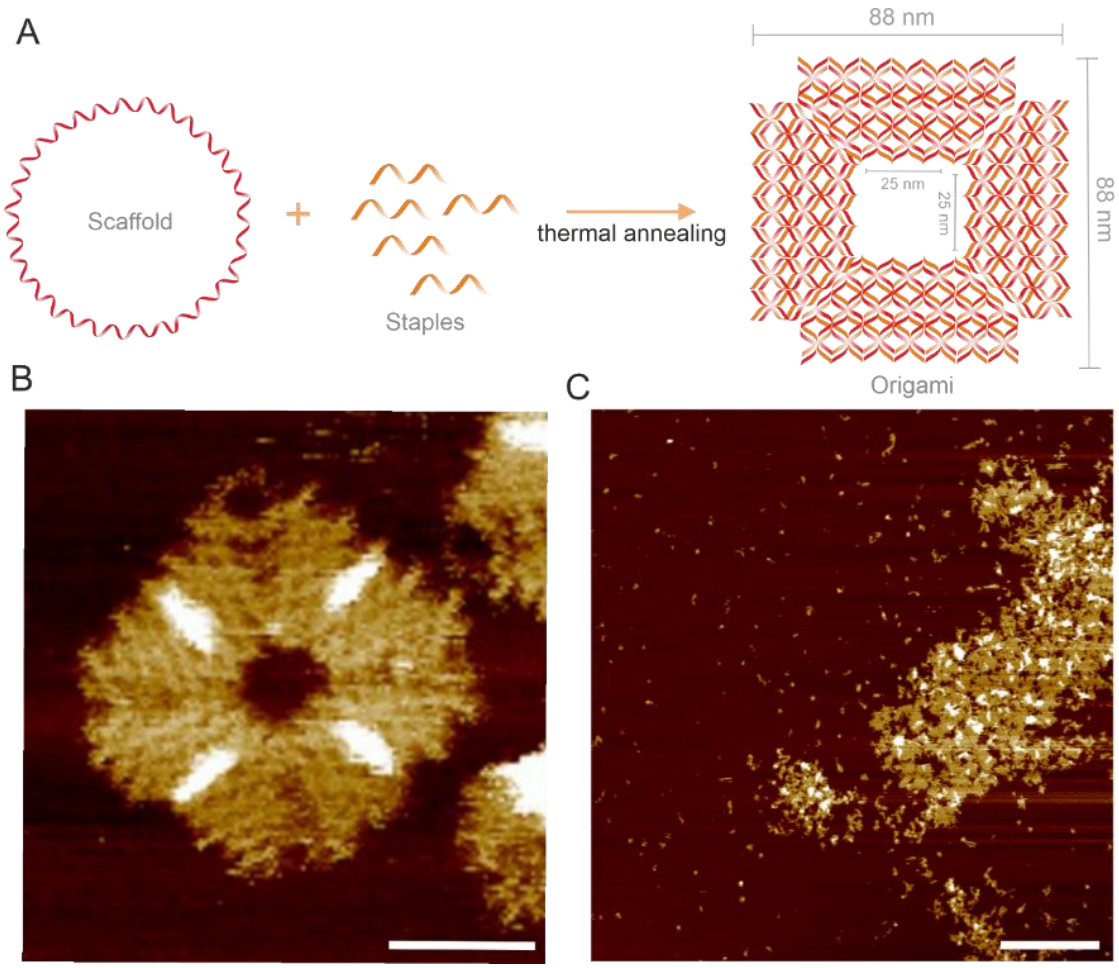

Figure 5:3 DNA origami design and folding. A) Illustration of DNA origami folding. M13mp18 scaffold is added with staples and thermally annealed to obtain a frame origami structure – four-fold symmetry frame (4FSF). The frame has an outer diameter of 88 x 88 nm and inner diameter of 25 x 25 nm. B) AFM micrograph confirming the folding of 4FSF in origami folding buffer (10 mM Tris-acetate, 10 mM MgAc, 1 mM EDTA, pH 7.4) (Scale bar: 50 nm). C) AFM micrograph of 4FSF folded in PBS (Scale bar: 200 nm).

To modify the original tile design into a frame-like structure without re-ordering a significant amount of staples, certain staple strands were replaced with different staples such that a second layer on top of the first layer was formed (white lines in Figure 5:3 B).

This exposed second layer consistently appeared as brighter spots in the AFM images of the DNA origami. Interestingly, in all AFM images acquired, the origami structures consistently adopted the same orientation, with the white lines always facing upwards towards the AFM tip. Structures with the second layer facing downwards (i.e., in an inverted orientation) were never observed, suggesting a preferred adsorption of the staple rich, more structurally continuous side onto the mica surface. I speculate that the surface with evenly distributed staples tends to be flatter and mechanically stiffer, promoting more stable binding to the mica or nickel-coated surface. In contrast, the side

with second layer, which introduces structural irregularities and flexibility, preferentially faces upwards towards the AFM tip.

5.2 Origami functionalisation with Streptavidin

The DNA origami contained binding sites, in the form of oligonucleotides, at three positions on each of the four inner edges, resulting in a total of twelve binding points (BP) (Figure 5:4). This enabled the attachment of proteins or biomolecules at 12 different sites in different combinations. Similar studies have reported that the avidity of protein binding can be enhanced by increasing the number of oligonucleotides and incorporating additional protein-capturing molecules, such as aptamers [12].

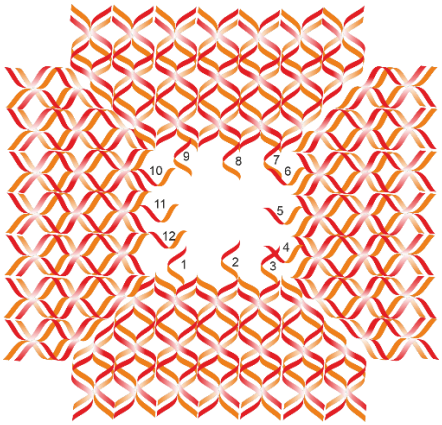

Figure 5:4 Illustration of DNA origami with 12 binding points.

I first evaluated the functionality of these binding points by incorporating the biotin-streptavidin model system to investigate whether the DNA origami with binding sites could successfully capture the protein at the centre. For this, I incorporated 75 nM biotin-labelled oligonucleotide during the folding of the DNA origami which was complimentary to the binding point. The DNA origami design provided control over both the number and position of binding points, allowing the incorporation of the biotinylated oligonucleotide in the desired configuration. DNA origami (4FSF) incorporated with four binding points without streptavidin in the centre showed an empty pocket within the origami as observed by Figure 5:5A. When these binding points were complimentarily bound with biotinylated oligo and subsequently streptavidin, a bright spot or high contrast region was observed in the centre pocket of 4FSF. I qualitatively analysed this using atomic force microscopy (Figure 5:5B). A similar effect was observed when two binding points and consequently biotinylated oligo was used to capture streptavidin in the centre pocket of 4FSF Figure 5:5C (Appendix A - .2). This proves that the binding point strategy is functional and can be applied to attach proteins. The designed oligonucleotide was complimentary to the binding point on DNA origami which led to the attachment of streptavidin. If this

oligonucleotide is utilised for conjugation of affimer proteins, the conjugate can be successfully incorporated to the DNA origami. The AFM images shown in Figure 5:5 confirms that the origami is inert on edges and does not tend to attach with each other as the structure in [13].

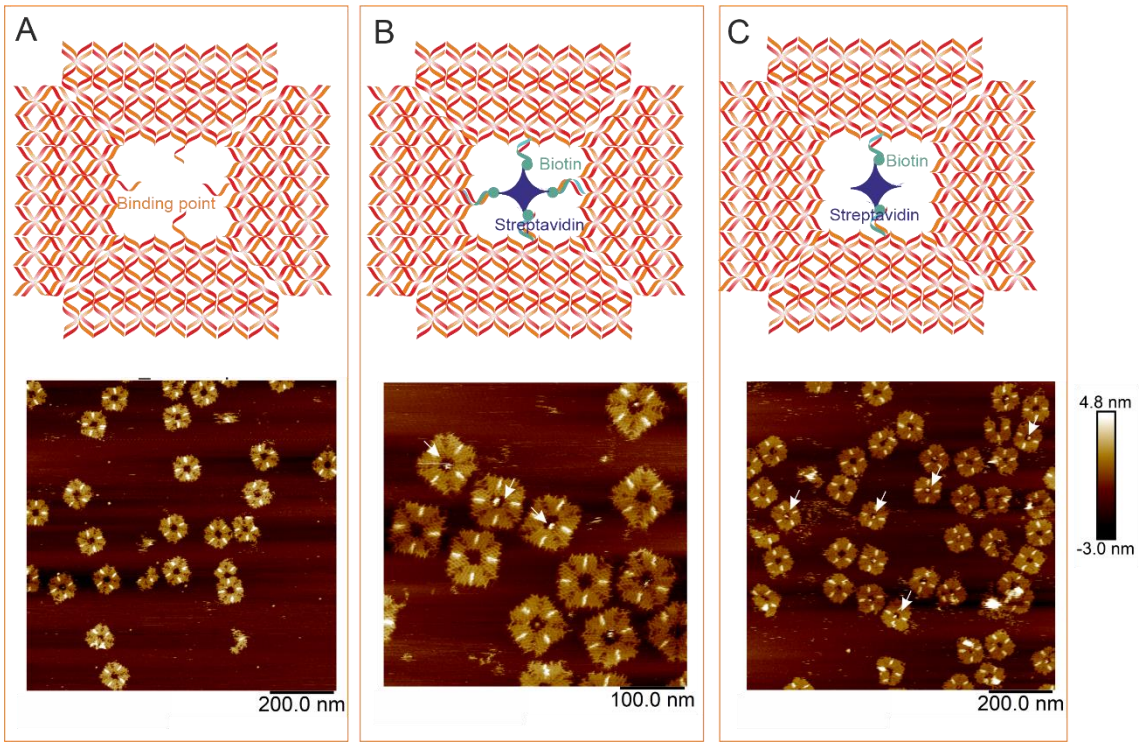

Figure 5:5 Streptavidin modified DNA origami. A) Illustration of DNA origami with 4 binding point and respective AFM micrograph (bottom). B) Illustration of DNA origami with 4 biotinylated oligo and streptavidin attached and respective AFM micrograph (bottom). C) Illustration of DNA origami with 2 biotinylated oligo and streptavidin bound and respective AFM micrograph in the bottom. Biotinylated oligo – cyan, Streptavidin – blue. Arrows in AFM images point to streptavidin.

5.3 Origami functionalisation with CRP

After validating the functionality of the binding points, I proceeded to anneal the affimer–oligonucleotide (22 bases) conjugate (conjugated and purified as demonstrated in detail in Chapter 4) to the pre-assembled DNA origami. The affimer used in this study is specific to the CRP protein, which served as the model target for binding experiments. To prepare the DNA origami with varying numbers of binding points, the 4FSF structure was folded incorporating 1 to 12 binding sites (specifically 1, 2, 4, 6, 8, 10, and 12), followed by purification using the SPRI method described in Chapter 3. Initially, I folded and purified the 4FSF DNA origami containing 12 binding points, reasoning that the higher number of binding sites, and consequently more affimers would enhance CRP binding efficiency. I incorporated 147 nM of the affimer–oligonucleotide conjugate by incubating at room

temperature; atomic force microscopy images revealed evidence of protein binding within the central pocket of the 4FSF structure as observed by the bright spot or high contrast feature in the centre. Unbound CRP, which appeared to retain its pentameric structure, was also observed in the zoomed-in images, as highlighted by the red circle in Figure 5:6B (bottom). I also tested annealing at 50˚, as this temperature is approximately 10˚ below the melting temperature (T_m) of the 22-base oligonucleotide (61˚), which is expected to promote specific and stable hybridisation while preserving structural integrity of DNA origami [315]. The affimer-oligonucleotide conjugate was incorporated immediately after SPRI purification during the thermal de-clumping step at 50˚C (Chapter 3). This approach minimized the number of purification steps, thereby enhancing both the structural integrity and yield of the functionalized DNA origami. I analysed the CRP attachment qualitatively using atomic force microscopy and observed the capture of CRP in the centre pocket of 4FSF (Figure 5:6). The percentage of CRP binding to the DNA origami was quantified based on the rules outlined in the materials and method (Chapter 2 - 2.1.7, Appendix A - .3). I observed that the percentage of CRP-functionalised origami was 8% when the affimer-oligonucleotide conjugate was annealed at room temperature, in contrast to 45% when annealing was performed at 50°C (Figure 5:8, Table 5-1).

Interestingly, I observed that in some cases, when zooming into a CRP-functionalised structure, the CRP was no longer visible. This is demonstrated in Figure 5:6B, where the top portion of the upper image is magnified in the lower image, revealing the absence of CRP after zooming. This could be attributed to the AFM tip dislodging or removing the CRP due to repeated scanning over the same area. Therefore, quantification was performed using large area AFM scans to minimize artefacts caused by repeated scanning.

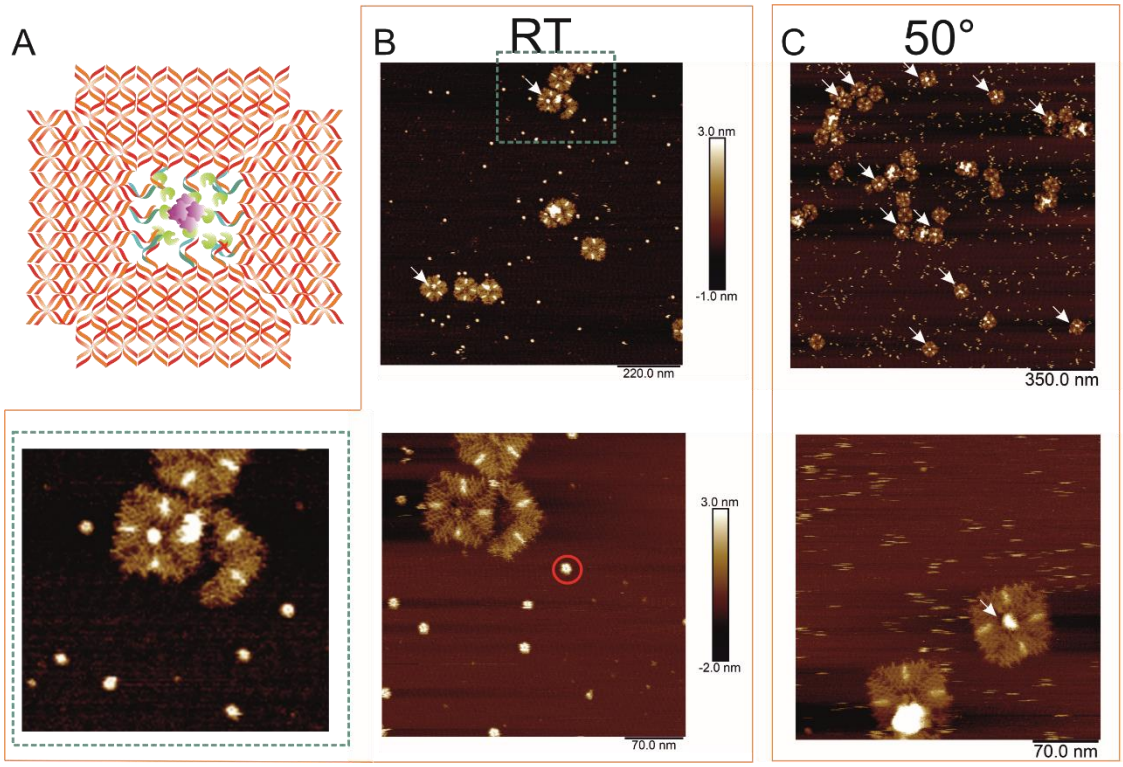

Figure 5:6 Functionalisation of 4FSF DNA origami using CRP. A) Illustration of 4FSF DNA origami with 12 binding points complimentarily bound with affimer-oligo conjugate (cyan) and CRP (purple). B) AFM micrographs of affimer-oligo conjugate attached to 4FSF at room temperature. Bottom - zoomed in scan of top image where CRP is no longer attached. Unbound CRP is circled red. The image in dotted cyan square is the zoomed in digital image of B (top image) C) AFM micrographs of affimer-oligo conjugate attached to 4FSF at 50^{o}. Bottom – zoomed in image. The white arrows indicate the CRP attachment.

To investigate the effect of binding point number on CRP attachment, I folded and purified 4FSF DNA origami structures containing 1, 2, 4 and 10 binding points, which were subsequently incubated with 280 nM of CRP (Figure 5:7). This series of experiments aimed to evaluate whether increasing the number of binding points on the 4FSF origami enhances the likelihood or stability of CRP attachment, based on the assumption that higher local valency could promote stronger or more frequent binding through multivalency effects. In all the cases, CRP was bound to the DNA origami in the centre as observed from AFM images. No significant structural deformation of the DNA origami was observed even with the maximum number of binding sites, suggesting that the functionalisation process preserved the mechanical integrity of the scaffold (Figure 5:7). While the white arrows in AFM images in Figure 5:7 indicate CRP functionalised origami, it also demonstrates the structures that are structurally intact.

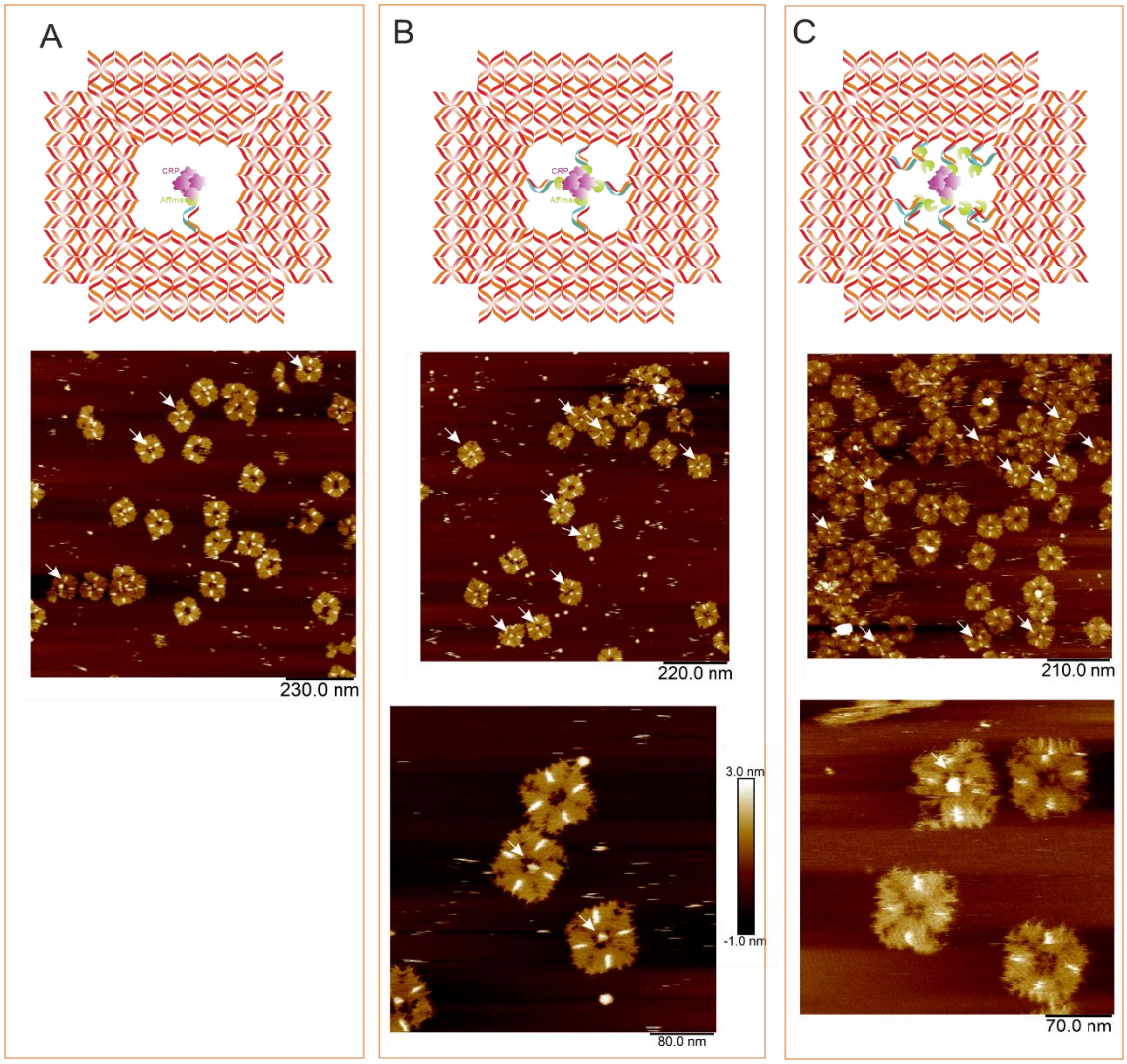

Figure 5:7 CRP attachment for 1, 4 and 10 binding points in 4FSF DNA origami. A) Illustration of CRP attachment to DNA origami folded with one binding point and respective AFM micrograph. B) Illustration of CRP attachment to DNA origami folded with four binding points and respective AFM micrograph. C) Illustration of CRP attachment to DNA origami folded with ten binding points and respective AFM micrograph. The white arrows indicate CRP attachment.

After checking the capture of CRP protein qualitatively using AFM images, I quantified the CRP attachment efficiency. I folded and purified a series of 4FSF DNA origami structures incorporating 1, 2, 4, 10, and 12 binding points, as well as a 12 binding point design where the affimer-oligonucleotide conjugate was annealed at room temperature (RT) rather than at an elevated temperature. Each of these designs was subsequently incubated with 280 nM CRP, and the percentage of CRP-bound origami was quantified using atomic force microscopy (AFM) based on rules outlined in Chapter 2 (2.1.7). The highest CRP binding efficiency was observed for the origami designed with two affimers to capture CRP, with 54% of the origami structures displaying CRP in the central pocket. In contrast, the 1BP design showed a lower binding efficiency of 37%. Increasing the

number of binding points beyond two did not lead to improved binding; the 4BP, 10BP, and 12BP designs yielded CRP binding efficiencies of 41%, 41%, and 45%, respectively (Figure 5:8,Table 5-1). These results suggest that while the presence of multiple binding points can initially enhance the avidity of the interaction by increasing the probability of CRP capture, an excessive number of binding points does not affect the binding [12, 316]. This could be due to steric hindrance within the central cavity, potential overcrowding of the binding sites, or impaired accessibility of the affimer moieties to the target protein.

Furthermore, the annealing conditions were found to play a critical role in the functionalisation process. When the 12BP design was annealed at room temperature, the CRP binding efficiency dropped sharply to only 8%, compared to 45% when annealed at 50°C. This substantial decrease indicates that insufficient hybridisation of the affimer-oligonucleotide conjugates at room temperature likely led to poor incorporation of functional binding sites (Table 5-1,Figure 5:8). Annealing at an appropriate temperature (in this case, 50°C, which is below the melting temperature of the 22-base oligonucleotide) ensures more complete and stable hybridisation when compared to at room temperature, thereby enhancing the availability of the binding sites for CRP capture. The binding percentages for all constructs fall within a relatively narrow range near 50% (37 % to 54 %). Two independent repeats were performed for each construct. One-way ANOVA revealed a statistically significant difference in binding between the groups ($F(4,5) = 5.41$, $p = 0.046$), indicating that the number of binding points influences CRP association. Overall, constructs with more than one number of binding sites tended to show increased binding, consistent with a multivalent interaction effect. I reckon that the structures might also be vulnerable to the AFM tip forces which could displace CRP proteins as previously reported in case of streptavidin [317].

Origami structure	**No of CRP-bound origami**	**Total origami counted**	**% of origami with CRP bound**
4FSF-1BP-CRP	55	146	37%
4FSF-2BP-CRP	164	304	54%
4FSF-4BP-CRP	80	192	41%
4FSF-10BP-CRP	85	209	41%
4FSF-12BP-CRP	112	248	45%
4FSF-12-BP-CRP (RT)	4	48	8 %

Table 5-1 Percentage of CRP-bound origami quantified from AFM images.

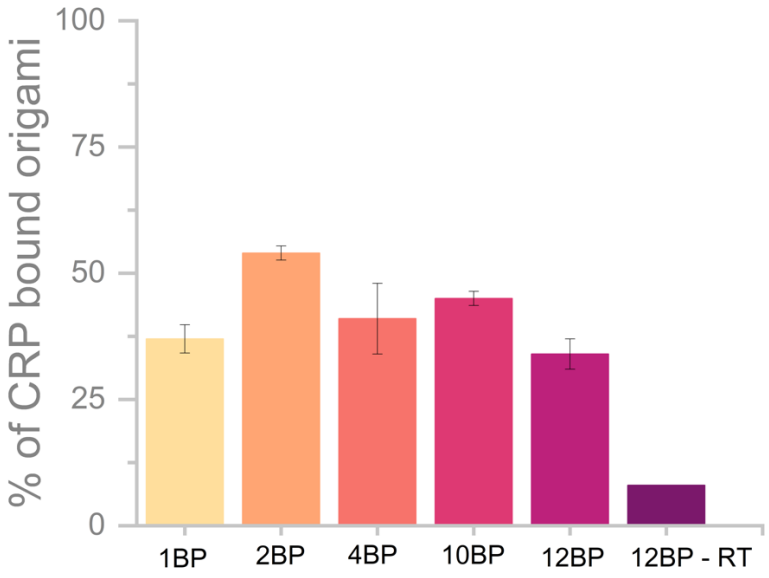

Figure 5:8 Bar graph demonstrating the percentage of CRP bound DNA origami 4FSF. BP indicate binding points. RT indicate at room temperature. For each construct, data represent the mean of the two independent experiments (± s.d). A one-way ANOVA revealed a statistically significant difference in functionalisation yield across the constructs (p = 0.046).

The 4FSF DNA origami structures were folded with the desired number of binding points and purified using the solid-phase reversible immobilization (SPRI) method. The affimer-oligonucleotide conjugate was annealed to the structures during the thermal de-clumping step, which constitutes the final stage of the SPRI procedure. This was followed by incubation with CRP. To remove excess CRP from the sample, an additional round of SPRI purification was performed. The AFM images, showing minimal background, further validate the effectiveness of the SPRI method as a purification strategy, as discussed in detail in Chapter 3 (Figure 5:7). While streptavidin functionalisation followed by SPRI purification resulted in approximately 85% protein-bound DNA origami (Chapter 3), CRP functionalisation with subsequent SPRI purification yielded a lower functionalisation efficiency of around ~50%. However, it should be noted that CRP functionalisation involved a more complex conjugation strategy compared to streptavidin binding, utilised a different DNA origami structure from that used in the previous chapter, and required multiple rounds of purification and thermal processing steps. Nevertheless, despite the multiple processing steps involved, a functionalisation efficiency of approximately 50% can be considered satisfactory under these conditions. In work reported by Rafat et.al, the maximum functionalisation efficiency observed when a protein of interest was conjugated with aptamers on DNA origami frame with two aptamers oriented at 180° was 27%. The maximum protein capture efficiency they ever observed was 67% when they oriented the binding aptamers at 90° angle [12].

Conclusion

In this chapter, I performed the CRP functionalisation of DNA origami frame using affimer proteins. For this, I used a four-fold symmetry frame with varying binding points and attached with affimer proteins. The oligonucleotide on which affimer was conjugated was complimentary to the binding point on the DNA origami. I demonstrated the successful binding of CRP on DNA origami frame 4FSF and validated it with atomic force microscopy. AFM is widely used as a morphological characterisation tool for imaging DNA origami and studying protein-DNA interactions [318]. The functionalisation of DNA origami structures with C-reactive protein (CRP) using an affimer-oligonucleotide conjugation strategy demonstrates a viable approach for site-specific integration of complex biomolecules onto DNA nanostructures. I was successful in achieving ~ 50% functionalisation efficiency for CRP bound DNA origami. The ability to stably anchor CRP on DNA origami paves the way for development of modular and programmable biosensing platforms capable of detecting relevant proteins with high spatial resolution. This methodology offers potential applications in single molecule sensing, diagnostic device development, studying protein-DNA interactions where precise spatial arrangement and functional control over protein attachment are critical [112, 239, 289]. This functionalised DNA origami structure could serve as an efficient and versatile platform for studying dynamic protein interactions, including protein–protein interactions and other biomolecular recognition events.

DNA origami frames functionalised with aptamers have previously been employed for the detection of CRP protein from serum samples [13]. Building on this approach, the system can be expanded to incorporate alternative protein binders; in this work, an affimer has been utilised as the molecular recognition element to achieve specific CRP binding. Affimers offer several advantages over traditional aptamers, including higher stability under a broad range of conditions, rapid and cost-effective production in bacterial expression systems, and the ability to engineer binding specificity and affinity through directed selection [240]. Moreover, their small size and robust folding make them well-suited for integration into nanoscale architectures such as DNA origami, enabling precise spatial control and enhanced target recognition in complex biological environments [296, 300, 319]. The functionalised DNA origami system described here is further employed in the subsequent chapter for the development of a protein sensing platform.

Chapter 6 Nanopipette detection of functionalized origami

Introduction

Nanopore technology has emerged as a cutting-edge method for biomolecular analysing at the single-molecule level [131]. Nanopore sensing involves the use of a nanometre-sized pore embedded in a membrane, through which analytes are translocated under the effect of an external electrical field. The membrane can be a biological material such as a lipid bilayer or fabricated from synthetic materials like glass or silicon nitride [224, 320, 321]. The translocation of a single molecules through the nanopore induces characteristic ion current modulation, and the resulting signal-defined by parameters such as current blockage amplitude, duration, and shape-provides critical insights into the size, conformation, and charge of the analytes [322], as previously discussed in Chapter 1 (1.3).

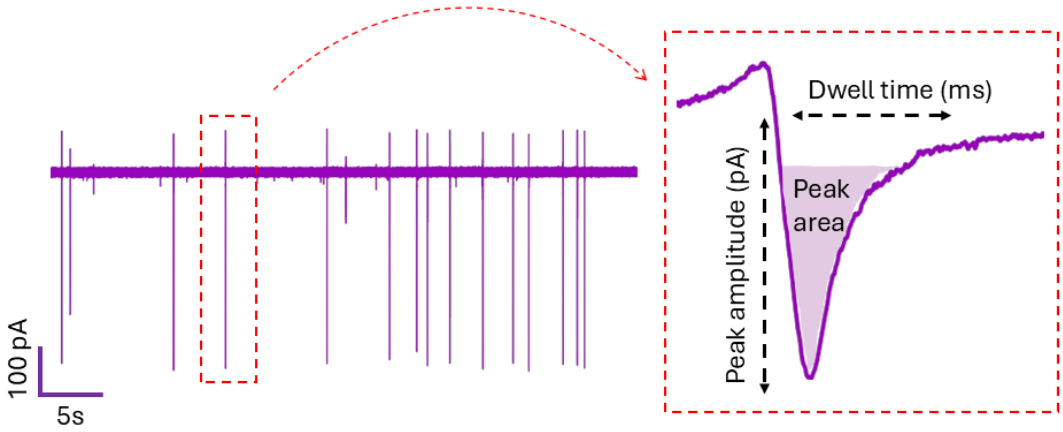

Figure 6:1 Ion current traces observed during analyte translocation through nanopores. The ion current peaks are defined by the height of the peak (Peak amplitude), width of the peak (Dwell time) and area of the peak (Peak area) which are characteristic of specific analytes.

Although recent advancements have enabled the reliable analysis of DNA and RNA using nanopores, the next frontier in this field is the sequencing of proteins [323]. Protein sequencing is of particular importance due to the central role that proteins play in cellular functions, as well as their potential to serve as clinical biomarkers. Timely detection of such proteins can enable early diagnosis, inform prognosis, and guide therapeutic decisions. Moreover, protein sensing is vital for monitoring treatment responses, studying cellular signalling pathways, and understanding dynamic biological processes. With the growing demand for rapid, sensitive, and point-of-care diagnostic tools, advancements in protein sensing technologies, including biosensors and nanopore-

based systems, are becoming increasingly important for both healthcare and personalized medicine.

Notably, Raveendran et al. recently proposed an innovative strategy utilizing DNA origami structures to capture and enhance the detection of proteins at the single-molecule level using nanopores. In this approach, a DNA origami frame was engineered with overhangs complementary to CRP-specific aptamers, enabling the selective capture of CRP protein. They demonstrated the detection of CRP at picomolar concentrations from complex biological fluids such as serum, highlighting the potential of DNA origami-assisted nanopore sensing for sensitive and selective protein detection [13].

Building on the work by Raveendran et al., the aim of this chapter is to develop a nanopore-based protein biosensing platform utilizing a four-fold symmetry DNA origami frame (4FSF) functionalised with affimer proteins as high-affinity binders for C-reactive protein (CRP), established in the last chapter (Figure 6:2). I will employ the stable DNA origami frame and also incorporate protein binder to the sensing system. Both affimer-functionalized and CRP-functionalized 4FSF origami constructs will be employed to investigate specific protein capture and translocation events through a nanopipette. The design, folding, purification, and conjugation of the 4FSF origami with affimer-oligonucleotide conjugates, as well as CRP attachment strategies, have been detailed in preceding chapters and characterized by AFM. Nanopore measurements will be performed to evaluate the feasibility of the protein-functionalised system for sensitive, single-molecule protein detection. Additionally, polyethylene glycol (PEG) will be incorporated into the electrolyte solution to enhance signal-to-noise ratios, following protocols established by Chau et al. [324]. This approach aims to address the challenges of detecting low-abundance, small proteins with high specificity and sensitivity.

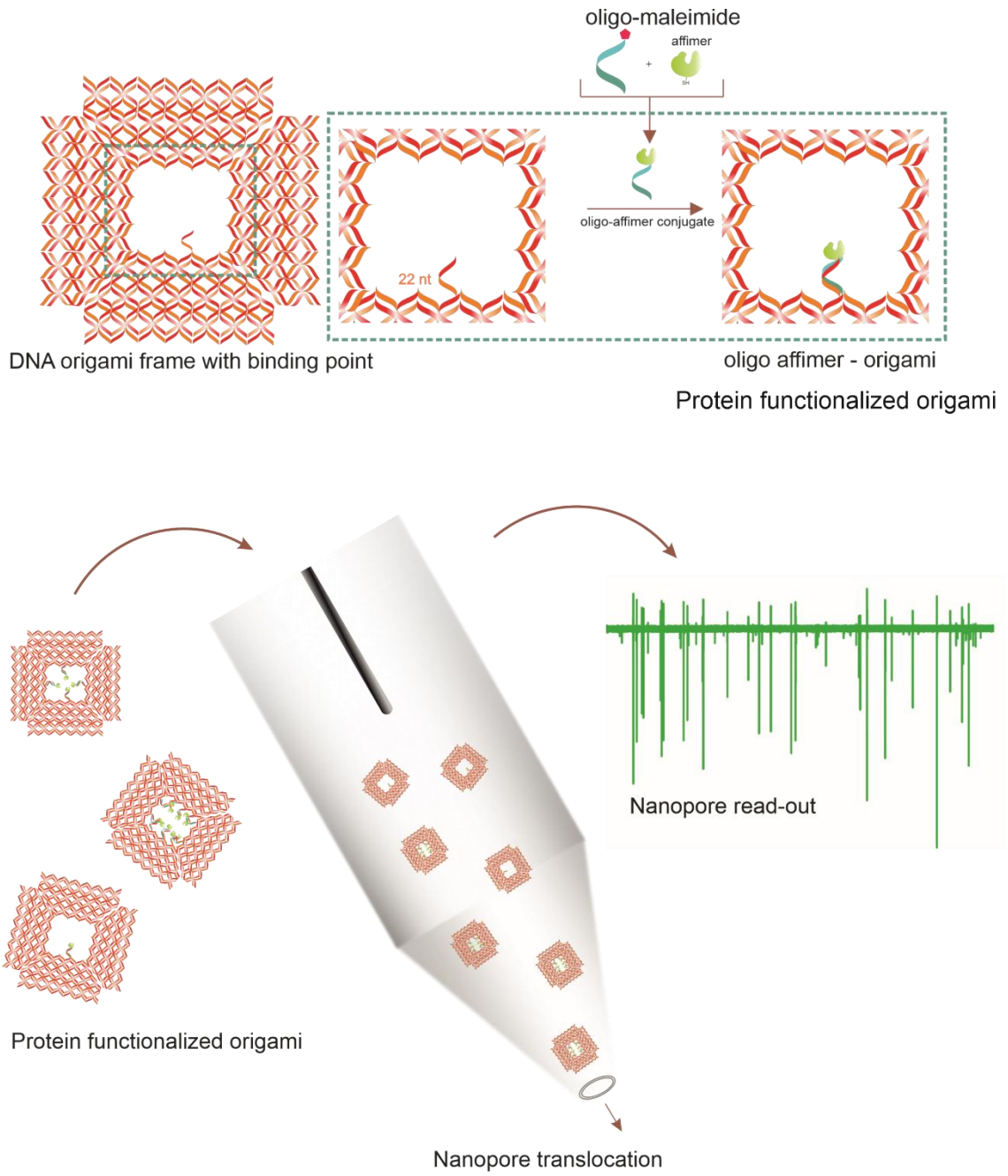

Figure 6:2 Overall aim of the study: The origami frame with one binding point illustrated in the top, the oligo-maleimide conjugated with affimer is annealed to origami frame to generate protein functionalized origami. The origami can be functionalized not just at one position but at multiple positions. The protein functionalized origami is filled into the nanopipette and translocated to outside to generate ion-current peaks as read-out.

Results and Discussion

6.1 Nanopore characterisation

The nanopore used in this study is a nanopipette which is fabricated from a glass capillary using a laser puller. The fabrication of nanopipettes is optimised to obtain the desired pore size mostly by adjusting features such as the amount of heat delivered to the glass and the pull strength. The details of the program used is described in the materials and method section (Chapter 2 - 2.7). The relevance of each parameter involved in the pulling of pipettes is described in the introduction section. In this study, I used two nanopipettes that were pulled using different parameters, with the main difference being the heat setting applied during the pulling process (Table 6-1, Table 6-2, Appendix A - .1). I performed this characterization to identify the appropriate nanopore size for analyte translocation and to ensure that the pore produced was stable and reproducible.

Heat	**filament**	**Velocity**	**Delay**	**Pull**
750	4	30	150	80
715	3	40	135	149

Table 6-1 Parameters used for pulling nanopipette with program 1

Heat	**filament**	**Velocity**	**Delay**	**Pull**
750	4	30	150	80
650	3	40	135	149

Table 6-2 Parameters used for pulling nanopipette with program 2.

The size of the pore is a crucial factor in providing a good signal to noise ratio to detect the translocation of an analyte [325]. The size of the pore can be determined either by scanning electron microscopy (SEM) or by measuring the current-voltage response. SEM results demonstrated a pore with diameter of 100 nm for program 1 and 142 nm for pore 2 as seen from Figure 6:3. The nanopore sizes selected matched the dimensions of the DNA origami structures folded and purified as described in Chapter 5, which serve as the analyte in this study. Based on the SEM measurements, I assumed that the observed pore sizes would provide a high signal-to-noise ratio during analyte translocation. A high signal-to-noise ratio is important in nanopore measurements as it enables reliable detection of translocation events and a clear distinction between true

current blockades and background noise, which is crucial for resolving molecular structures [326]. Once the optimal parameters for reproducible nanopipette fabrication were identified, multiple nanopipettes were pulled from glass capillaries and characterized for use in analyte screening, as discussed in the following section.

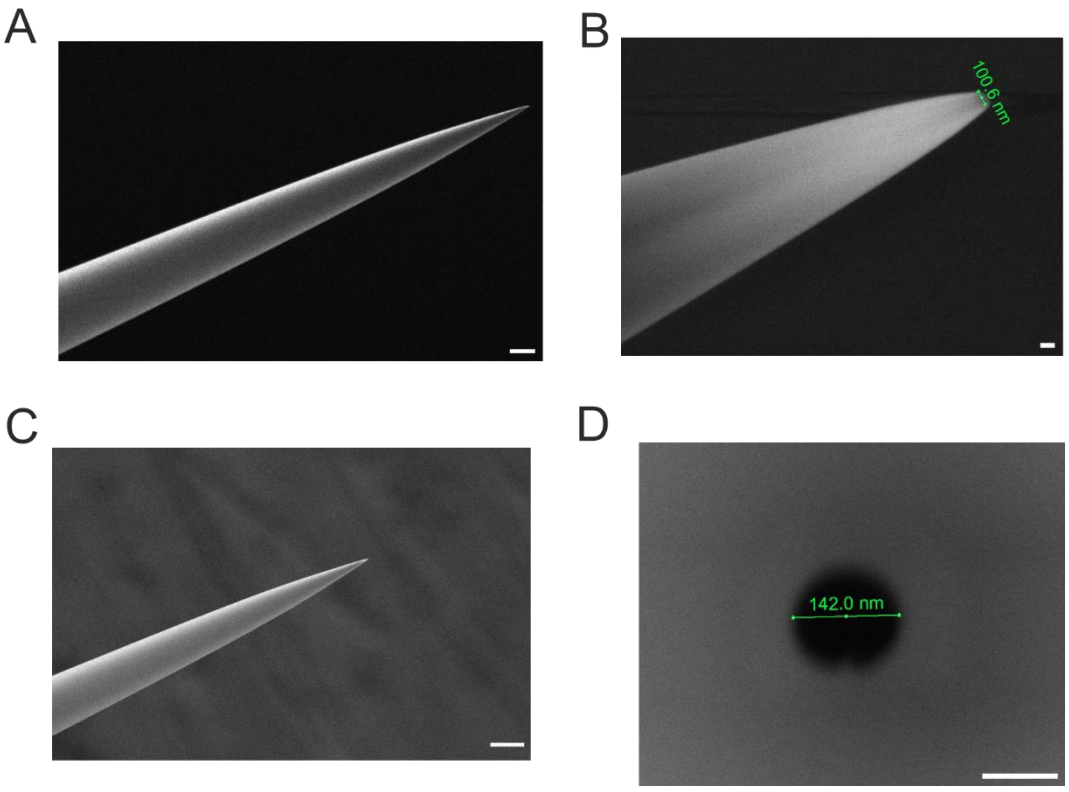

Figure 6:3 Scanning electron microscopy images of two nanopipettes pulled using Program 1 (A and B), and Program 2 (C and D). A) Side view of a nanopipette (scale bar - 5 µm). B) side view (zoomed in) view of nanopipette with pore size 100 nm (scale bar - 0.1 µm). C) Side view of nanopipette (scale bar – 10 µm) D) cross section view of nanopipette (scale bar – 100 nm).

While SEM provides accurate measurements of pore size and geometry, it is a time consuming technique due to the need for conductive coating, careful mounting of fragile glass structures, and detailed instrument alignment [217]. Therefore, current-voltage (I-V) characterization was performed after each nanopipette was pulled, as it offered a quicker and more practical alternative for assessing pore dimensions.

To estimate the nanopore size and assess its stability, I performed current-voltage (I-V) measurements by applying a linear voltage sweep from -500 mV to +500 mV and recording the resulting ionic current. The nanopipette was filled with 0.1 M KCl and immersed in the same electrolyte solution to maintain symmetric ionic conditions. Ag/AgCl electrodes were placed inside and outside the pipette, serving as the working and reference electrodes, respectively (Figure 6:4). This setup enabled consistent

measurement of ionic current across the nanopore, with the resulting I-V response used to determine the pore conductance and infer its size. Under ideal conditions, the I-V response is expected to be linear, indicating ohmic behaviour and a stable open pore without gating or leakage. From the slope of the I-V curve, the conductance of the pore can be calculated, which is inversely related to the resistance. Since the nanopore acts as a resistor in the ionic circuit, its resistance reflects the geometric dimensions of the pore, such as diameter. For each experiment, the resistance was noted to ensure it remained consistent, indicating that the nanopore remained stable and unchanged across measurements.

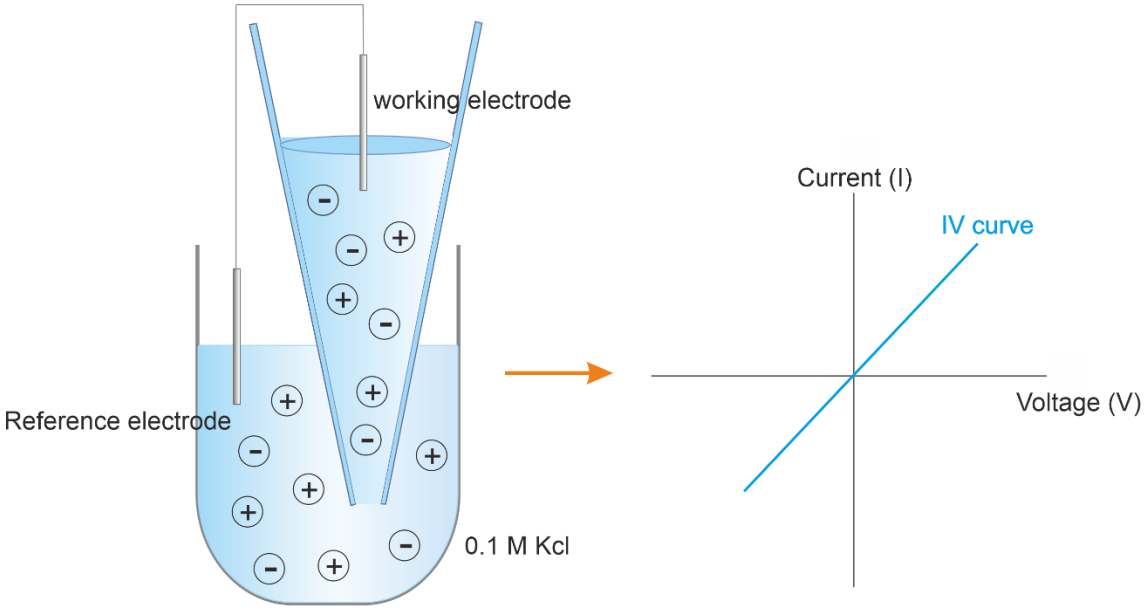

Figure 6:4 I-V characterisation of nanopipette. The nanopipette filled with electrolyte (100 mM KCl) is immersed in the same electrolyte and a voltage range of -500 mV to +500 mV is applied to record the IV-curve.

IV curve was recorded for each pulled nanopipette to characterise the electrical properties of the pore, specifically conductance properties. The IV curve displayed a linear relationship between voltage and current indicative of ohmic behaviour of the nanopipette in study. I observed a current of approximately -3.9 nA at -500 mV and +3.7 nA at +500 mV, resulting in a rectification ratio of about 1.08 (calculated as -3.9/+3.7). This near-symmetrical response indicates a linear, or ohmic, behaviour of the system over this voltage range. This indicates that there is no current leakage, the system is behaving well with stability. Furthermore, it is essential to evaluate the reproducibility of the pore, as this serves as a criterion for cross validating the right nanopore during each experiments.

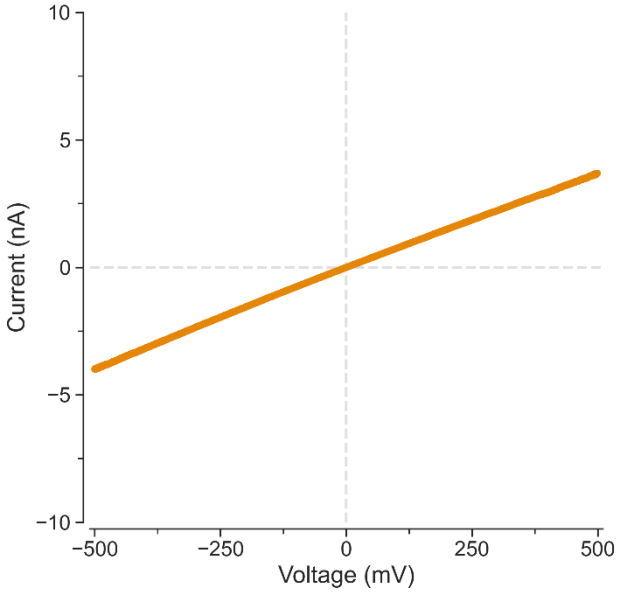

Figure 6:5 IV curve of nanopipette shown. A with 0.1 M KCl inside the pipette and outside in electrolyte bath. The graph represents a linear relationship between the voltage and current. (n = 3)

To assess the consistency of nanopipette fabrication, scanning electron microscopy (SEM) was first employed to verify pore geometry and estimate tip dimensions. This was followed by current-voltage (I-V) measurements to evaluate the electrochemical behaviour of each nanopipette. Resistance was used as a proxy for pore size and structural consistency. For each fabrication protocol (Program 1 and Program 2), 20 independent nanopipettes were characterized. The recorded resistance values demonstrated strong consistency across experiments, indicating high reproducibility in the fabrication process. Box plot analysis (Figure 6:6) further confirm that both programs yield nanopipettes with stable electrical properties and consistent pore dimensions. These results validate the reliability of both fabrication protocols and support their use for applications requiring uniform nanopipette performance.

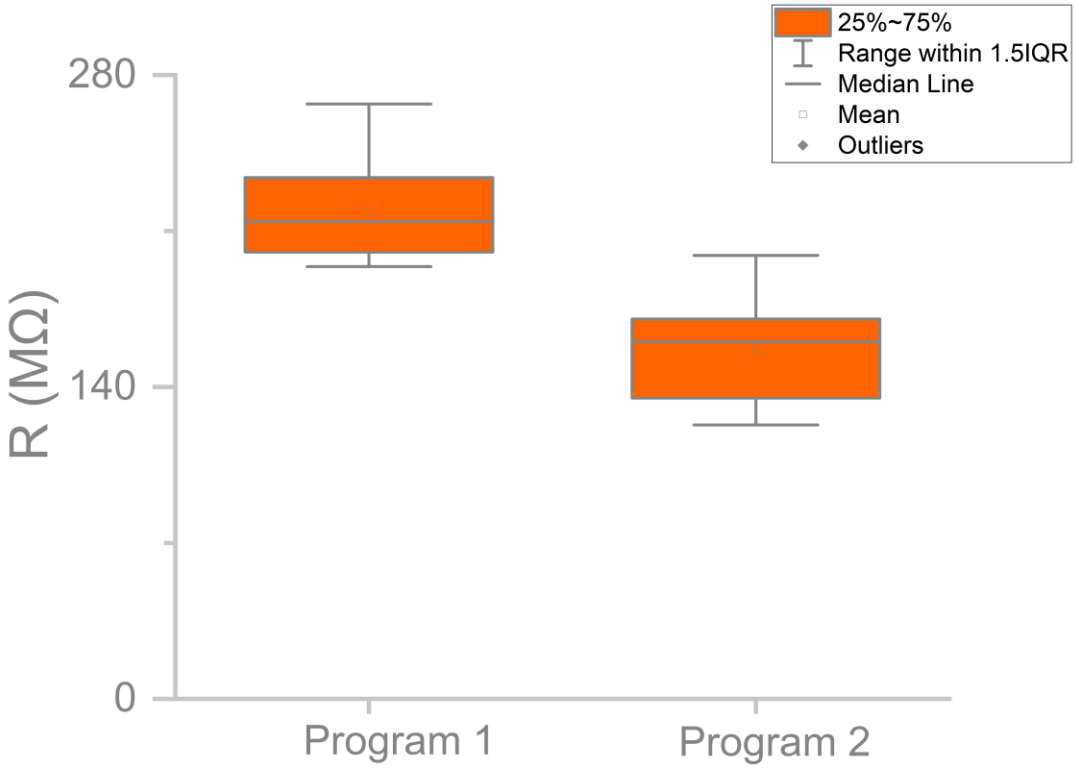

Figure 6:6 Box plot representation of resistance values measured from nanopipettes fabricated using Program 1 and Program 2 (n = 20 for each group). Resistance was extracted from Clampex software under symmetric electrolyte conditions. Each box represents the interquartile range (IQR, 25th to 75th percentile), the horizontal line indicates the median, and whiskers denote the minimum and maximum values within 1.5 x IQR. Individual points beyond the whiskers are plotted as outliers.

6.2 Analyte translocation through nanopipette

In this section, the translocation behaviour of analytes was studied as they were electrophoretically driven through a nanopipette under an applied voltage. The nanopipette was filled with the analyte dissolved in an electrolyte solution (100 mM KCl) and connected to a working Ag/AgCl electrode. The nanopipette was immersed in a bath containing 100 mM KCl with a reference Ag/AgCl electrode (Figure 6:7A). In the absence of analyte, application of a constant voltage across the two electrodes produced a stable baseline ionic current, indicating system stability and absence of unwanted signal fluctuations (Figure 6:7B). Upon introducing analytes into the nanopipette, their translocations through the pore under the applied voltage generated ion current peaks, indicating translocation events (Figure 6:7 C). Ion current peaks observed during analyte translocation can be characterized by three key features: peak amplitude**,** dwell time**,** and peak area, as described in the introduction (Chapter 1-1.3)**.** The peak amplitude

corresponds to the current deviation from the baseline and represents the magnitude of the ion current modulation caused by the analyte. The dwell time, defined as the width of the peak, indicates the duration for which the analyte resides within the nanopore. The peak area, calculated as the product of amplitude and dwell time, provides a quantitative measure of individual translocation events (Figure 6:7 inset).

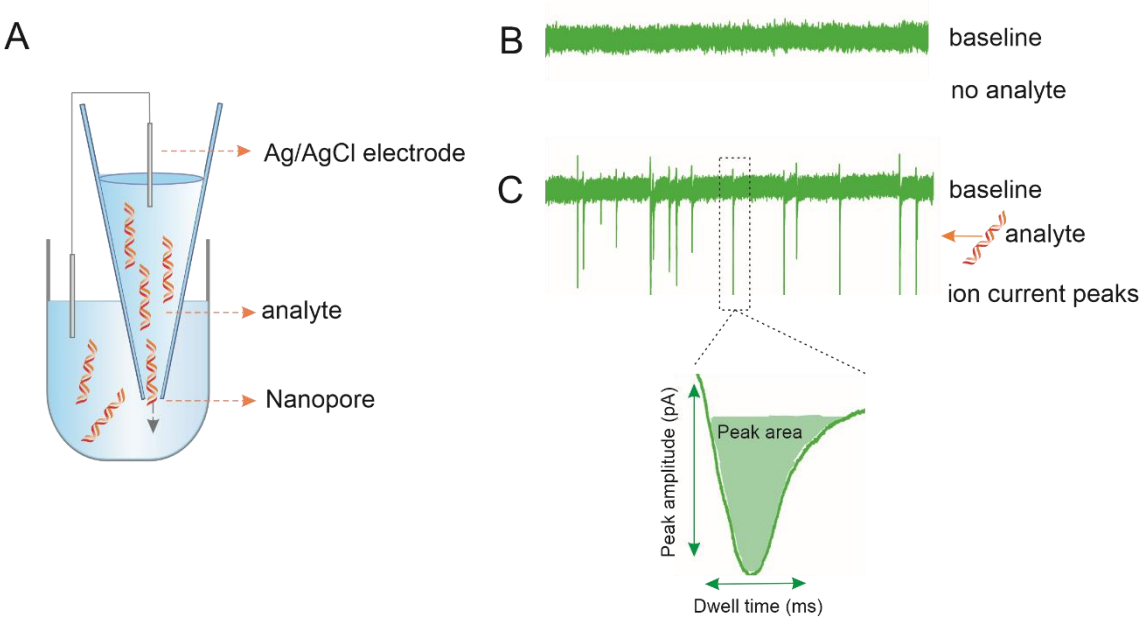

Figure 6:7 A) Illustration of nanopore set up for analyte translocation. B) Ion current trace when no analyte is present C) Ion current trace when an analyte is translocated through nanopore. Inset demonstrates characteristics of a single ion current peak.

6.2.1 Nanopore detection of origami structures

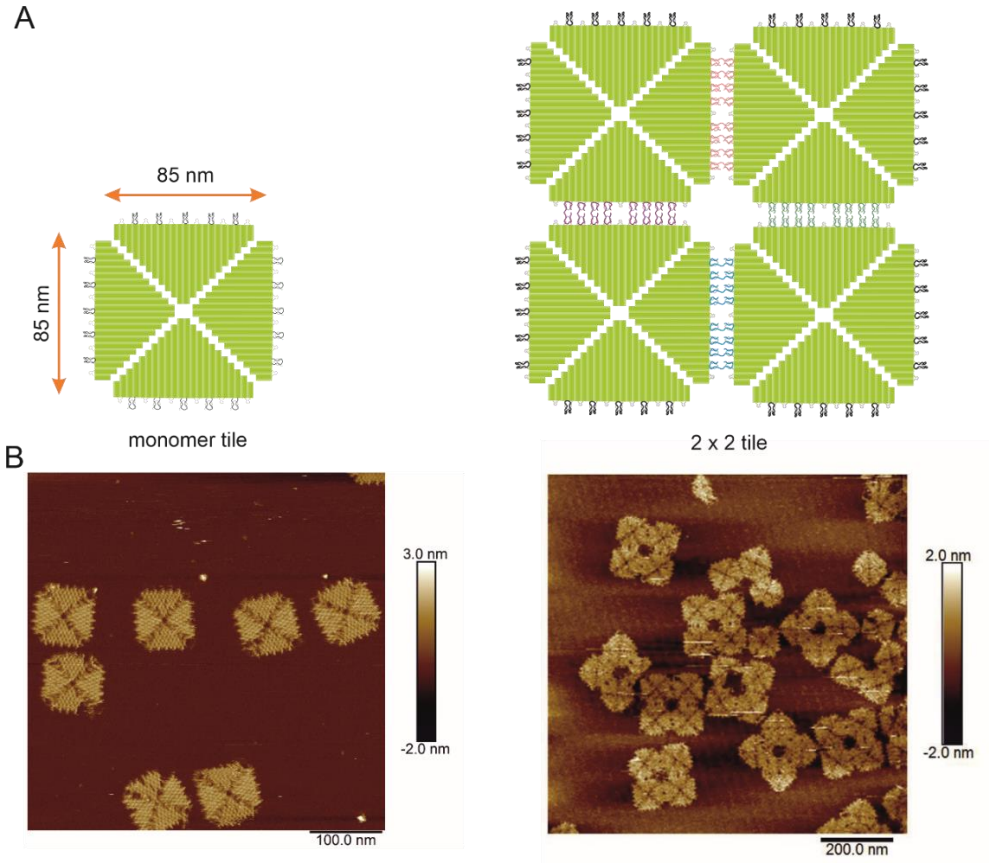

Figure 6:8 A) Illustration of monomer (88 x 88 nm) and tetramer (170 x 170 nm) design of DNA origami. B) AFM micrographs of monomer (scale bar: 100 nm) and tetramer tile (scale bar: 200 nm). (Tetramer image adapted from [327])

To validate the nanopore setup for its use as a sensor, origami tiles were detected using nanopipettes. An origami monomer tile (88 nm × 88 nm) and a tetramer (170 x 170 nm) tile comprising a 2 × 2 array of monomers adapted from Tikhomirov et al. were folded and characterized using AFM to confirm successful folding [263] (Figure 6:8). A 140 nm pore was employed as the sensing element to discriminate between the DNA origami tile monomer and tetramer, based on differences in their ionic current signatures. The pore size was selected based on theoretical considerations, as it lies between the approximate sizes of the two analytes (88 nm for the monomer and 170 nm for the tetramer), offering a balance that enables effective detection while maintaining a favourable signal-to-noise ratio.

To enable discrimination between the smaller monomer tile and the larger tetramer, 50% (w/v) 35K PEG was incorporated into the electrolyte solution (see method session for the electrolyte preparation). Analytes were loaded into the nanopipette and immersed in an external electrolyte solution containing 50% (w/v) PEG. I first examined the

translocation of monomer tiles under a constant negative voltage bias of -300 mV. Negative voltages repel the negatively charged DNA origami structures, driving them through the nanopore. DNA origami structures are negatively charged at physiological pH due to the phosphate backbone of the DNA strands. Each phosphate group carries a negative charge, and under physiological buffer conditions (pH 7.4 used here), these groups remain deprotonated. As DNA origami consists of hundreds to thousands of base pairs arranged into complex shapes, the cumulative negative charge is substantial. This net negative charge causes DNA origami to migrate toward the positively biased electrode during electrophoretic transport, enabling controlled movement through the nanopore under applied electric fields [328]. Without PEG, the ion current signals for monomer tiles were too small to detect reliably. However, the addition of PEG produced significantly larger ion current peaks (Figure 6:9). The translocation events in the PEG system generated well-defined ion current peaks, from which the peak amplitude (maximum current deviation from the baseline) and dwell time (duration of the event) were calculated. The average peak amplitude of monomer tiles without PEG was estimated to be 0.04 ± 0.01 nA, whereas in the presence of 50% (w/v) 35K PEG, it increased to 0.14 ± 0.03 nA. This represents a 3.5-fold enhancement in peak amplitude, indicating that PEG significantly amplifies the ion current signal during translocation.

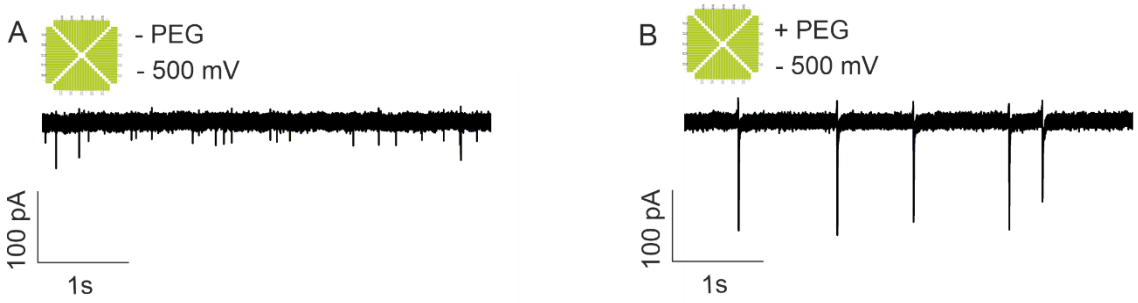

Figure 6:9 Ion current traces of monomer tile translocation through nanopore A. without PEG, B. with PEG in electrolyte at -300 mV.

A scatter plot of peak amplitude vs dwell time revealed that a homogeneous population of events was observed, clustering within a defined region. Although, some outliers were observed with lower and larger peak amplitude which could be due to the presence of broken origami and a minor population of analyte aggregates [329, 330].

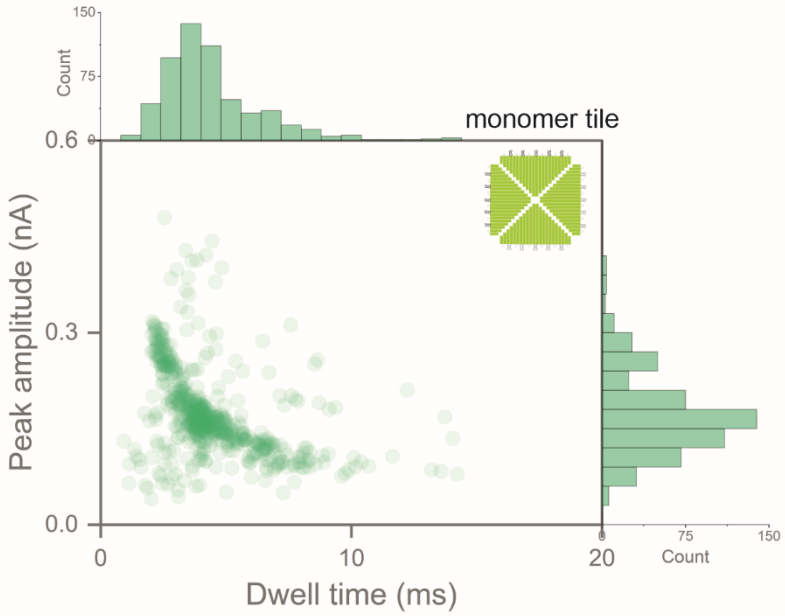

Figure 6:10 Scatter plot and histogram of monomer tile translocated through nanopipette with PEG in electrolyte bath.

Control experiments were conducted to evaluate background activity under various conditions. At both 0 mV and +300 mV applied voltage, no ion current events were detected. Similarly, in the absence of analyte, no events were observed even at -300 mV. These findings confirm that translocation events occur specifically at negative voltages and are dependent on the presence of analyte, highlighting both directional and molecular specificity. Moreover, no events were detected at 0 mV even in the presence of analyte, supporting that electrophoretic forces are required to drive DNA origami through the nanopore (Figure 6:11B). The absence of events at negative voltage without analyte further confirms that the detected signals originate from DNA origami translocations (Figure 6:11C). These results are consistent with previous studies demonstrating voltage-driven, electrophoretic transport of nucleic acids through nanopores [331-333].

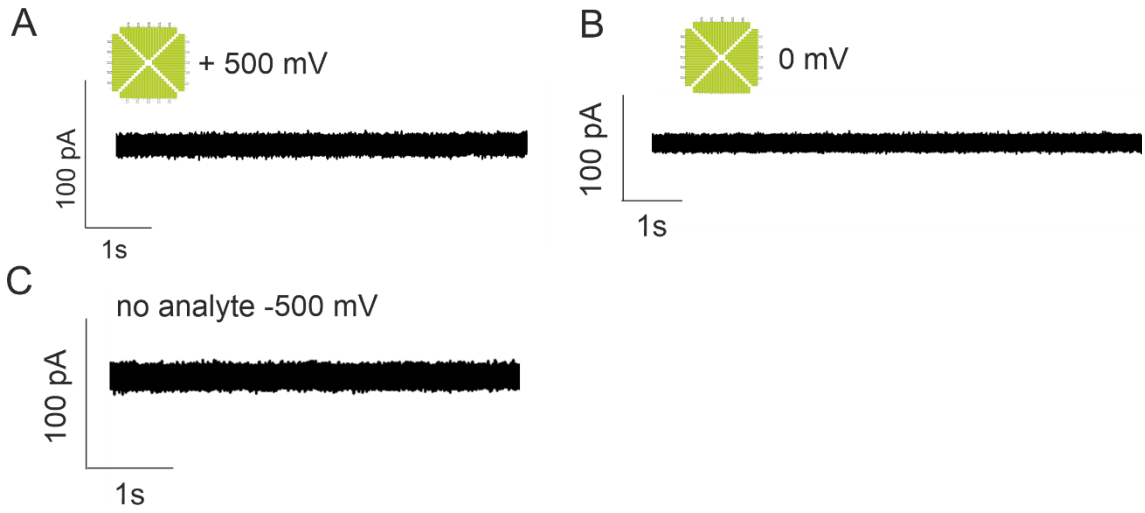

Figure 6:11 Ion current traces of A. monomer tile at positive voltage, B. monomer tiles at zero voltage, C. without any analyte at negative voltage.

Next, I examined the translocation of the tetramer tile through nanopore with and without PEG in electrolyte buffer. (Figure 6:12). The ion current signals generated from the tetramer tiles in an electrolyte bath without PEG were significantly smaller compared to those obtained in the presence of PEG. The presence of PEG in the electrolyte bath led to a substantial increase in the average peak amplitude of the tetramer ion current signals, rising from 0.04 ± 0.01 nA (without PEG) to 0.26 ± 0.13 nA (with PEG).

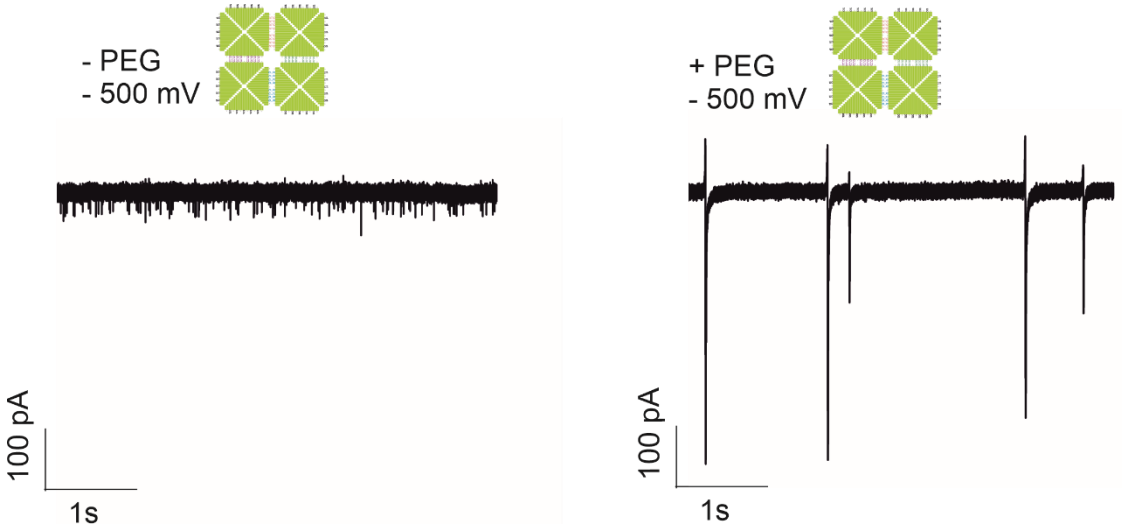

Figure 6:12 Ion current traces of 2 x 2 origami at – 500 mV A. without PEG B. with PEG in electrolyte bath.

Next, I compared the translocation signals of the monomer and the tetramer in the presence of PEG in electrolyte bath to check if the nanopipette sensor can discriminate between the monomer and tetramer. To differentiate between monomeric and tetrameric DNA tiles, ionic current signals were compared which were recorded with nanopipette

(Figure 6:13). The left panel shows representative traces for monomeric tiles, where uniform current blockade events were observed, highlighted by the green-shaded region. These blockades were uniform in amplitude with 0.14 ± 0.03 nA, indicating a consistent interaction of monomeric structures with the nanopipette tip. In contrast, the right panel corresponds to recordings obtained with tetrameric tiles, where two distinct populations of events emerged. The first type, similar in amplitude in to the monomer events, is again shaded in green, suggesting the presence of monomer tiles in the tetramer assembly sample. This can be observed from the AFM images in Figure 6:8 (right-bottom) where monomer tiles are also present in tetramer images. A second class of deeper and longer-lasting blockades (shaded in purple) was also observed, likely arising from the entire tetrameric structure engaging with the nanopipette tip. These distinct current signatures confirm that the nanopipette can effectively resolve monomeric and multimeric forms based on their characteristic blockade profiles (Figure 6:13).

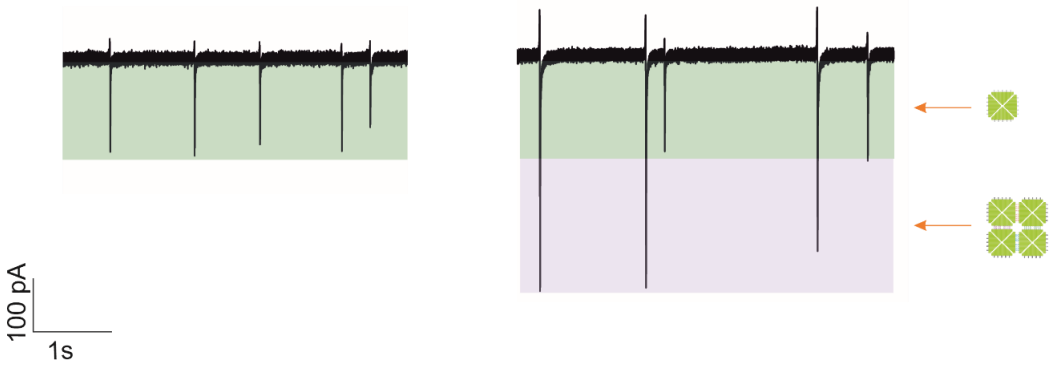

Figure 6:13 Ion current traces for monomer tile (left) shaded in green colour and tetramer tiles shaded in lavender.

The scatter plot of peak amplitude versus dwell time for both monomeric and tetrameric tiles further supports the presence of two distinct event populations in the tetramer data. One population overlaps with the monomeric events while the second population characterized by higher amplitudes is attributed to the full tetrameric structures, confirming the coexistence of both species in the tetramer sample (Figure 6:14). The presence of two distinct event populations was evident from the histogram, with monomer and tetramer events highlighted in green and orange, respectively. Monomeric tiles exhibited a narrow distribution with an average peak amplitude of 0.20 ± 0.07 nA, whereas tetrameric tiles showed a broader distribution centered at 0.43 ± 0.20 nA, consistent with the presence of more than one structures in tetramer sample.

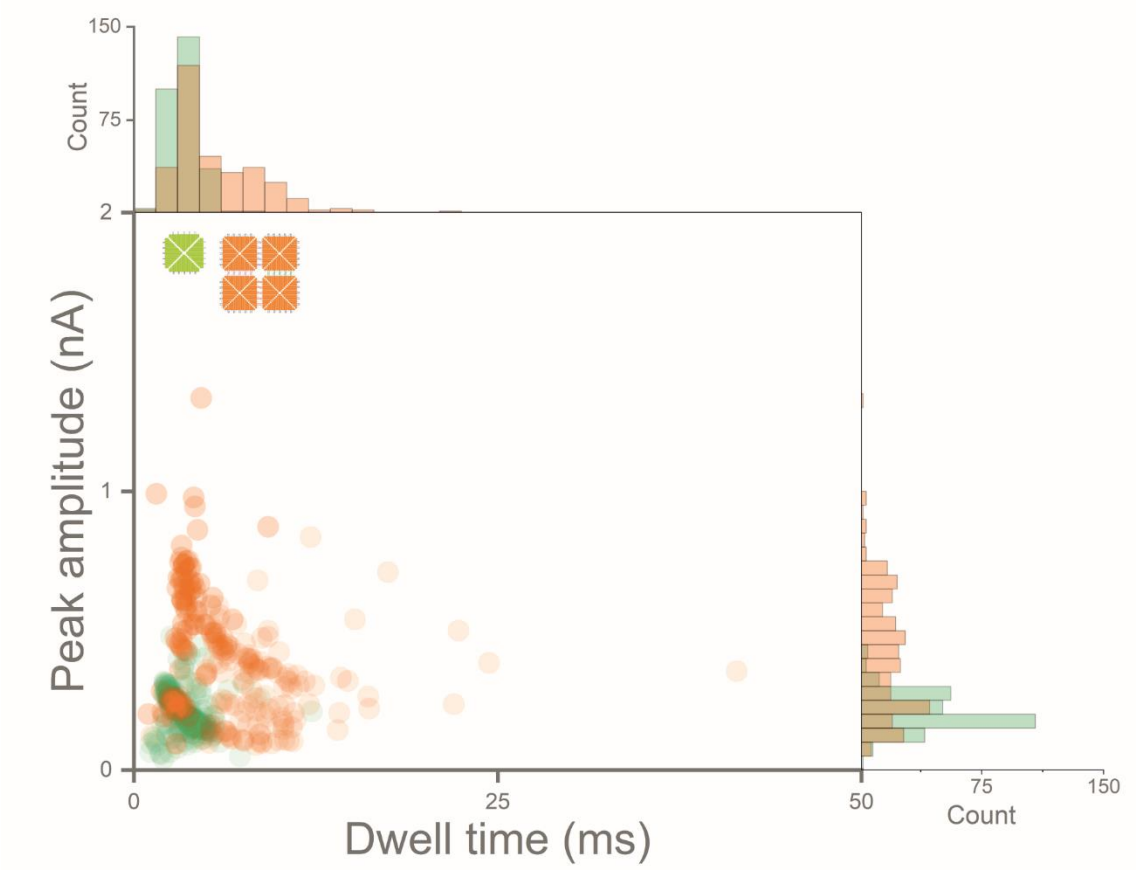

Figure 6:14 Scatter plot and histogram of monomer tile (n = 287) and 2 x 2 tile (N = 327)

Although both species were detectable without PEG, the addition of PEG significantly improved the quality of signal detection. PEG has been reported to enhance the signal-to-noise ratio for nucleic acids and proteins by amplifying ionic current signals and increasing event dwell times [324]. In this context, PEG facilitated clearer separation of translocation events corresponding to the two tile types, allowing more accurate discrimination and reducing event overlap. This improvement was critical for confidently resolving subtle differences in particle size and behaviour under otherwise similar experimental conditions.

This validated that the nanopore sensor was able to discriminate two extreme assembly of nanostructures, this provides preliminary evidence that in addition to methods like AFM and agarose gel electrophoresis which are typically used to characterise nanostructures nanopore sensors could be employed to determine the assembly yield of nanostructures [68, 263]. In summary, my preliminary work lays the foundation for using nanopipette-based sensing to distinguish between distinct DNA nanostructures, such as monomeric and tetrameric tiles, at the single-molecule level [327]. By demonstrating that characteristic current signatures can be reliably correlated with different assembly states, this approach offers a rapid, label-free, and cost-effective alternative to traditional

methods like agarose gel electrophoresis and AFM. While gel electrophoresis provides bulk yield estimates and AFM offers structural insight at high resolution, both methods face limitations in throughput, sensitivity, and representation of heterogeneous populations. In contrast, nanopore-based detection-such as that achieved with nanopipettes-enables real-time, non-destructive analysis with statistically meaningful data collected within minutes. My work provides a stepping stone toward more advanced applications, including high-throughput quantification, real-time monitoring of assembly/disassembly processes, and even the development of purification strategies based on translocation profiles. As the field evolves, integrating this platform with machine learning and parallelized detection systems could further enhance its power for profiling increasingly complex DNA origami assemblies.

6.2.2 Nanopore detection of functional origamis

After demonstrating the ability of nanopipettes to discriminate between DNA origami structures based on differences in size-specifically, now I will investigate whether this sensing strategy can be extended to detect protein-functionalised DNA origami. The aim of this section is to explore the feasibility of using nanopipette-based measurements to identify DNA origami structures carrying specific protein cargo. As a model system, I functionalised C-reactive protein (CRP) onto a DNA origami frame (4FSF) using a high-affinity affimer binder. The design and assembly of the 4FSF origami structure, along with the protein functionalisation strategy, are described in detail in Chapter 5, and purification was performed using the SPRI method outlined in Chapter 3.

The aim of this part was to detect CRP protein which is bound with origami, and also compare it with origami containing affimer . The affimer, a small engineered binding protein of approximately 12 kDa and less than 4 nm in size, was used to specifically bind CRP, a pentameric protein of ~120 kDa and approximately 10 nm in diameter [296, 334], as previously discussed in Chapter 1 (1.6). This system provides a platform to test whether the addition of protein components to DNA nanostructures produces distinguishable changes in ion current signatures, allowing for label-free detection of protein-functionalised origami at the single-molecule level. It has been previously reported that differences between an origami tile and a frame could be detected using a nanopipette sensor [328]. It was therefore hypothesized that the presence of a protein capable of filling the void in the DNA origami frame could be distinguished from origami structures lacking the protein.

Firstly, 4FSF origami were filled into the nanopipette at 0.5 nM, voltage of -500 mV was applied using two Ag/AgCl electrodes, with one positioned inside the nanopore and the other in the surrounding electrolyte bath containing 50% 35 K PEG in 100 mM KCl. I

applied negative voltages to push the negatively charged origami structures through the pore. Each ion current peak corresponds to one molecule translocating through the pore. When empty 4FSF origami structures translocated through the nanopore, ion current peaks were observed, as depicted in Figure 6:15 (left). Scatter plot and histogram was plotted with peak amplitude and dwell time values to obtain a dense population around 0.25 nA peak amplitude.

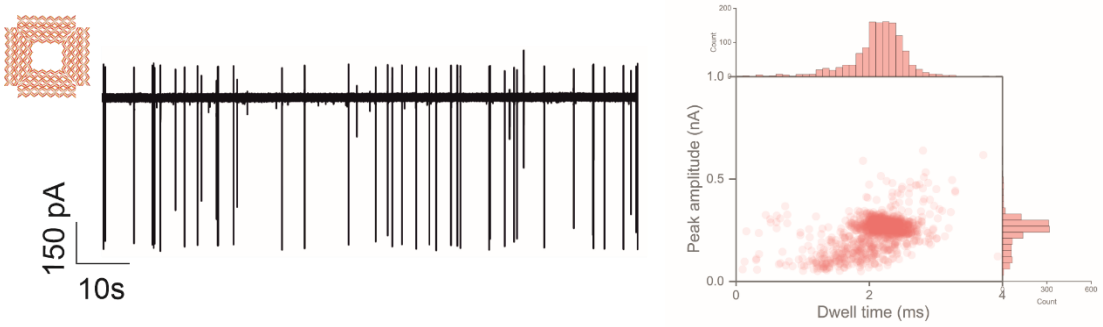

Figure 6:15 Ion current trace of origami frame (4FSF) and respective scatter plot and histogram (plotted from 1274 events).

6.2.2.1 Detection of CRP functionalised DNA origami

I chose a pore diameter of approximately 100 nm together with 50% 35K PEG electrolyte for translocating CRP-functionalised DNA origami, as it would be sufficiently large to accommodate the 88 × 88 nm 4FSF origami while still maintaining an adequate signal-to-noise ratio. Three origami systems were compared - empty 4FSF origami, single affimer-functionalised 4FSF origami and CRP-functionalised 4FSF origami. As described in Chapter 5, I have incorporated binding points (oligonucleotide) which complimentarily bind to the oligonucleotide conjugated with affimer. The affimer is specific for CRP therefore enabling the binding of CRP to affimer. This is characterised using AFM in Chapter 5 and SPR in Chapter 4. 0.5 nM of each sample were separately translocated through the nanopipette to produce ion current peaks. The ion current traces for empty 4FSF DNA origami (containing one binding site), 4FSF with a single affimer attached, and 4FSF with CRP protein bound are shown in the Figure 6:16. The trace for 4FSF origami shows homogeneous peaks, whereas the traces for 4FSF origami with a single affimer attached and with CRP bound exhibit a heterogeneous population of ion current peaks. This indicates a clear distinction in the translocation behaviour of empty 4FSF origami and protein-functionalised origami.

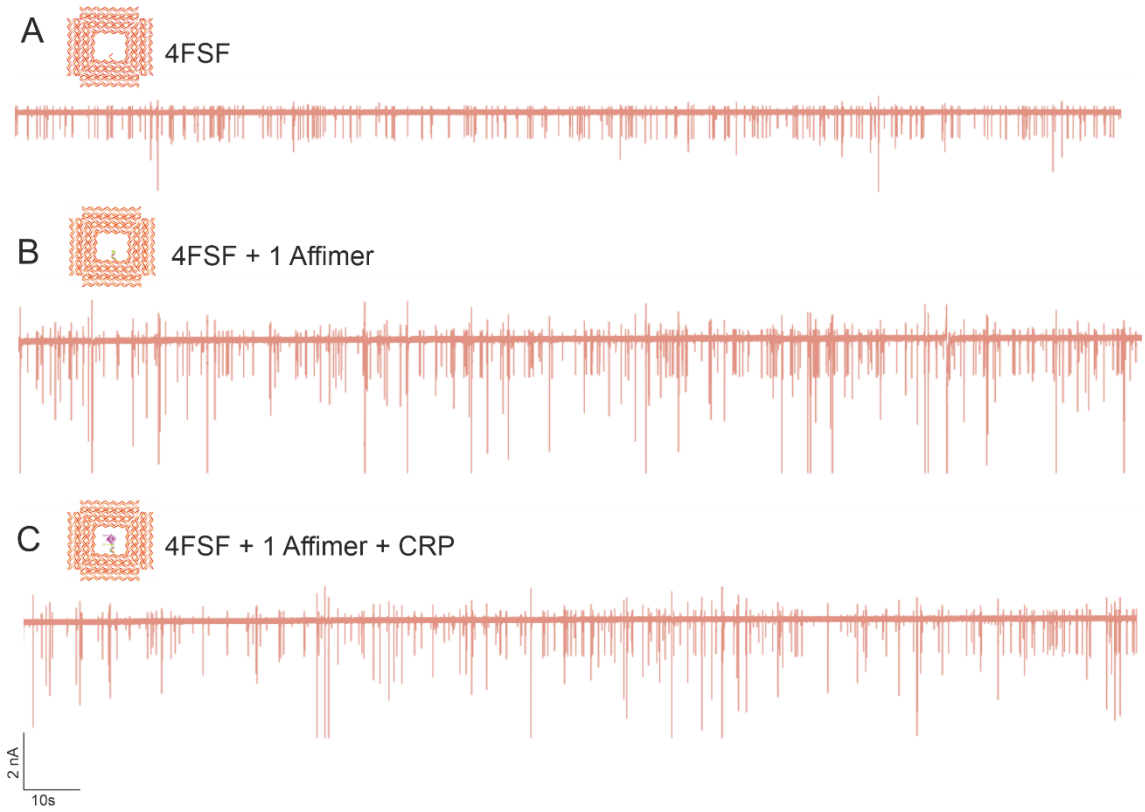

Figure 6:16 Ion current trace for 4FSF origami, 4FSF origami-Affimer and 4FSF origami-CRP recorded for 200 s.

This is further demonstrated by the scatter plot, where a distinct homogeneous population is observed for the empty 4FSF origami, in contrast to the multiple populations seen for 4FSF functionalised with a single affimer and with CRP. An average peak amplitude of 0.92 ± 0.27 nA was recorded for the empty 4FSF origami, indicating consistent translocation behaviour. In the scatter plots for the affimer and CRP functionalised samples, a population corresponding to the empty origami was still present, as expected. However, no clear distinction could be made between the additional populations observed in these two samples, as both displayed heterogeneous distributions beyond the population associated with the empty 4FSF origami. This suggests that while the presence of affimer or CRP alters the ion current signature, the differences between the two protein-bound states are not readily distinguishable based on scatter plot data alone.

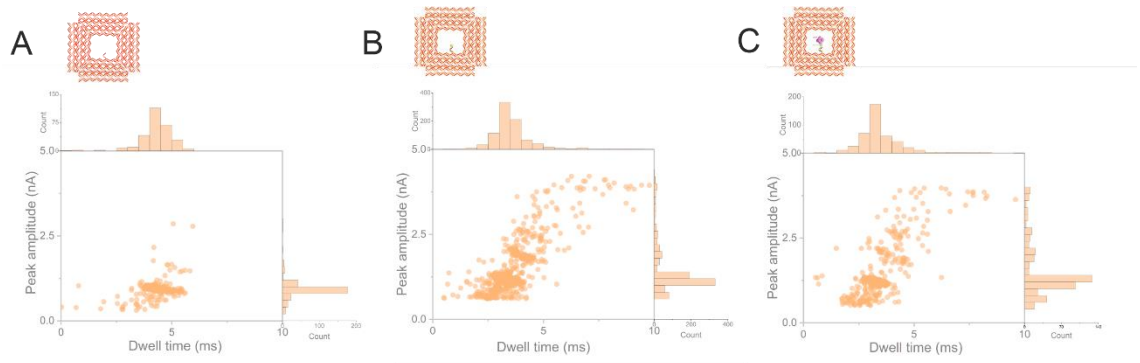

Figure 6:17 Scatter plot for A) Empty 4FSF-origami with a single binding point (280 events). B) 4FSF origami + Affimer (886 events) C) 4FSF origami + Affimer + CRP (435 events).

For further analysis, I employed a resampling method called bootstrapping (Chapter 2 for detailed method and approach) and I examined the peak area characteristic as this is a quantitative value that includes both peak amplitude and dwell time. Using bootstrapping analysis on the peak amplitude values from the empty 4FSF origami dataset, I identified a dominant, narrow distribution of event amplitudes, forming a distinct population (Figure 6:18). This population was defined as Range 1, representing characteristic peak areas arising from empty 4FSF origami translocating through the pore. The mean and spread of this distribution were used to define the upper boundary of Range 1. Events falling beyond this range were classified as Range 2, indicating larger or more complex structures such as origami functionalised with affimers or CRP proteins. This classification was supported by both scatter plots and kernel density estimates, which showed a homogeneous population for empty origami and broader, heterogeneous distributions for functionalised constructs (Figure 6:18C and D). Importantly, both affimer and CRP modified origami samples exhibited a subpopulation overlapping with Range 1 (reflecting the base origami signal), along with additional populations extending into Range 2, consistent with successful functionalisation.

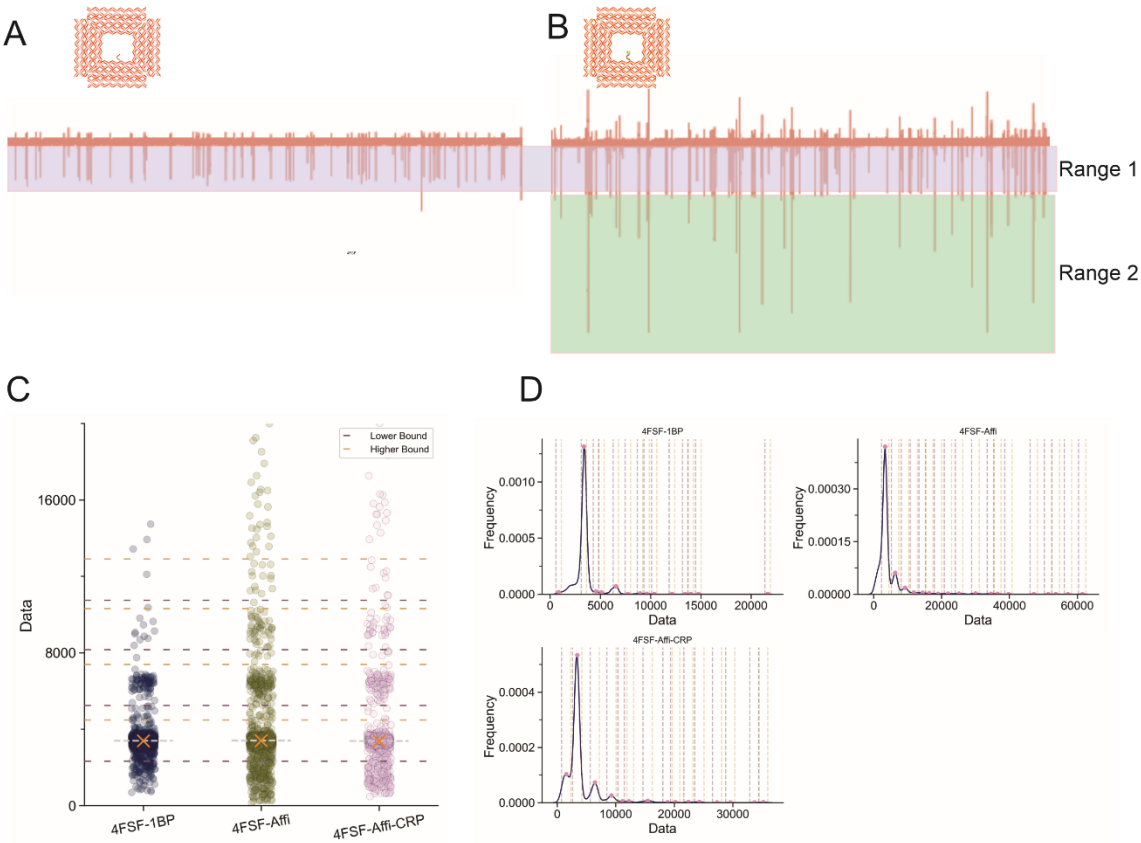

Figure 6:18 Bootstrapping analysis of empty 4FSF origami, affimer-functionalised 4FSF origami and CRP-functionalised 4FSF origami. A) Ion current trace for empty 4FSF origami showcasing a homogenous distribution of peaks. B) Ion current trace for affimer-functionalised 4FSF origami as a demonstration of how ranges are assigned in analysis. Range 1 is assigned to empty 4FSF origami and Range 2 is assigned for any signal with amplitude beyond empty 4FSF origami. C) Scatter plots of empty 4FSF origami, affimer functionalised 4FSF origami and CRP functionalised 4FSF origami. The dotted line represents the cluster in which the data points for range 1 and 2 reside. D) Kernel density estimation and decision for picking ranges.

Next, I quantified the proportion of data points falling within each defined range to estimate the distribution of the population across non-functionalized and functionalized states. Specifically, I calculated the percentage of data points that lay within Range 1 (non-functionalized) and those that exceeded this threshold into Range 2 (indicative of functionalization). This allowed us to assess the extent of successful modification across different conditions. As expected, the majority of data points from the 4FSF-1BP group were confined to Range 1, consistent with its role as a negative control. In contrast, a significantly larger proportion of data from the 4FSF-Affi and 4FSF-Affi-CRP groups extended into Range 2, highlighting the presence of functional modifications. Interestingly, when 4FSF with one affimer was translocated through the nanopore, we observed 25% of ion current peaks in range 2. This meant that the sensor we have developed could detect a difference in mass of 12,000 Da or a diameter less than 4 nm [296]. As described in previous sections, C-reactive protein (CRP) is a clinically relevant biomarker, and we aimed to evaluate whether the sensor platform we developed could

effectively detect CRP (120 kDa) when bound to its specific affimer within the DNA origami frame (4FSF). Surprisingly, we observed no significant shift in the overall signal distribution when CRP protein was bound to the affimer inside the DNA origami frame (Figure 6:19). Despite successful functionalization of the DNA origami with affimers, the addition of CRP did not lead to a clear change in signal amplitude when compared to the affimer-only condition. Quantitatively, approximately 25% of the data points for the CRP-functionalized DNA origami fell into Range 2, the region previously defined as indicative of functionalization. This proportion is comparable to the affimer-only condition and does not suggest a substantial enhancement in signal due to CRP binding. These results imply that either the binding of CRP does not generate a detectable change in the signal used in this assay, CRP could have detached from its binding site on DNA origami, or that the current resolution and sensitivity of the platform are insufficient to distinguish CRP-bound from affimer-only states.

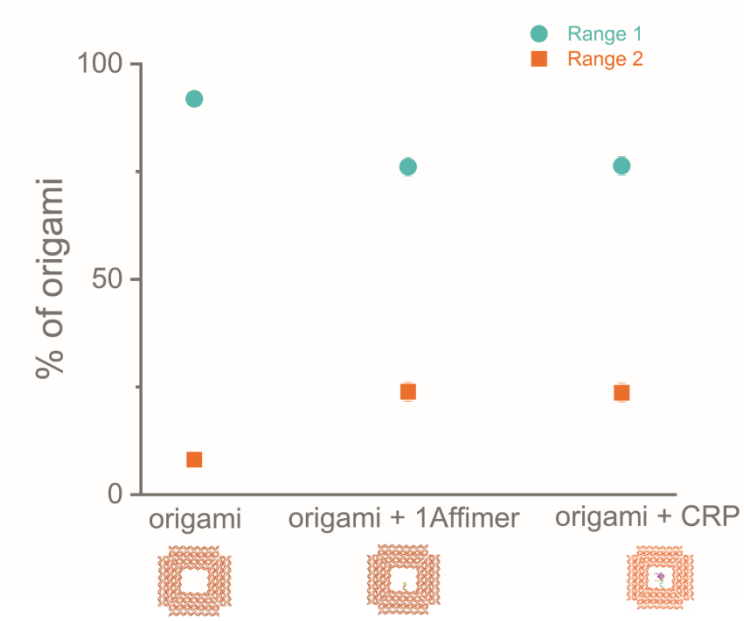

Figure 6:19 Plot showing percentage of ion current peaks in each range. The value corresponds to the percentage of origami in each range. Range 1 corresponds to non-functionalized origami depicted by cyan colour in round shape. Range 2 corresponds to functionalised origami depicted by orange colour in square shape. Error bars represent standard deviation obtained from bootstrap resampling.

An addition of 12 kDa (affimer) in mass to the DNA origami resulted in a 25% increase in the number of events with higher peak amplitude. However, a further addition of 120 kDa (CRP) did not produce any change in the ion current peaks. This observation raised the question of whether the change in ion current during analyte translocation through the nanopore is indeed driven by mass or if any other factors contribute. To investigate this, we designed a DNA origami frame (4FSF) incorporating ten affimers arranged within the central void. The total molecular mass of the ten affimers was approximately 120 kDa, which closely matches the molecular weight of the CRP protein. For comparison,

the CRP protein alone has a molecular mass of approximately 120 kDa. Range 1 corresponds to un-functionalised or empty DNA origami structures, while range 2 is associated with functionalised 4FSF. For the unmodified 4FSF DNA origami, 92% of events fell into range 1 and only 8% into range 2. Upon functionalisation with a single CRP-affimer complex, range 1 events decreased to 76%, while range 2 increased to 24%. In the case of the DNA origami functionalised with ten affimers, only 33% of events remained in range 1, while 68% shifted to range 2 (Figure 6:20). Interestingly, a significant difference in the proportion of events within range 2 was observed between the DNA origami structures. The 4FSF DNA origami functionalised with ten affimers yielded approximately 68% of events in range 2, whereas the CRP-bound origami produced only 25%. Although the combined molecular mass of ten affimers is approximately equivalent to that of the CRP-affimer complex (~120 kDa), the two configurations resulted in markedly different signal distributions. This suggests that nanopore translocation is not governed solely by molecular mass, as structures with equivalent mass produced distinct signatures and substantially different proportions of events within the functionalised signal range.

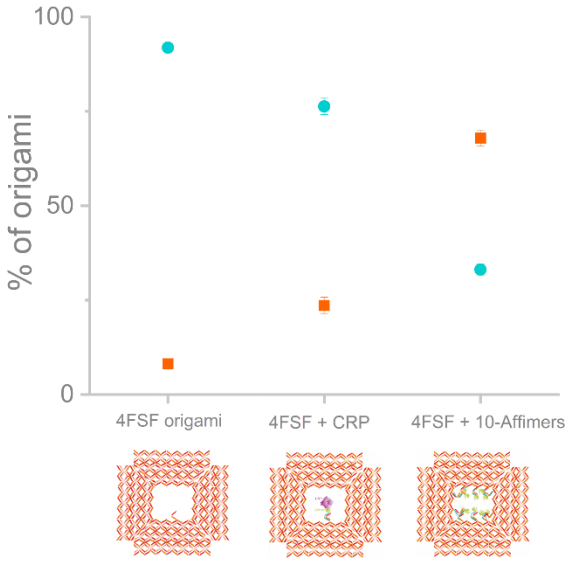

Figure 6:20 Plot showing percentage of ion current peaks in range 1 and 2 for empty 4FSF, 4FSF + CRP, and 4FSF + 10 Affimers. Range 1 corresponds to non-functionalized origami depicted by cyan colour in round shape. Range 2 corresponds to functionalised origami depicted by orange colour in square shape. Error bars represent standard deviation obtained from bootstrap resampling. For each construct, the data represents the mean of two independent experiments (p-value = 0.0005).

6.2.2.2 Detection of affimer functionalised DNA origami

While CRP functionalisation did not produce a marked change in the proportion of events in range 2 (functionalised origami) compared to origami with a single affimer, a significant increase was observed when multiple affimers were introduced. Specifically, the 4FSF

DNA origami with one affimer showed approximately 25% of events in range 2, which was comparable to the 4FSF-CRP structure. However, when eight affimers were attached to the 4FSF frame, the proportion of events in range 2 increased substantially to 67.90%. This notable difference suggests that the degree of functionalisation has a measurable impact on the translocation signal. These findings raised the possibility that the nanopore system may be sensitive enough to detect and distinguish varying numbers of affimers on the DNA origami structure.

For this investigation, DNA origami structures were folded with varying numbers and combinations of binding sites (oligonucleotides), as described in Chapter 2 (2.5), and were characterised using the procedures outlined in Chapter 5. As the binding sites on the DNA origami were complementary to the oligonucleotides conjugated to the affimers, it was possible to fold origami structures functionalised with 1, 2, 4, 6, 8, 10, and 12 affimers (Figure 6:21).

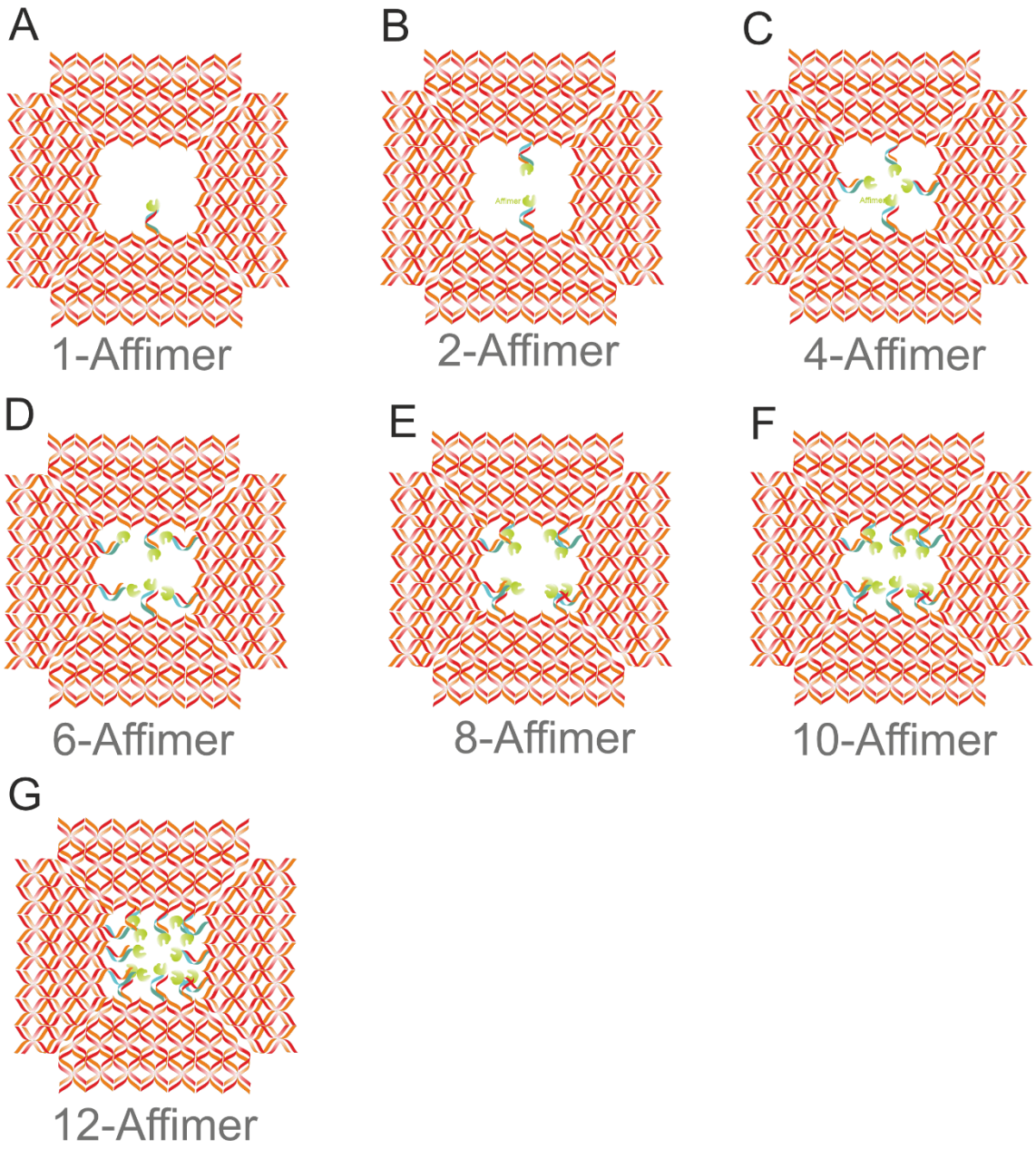

Figure 6:21 Illustration of 4FSF origami with A) one affimer, B) two affimers C) four affimers, D) six affimers, E) eight affimers, F) ten affimers, G) twelve affimers. The green icon represents the affimer.

Each of the affimer-functionalised DNA origami structures was translocated through a nanopore with an approximate diameter of 100 nm. The attachment of affimers to the origami resulted in peaks with larger ion current amplitude compared to empty origami upon translocation, as evident from the ion current traces (Figure 6:22). A homogeneous population distribution was noted for the empty origami, in contrast to the functionalized origami structures (Figure 6:22A). Some outliers were observed in empty 4FSF origami samples. I speculate that these may be due to mis-folded or partially folded structures, or possibly due to instrumental noise. Similar behaviour has been reported before [13, 326]. Ion current traces as observed for 4FSF with 1 affimer and above indicated the

presence of populations with higher peak amplitudes in the functionalized origami compared to the empty origami (Figure 6:22). Origami functionalised with at least one affimer displayed higher peak amplitudes than those without affimer as qualitatively visualised from the trace. Similarly, the number of ion current peaks with high amplitude were found to be increasing with increasing number of affimers attached to 4FSF origami. This provided a preliminary indication that functionalised 4FSF origami structures could be differentiated based on the number of proteins attached.

Next, I plotted scatter graphs with peak amplitude (length of an ion current peak) and dwell time (width of an ion current peak) and observed a homogenous population of events for 4FSF origami which was not functionalised. An average peak amplitude value of 0.24 ± 0.08 nA and dwell time of 2.1 ± 0.43 ms was observed for empty 4FSF origami. I observed data points corresponding to values higher than those observed for empty 4FSF origami as indicated in scatter plots below Figure 6:23. Further analysis using bootstrapping was employed to obtain quantitative values for percentage of origami that was functionalised.

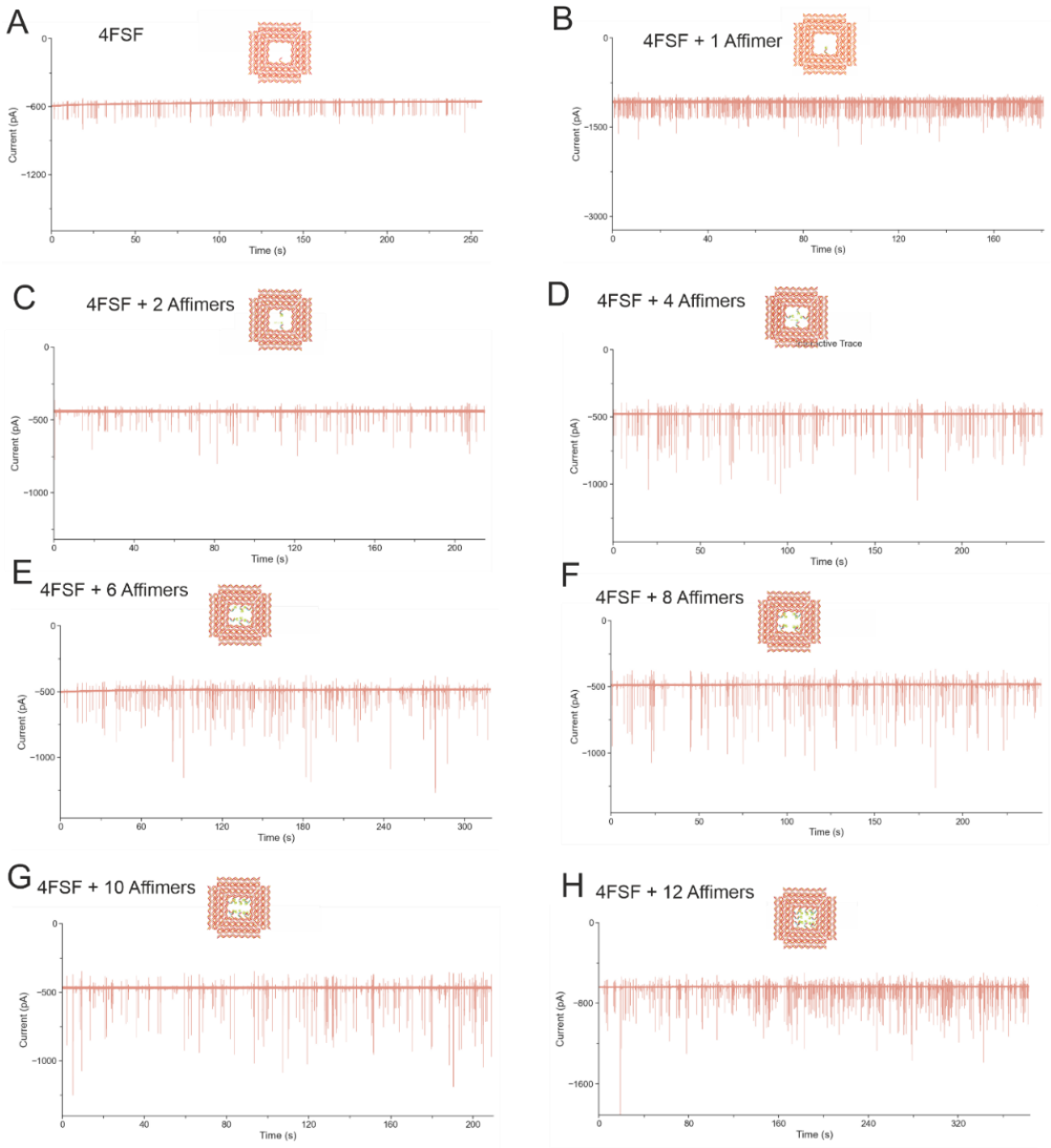

Figure 6:22 Raw ion current traces for 4FSF origami functionalised with A) no affimers, B) 1 affimers, C) 2 affimers, D) 4 affimers, E) 6 affimers, and F) 8 affimers, G) 10 affimers, and H) 12 affimers.

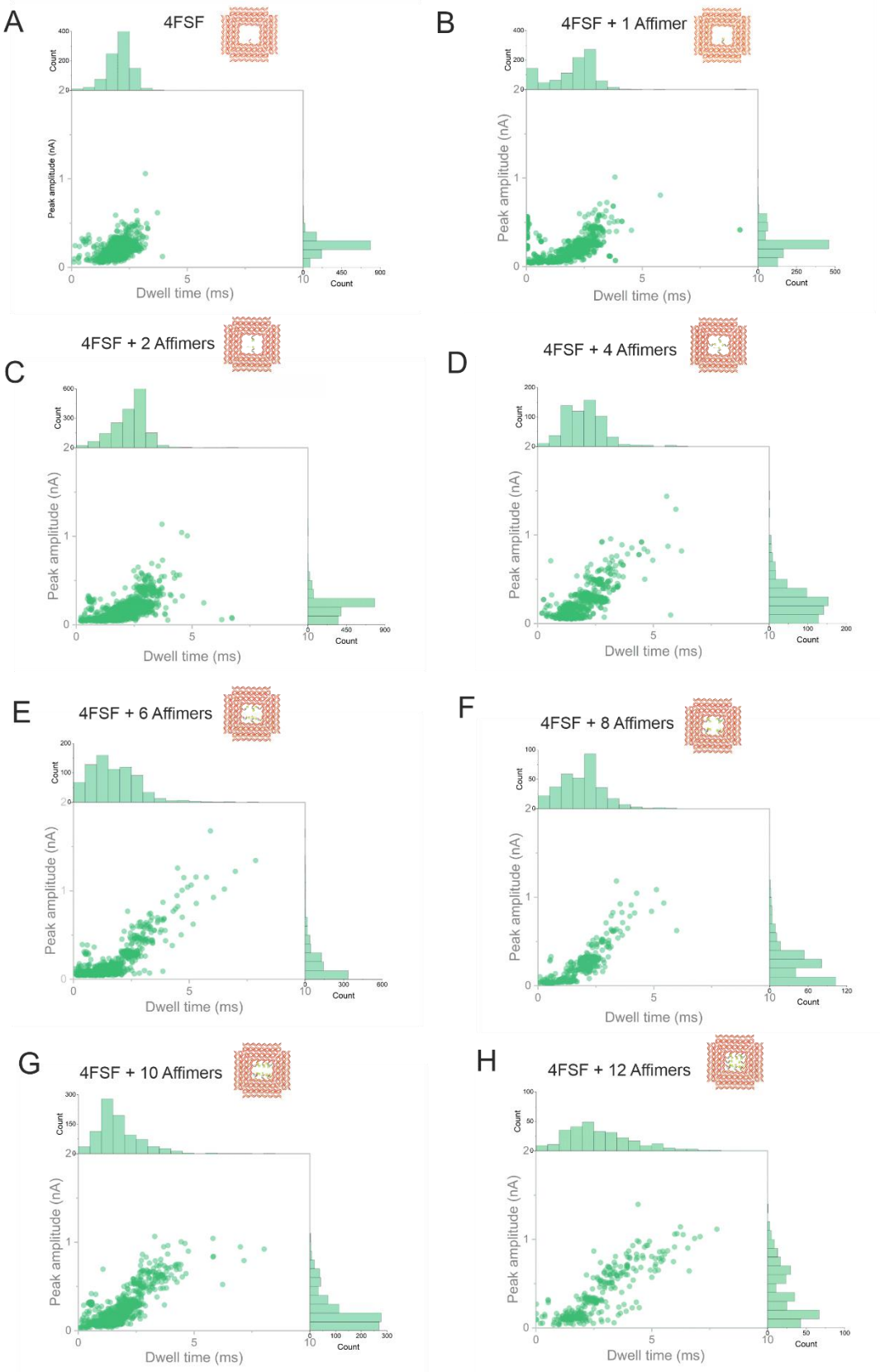

Figure 6:23 Scatter plot of Dwell time (ms) vs Peak amplitude (nA) for A) empty 4FSF origami (1274 events), B) 4FSF + 1 Affimer (934 events), C) 4FSF + 2 Affimers (1669 events), D) 4FSF + 4 Affimers (622 events), E) 4FSF + 6 Affimers (746 events), F) 4FSF + 8 Affimers (330 events), G) 4FSF + 10 Affimers (877 events), and H) 4FSF + 12 Affimers (283 events).

With the bootstrap method, an example is presented below (Figure 6:24), showing how range 1 and range 2 were defined based on the ion current traces for three conditions: empty 4FSF origami, 4FSF with one affimer, and 4FSF with ten affimers (Figure 6:24). The ion current trace for the empty 4FSF origami exhibited a relatively homogeneous population of peaks, which were designated as range 1. In contrast, 4FSF structures functionalised with one or ten affimers showed a more heterogeneous distribution of events. Peaks that deviated significantly from those observed for the empty origami were classified as range 2, indicating a different translocation behaviour likely caused by the presence of affimers.

Figure 6:24 Ion current traces of 4FSF origami with 0, one and ten affimer binding points. Range 1 is shaded in green and range 2 is shaded in lavender.

First, I assessed the reproducibility of translocating the functionalised origami structures through nanopore. For this, I selected the 4FSF origami with one affimer functionalised to it and translocated it through two different nanopipettes which were fabricated separately but using the same program. Ion current traces were recorded and peak area extracted for analysis. I observed 78% of the events (unfunctionalized origami) fell into range 1 for pipette 1 and 22 % (functionalised) into range 2. Same percentage (79% and 21%) was observed when the same sample was translocated through pipette 2 (Figure 6:25). The percentage observed here is comparable with the data presented in 6.2.2.1 where 75% and 25% of peaks fell under range 1 and 2 for 4FSF origami functionalised with one affimer. This confirmed the reproducibility of translocation experiments and analysis.

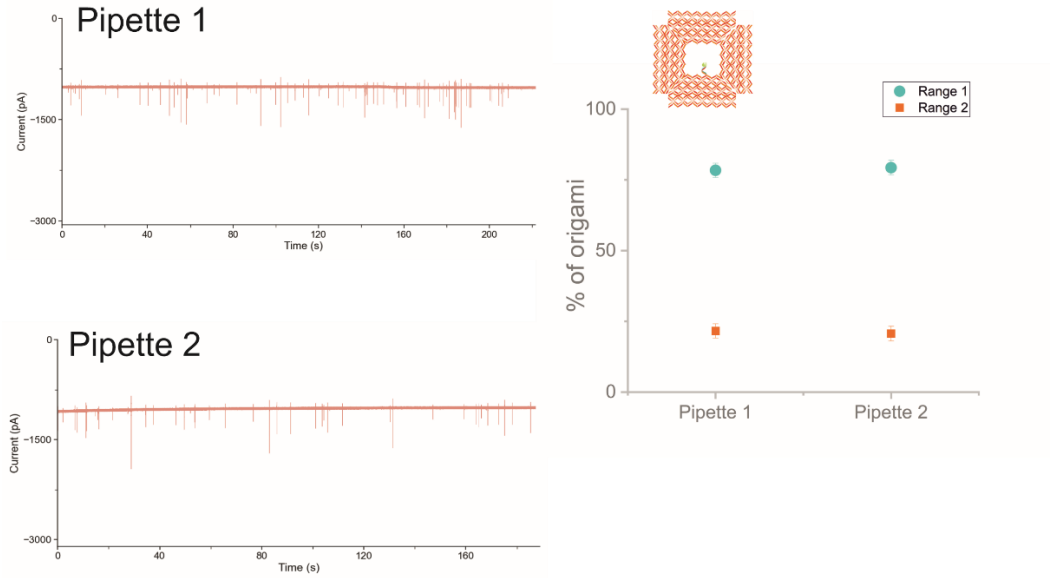

Figure 6:25 Graph showing percentage of origami in range 1 and range 2 for sample 4FSF + 1 Affimer translocated through two different pipettes. The error bar indicate standard deviation.

Next, I adopted the same method to analyse origami functionalised with one, two, four, six, eight, ten and twelve affimers and checked if it produced any quantitative difference in percentage of functionalised structures. Interestingly, we observed that as the number of affimers functionalized to the origami increased, the percentage of the population falling within range 2, representing functionalized origami, exhibited a corresponding increase (Figure 6:26). The trend was accompanied by a corresponding decline in the population within range 1. The empty DNA origami frame exhibited 95% of signals within range 1, confirming absence of functionalisation and only 5 % falling within range 2. Functionalization of the origami structure with a single affimer resulted in a significant increase in population percentage to 20%, compared to the unfunctionalized origami. As the number of affimers attached to the origami increased to 2, 4, 6, 8, 10, and 12, the population percentages rose incrementally to approximately 25%, 33%, 40%, 41%, 62%, and 70%, respectively. This experiment was repeated to check the reproducibility and observed same trend. The percentages observed in range 2 for the repeat experiment - conducted using fresh samples and different pipette pulled with same parameters - were 3%, 6%, 18%, 33%, 41%, 58%, 59%, 60% for 0, 1, 2, 4, 6, 8, 10, and 12 affimers functionalised on DNA origami, respectively. These findings demonstrate that the nanopore sensor developed in this study is capable of detecting a difference in attachment of proteins as small as 12,000 Da to the origami.

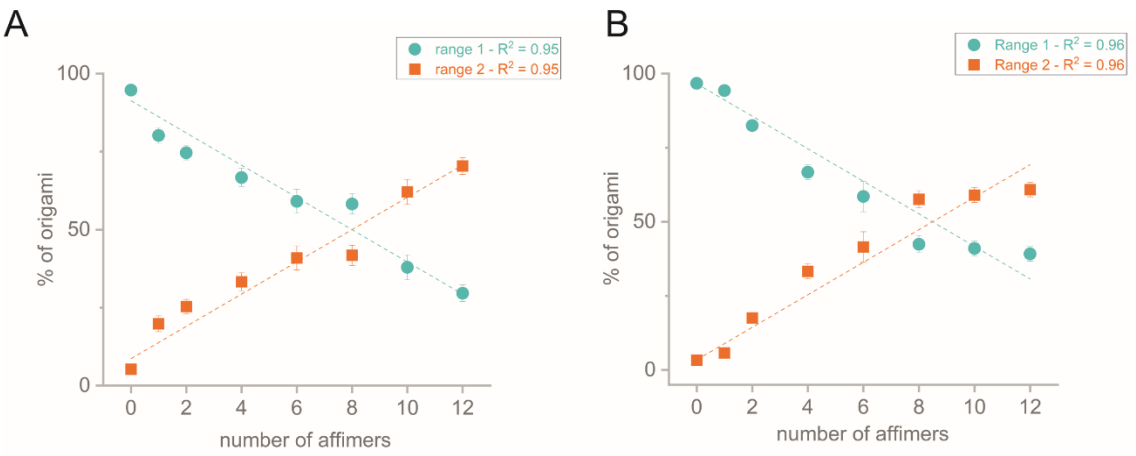

Figure 6:26 Plot denoting the percentage of origami in range 1 and range 2. Range 1 is depicted by blue round dots and range 2 is depicted by square orange dots. A and B are repeats done with fresh batch of sample in different pipettes pulled with the same parameters. Linear regression analysis yielded R^2 values of 0.95 and 0.96 reflecting high correlation between number of affimers and functionalised origami population. A and B are independent experiments (A one-way ANOVA yielded p-value <0.001).

I was able to demonstrate the same trend in the percentage of origami falling within Range 2 with increasing numbers of bound affimers, even when the structures were translocated through a nanopipette fabricated using a different program but with approximately the same pore size (Appendix A - .2). I observed a 25% population in range 2 when 2 affimers were bound with 4FSF frame, then increasing to 40%, 53%, 62%, 69%, and 80% with increasing number of affimers from 4, 6, 8, 10, and 12. This further provide evidence on the reproducibility of the method in assessing number of affimers attached to origami.

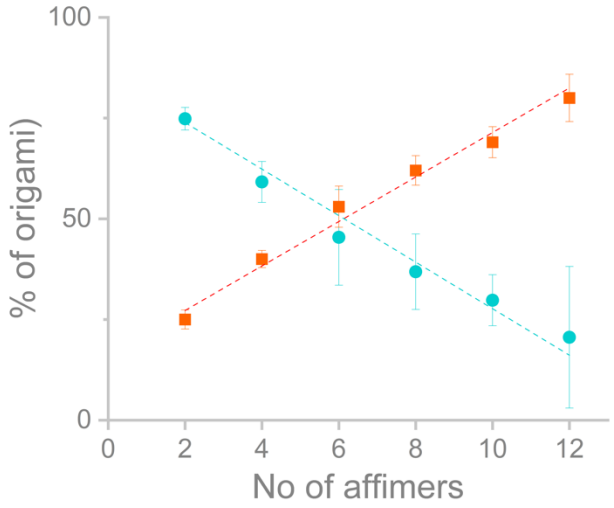

Figure 6:27 Plot denoting the percentage of origami in range 1 and range 2. Range 1 is depicted by blue round dots and range 2 is depicted by square orange dots. Linear regression analysis yielded R^2 values of 0.95 and 0.96 reflecting high correlation between number of affimers and functionalised origami population. The data is combined from 2 experiments.

To investigate whether the observed increase in percentage within range 2 was dependent on the yield of functionalisation, I selected origami structures with a single binding point and conjugated them with increasing concentrations of affimer-oligonucleotide constructs. If the observed increase in percentage were yield-dependent, we would expect a proportional rise, similar to the data presented in Figure 6:26. I speculated that providing an excess of affimer-oligonucleotide to origami structures with single binding point would enhance the functionalisation yield, resulting in a range 2 population percentage comparable to that observed in Figure 6:26. Origami structures with one binding site were incubated with affimer-oligo concentrations at 5x (10 nM), 10x (20 nM), 50x (100 nM), and 100x (200 nM) excess to that of origami which was at 2 nM concentration. I extracted the peak area values, underwent bootstrapping and checked the population percentage within range 2 to analyse this. Surprisingly, increasing the concentration of affimer-oligonucleotide did not lead to a higher percentage in Range 2; instead a decline was observed (Figure 6:28). This confirms that the observed trend in Figure 6:26 is not yield dependent but due to some other effect specifically attributing to the binding of affimer to origami.

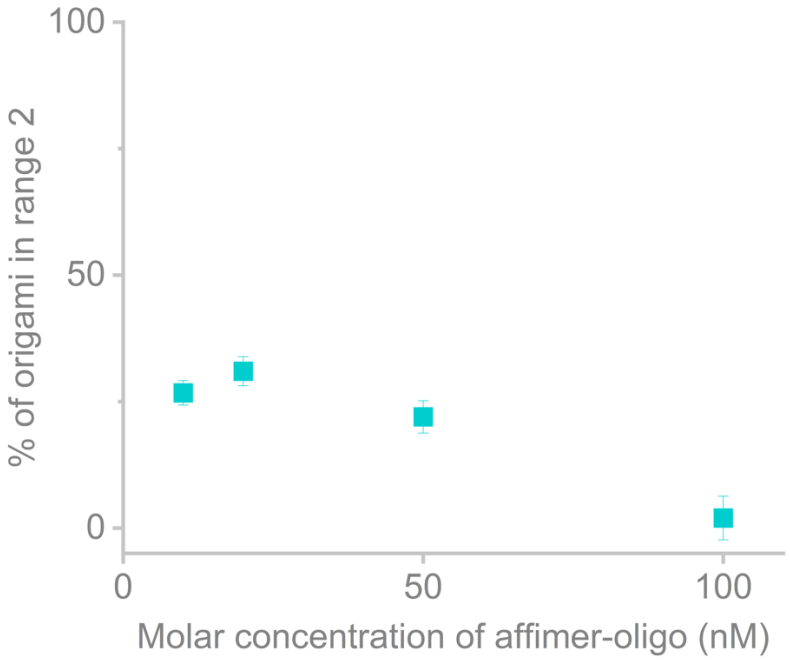

Figure 6:28 Percentage of origami in range 2 corresponding to increasing concentration of affimer-oligo constructs added to DNA origami with one binding point.

At 5x, 10x, and 50x concentrations, approximately 25% of peaks were observed in range 2, consistent with the data presented in Figure 6:26. However, at 100x concentration, functionalised origami structures population declined, likely due to the saturation of affimer-oligonucleotide, resulting in tiny peaks corresponding to affimer-oligonucleotide constructs. To confirm if the small peaks corresponded to affimer-oligonucleotide constructs, I translocated affimer-oligonucleotide through nanopore with same diameter used for 4FSF + 1 Affimer with 10 times affimer-oligonucleotide. Similar small peaks were observed when affimer-oligonucleotide were passed through the nanopore indicating the presence of the same constructs in the 4FSF origami with one affimer and 10x affimer-oligonucleotide added (Figure 6:29).

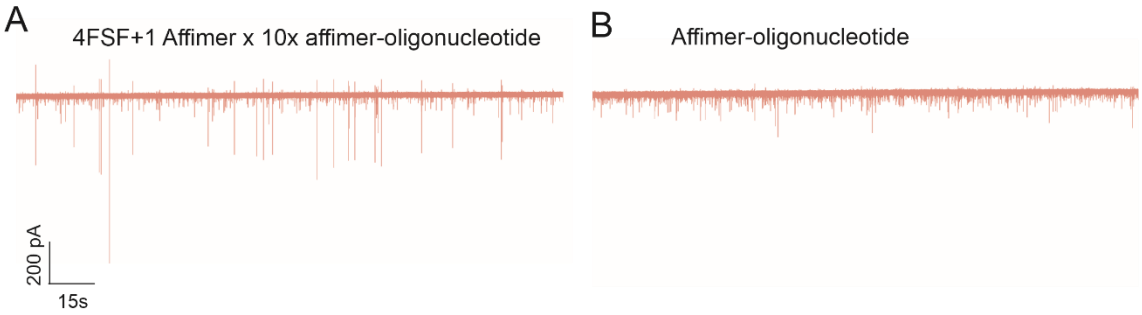

Figure 6:29 Ion current trace for origami + 1 binding point incubated with 100x excess of affimer-oligonucleotide.

Next, I investigated the effect of adding varying amounts of affimer-oligonucleotides to 4FSF origami containing ten binding points. This experiment aimed to eliminate any influence from random interference. Affimer-oligonucleotides were added at concentrations of 2.5x, 5x, 10x, 50x and 100x relative to the amount required for full functionalisation of the ten affimer sites. A population percentage of approximately 25% was observed in range 2 (functionalise origami) when 2.5x and 5x concentrations of affimer-oligonucleotides were added, which corresponds to the signal profile typically associated with origami functionalised with a single affimer. I speculate that under these conditions, only one of the ten available binding sites may be functionalised, resulting in signals similar to those observed for 4FSF origami with one affimer. The addition of 10x and 50x excess affimer-oligonucleotides resulted in a population percentage of approximately 50%, which aligns with the values observed for 4FSF origami functionalised with ten affimers Figure 6:30. Increasing the concentration beyond this, for example to 100x excess did not produce any significant change from 50%. This provide an evidence that observed change is not random but can be controlled indicating reliability of functionalisation process.

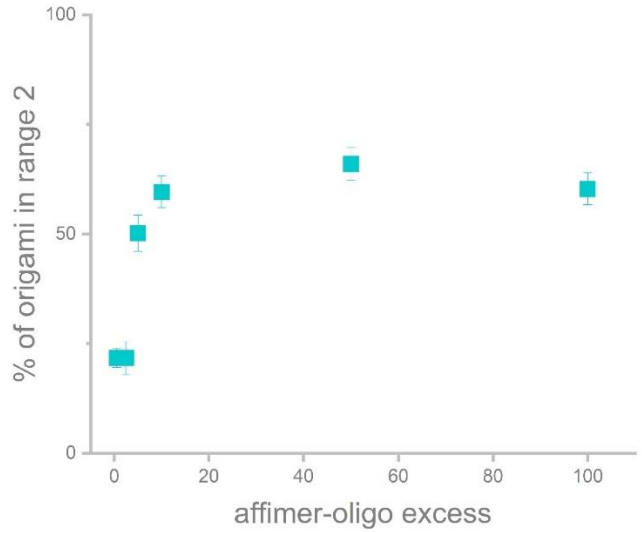

Figure 6:30 percentage of origami in range 2 corresponding to affimer oligo excess conjugated to DNA origami with 10 binding points.

To eliminate the possibility of non-specific binding of affimer proteins to the 4FSF origami frame, I performed control experiments by adding 225 nM of affimer proteins to 10 nM of 4FSF origami structures with 2, 4, 6, 8, 10 and 12 binding points (oligonucleotides). I observed a a population percentage of around 100 % in range 1 for all the structures indicating all of them were non-functionalised. A percentage close to 0 % was observed in range 2 for all the structures further indicating the absence of functionalisation (Figure

6:31). This confirms that the affimer proteins do not non-specifically bind to the origami structures and the trend that was observed in Figure 6:26 has no effect from random non-specific affimer interaction with origami.

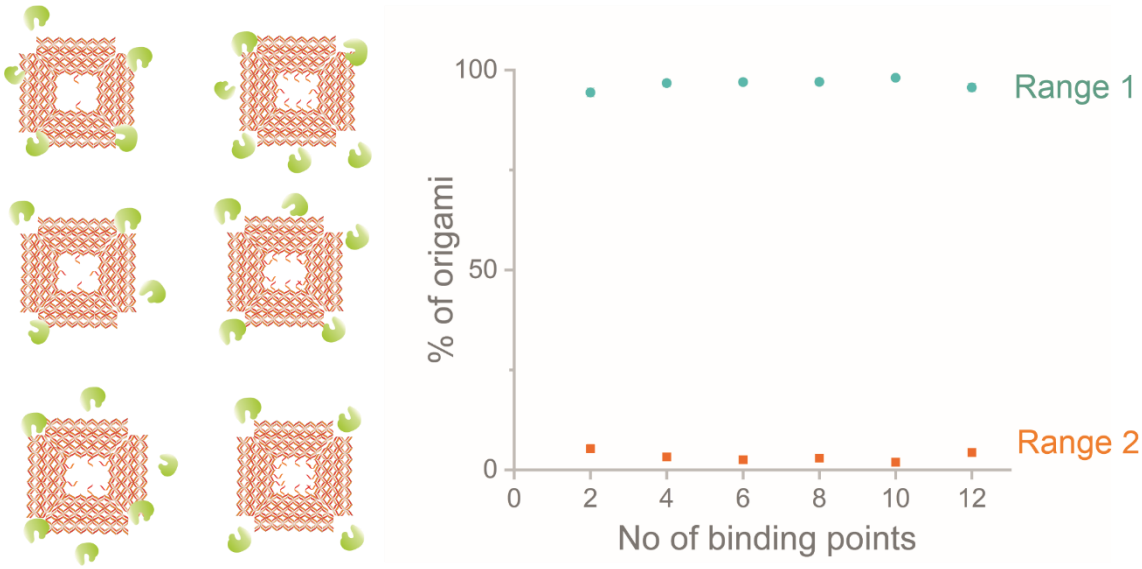

Figure 6:31 Percentage of origami in range 1 and range 2 for origami mixed with affimer without oligo-maleimide.

I also investigated whether the effect of affimer binding on 4FSF origami frame in Figure 6:26 was specific to protein binding and not due to the interaction involving oligonucleotide to which affimer is conjugated. For this, I hybridised the 22 bases long oligonucleotide to the binding points on 4FSF origami frame and translocated through nanopore. No affimer was added to this construct. I observed a percentage close to 100 for all the 4FSF origami structures (with 2, 4, 6, 8, 10, and 12 binding points) bound with complimentary oligonucleotides in range 1 (Figure 6:32). This indicated that the major population in the sample were non-functionalised thereby confirming that oligonucleotide itself do not contribute to any ion current changes as compared to empty 4FSF origami. In contrast to this, the population percentage for all the samples in range 1 were close to 0 further confirming the signals observed in Figure 6:26 is due to affimer interaction with nanopore.

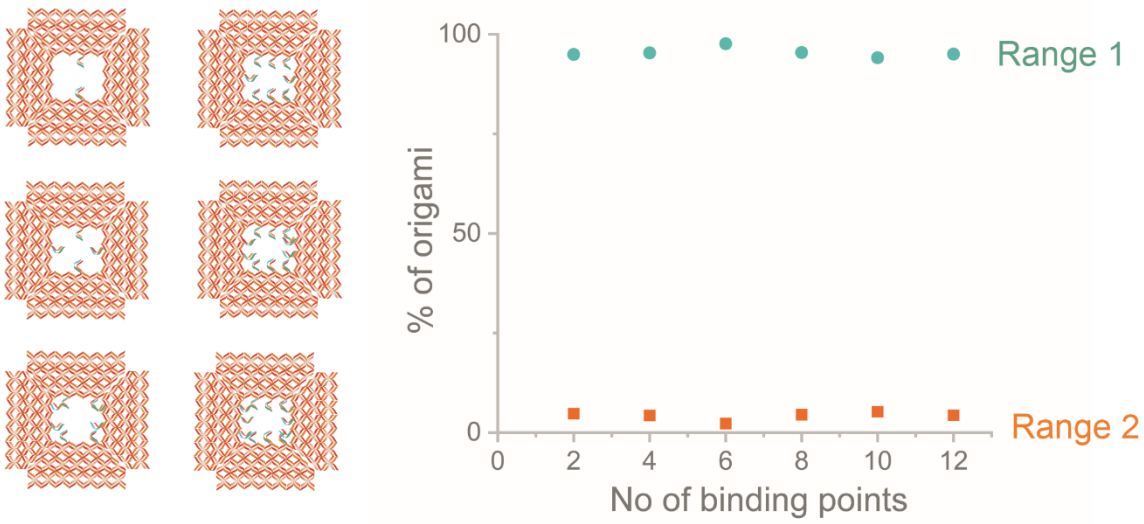

Figure 6:32 Percentage of origami in range 1 and range 2 for origami with complimentary strand bound to oligo binding point to affimer. The cyan strands in the illustration on left indicate the complimentary strand that bound to binding point (orange) on origami.

Conclusion

This chapter explored the nanopore translocation of DNA origami structures and protein-functionalized DNA origami. The incorporation of PEG in the electrolyte system enabled the detection of a monomer and tetramer tile. The nanopore sensor demonstrated its potential as a complementary tool to techniques such as atomic force microscopy (AFM) and agarose gel electrophoresis for quantifying DNA origami structures. In addition to this, I have successfully demonstrated how addition of proteins as small as affimers on DNA origami structures could affect the translocation behaviour. The origami-nanopore sensor I developed here offers a label free single molecule detection of proteins at high resolution.

The detection of small proteins holds significant relevance for clinical diagnostics, highlighting the importance of developing biosensors capable of identifying these molecules. Many biomarkers are small proteins which could act as early indicators of disease. I have demonstrated in this chapter how small proteins could be detected using DNA origami and nanopore technology and this could be a stepping stone for small biomarker diagnostic detection. It would be interesting to understand the mechanism involved in the change observed by addition of affimers. I consistently observed a significant change in percentage of functionalised origami with addition of affimer proteins. It is interesting that the number of events are increased with increasing number of affimers rather than the ion current characteristics. I speculate that the interaction of protein with DNA origami is inducing a change in the origami structure thus affecting the

translocation signals. Such effects have been observed where binding of proteins on DNA origami could cause structural changes and bending in DNA [335].

Reports suggest that the translocation of DNA origami through nanopores may be influenced by structural rigidity changes. It has been proposed that nanostructures in solution undergo alterations in shape and flexibility which could explain the observed changes in origami translocation [336, 337]. Additional evidence is required to validate this hypothesis. Furthermore, protein binding to DNA origami may modify its structural features, such as rigidity or flexibility, potentially impacting nanopore signals [335].

Interestingly, we observed specific and reproducible signals corresponding to the attachment of different numbers of affimer proteins to the DNA origami, which could not be explained solely by the mass of the proteins. This finding underscores the potential for detecting tiny proteins, paving the way for advanced protein sensing and the efficient detection of small biomarkers within complex protein mixtures. Such advancements could play a critical role in clinical diagnostics.

Chapter 7 Thesis Conclusion and Future outlook

7.1 Conclusion

Single molecule detection has been at the forefront for diagnostic development, genome analysis and understanding cellular processes enabling the direct observation of molecular dynamics, interactions, and rare events that are otherwise lost in bulk measurements. Among this, nanopore technology has advanced in the past years for its label free, picomolar, nucleotide resolution detection, the translatability of which could be observed from the commercialised device, e.g. MinION by Oxford nanopore technology. In this work I demonstrate the development of novel strategies for biosensor development and focused on using DNA origami with nanopores for protein detection.

7.1.1 DNA origami purification

I have demonstrated the use of SPRI beads, commonly used in next generation sequencing preparation as an innovative method for purification of DNA origami with high yield and structural integrity. This method offers significant contribution to the field of nanotechnology and culminates in an advancement of the existing techniques developed for purification, such as PEG precipitation, column filtration, agarose gel electrophoresis, and chromatography methods [110, 111, 287]. I optimised the ratio of the volume of SPRI beads that has to be used for purification to retain high yield and removing excess amount of oligonucleotides. The main advantage of this method is that it is universal and can be applied to a wide range of origami designs. Importantly, I have used this technique to remove excess functional molecules from DNA origami structures which might otherwise interfere with downstream applications. When using large proteins to functionalise origami, it is difficult to qualitatively and quantitatively assess the functionalisation using methods like AFM due to background signals. This has been solved by using SPRI method and I have demonstrated the removal of excess functional proteins from origami by using streptavidin and C-reactive protein as model analytes. The SPRI method gives high yield even after repeated rounds of purification which might be needed for complex functionalisation strategies. I further validated the method by comparing with a most commonly used S-400 spin columns and SPRI could retain higher yield when compared to the purification columns. I envision that this purification technique is scalable and could be employed in industrial settings for parallel purification of large volume DNA origami samples. This is of relevance in fields such as drug delivery and vaccine development where large quantities of origami structures are required [96, 100].

7.1.2 Protein-functionalised DNA origami carrier development

In chapter 3, I demonstrated the development of functionalised origami and incorporated affimer as a binding moiety to capture CRP protein within a DNA origami frame. For this, I first conjugated the affimer proteins with an oligonucleotide via maleimide-thiol reaction. I characterised the affimer-oligonucleotide conjugate using mass spectrometry and gel analysis and optimised the right conditions for conjugation. As the oligonucleotide with affimer was complementary to the binding point (oligonucleotide) on DNA origami, I was able to successfully attach it on the DNA which was analysed using AFM by spotting CRP protein in the centre pocket. The origami is a suitable structure to study specific binding of proteins due to the ability to precisely engineer the attachment of molecules at specific position with high resolution. A percentage above 30% of functionalisation was achieved for DNA origami with any combination of binding points as analysed by counting the number of CRP-bound DNA origami structures from AFM images. I have expanded upon the work by Raveendran et.al and broadened the category of binder molecules used for functionalisation by discussing the use of protein-based binders. The protein binders outperform DNA binders by not being susceptible to nuclease degradation, high affinity and stability, and better performance in complex environment [240, 338]. The precise positioning of proteins at specific sites offers application of using these structures for studying protein-DNA interactions, carrying out enzymatic processes, and targeted drug delivery [11, 253, 288]. My work culminates in the development of a DNA origami with multiple binding sites for proteins and characterised its functionality hence providing a model structure for such applications.

7.1.3 Biosensor development

I have demonstrated the development of a nanopipette based biosensor for detection of proteins. I optimised the nanopore size for protein analysis and characterised it based on the parameters generated during the translocation of functionalised DNA origami through nanopore. I established the use of nanopipette sensor for discriminating between monomer and tetramer origami which could serve as a characterisation technique for determining assembly yield of nanostructures. This method could compliment other available characterisation technique such as agarose gel electrophoresis and atomic force microscopy [327]. Though detection of C-reactive protein captured on DNA origami was not detected, I was able to demonstrate the detection of sequential addition of affimer proteins on DNA origami and differentiate based on their numbers by estimating the percentage of functionalisation. Approximately, 25% of functionalisation was observed for one affimer bound to origami which increased consistently with increasing

number of affimer to obtain around 70% for 12 affimers. I compared the detection of CRP with that of 10 affimers which matched in mass but resulted in a completely different results opening up the discussion of whether it is the mass that contributed to the changes in ion current signals. Interestingly, it was the number of the ion current peaks that increased with increasing number of affimers and not the peak characteristics. The results I observed were consistent as experimental repeats reproduced the same results hence confirming the reproducibility and efficiency in developing biosensor for detecting precise attachment of proteins on DNA origami. Further studies would be required to elucidate the mechanism of changes in ion current signals and the trend observed with increasing number of affimers as that could provide more insights into developing a robust and reliable nanopore sensor. Protein detection is of significant relevance in small molecule detection especially because many relevant biomarkers are small and the sensitive sensor I have developed could be used further for detection of these molecules. Moreover, the ability to quantify the percentage of protein functionalised origamis could open up possibilities where the efficiency of functionalisation could be checked with nanopore technology, and this could be used as an additional characterisation technique to atomic force microscopy.

7.2 Ongoing and Future work

The origami purification method that I have established in this work and the sensor development has potential for further development that could enable scalability and application in industrial setting and building better biosensors for various applications. In collaboration with other research groups, I obtained interesting preliminary data which is discussed in the next sections.

7.2.1 Automation of SPRI purification of DNA origami

The SPRI purification technique has the possibility of expanding from lab bench to industrial setting, by automation on the procedure. Successful implementation of parallel or high through-put purification would enable handling larger volumes of origami with increased scalability. This would mean the adaptation of technique not only in academia but also in industrial setting especially if large volumes of origami are needed in drug delivery and vaccine development.

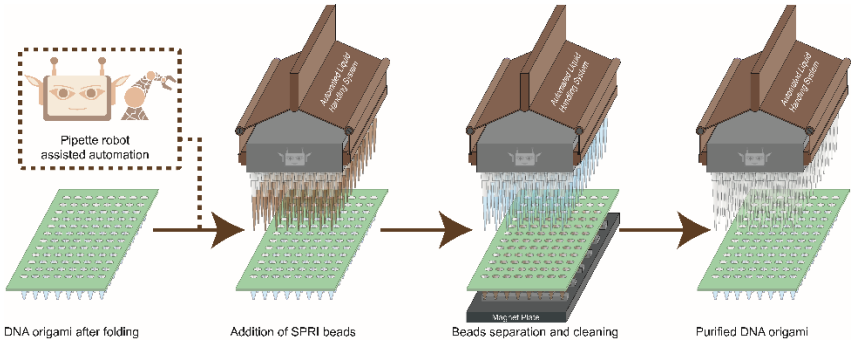

Figure 7:1 Illustration of liquid handling robot performing parallel purification of multiple samples of DNA origami. (Adapted from [275])

The robot assisted purification could purify the DNA origami structures as confirmed by agarose gel analysis and AFM images as indicated by Figure 7:2 and Figure 7:3. This demonstrates the evidence that the SPRI method could be automated.

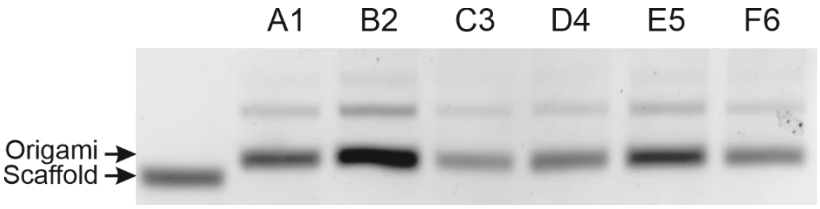

Figure 7:2 Agarose gel electrophoresis image of origami purified using SPRI technique coupled to robot. The wells indicate the samples taken from random wells in 96 well plate. (Gel was performed by Dr. Chau).

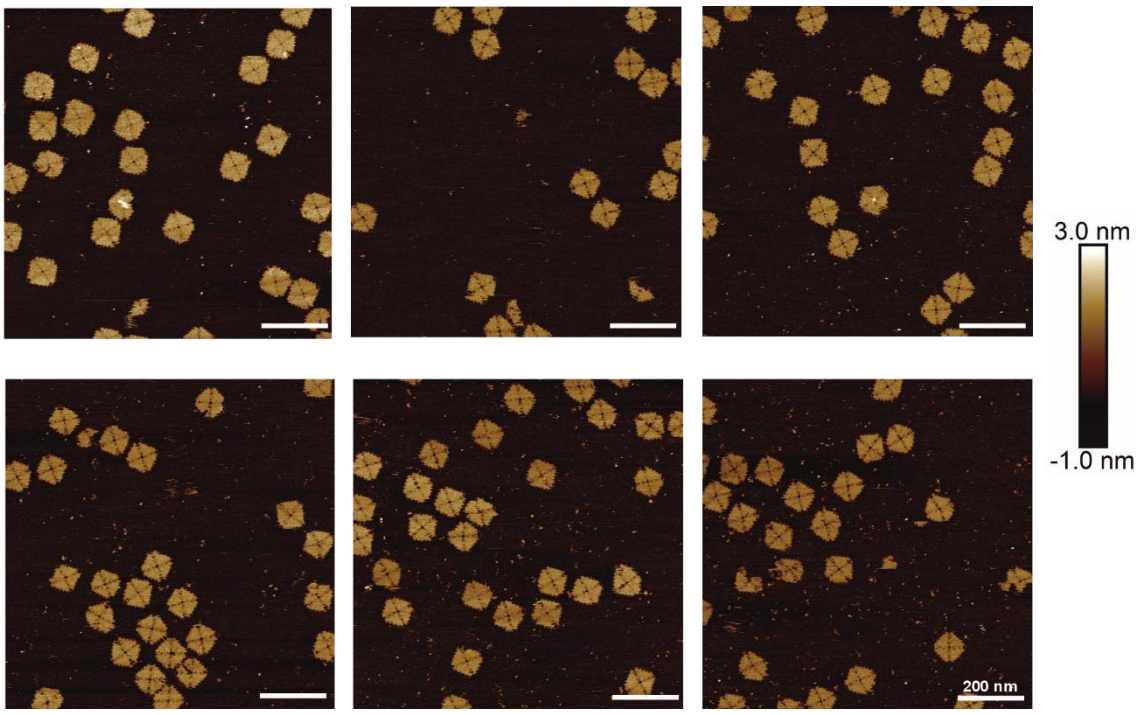

Figure 7:3 AFM images of samples taken from random wells of 96 well plate spot check.

Automation and scalability is the key advantage of SPRI technique and this could be further used for applications like drug delivery and vaccine development. Studies have been reported where DNA origami is used for drug delivery, for example, Li et.al has demonstrated the use of DNA origami as a thrombin delivery vehicle in vivo to tumour associated blood vessels for inhibiting tumour growth. This was showcased as having promising therapeutic potential preventing the formation of metastasis in melanoma mouse model drug [10]. Similarly, a drug delivery platform for slowing bacterial growth, thus antimicrobial resistance has been reported which uses DNA origami with aptamer technology. In this work, DNA origami has been designed to specifically target bacteria and deliver lysozyme to kill bacteria [339]. Automation would be of significant in these applications as large volumes of origami would need to be synthesised and produced in a factory settings.

7.2.2 DNA origami for protein interaction study

The CRP functionalised DNA origami structures I have developed in Chapter 5 could be used as a model system to study protein interaction with DNA. As multiple affimers are employed to capture CRP protein in the DNA origami central pocket, it would be interesting to see the interactions of CRP within the central pocket of DNA origami. This would enable the use of origami structures to elucidate and resolve the dynamics of protein-DNA or protein-protein interactions. Similar studies have been reported where DNA origami frame is used to systematically engineer multiple aptamer ligands for a

binding target protein. They have demonstrated the precise positioning of aptamers and capture of streptavidin and thrombin and demonstrated how multiple binding moieties could enable effective capture of target protein. In collaborating with Dr. George Heath of University of Leeds, we together employed the state-of-the art high-speed atomic force microscopy and localised AFM approach to investigate the CRP's binding interaction with affimers [340]. When the high-speed imaging was done with 4FSF origami attached with CRP by 4 affimers, a bright or high contrast region was observed in the centre representing CRP protein. The four binding points that were used to capture CRP were clearly visible from the AFM Images which were not achievable with my AFM approach. The analysis further resolved a molecular model like structure for DNA origami with CRP in the centre.

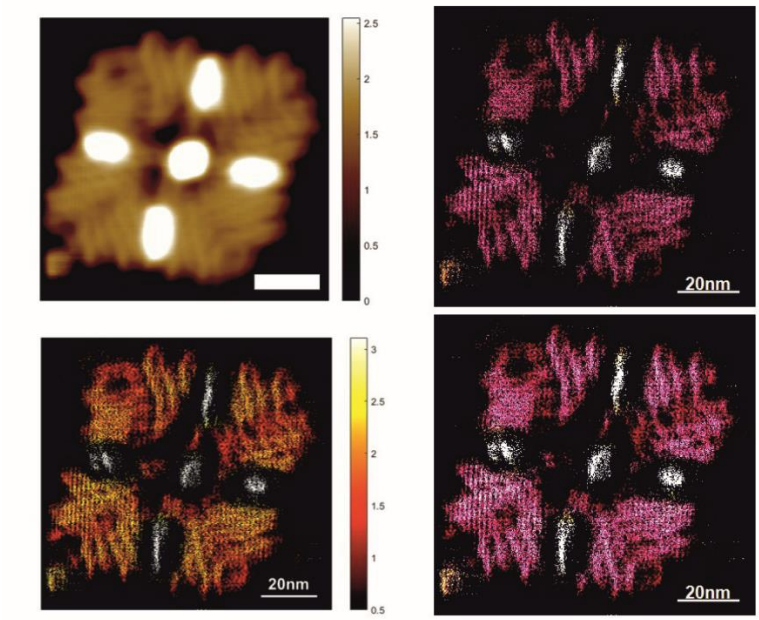

Figure 7:4 High speed AFM images of 4FSF-CRP captured with 4 affimers in the centre (top left). Other images in the figure are the model structures obtained through localised AFM in the Nanolocz software (perfomed by Dr. Varun Gupta).

This could also be developed further to attempt to resolve the protein orientation within the DNA origami thus providing added structural information, and the preliminary data showed a CRP protein with five subunits forming a pentameric ring, in agreement with its crystal structure (Figure 7:5). The pentameric ring appeared to be slightly tilted towards the plane of the page, indicating the CRP is captured at an angle.

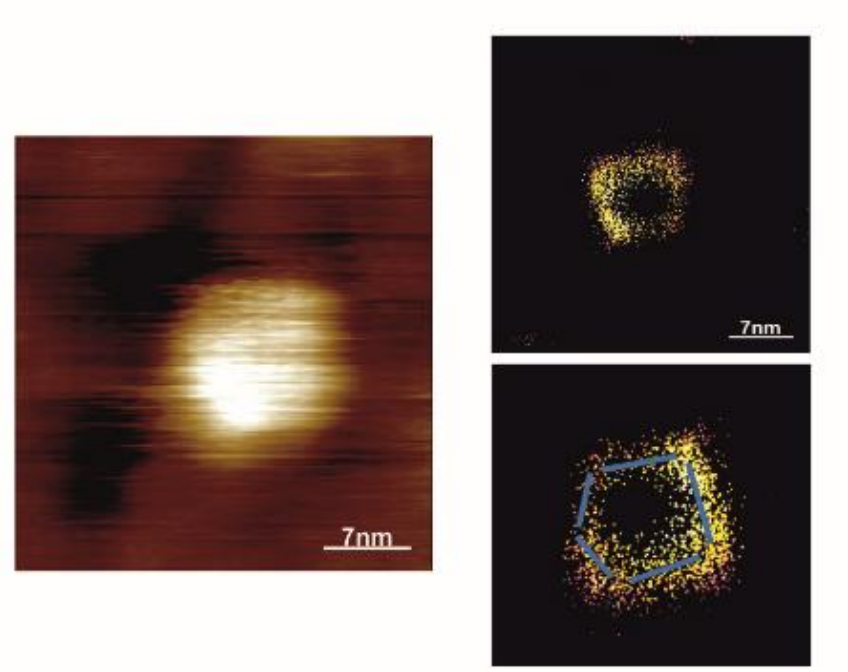

Figure 7:5 Analysis indicating preliminary evidence of resolving the subunits of CRP protein within DNA origami.

Additionally, through the high-speed imaging video, I observed the capture of CRP molecules by affimers and it bounced between the affimers indicating the dynamic interaction of CRP with the affimer-oligonucleotide within the central pocket. I hypothesised that by providing multiple affimers within the frame's cavity could changes the binding dynamic between the CRP and the affimers.

Videos were recorded that indicated dynamic movement and interaction of CRP with oligonucleotides within the DNA origami (4FSF with four affimers). I exported the frames in the video and each frame is exported at a time difference of 8s. I observed the high contrast or bright spot within the DNA origami cavity (top left in the image in Figure 7:6). At 0s, the CRP protein is inclined towards the right of the central cavity, whereas at 76 s, the CRP has shifted its position to the centre. At 128s, the CRP has positioned itself towards the top left within the central cavity. This type of shift in the position is spotted throughout the frames of images strongly indicating the dynamic interaction of CRP protein with its binding partner, affimer-oligonucleotide.

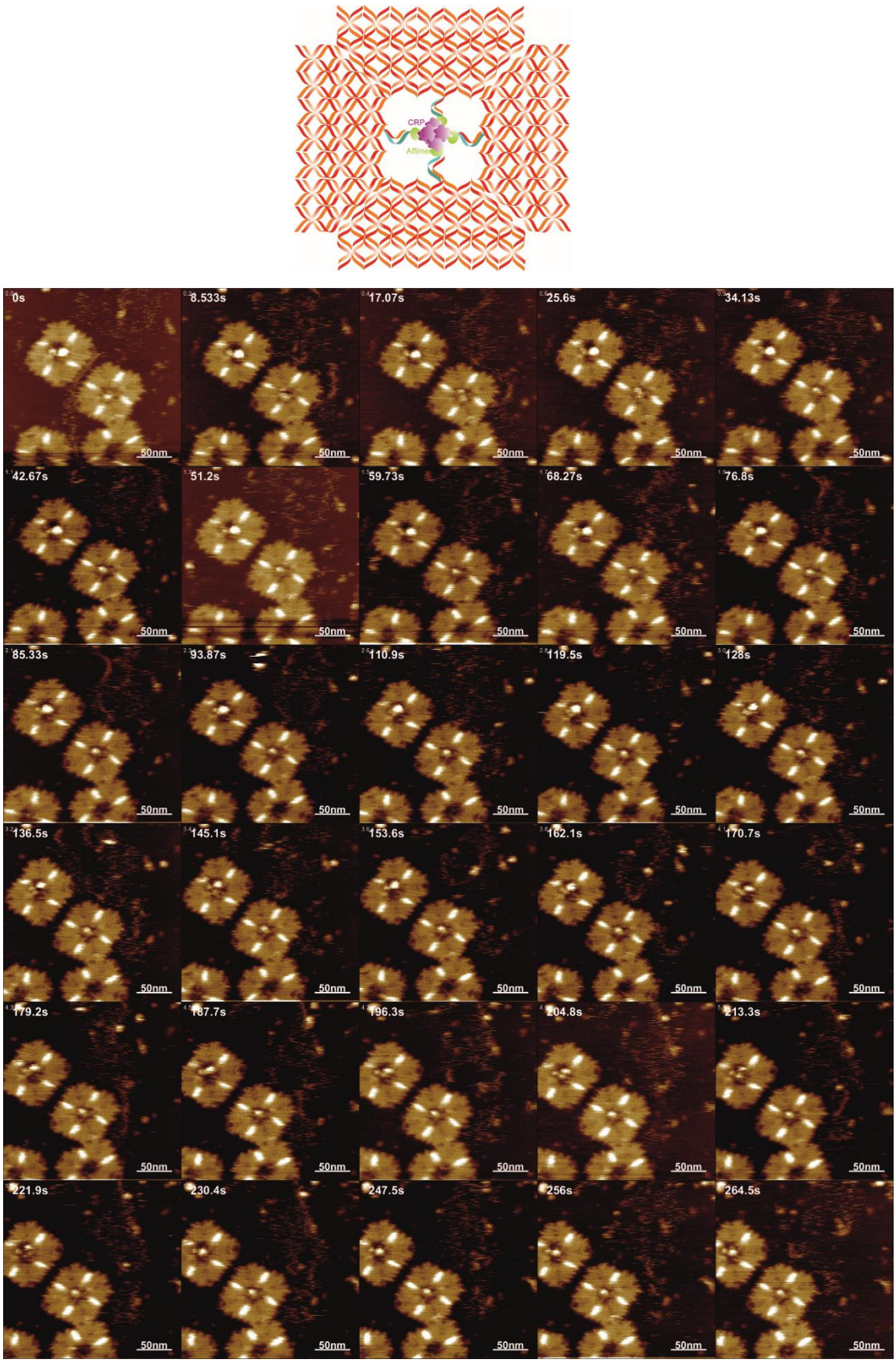

Figure 7:6 Exported frames from video of CRP interacting with affimer within a DNA origami frame.

This strongly suggest the capability of utilising this structure to study dynamic biomolecule interaction. I envision that this can be used to specifically position the active sites of enzymes or allosteric proteins and study their diffusion or binding kinetics with DNA or other biomolecules. Such applications can be of relevance to study the single molecule binding kinetics and interaction of proteins like polymerases with DNA real time.

I observed the multivalent dynamic competition between the affimer proteins to capture CRP protein on DNA origami (see arrows). This indicates the continuous capture of CRP protein and holding it within the cavity due to the presence of more than one binding partners. This enables the multivalent and rapid capture of CRP protein generating the possibility of using such system to mimic biologically relevant binding kinetics.

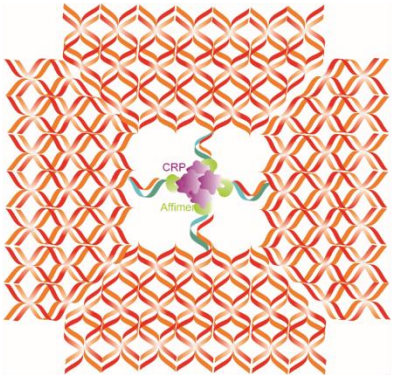

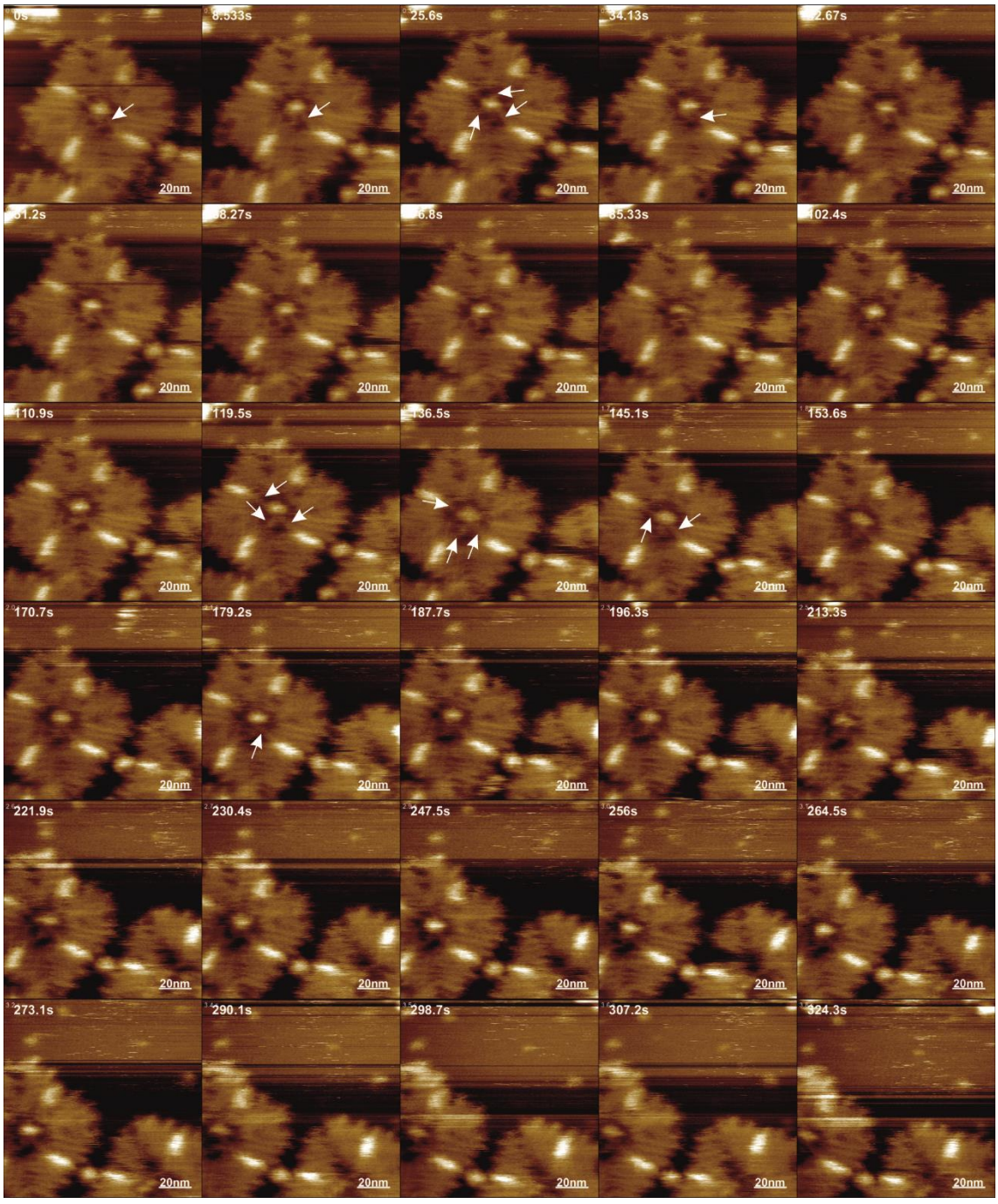

Figure 7:7 High speed AFM images of DNA origami with CRP captured in the centre using four affimer-oligonucleotide conjugates.

7.2.3 Mechanical properties of functionalised DNA origami

In Chapter 6, I developed a biosensor for detection of affimer proteins and observed a trend of increasing the number of ion current peaks in the functionalised range with increasing number of affimers. It is interesting to note that the number of signals are increasing rather than the peak characteristic with increasing affimers. I assume that affimer binding induces significant structural changes in the DNA origami, with the extent of these changes depending on the number of affimers bound. These structural modifications are likely to influence the translocation behaviour through the nanopore, thereby affecting the distribution and characteristics of the ion current peaks. I presume that the protein binding could be making the origami structure more rigid causing bending or other structural changes affecting the translocation behaviour. However, further studies are required to confirm this. I envision that resolving such mechanical changes upon protein binding to DNA origami could be translated to developing mechanistic sensors that are sensitive to protein-DNA interactions.

Structural changes within DNA origami while translocated through nanopore is previously demonstrated [341]. In this work, the flexibility of DNA origami is controlled by DNA strand hybridisation and protein interactions. The solid state nanopore developed is able to monitor the confirmational changes in DNA origami structures. Previous studies have indicated that protein binding can alter the mechanical flexibility of DNA nanostructures [335]. This research can be extended to explore the biophysical aspects of nanopore translocation, which may improve the future design of nanopore sensors. Techniques such as cryo-electron microscopy (Cryo-EM) could be employed to examine the orientation of proteins within the DNA origami and further elucidate their role in nanopore translocation mechanics. The changes in the structure of DNA origami upon binding of CRP protein could be investigated using CryoEM. For this, I folded and purified 4FSF DNA origami with four binding points and affimer and was incubated with CRP protein for its capture. Preliminary evidence showed structures similar to CRP functionalised to 4FSF origami. It has previously been reported that DNA origami structures can restrain the protein orientation during Cryo-EM, particularly for small proteins that are otherwise challenging to characterize [342].

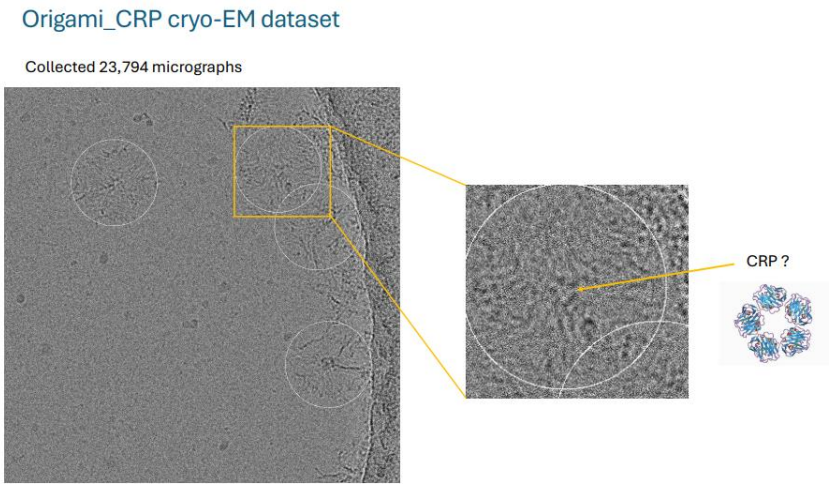

Figure 7:8 Preliminary evidence of detection of 4FSF-CRP with 4 affimers. (in collaboration with Cryo-EM facility, Astbury centre for structural biology, performed by Dr. Oksana)

Additionally, molecular simulation studies could provide further insight into the structural changes induced by protein functionalization and their impact on translocation dynamics. Computational models have previously been utilized to investigate the three-dimensional conformation and mechanical stability of DNA origami in solution [336]. Such modelling approaches could be applied in a nanopore context to clarify the mechanical and structural alterations that occur upon protein binding while translocating through nanopore.

Bibliography

[1] M. Cox and D. Nelson, *Lehninger Principles of Biochemistry*. 2000.

[2] C. M. Dobson, "Protein folding and misfolding," *Nature,* vol. 426, no. 6968, pp. 884-890, 2003/12/01 2003, doi: 10.1038/nature02261.

[3] S. F. Kingsmore, "Multiplexed protein measurement: technologies and applications of protein and antibody arrays," *Nature Reviews Drug Discovery,* vol. 5, no. 4, pp. 310-321, 2006/04/01 2006, doi: 10.1038/nrd2006.

[4] N. Varongchayakul, J. Song, A. Meller, and M. W. Grinstaff, "Single-molecule protein sensing in a nanopore: a tutorial," in *Chemical Society reviews* vol. 47, ed: NLM (Medline), 2018, pp. 8512-8524.

[5] J. J. Gooding and K. Gaus, "Single-Molecule Sensors: Challenges and Opportunities for Quantitative Analysis," *Angew Chem Int Ed Engl,* vol. 55, no. 38, pp. 11354-66, Sep 12 2016, doi: 10.1002/anie.201600495.

[6] A. Diaspro and R. Rolandi, "Atomic force microscopy [Guest Editorial]," *IEEE Engineering in Medicine and Biology Magazine,* vol. 16, no. 2, pp. 26-27, 1997, doi: 10.1109/MEMB.1997.582172.

[7] C. Plesa, S. W. Kowalczyk, R. Zinsmeester, A. Y. Grosberg, Y. Rabin, and C. Dekker, "Fast translocation of proteins through solid state nanopores," *Nano Letters,* vol. 13, no. 2, pp. 658-663, 2013/2// 2013, doi: 10.1021/nl3042678.

[8] N. A. Bell and U. F. Keyser, "Specific protein detection using designed DNA carriers and nanopores," *J Am Chem Soc,* vol. 137, no. 5, pp. 2035-41, Feb 11 2015, doi: 10.1021/ja512521w.

[9] P. W. K. Rothemund, "Folding DNA to create nanoscale shapes and patterns," in *Nature* vol. 440, ed, 2006, pp. 297-302.

[10] S. Li *et al.*, "A DNA nanorobot functions as a cancer therapeutic in response to a molecular trigger in vivo," *Nature Biotechnology,* vol. 36, no. 3, pp. 258-264, 2018/3// 2018, doi: 10.1038/nbt.4071.

[11] N. V. Voigt *et al.*, "Single-molecule chemical reactions on DNA origami," *Nature Nanotechnology,* vol. 5, no. 3, pp. 200-203, 2010, doi: 10.1038/NNANO.2010.5.

[12] A. Aghebat Rafat, S. Sagredo, M. Thalhammer, and F. C. Simmel, "Barcoded DNA origami structures for multiplexed optimization and enrichment of DNA-based protein-binding cavities," *Nature Chemistry,* vol. 12, no. 9, pp. 852-859, 2020/9// 2020, doi: 10.1038/s41557-020-0504-6.

[13] M. Raveendran, A. J. Lee, R. Sharma, C. Wälti, and P. Actis, "Rational design of DNA nanostructures for single molecule biosensing," *Nature*

Communications, vol. 11, no. 1, 2020/12// 2020, doi: 10.1038/s41467-020-18132-1.

[14] M. A. Eckert *et al.*, "Novel molecular and nanosensors for in vivo sensing," *Theranostics,* vol. 3, no. 8, pp. 583-94, 2013, doi: 10.7150/thno.6584.

[15] Z. Gan *et al.*, "Advances in Aptamer-Based Biosensors and Cell-Internalizing SELEX Technology for Diagnostic and Therapeutic Application," *Biosensors (Basel),* vol. 12, no. 11, Oct 25 2022, doi: 10.3390/bios12110922.

[16] S. Patil *et al.*, "Origami-Inspired Biosensors: Exploring Diverse Applications and Techniques for Shape-Changing Sensor Platforms," *Chemosensors,* vol. 12, no. 12, 2024, doi: 10.3390/chemosensors12120276.

[17] J. F. Miescher, "On the Chemical Composition of Pus Cells.," *Medisch-chemische Untersuchungen,* vol. 4, pp. 441-460, 1871.

[18] T. Miescher, "Das Protamin, eine neue organische Basis aus den Samenfäden des Rheinlachses," *Zeitschrift für analytische Chemie,* vol. 13, no. 1, pp. 325-326, 1874/12/01 1874, doi: 10.1007/BF01302341.

[19] P. Portin, "The birth and development of the DNA theory of inheritance: sixty years since the discovery of the structure of DNA," *Journal of Genetics,* vol. 93, 293-302, 2014.

[20] A. Kossel and A. Neumann, "Ueber das Thymin, ein Spaltungsproduct der Nucleïnsäure," *Berichte der deutschen chemischen Gesellschaft,* vol. 26, no. 3, pp. 2753-2756, 1893, doi: https://doi.org/10.1002/cber.18930260379.

[21] O. T. Avery, C. M. MacLeod, and M. McCarty, "Studies on the Chemical Nature of the Substance Inducing Transformation of Pneumococcal Types," *Molecular Medicine,* vol. 1, no. 4, pp. 344-365, 1995/05/01 1995, doi: 10.1007/BF03401572.

[22] E. Chargaff, E. Vischer, R. Doniger, C. Green, and F. Misani, "THE COMPOSITION OF THE DESOXYPENTOSE NUCLEIC ACIDS OF THYMUS AND SPLEEN," *Journal of Biological Chemistry,* vol. 177, no. 1, pp. 405-416, 1949/01/01/ 1949, doi: https://doi.org/10.1016/S0021-9258(18)57098-8.

[23] E. Chargaff, "Structure and function of nucleic acids as cell constituents," *Federation proceedings,* no. 0014-9446, pp. 10:654–659, 1951.

[24] M. H. F. Wilkins, A. R. Stokes, and H. R. Wilson, "Molecular Structure of Nucleic Acids: Molecular Structure of Deoxypentose Nucleic Acids," *Nature,* vol. 171, no. 4356, pp. 738-740, 1953/04/01 1953, doi: 10.1038/171738a0.

[25] R. E. Franklin and R. G. Gosling, "Molecular Configuration in Sodium Thymonucleate," *Nature,* vol. 171, no. 4356, pp. 740-741, 1953/04/01 1953, doi: 10.1038/171740a0.

[26] J. D. Watson and F. H. C. Crick, "Molecular Structure of Nucleic Acids: A Structure for Deoxyribose Nucleic Acid," *Nature,* vol. 171, no. 4356, pp. 737-738, 1953/04/01 1953, doi: 10.1038/171737a0.

[27] N. C. Seeman, "Nanomaterials based on DNA," *Annu Rev Biochem,* vol. 79, pp. 65-87, 2010, doi: 10.1146/annurev-biochem-060308-102244.

[28] H. University, "DNA structure and Chemistry," ch. 8.

[29] J. A. Alberts B, Lewis J, et al., *The Structure and Function of DNA.*, 4th edition ed. New York: Garland Science, 2002.

[30] F. Crick, "Central Dogma of Molecular Biology," *Nature,* vol. 227, no. 5258, pp. 561-563, 1970/08/01 1970, doi: 10.1038/227561a0.

[31] N. C. Seeman, "Nucleic Acid Junctions and Lattices " *J. theor. Biol. ,* vol. 99, pp. 237-247, 1981.

[32] B. Alberts, "DNA replication and recombination," *Nature,* vol. 421, no. 6921, pp. 431-435, 2003/01/01 2003, doi: 10.1038/nature01407.

[33] T. R. Broker and I. R. Lehman, "Branched DNA molecules: Intermediates in T4 recombination," *Journal of Molecular Biology,* vol. 60, no. 1, pp. 131-149, 1971/08/28/ 1971, doi: https://doi.org/10.1016/0022-2836(71)90453-0.

[34] J. Chen and N. C. Seeman, "Synthesis from DNA of a molecule with the connectivity of a cube," *Nature,* vol. 350, no. 6319, pp. 631-633, 1991/04/01 1991, doi: 10.1038/350631a0.

[35] R. Holliday, "A mechanism for gene conversion in fungi," *Genetical Research,* vol. 5, no. 2, pp. 282-304, 2009, doi: 10.1017/s0016672300001233.

[36] Emerson.S, *In: Genetic Organization (E. W. Caspari and A. W. Ravin eds),* . New York: Academic Press, 1969.

[37] H. M. Sobell, "Molecular Mechanism for Genetic Recombination," *Proceedings of the National Academy of Sciences,* vol. 69, no. 9, pp. 2483-2487, 1972/09/01 1972, doi: 10.1073/pnas.69.9.2483.

[38] E. Ban and C. R. Picu, "Strength of DNA Sticky End Links," *Biomacromolecules,* vol. 15, no. 1, pp. 143-149, 2014/01/13 2014, doi: 10.1021/bm401425k.

[39] *DNA Nanotechnology* (Methods in Molecular Biology). New York: Humana New York, NY, 2018.

[40] T. J. Fu and N. C. Seeman, "DNA double-crossover molecules," *Biochemistry,* vol. 32, no. 13, pp. 3211-3220, 1993/04/01 1993, doi: 10.1021/bi00064a003.

[41] P. Sa-Ardyen, A. V. Vologodskii, and N. C. Seeman, "The Flexibility of DNA Double Crossover Molecules," *Biophysical Journal,* vol. 84, no. 6, pp. 3829-3837, 2003/06/01/ 2003, doi: https://doi.org/10.1016/S0006-3495(03)75110-8.

[42] R.-I. Ma, N. R. Kallenbach, R. D. Sheardy, M. L. Petrillo, and N. C. Seeman, "Three-arm nucleic acid junctions are flexible," *Nucleic Acids Research,* vol. 14, no. 24, pp. 9745-9753, 1986, doi: 10.1093/nar/14.24.9745.

[43] M. L. Petrillo, C. J. Newton, R. P. Cunningham, R.-I. Ma, N. R. Kallenbach, and N. C. Seeman, "The ligation and flexibility of four-arm DNA junctions," *Biopolymers,* vol. 27, no. 9, pp. 1337-1352, 1988/09/01 1988, doi: https://doi.org/10.1002/bip.360270902.

[44] R. P. Goodman *et al.*, "Rapid Chiral Assembly of Rigid DNA Building Blocks for Molecular Nanofabrication," *Science,* vol. 310, no. 5754, pp. 1661-1665, 2005/12/09 2005, doi: 10.1126/science.1120367.

[45] W. M. Shih, J. D. Quispe, and G. F. Joyce, "A 1.7-kilobase single-stranded DNA that folds into a nanoscale octahedron," *Nature,* vol. 427, no. 6975, pp. 618-621, 2004/02/01 2004, doi: 10.1038/nature02307.

[46] H. Yan, T. H. LaBean, L. Feng, and J. H. Reif, "Directed nucleation assembly of DNA tile complexes for barcode-patterned lattices," *Proceedings of the National Academy of Sciences,* vol. 100, no. 14, pp. 8103-8108, 2003/07/08 2003, doi: 10.1073/pnas.1032954100.

[47] S. M. Douglas, A. H. Marblestone, S. Teerapittayanon, A. Vazquez, G. M. Church, and W. M. Shih, "Rapid prototyping of 3D DNA-origami shapes with caDNAno," *Nucleic Acids Research,* vol. 37, no. 15, pp. 5001-5006, 2009, doi: 10.1093/nar/gkp436.

[48] S. Dey *et al.*, "DNA origami," *Nature Reviews Methods Primers,* vol. 1, no. 1, 2021, doi: 10.1038/s43586-020-00009-8.

[49] E. Benson *et al.*, "DNA rendering of polyhedral meshes at the nanoscale," *Nature,* vol. 523, no. 7561, pp. 441-444, 2015/07/01 2015, doi: 10.1038/nature14586.

[50] R. Veneziano *et al.*, "Designer nanoscale DNA assemblies programmed from the top down," *Science,* vol. 352, no. 6293, pp. 1534-1534, 2016/06/24 2016, doi: 10.1126/science.aaf4388.

[51] H. Jun *et al.*, "Automated Sequence Design of 3D Polyhedral Wireframe DNA Origami with Honeycomb Edges," *ACS Nano,* vol. 13, no. 2, pp. 2083-2093, 2019/02/26 2019, doi: 10.1021/acsnano.8b08671.

[52] E. Benson, A. Mohammed, A. Bosco, A. I. Teixeira, P. Orponen, and B. Högberg, "Computer-Aided Production of Scaffolded DNA Nanostructures from Flat Sheet Meshes," *Angewandte Chemie International Edition,* vol. 55, no. 31, pp. 8869-8872, 2016/07/25 2016, doi: https://doi.org/10.1002/anie.201602446.

[53] H. Jun *et al.*, "Autonomously designed free-form 2D DNA origami," *Science Advances,* vol. 5, no. 1, p. eaav0655, doi: 10.1126/sciadv.aav0655.

[54] H. Jun, X. Wang, W. P. Bricker, S. Jackson, and M. Bathe, "Rapid Prototyping of Wireframe Scaffolded DNA Origami using ATHENA," *bioRxiv,* 2020.

[55] J. Yoo and A. Aksimentiev, "In situ structure and dynamics of DNA origami determined through molecular dynamics simulations," *Proceedings of the National Academy of Sciences,* vol. 110, no. 50, pp. 20099-20104, 2013/12/10 2013, doi: 10.1073/pnas.1316521110.

[56] J. Wohlert, W. K. den Otter, O. Edholm, and W. J. Briels, "Free energy of a trans-membrane pore calculated from atomistic molecular dynamics simulations," *The Journal of Chemical Physics,* vol. 124, no. 15, p. 154905, 2006, doi: 10.1063/1.2171965.

[57] K. Pan, D.-N. Kim, F. Zhang, M. R. Adendorff, H. Yan, and M. Bathe, "Lattice-free prediction of three-dimensional structure of programmed DNA assemblies," *Nature Communications,* vol. 5, no. 1, p. 5578, 2014/12/03 2014, doi: 10.1038/ncomms6578.

[58] R. V. Reshetnikov *et al.*, "A coarse-grained model for DNA origami," *Nucleic Acids Research,* vol. 46, no. 3, pp. 1102-1112, 2018, doi: 10.1093/nar/gkx1262.

[59] E. Poppleton, J. Bohlin, M. Matthies, S. Sharma, F. Zhang, and P. Šulc, "Design, optimization and analysis of large DNA and RNA nanostructures through interactive visualization, editing and molecular simulation," *Nucleic Acids Research,* vol. 48, no. 12, pp. e72-e72, 2020, doi: 10.1093/nar/gkaa417.

[60] J. P. K. Doye *et al.*, "Coarse-graining DNA for simulations of DNA nanotechnology," *Physical Chemistry Chemical Physics,* 10.1039/C3CP53545B vol. 15, no. 47, pp. 20395-20414, 2013, doi: 10.1039/C3CP53545B.

[61] B. E. K. Snodin *et al.*, "Introducing improved structural properties and salt dependence into a coarse-grained model of DNA," *The Journal of Chemical Physics,* vol. 142, no. 23, p. 234901, 2015, doi: 10.1063/1.4921957.

[62] C. Maffeo and A. Aksimentiev, "MrDNA: a multi-resolution model for predicting the structure and dynamics of DNA systems," *Nucleic Acids Research,* vol. 48, no. 9, pp. 5135-5146, 2020, doi: 10.1093/nar/gkaa200.

[63] P. M. Nafisi, T. Aksel, and S. M. Douglas, "Construction of a novel phagemid to produce custom DNA origami scaffolds," *Synthetic Biology,* vol. 3, no. 1, p. ysy015, 2018, doi: 10.1093/synbio/ysy015.

[64] R. Veneziano, T. R. Shepherd, S. Ratanalert, L. Bellou, C. Tao, and M. Bathe, "In vitro synthesis of gene-length single-stranded DNA," *Scientific Reports,* vol. 8, no. 1, p. 6548, 2018/04/25 2018, doi: 10.1038/s41598-018-24677-5.

[65] H. Zhang, J. Chao, D. Pan, H. Liu, Q. Huang, and C. Fan, "Folding super-sized DNA origami with scaffold strands from long-range PCR," *Chemical*

Communications, 10.1039/C2CC32204H vol. 48, no. 51, pp. 6405-6407, 2012, doi: 10.1039/C2CC32204H.

[66] T. G. Martin and H. Dietz, "Magnesium-free self-assembly of multi-layer DNA objects," *Nature Communications,* vol. 3, no. 1, p. 1103, 2012/10/02 2012, doi: 10.1038/ncomms2095.

[67] F. Hong, F. Zhang, Y. Liu, and H. Yan, "DNA Origami: Scaffolds for Creating Higher Order Structures," *Chemical Reviews,* vol. 117, no. 20, pp. 12584-12640, 2017/10/25 2017, doi: 10.1021/acs.chemrev.6b00825.

[68] K. E. Dunn, F. Dannenberg, T. E. Ouldridge, M. Kwiatkowska, A. J. Turberfield, and J. Bath, "Guiding the folding pathway of DNA origami," *Nature,* vol. 525, no. 7567, pp. 82-86, 2015/9// 2015, doi: 10.1038/nature14860.

[69] N. Kern, R. Dong, S. M. Douglas, R. D. Vale, and M. A. Morrissey, "Tight nanoscale clustering of Fcγ receptors using DNA origami promotes phagocytosis," *eLife,* vol. 10, p. e68311, 2021/06/03 2021, doi: 10.7554/eLife.68311.

[70] R. Dong, T. Aksel, W. Chan, R. N. Germain, R. D. Vale, and S. M. Douglas, "DNA origami patterning of synthetic T cell receptors reveals spatial control of the sensitivity and kinetics of signal activation," *Proceedings of the National Academy of Sciences,* vol. 118, no. 40, p. e2109057118, 2021, doi: doi:10.1073/pnas.2109057118.

[71] D. Selnihhin, S. M. Sparvath, S. Preus, V. Birkedal, and E. S. Andersen, "Multifluorophore DNA Origami Beacon as a Biosensing Platform," *ACS Nano,* vol. 12, no. 6, pp. 5699-5708, 2018/06/26 2018, doi: 10.1021/acsnano.8b01510.

[72] M. M. C. Bastings *et al.*, "Modulation of the Cellular Uptake of DNA Origami through Control over Mass and Shape," *Nano Letters,* vol. 18, no. 6, pp. 3557-3564, 2018/06/13 2018, doi: 10.1021/acs.nanolett.8b00660.

[73] H. Zhang *et al.*, "DNA nanostructures coordinate gene silencing in mature plants," *Proceedings of the National Academy of Sciences,* vol. 116, no. 15, pp. 7543-7548, 2019/04/09 2019, doi: 10.1073/pnas.1818290116.

[74] J. Hellmeier *et al.*, "DNA origami demonstrate the unique stimulatory power of single pMHCs as T cell antigens," *Proceedings of the National Academy of Sciences,* vol. 118, no. 4, p. e2016857118, 2021/01/26 2021, doi: 10.1073/pnas.2016857118.

[75] A. Czogalla *et al.*, "Amphipathic DNA Origami Nanoparticles to Scaffold and Deform Lipid Membrane Vesicles," *Angewandte Chemie International Edition,* vol. 54, no. 22, pp. 6501-6505, 2015/05/26 2015, doi: https://doi.org/10.1002/anie.201501173.

[76] X. Wu *et al.*, "An RNA/DNA hybrid origami-based nanoplatform for efficient gene therapy," *Nanoscale,* 10.1039/D1NR00517K vol. 13, no. 30, pp. 12848-12853, 2021, doi: 10.1039/D1NR00517K.

[77] K. Liu, C. Xu, and J. Liu, "Regulation of cell binding and entry by DNA origami mediated spatial distribution of aptamers," *Journal of Materials Chemistry B,* 10.1039/D0TB00663G vol. 8, no. 31, pp. 6802-6809, 2020, doi: 10.1039/D0TB00663G.

[78] Z. Lu, Y. Wang, D. Xu, and L. Pang, "Aptamer-tagged DNA origami for spatially addressable detection of aflatoxin B1," *Chemical Communications,* 10.1039/C6CC08831G vol. 53, no. 5, pp. 941-944, 2017, doi: 10.1039/C6CC08831G.

[79] M. W. Grome, Z. Zhang, F. Pincet, and C. Lin, "Vesicle Tubulation with Self-Assembling DNA Nanosprings," *Angewandte Chemie International Edition,* vol. 57, no. 19, pp. 5330-5334, 2018/05/04 2018, doi: https://doi.org/10.1002/anie.201800141.

[80] K. Numajiri, T. Yamazaki, M. Kimura, A. Kuzuya, and M. Komiyama, "Discrete and Active Enzyme Nanoarrays on DNA Origami Scaffolds Purified by Affinity Tag Separation," *Journal of the American Chemical Society,* vol. 132, no. 29, pp. 9937-9939, 2010/07/28 2010, doi: 10.1021/ja104702q.

[81] R. S. Sørensen, A. H. Okholm, D. Schaffert, A. L. B. Kodal, K. V. Gothelf, and J. Kjems, "Enzymatic Ligation of Large Biomolecules to DNA," *ACS Nano,* vol. 7, no. 9, pp. 8098-8104, 2013/09/24 2013, doi: 10.1021/nn403386f.

[82] X. Chen, B. Jia, Z. Lu, L. Liao, H. Yu, and Z. Li, "Aptamer-Integrated Scaffolds for Biologically Functional DNA Origami Structures," *ACS Applied Materials & Interfaces,* vol. 13, no. 33, pp. 39711-39718, 2021/08/25 2021, doi: 10.1021/acsami.1c09307.

[83] M. Madsen and K. V. Gothelf, "Chemistries for DNA Nanotechnology," *Chemical Reviews,* vol. 119, no. 10, pp. 6384-6458, 2019/05/22 2019, doi: 10.1021/acs.chemrev.8b00570.

[84] T. Fang, J. Alvelid, J. Spratt, E. Ambrosetti, I. Testa, and A. I. Teixeira, "Spatial Regulation of T-Cell Signaling by Programmed Death-Ligand 1 on Wireframe DNA Origami Flat Sheets," *ACS Nano,* vol. 15, no. 2, pp. 3441-3452, 2021/02/23 2021, doi: 10.1021/acsnano.0c10632.

[85] B. J. H. M. Rosier *et al.*, "Proximity-induced caspase-9 activation on a DNA origami-based synthetic apoptosome," *Nature Catalysis,* vol. 3, no. 3, pp. 295-306, 2020/03/01 2020, doi: 10.1038/s41929-019-0403-7.

[86] W. P. Klein *et al.*, "Enhanced Catalysis from Multienzyme Cascades Assembled on a DNA Origami Triangle," *ACS Nano,* vol. 13, no. 12, pp. 13677-13689, 2019/12/24 2019, doi: 10.1021/acsnano.9b05746.

[87] D. Wang *et al.*, "An Addressable 2D Heterogeneous Nanoreactor to Study the Enzyme-Catalyzed Reaction at the Interface," *Small,* vol. 13, no. 43, p. 1700594, 2017, doi: https://doi.org/10.1002/smll.201700594.

[88] R. E. Kohman, S. S. Cha, H.-Y. Man, and X. Han, "Light-Triggered Release of Bioactive Molecules from DNA Nanostructures," *Nano Letters,* vol. 16, no. 4, pp. 2781-2785, 2016/04/13 2016, doi: 10.1021/acs.nanolett.6b00530.

[89] A. S. Eklund, A. Comberlato, I. A. Parish, R. Jungmann, and M. M. C. Bastings, "Quantification of Strand Accessibility in Biostable DNA Origami with Single-Staple Resolution," *ACS Nano,* vol. 15, no. 11, pp. 17668-17677, 2021/11/23 2021, doi: 10.1021/acsnano.1c05540.

[90] E. Silvester *et al.*, "DNA origami signposts for identifying proteins on cell membranes by electron cryotomography," *Cell,* vol. 184, no. 4, pp. 1110-1121.e16, 2021, doi: 10.1016/j.cell.2021.01.033.

[91] D. Daems *et al.*, "Controlling the Bioreceptor Spatial Distribution at the Nanoscale for Single Molecule Counting in Microwell Arrays," *ACS Sensors,* vol. 4, no. 9, pp. 2327-2335, 2019/09/27 2019, doi: 10.1021/acssensors.9b00877.

[92] Q. Pan *et al.*, "Aptamer-Functionalized DNA Origami for Targeted Codelivery of Antisense Oligonucleotides and Doxorubicin to Enhance Therapy in Drug-Resistant Cancer Cells," *ACS Applied Materials & Interfaces,* vol. 12, no. 1, pp. 400-409, 2020/01/08 2020, doi: 10.1021/acsami.9b20707.

[93] Z. Wang *et al.*, "A Tubular DNA Nanodevice as a siRNA/Chemo-Drug Co-delivery Vehicle for Combined Cancer Therapy," *Angewandte Chemie International Edition,* vol. 60, no. 5, pp. 2594-2598, 2021/02/01 2021, doi: https://doi.org/10.1002/anie.202009842.

[94] R. Veneziano *et al.*, "Role of nanoscale antigen organization on B-cell activation probed using DNA origami," *Nature Nanotechnology,* vol. 15, no. 8, pp. 716-723, 2020/08/01 2020, doi: 10.1038/s41565-020-0719-0.

[95] N. P. Agarwal, M. Matthies, F. N. Gür, K. Osada, and T. L. Schmidt, "Block Copolymer Micellization as a Protection Strategy for DNA Origami," *Angewandte Chemie International Edition,* vol. 56, no. 20, pp. 5460-5464, 2017/05/08 2017, doi: https://doi.org/10.1002/anie.201608873.

[96] S. Liu *et al.*, "A DNA nanodevice-based vaccine for cancer immunotherapy," *Nature Materials,* vol. 20, no. 3, pp. 421-430, 2021/03/01 2021, doi: 10.1038/s41563-020-0793-6.

[97] A. Khmelinskaia, J. Mücksch, E. P. Petrov, H. G. Franquelim, and P. Schwille, "Control of Membrane Binding and Diffusion of Cholesteryl-Modified DNA Origami Nanostructures by DNA Spacers," *Langmuir,* vol. 34, no. 49, pp. 14921-14931, 2018/12/11 2018, doi: 10.1021/acs.langmuir.8b01850.

[98] S. Iwabuchi, I. Kawamata, S. Murata, and S.-i. M. Nomura, "A large, square-shaped, DNA origami nanopore with sealing function on a giant vesicle membrane," *Chemical Communications,* 10.1039/D0CC07412H vol. 57, no. 24, pp. 2990-2993, 2021, doi: 10.1039/D0CC07412H.

[99] R. O. Pedersen, E. G. Loboa, and T. H. LaBean, "Sensitization of transforming growth factor-β signaling by multiple peptides patterned on DNA nanostructures," *Biomacromolecules,* vol. 14 12, pp. 4157-60, 2013.

[100] Q. Zhang *et al.*, "DNA Origami as an In Vivo Drug Delivery Vehicle for Cancer Therapy," *ACS Nano,* vol. 8, no. 7, pp. 6633-6643, 2014/07/22 2014, doi: 10.1021/nn502058j.

[101] X. Ouyang *et al.*, "Docking of Antibodies into the Cavities of DNA Origami Structures," *Angewandte Chemie International Edition,* vol. 56, no. 46, pp. 14423-14427, 2017/11/13 2017, doi: https://doi.org/10.1002/anie.201706765.

[102] S. Arnon *et al.*, "Thought-Controlled Nanoscale Robots in a Living Host," *PLOS ONE,* vol. 11, no. 8, p. e0161227, 2016, doi: 10.1371/journal.pone.0161227.

[103] P. D. E. Fisher *et al.*, "A Programmable DNA Origami Platform for Organizing Intrinsically Disordered Nucleoporins within Nanopore Confinement," *ACS Nano,* vol. 12, no. 2, pp. 1508-1518, 2018/02/27 2018, doi: 10.1021/acsnano.7b08044.

[104] J. Hellmeier *et al.*, "Strategies for the Site-Specific Decoration of DNA Origami Nanostructures with Functionally Intact Proteins," *ACS Nano,* vol. 15, no. 9, pp. 15057-15068, 2021/09/28 2021, doi: 10.1021/acsnano.1c05411.

[105] A. Mukhortava and M. Schlierf, "Efficient Formation of Site-Specific Protein–DNA Hybrids Using Copper-Free Click Chemistry," *Bioconjugate Chemistry,* vol. 27, no. 7, pp. 1559-1563, 2016/07/20 2016, doi: 10.1021/acs.bioconjchem.6b00120.

[106] L. M. van der Sleen and K. M. Tych, "Bioconjugation Strategies for Connecting Proteins to DNA-Linkers for Single-Molecule Force-Based Experiments," *Nanomaterials*, vol. 11, no. 9*,* doi: 10.3390/nano11092424.

[107] M. Synakewicz, D. Bauer, M. Rief, and L. S. Itzhaki, "Bioorthogonal protein-DNA conjugation methods for force spectroscopy," *Scientific Reports,* vol. 9, no. 1, p. 13820, 2019/09/25 2019, doi: 10.1038/s41598-019-49843-1.

[108] I. Murphy *et al.*, "A method for site-specifically tethering the enzyme urease to DNA origami with sustained activity," *arXiv preprint arXiv:2409.03040,* 2024.

[109] G. A. Knappe, E.-C. Wamhoff, and M. Bathe, "Functionalizing DNA origami to investigate and interact with biological systems," *Nature Reviews Materials,* vol. 8, no. 2, pp. 123-138, 2023/02/01 2023, doi: 10.1038/s41578-022-00517-x.

[110] C. Lin, S. D. Perrault, M. Kwak, F. Graf, and W. M. Shih, "Purification of DNA-origami nanostructures by rate-zonal centrifugation," *Nucleic Acids Research,* vol. 41, no. 2, pp. e40-e40, 2013, doi: 10.1093/nar/gks1070.

[111] E. Stahl, T. G. Martin, F. Praetorius, and H. Dietz, "Facile and Scalable Preparation of Pure and Dense DNA Origami Solutions," *Angewandte Chemie*

International Edition, vol. 53, no. 47, pp. 12735-12740, 2014/11/17 2014, doi: https://doi.org/10.1002/anie.201405991.

[112] R. F. Sommese, R. F. Hariadi, K. Kim, M. Liu, M. J. Tyska, and S. Sivaramakrishnan, "Patterning protein complexes on DNA nanostructures using a GFP nanobody," *Protein Science,* vol. 25, no. 11, pp. 2089-2094, 2016/11/01 2016, doi: https://doi.org/10.1002/pro.3020.

[113] V. Verma, L. Mallik, R. F. Hariadi, S. Sivaramakrishnan, G. Skiniotis, and A. P. Joglekar, "Using Protein Dimers to Maximize the Protein Hybridization Efficiency with Multisite DNA Origami Scaffolds," *PLOS ONE,* vol. 10, no. 9, p. e0137125, 2015, doi: 10.1371/journal.pone.0137125.

[114] A. Shaw, E. Benson, and B. Högberg, "Purification of Functionalized DNA Origami Nanostructures," *ACS Nano,* vol. 9, no. 5, pp. 4968-4975, 2015/05/26 2015, doi: 10.1021/nn507035g.

[115] S. M. Douglas, I. Bachelet, and G. M. Church, "A Logic-Gated Nanorobot for Targeted Transport of Molecular Payloads," *Science,* vol. 335, no. 6070, pp. 831-834, 2012/02/17 2012, doi: 10.1126/science.1214081.

[116] J. R. Burns, B. Lamarre, A. L. B. Pyne, J. E. Noble, and M. G. Ryadnov, "DNA Origami Inside-Out Viruses," *ACS synthetic biology,* vol. 7 3, pp. 767-773, 2018.

[117] A. Shaw *et al.*, "Spatial control of membrane receptor function using ligand nanocalipers," *Nature Methods,* vol. 11, no. 8, pp. 841-846, 2014/08/01 2014, doi: 10.1038/nmeth.3025.

[118] Y. Deng *et al.*, "Intracellular Delivery of Nanomaterials via an Inertial Microfluidic Cell Hydroporator," *Nano Letters,* vol. 18, no. 4, pp. 2705-2710, 2018/04/11 2018, doi: 10.1021/acs.nanolett.8b00704.

[119] D. H. Schaffert *et al.*, "Intracellular Delivery of a Planar DNA Origami Structure by the Transferrin-Receptor Internalization Pathway," *Small,* vol. 12, no. 19, pp. 2634-2640, 2016/05/01 2016, doi: https://doi.org/10.1002/smll.201503934.

[120] H. Bayley and C. R. Martin, "Resistive-Pulse SensingFrom Microbes to Molecules," *Chemical Reviews,* vol. 100, no. 7, pp. 2575-2594, 2000/07/01 2000, doi: 10.1021/cr980099g.

[121] R. Nazarian, E. Lee, B. Siegel, C. Kuo, S. Acharya, and J. Schmidt, "Quantitative Measurements of Protein Volume and Concentration using Hydrogel-Backed Nanopores," *ACS Sens,* vol. 6, no. 3, pp. 722-726, Mar 26 2021, doi: 10.1021/acssensors.1c00284.

[122] C. Wloka *et al.*, "Label-Free and Real-Time Detection of Protein Ubiquitination with a Biological Nanopore," *ACS Nano,* vol. 11, no. 5, pp. 4387-4394, May 23 2017, doi: 10.1021/acsnano.6b07760.

[123] V. Van Meervelt *et al.*, "Real-Time Conformational Changes and Controlled Orientation of Native Proteins Inside a Protein Nanoreactor," *J Am Chem Soc,* vol. 139, no. 51, pp. 18640-18646, Dec 27 2017, doi: 10.1021/jacs.7b10106.

[124] P. Waduge *et al.*, "Nanopore-Based Measurements of Protein Size, Fluctuations, and Conformational Changes," *ACS Nano,* vol. 11, no. 6, pp. 5706-5716, Jun 27 2017, doi: 10.1021/acsnano.7b01212.

[125] E. C. Yusko *et al.*, "Real-time shape approximation and fingerprinting of single proteins using a nanopore," *Nat Nanotechnol,* vol. 12, no. 4, pp. 360-367, May 2017, doi: 10.1038/nnano.2016.267.

[126] J. Nivala, D. B. Marks, and M. Akeson, "Unfoldase-mediated protein translocation through an alpha-hemolysin nanopore," *Nat Biotechnol,* vol. 31, no. 3, pp. 247-50, Mar 2013, doi: 10.1038/nbt.2503.

[127] E. C. Yusko *et al.*, "Controlling protein translocation through nanopores with bio-inspired fluid walls," *Nat Nanotechnol,* vol. 6, no. 4, pp. 253-60, Apr 2011, doi: 10.1038/nnano.2011.12.

[128] D. Rodriguez-Larrea and H. Bayley, "Multistep protein unfolding during nanopore translocation," *Nat Nanotechnol,* vol. 8, no. 4, pp. 288-95, Apr 2013, doi: 10.1038/nnano.2013.22.

[129] J. J. Kasianowicz, E. Brandin, D. Branton, and D. W. Deamer, "Characterization of individual polynucleotide molecules using a membrane channel," *Proceedings of the National Academy of Sciences,* vol. 93, no. 24, pp. 13770-13773, 1996/11/26 1996, doi: 10.1073/pnas.93.24.13770.

[130] H. Bhatti *et al.*, "Recent advances in biological nanopores for nanopore sequencing, sensing and comparison of functional variations in MspA mutants," *RSC Advances,* vol. 11, no. 46, pp. 28996-29014, 2021, doi: 10.1039/d1ra02364k.

[131] O. Braha *et al.*, "Designed protein pores as components for biosensors," *Chemistry & Biology,* vol. 4, no. 7, pp. 497-505, 1997/07/01/ 1997, doi: https://doi.org/10.1016/S1074-5521(97)90321-5.

[132] M. Soskine, A. Biesemans, B. Moeyaert, S. Cheley, H. Bayley, and G. Maglia, "An engineered ClyA nanopore detects folded target proteins by selective external association and pore entry," *Nano Lett,* vol. 12, no. 9, pp. 4895-900, Sep 12 2012, doi: 10.1021/nl3024438.

[133] L. Payet *et al.*, "Temperature Effect on Ionic Current and ssDNA Transport through Nanopores," *Biophys J,* vol. 109, no. 8, pp. 1600-7, Oct 20 2015, doi: 10.1016/j.bpj.2015.08.043.

[134] F. Piguet, H. Ouldali, M. Pastoriza-Gallego, P. Manivet, J. Pelta, and A. Oukhaled, "Identification of single amino acid differences in uniformly charged homopolymeric peptides with aerolysin nanopore," *Nat Commun,* vol. 9, no. 1, p. 966, Mar 6 2018, doi: 10.1038/s41467-018-03418-2.

[135] M. P. Tom Z. Butlera , Ian M. Derringtona , Michael Niederweisb, and Jens H. Gundlach, "Single-molecule DNA detection with an engineeredMspA protein nanopore," *PNAS,* vol. 105, no. 52, pp. 20647–20652, 2008.

[136] G. Huang, K. Willems, M. Soskine, C. Wloka, and G. Maglia, "Electro-osmotic capture and ionic discrimination of peptide and protein biomarkers with FraC nanopores," *Nat Commun,* vol. 8, no. 1, p. 935, Oct 16 2017, doi: 10.1038/s41467-017-01006-4.

[137] G. M. Cherf, K. R. Lieberman, H. Rashid, C. E. Lam, K. Karplus, and M. Akeson, "Automated forward and reverse ratcheting of DNA in a nanopore at 5-A precision," *Nat Biotechnol,* vol. 30, no. 4, pp. 344-8, Feb 14 2012, doi: 10.1038/nbt.2147.

[138] J. Clarke, H. C. Wu, L. Jayasinghe, A. Patel, S. Reid, and H. Bayley, "Continuous base identification for single-molecule nanopore DNA sequencing," *Nat Nanotechnol,* vol. 4, no. 4, pp. 265-70, Apr 2009, doi: 10.1038/nnano.2009.12.

[139] C. Cao, Y. L. Ying, Z. L. Hu, D. F. Liao, H. Tian, and Y. T. Long, "Discrimination of oligonucleotides of different lengths with a wild-type aerolysin nanopore," *Nat Nanotechnol,* vol. 11, no. 8, pp. 713-8, Aug 2016, doi: 10.1038/nnano.2016.66.

[140] E. A. Manrao *et al.*, "Reading DNA at single-nucleotide resolution with a mutant MspA nanopore and phi29 DNA polymerase," *Nat Biotechnol,* vol. 30, no. 4, pp. 349-53, Mar 25 2012, doi: 10.1038/nbt.2171.

[141] D. R. Garalde *et al.*, "Highly parallel direct RNA sequencing on an array of nanopores," *Nat Methods,* vol. 15, no. 3, pp. 201-206, Mar 2018, doi: 10.1038/nmeth.4577.

[142] T. C. Sutherland, Y. T. Long, R. I. Stefureac, I. Bediako-Amoa, H. B. Kraatz, and J. S. Lee, "Structure of peptides investigated by nanopore analysis," *Nano Letters,* vol. 4, no. 7, pp. 1273-1277, 2004/7// 2004, doi: 10.1021/nl049413e.

[143] L. Movileanu, J. P. Schmittschmitt, J. M. Scholtz, and H. Bayley, "Interactions of peptides with a protein pore," *Biophys J,* vol. 89, no. 2, pp. 1030-45, Aug 2005, doi: 10.1529/biophysj.104.057406.

[144] A. Sauciuc and G. Maglia, "Controlled Translocation of Proteins through a Biological Nanopore for Single-Protein Fingerprint Identification," *Nano Lett,* vol. 24, no. 44, pp. 14118-14124, Nov 6 2024, doi: 10.1021/acs.nanolett.4c04510.

[145] C. Cao *et al.*, "Deep Learning-Assisted Single-Molecule Detection of Protein Post-translational Modifications with a Biological Nanopore," *ACS Nano,* vol. 18, no. 2, pp. 1504-1515, Jan 16 2024, doi: 10.1021/acsnano.3c08623.

[146] S. H. Liviu Movileanu, Orit Braha, and Hagan Bayley, "Detecting protein analytes that modulate transmembrane movement of a polymer chain within a single protein pore," *Nature Biotechnology,* vol. 18, pp. 1091-1095, 2000.

[147] S. Zernia, N. J. van der Heide, N. S. Galenkamp, G. Gouridis, and G. Maglia, "Current Blockades of Proteins inside Nanopores for Real-Time Metabolome Analysis," *ACS Nano,* vol. 14, no. 2, pp. 2296-2307, Feb 25 2020, doi: 10.1021/acsnano.9b09434.

[148] A. Squires, E. Atas, and A. Meller, "Nanopore sensing of individual transcription factors bound to DNA," *Scientific Reports,* vol. 5, 2015/6// 2015, doi: 10.1038/srep11643.

[149] A. Crnkovic, M. Srnko, and G. Anderluh, "Biological Nanopores: Engineering on Demand," *Life (Basel),* vol. 11, no. 1, Jan 5 2021, doi: 10.3390/life11010027.

[150] F. Haque, J. Li, H. C. Wu, X. J. Liang, and P. Guo, "Solid-State and Biological Nanopore for Real-Time Sensing of Single Chemical and Sequencing of DNA," *Nano Today,* vol. 8, no. 1, pp. 56-74, Feb 2013, doi: 10.1016/j.nantod.2012.12.008.

[151] D. S. Jiali Li, Ciaran McMullan, Daniel Branton, Michael J. Aziz² & Jene A. Golovchenko, "Ion-beam sculpting at nanometre

length scales," *Nature,* vol. 412, pp. 166-169, 2001.

[152] T. Gilboa, A. Zrehen, A. Girsault, and A. Meller, "Optically-Monitored Nanopore Fabrication Using a Focused Laser Beam," *Sci Rep,* vol. 8, no. 1, p. 9765, Jun 27 2018, doi: 10.1038/s41598-018-28136-z.

[153] H. Yamazaki, R. Hu, Q. Zhao, and M. Wanunu, "Photothermally Assisted Thinning of Silicon Nitride Membranes for Ultrathin Asymmetric Nanopores," *ACS Nano,* vol. 12, no. 12, pp. 12472-12481, Dec 26 2018, doi: 10.1021/acsnano.8b06805.

[154] A. J. Storm, J. H. Chen, X. S. Ling, H. W. Zandbergen, and C. Dekker, "Fabrication of solid-state nanopores with single-nanometre precision," *Nat Mater,* vol. 2, no. 8, pp. 537-40, Aug 2003, doi: 10.1038/nmat941.

[155] H. Kwok, K. Briggs, and V. Tabard-Cossa, "Nanopore fabrication by controlled dielectric breakdown," *PLoS One,* vol. 9, no. 3, p. e92880, 2014, doi: 10.1371/journal.pone.0092880.

[156] M. Waugh *et al.*, "Solid-state nanopore fabrication by automated controlled breakdown," *Nat Protoc,* vol. 15, no. 1, pp. 122-143, Jan 2020, doi: 10.1038/s41596-019-0255-2.

[157] D. S. Talaga and J. Li, "Single-molecule protein unfolding in solid state nanopores," *Journal of the American Chemical Society,* vol. 131, no. 26, pp. 9287-9297, 2009/7// 2009, doi: 10.1021/ja901088b.

[158] B. M. Venkatesan, A. B. Shah, J. M. Zuo, and R. Bashir, "DNA Sensing using Nano-crystalline Surface Enhanced Al(2)O(3) Nanopore Sensors," *Adv Funct Mater,* vol. 20, no. 8, pp. 1266-1275, Apr 23 2010, doi: 10.1002/adfm.200902128.

[159] B. M. Venkatesan, B. Dorvel, S. Yemenicioglu, N. Watkins, I. Petrov, and R. Bashir, "Highly Sensitive, Mechanically Stable Nanopore Sensors for DNA Analysis," *Adv Mater,* vol. 21, no. 27, p. 2771, Jul 20 2009, doi: 10.1002/adma.200803786.

[160] K. B. Park *et al.*, "Highly reliable and low-noise solid-state nanopores with an atomic layer deposited ZnO membrane on a quartz substrate," *Nanoscale,* vol. 9, no. 47, pp. 18772-18780, Dec 7 2017, doi: 10.1039/c7nr05755e.

[161] R. Wang, T. Gilboa, J. Song, D. Huttner, M. W. Grinstaff, and A. Meller, "Single-Molecule Discrimination of Labeled DNAs and Polypeptides Using Photoluminescent-Free TiO(2) Nanopores," *ACS Nano,* vol. 12, no. 11, pp. 11648-11656, Nov 27 2018, doi: 10.1021/acsnano.8b07055.

[162] C. A. Merchant *et al.*, "DNA Translocation through Graphene Nanopores," *Nano Letters,* vol. 10, no. 8, pp. 2915-2921, 2010/08/11 2010, doi: 10.1021/nl101046t.

[163] S. Garaj, W. Hubbard, A. Reina, J. Kong, D. Branton, and J. A. Golovchenko, "Graphene as a subnanometre trans-electrode membrane," *Nature,* vol. 467, no. 7312, pp. 190-193, 2010/9// 2010, doi: 10.1038/nature09379.

[164] A. T. Kuan, B. Lu, P. Xie, T. Szalay, and J. A. Golovchenko, "Electrical pulse fabrication of graphene nanopores in electrolyte solution," *Appl Phys Lett,* vol. 106, no. 20, p. 203109, May 18 2015, doi: 10.1063/1.4921620.

[165] K. Liu, J. Feng, A. Kis, and A. Radenovic, "Atomically Thin Molybdenum Disulfide Nanopores with High Sensitivity for DNA Translocation," *ACS Nano,* vol. 8, no. 3, pp. 2504-2511, 2014/03/25 2014, doi: 10.1021/nn406102h.

[166] M. Graf *et al.*, "Fabrication and practical applications of molybdenum disulfide nanopores," *Nat Protoc,* vol. 14, no. 4, pp. 1130-1168, Apr 2019, doi: 10.1038/s41596-019-0131-0.

[167] J. Feng *et al.*, "Identification of single nucleotides in MoS 2 nanopores," *Nature Nanotechnology,* vol. 10, no. 12, pp. 1070-1076, 2015/12// 2015, doi: 10.1038/nnano.2015.219.

[168] J. Larkin, R. Y. Henley, M. Muthukumar, J. K. Rosenstein, and M. Wanunu, "High-bandwidth protein analysis using solid-state nanopores," *Biophysical Journal,* vol. 106, no. 3, pp. 696-704, 2014/2// 2014, doi: 10.1016/j.bpj.2013.12.025.

[169] D. K. Meng-Yue Wu, Mathijs Zandbergen, and Henny Zandbergen, "Formation of nanopores in a SiN/SiO2 membrane with an electron beam," *APPLIED PHYSICS LETTERS,* vol. 87, 2005, doi: 10.1063/1.2043247兴.

[170] M. J. Kim, M. Wanunu, D. C. Bell, and A. Meller, "Rapid Fabrication of Uniformly Sized Nanopores and Nanopore Arrays for Parallel DNA Analysis," *Advanced Materials,* vol. 18, no. 23, pp. 3149-3153, 2006, doi: 10.1002/adma.200601191.

[171] J. Larkin, R. Y. Henley, V. Jadhav, J. Korlach, and M. Wanunu, "Length-independent DNA packing into nanopore zero-mode waveguides for low-input DNA sequencing," *Nat Nanotechnol,* vol. 12, no. 12, pp. 1169-1175, Dec 2017, doi: 10.1038/nnano.2017.176.

[172] L. Sainiemi, K. Grigoras, and S. Franssila, "Suspended nanostructured alumina membranes," *Nanotechnology,* vol. 20, no. 7, p. 075306, 2009/01/23 2009, doi: 10.1088/0957-4484/20/7/075306.

[173] J. Larkin, R. Henley, D. C. Bell, T. Cohen-Karni, J. K. Rosenstein, and M. Wanunu, "Slow DNA Transport through Nanopores in Hafnium Oxide Membranes," *ACS Nano,* vol. 7, no. 11, pp. 10121-10128, 2013/11/26 2013, doi: 10.1021/nn404326f.

[174] J. Shim, J. A. Rivera, and R. Bashir, "Electron beam induced local crystallization of HfO2 nanopores for biosensing applications," *Nanoscale,* vol. 5, no. 22, 2013, doi: 10.1039/c3nr02608f.

[175] P. Waduge, J. Larkin, M. Upmanyu, S. Kar, and M. Wanunu, "Programmed Synthesis of Freestanding Graphene Nanomembrane Arrays," *Small,* vol. 11, no. 5, pp. 597-603, 2014, doi: 10.1002/smll.201402230.

[176] G. F. Schneider *et al.*, "Tailoring the hydrophobicity of graphene for its use as nanopores for DNA translocation," *Nature Communications,* vol. 4, no. 1, 2013, doi: 10.1038/ncomms3619.

[177] M. I. Walker, R. S. Weatherup, N. A. W. Bell, S. Hofmann, and U. F. Keyser, "Free-standing graphene membranes on glass nanopores for ionic current measurements," *Applied Physics Letters,* vol. 106, no. 2, 2015, doi: 10.1063/1.4906236.

[178] S. Liu *et al.*, "Boron Nitride Nanopores: Highly Sensitive DNA Single-Molecule Detectors," *Advanced Materials,* vol. 25, no. 33, pp. 4549-4554, 2013, doi: 10.1002/adma.201301336.

[179] Z. Zhou *et al.*, "DNA Translocation through Hydrophilic Nanopore in Hexagonal Boron Nitride," *Scientific Reports,* vol. 3, no. 1, 2013, doi: 10.1038/srep03287.

[180] G. Danda *et al.*, "Monolayer WS2 Nanopores for DNA Translocation with Light-Adjustable Sizes," *ACS Nano,* vol. 11, no. 2, pp. 1937-1945, 2017/02/28 2017, doi: 10.1021/acsnano.6b08028.

[181] Y. Shen *et al.*, "In Situ Repair of 2D Chalcogenides under Electron Beam Irradiation," *Adv Mater,* vol. 30, no. 14, p. e1705954, Apr 2018, doi: 10.1002/adma.201705954.

[182] I. B. Pradeep Waduge, Joseph Larkin, Robert Y. Henley, Kenneth Goodfellow, Adam C. Graham, David C. Bell, Nick Vamivakas, Swastik Kar, and Meni Wanunu, "Direct and Scalable Deposition of Atomically Thin Low-Noise MoS2 Membranes on Apertures," *ACS Nano,* vol. 9, no. 7, pp. 7352–7359, 2015.

[183] M. Mojtabavi, A. VahidMohammadi, W. Liang, M. Beidaghi, and M. Wanunu, "Single-Molecule Sensing Using Nanopores in Two-Dimensional Transition Metal Carbide (MXene) Membranes," *ACS Nano,* vol. 13, no. 3, pp. 3042-3053, 2019/03/26 2019, doi: 10.1021/acsnano.8b08017.

[184] L. Xue, H. Yamazaki, R. Ren, M. Wanunu, A. P. Ivanov, and J. B. Edel, "Solid-state nanopore sensors," *Nature Reviews Materials,* vol. 5, no. 12, pp. 931-951, 2020, doi: 10.1038/s41578-020-0229-6.

[185] C. S. Arnold J. Storm, Jianghua Chen, Henny Zandbergen, Jean-Franc¸ois Joanny, and Cees Dekker, "Fast DNA Translocation through aSolid-State Nanopore," *NANO Letters,* vol. 5, no. 7, pp. 1193-1197, 2005.

[186] H. Cun *et al.*, "Wafer-scale MOCVD growth of monolayer MoS2 on sapphire and SiO2," *Nano Research,* vol. 12, no. 10, pp. 2646-2652, 2019, doi: 10.1007/s12274-019-2502-9.

[187] J. Feng *et al.*, "Electrochemical Reaction in Single Layer MoS2: Nanopores Opened Atom by Atom," *Nano Lett,* vol. 15, no. 5, pp. 3431-8, May 13 2015, doi: 10.1021/acs.nanolett.5b00768.

[188] T. Gilboa, E. Zvuloni, A. Zrehen, A. H. Squires, and A. Meller, "Automated, Ultra-Fast Laser-Drilling of Nanometer Scale Pores and Nanopore Arrays in Aqueous Solutions," *Advanced Functional Materials,* vol. 30, no. 18, 2019, doi: 10.1002/adfm.201900642.

[189] M. Wanunu, T. Dadosh, V. Ray, J. Jin, L. McReynolds, and M. Drndic, "Rapid electronic detection of probe-specific microRNAs using thin nanopore sensors," *Nat Nanotechnol,* vol. 5, no. 11, pp. 807-14, Nov 2010, doi: 10.1038/nnano.2010.202.

[190] R. Y. Henley, B. A. Ashcroft, I. Farrell, B. S. Cooperman, S. M. Lindsay, and M. Wanunu, "Electrophoretic Deformation of Individual Transfer RNA Molecules Reveals Their Identity," *Nano Lett,* vol. 16, no. 1, pp. 138-44, Jan 13 2016, doi: 10.1021/acs.nanolett.5b03331.

[191] A. R. Hall, A. Scott, D. Rotem, K. K. Mehta, H. Bayley, and C. Dekker, "Hybrid pore formation by directed insertion of α-haemolysin into solid-state nanopores," *Nature Nanotechnology,* vol. 5, no. 12, pp. 874-877, 2010, doi: 10.1038/nnano.2010.237.

[192] C. R. Engst, M. Ablay, G. Divitini, C. Ducati, T. Liedl, and U. F. Keyser, "DNA Origami Nanopores," *Nano Letters,* vol. 12, no. 1, pp. 512-517, 2012/01/11 2012, doi: 10.1021/nl204098n.

[193] V. A. Martin Langecker, Thomas G. Martin, Jonathan List, Stephan Renner, Michael Mayer, Hendrik Dietz, Friedrich C. Simmel, "Synthetic Lipid Membrane Channels Formed by Designed DNA Nanostructures," *SCIENCE,* vol. 338, pp. 932-936, 2012.

[194] B. Cressiot, S. J. Greive, M. Mojtabavi, A. A. Antson, and M. Wanunu, "Thermostable virus portal proteins as reprogrammable adapters for solid-state

nanopore sensors," *Nature Communications,* vol. 9, no. 1, 2018, doi: 10.1038/s41467-018-07116-x.

[195] M. Barber, "A new method of isolating microorganisms," *J Kans Med Soc,* 1904.

[196] G. Ling and R. W. Gerard, "The normal membrane potential of frog sartorius fibers," *Journal of Cellular and Comparative Physiology,* vol. 34, no. 3, pp. 383-396, 1949/12/01 1949, doi: https://doi.org/10.1002/jcp.1030340304.

[197] S. Umehara, M. Karhanek, R. W. Davis, and N. Pourmand, "Label-free biosensing with functionalized nanopipette probes," *Proceedings of the National Academy of Sciences,* vol. 106, no. 12, pp. 4611-4616, 2009/03/24 2009, doi: 10.1073/pnas.0900306106.

[198] "Allen J. Bard and Larry R. Faulkner, Electrochemical Methods: Fundamentals and Applications, New York: Wiley, 2001, 2nd ed," *Russian Journal of Electrochemistry,* vol. 38, no. 12, pp. 1364-1365, 2002/12/01 2002, doi: 10.1023/A:1021637209564.

[199] S. Buyukdagli, "Dielectric Manipulation of Polymer Translocation Dynamics in Engineered Membrane Nanopores," *Langmuir,* vol. 38, no. 1, pp. 122-131, 2022/01/11 2022, doi: 10.1021/acs.langmuir.1c02174.

[200] I. Jou and M. Muthukumar, "Effects of Nanopore Charge Decorations on the Translocation Dynamics of DNA," *Biophysical Journal,* vol. 113, no. 8, pp. 1664-1672, 2017, doi: 10.1016/j.bpj.2017.08.045.

[201] J. Stanley and N. Pourmand, "Nanopipettes—The past and the present," *APL Materials,* vol. 8, no. 10, 2020, doi: 10.1063/5.0020011.

[202] N. Ermann, N. Hanikel, V. Wang, K. Chen, N. E. Weckman, and U. F. Keyser, "Promoting single-file DNA translocations through nanopores using electro-osmotic flow," *The Journal of Chemical Physics,* vol. 149, no. 16, 2018, doi: 10.1063/1.5031010.

[203] F. Boskovic, C. Maffeo, G. Patino-Guillen, R. Tivony, A. Aksimentiev, and U. F. Keyser, "Nanopore Translocation Reveals Electrophoretic Force on Noncanonical RNA:DNA Double Helix," *ACS Nano,* vol. 18, no. 23, pp. 15013-15024, Jun 11 2024, doi: 10.1021/acsnano.4c01466.

[204] "Electroosmotic flow across nanopores for single-molecule protein sequencing," *Nat Biotechnol,* vol. 42, no. 8, pp. 1192-1193, Aug 2024, doi: 10.1038/s41587-023-01976-5.

[205] R. A. L. a. J. L. Rae, "The Use of Quartz Patch Pipettes for Low Noise Single Channel Recording," *Biophysical Journal,* vol. 65, pp. 1666-1677, 1993.

[206] J.-L. Munoz and J. A. Coles, "Quartz micropipettes for intracellular voltage microelectrodes and ion-selective microelectrodes," *Journal of Neuroscience Methods,* vol. 22, no. 1, pp. 57-64, 1987/11/01/ 1987, doi: https://doi.org/10.1016/0165-0270(87)90090-2.

[207] R. Gao, L.-F. Cui, L.-Q. Ruan, Y.-L. Ying, and Y.-T. Long, "A Closed-Type Wireless Nanopore Electrode for Analyzing Single Nanoparticles," *JoVE,* no. 145, p. e59003, 2019/03/20 2019, doi: doi:10.3791/59003.

[208] C. A. Morris, A. K. Friedman, and L. A. Baker, "Applications of nanopipettes in the analytical sciences," *Analyst,* vol. 135, no. 9, pp. 2190-2202, 2010, doi: 10.1039/c0an00156b.

[209] M. S. a. S. Hennig. Preparation and Loading of Nanopipettes [Online] Available: https://analyticalscience.wiley.com/content/article-do/preparation-and-loading-nanopipettes

[210] B. S. a. E. Neher, *Single-Channel Recording*. New York: Plenum Press, 1995.

[211] E. J. Harris, "Tools in Biology: Glass Microelectrodes. Marc Lavallee, Otto F. Schanne, and Normand G. Hebert, Eds. Wiley, New York, 1969. xviii + 446 pp., illus. $22.50," *Science,* vol. 166, no. 3903, pp. 368-369, 1969/10/17 1969, doi: 10.1126/science.166.3903.368.b.

[212] M. Trivedi and N. Nirmalkar, "Ion transport and current rectification in a charged conical nanopore filled with viscoelastic fluids," *Sci Rep,* vol. 12, no. 1, p. 2547, Feb 15 2022, doi: 10.1038/s41598-022-06079-w.

[213] E. A. Vitol, Z. Orynbayeva, M. J. Bouchard, J. Azizkhan-Clifford, G. Friedman, and Y. Gogotsi, "In Situ Intracellular Spectroscopy with Surface Enhanced Raman Spectroscopy (SERS)-Enabled Nanopipettes," *ACS Nano,* vol. 3, no. 11, pp. 3529-3536, 2009/11/24 2009, doi: 10.1021/nn9010768.

[214] S. Ding, C. Gao, and L. Q. Gu, "Capturing single molecules of immunoglobulin and ricin with an aptamer-encoded glass nanopore," *Anal Chem,* vol. 81, no. 16, pp. 6649-55, Aug 15 2009, doi: 10.1021/ac9006705.

[215] P. Actis *et al.*, "Reversible thrombin detection by aptamer functionalized STING sensors," *Biosens Bioelectron,* vol. 26, no. 11, pp. 4503-7, Jul 15 2011, doi: 10.1016/j.bios.2011.05.010.

[216] M. K. Senkei Umeharaa, Ronald W. Davisb and Nader Pourmand, "Label-free biosensing with functionalized nanopipette probes," *PNAS,* vol. 106, no. 12, pp. 4611-4616, 2009.

[217] L. J. Steinbock, O. Otto, C. Chimerel, J. Gornall, and U. F. Keyser, "Detecting DNA Folding with Nanocapillaries," *Nano Letters,* vol. 10, no. 7, pp. 2493-2497, 2010/07/14 2010, doi: 10.1021/nl100997s.

[218] M. Raveendran, A. R. Leach, T. Hopes, J. L. Aspden, and P. Actis, "Ribosome Fingerprinting with a Solid-State Nanopore," *ACS Sensors,* vol. 5, no. 11, pp. 3533-3539, 2020/11/25 2020, doi: 10.1021/acssensors.0c01642.

[219] A. A. Zuber, E. Klantsataya, and A. Bachhuka, "Biosensing," *Comprehensive Nanoscience and Nanotechnology,* 2019.

[220] R. A. Nascimento, R. E. Özel, W. H. Mak, M. Mulato, B. Singaram, and N. Pourmand, "Single Cell "Glucose Nanosensor" Verifies Elevated Glucose Levels in Individual Cancer Cells," (in eng), no. 1530-6992.

[221] I. Palchetti and M. Mascini, "Nucleic acid biosensors for environmental pollution monitoring," *Analyst,* 10.1039/B802920M vol. 133, no. 7, pp. 846-854, 2008, doi: 10.1039/B802920M.

[222] P. Jolly, P. Estrela, and M. Ladomery, "Oligonucleotide-based systems: DNA, microRNAs, DNA/RNA aptamers," *Essays in Biochemistry,* vol. 60, no. 1, pp. 27-35, 2016, doi: 10.1042/EBC20150004.

[223] M. Colombo, C. Mizzotti, S. Masiero, M. M. Kater, and P. Pesaresi, "Peptide aptamers: The versatile role of specific protein function inhibitors in plant biotechnology," *Journal of Integrative Plant Biology,* vol. 57, no. 11, pp. 892-901, 2015/11/01 2015, doi: https://doi.org/10.1111/jipb.12368.

[224] P. Actis, A. C. Mak, and N. Pourmand, "Functionalized nanopipettes: Toward label-free, single cell biosensors," *Bioanalytical Reviews,* vol. 1, no. 2, pp. 177-185, 2010, doi: 10.1007/s12566-010-0013-y.

[225] S. Cai, J. Y. Y. Sze, A. P. Ivanov, and J. B. Edel, "Small molecule electro-optical binding assay using nanopores," *Nat Commun,* vol. 10, no. 1, p. 1797, Apr 17 2019, doi: 10.1038/s41467-019-09476-4.

[226] J. Y. Y. Sze, A. P. Ivanov, A. E. G. Cass, and J. B. Edel, "Single molecule multiplexed nanopore protein screening in human serum using aptamer modified DNA carriers," *Nat Commun,* vol. 8, no. 1, p. 1552, Nov 16 2017, doi: 10.1038/s41467-017-01584-3.

[227] M. Firnkes, D. Pedone, J. Knezevic, M. Döblinger, and U. Rant, "Electrically facilitated translocations of proteins through silicon nitride nanopores: conjoint and competitive action of diffusion, electrophoresis, and electroosmosis," (in eng), *Nano letters,* vol. 10, no. 6, pp. 2162-2167, 2010/06// 2010, doi: 10.1021/nl100861c.

[228] N. A. W. Bell and U. F. Keyser, "Digitally encoded DNA nanostructures for multiplexed, single-molecule protein sensing with nanopores," *Nature Nanotechnology,* vol. 11, no. 7, pp. 645-651, 2016/7// 2016, doi: 10.1038/nnano.2016.50.

[229] N. E. Weckman *et al.*, "Multiplexed DNA Identification Using Site Specific dCas9 Barcodes and Nanopore Sensing," *ACS Sensors,* vol. 4, no. 8, pp. 2065-2072, 2019/08/23 2019, doi: 10.1021/acssensors.9b00686.

[230] M. Karhanek, J. T. Kemp, N. Pourmand, R. W. Davis, and C. D. Webb, "Single DNA Molecule Detection Using Nanopipettes and Nanoparticles," *Nano Letters,* vol. 5, no. 2, pp. 403-407, 2005/02/01 2005, doi: 10.1021/nl0480464.

[231] Y. Wang, K. Kececi, M. V. Mirkin, V. Mani, N. Sardesai, and J. F. Rusling, "Resistive-pulse measurements with nanopipettes: detection of Au nanoparticles and nanoparticle-bound anti-peanut IgY," *Chemical Science,*

10.1039/C2SC21502K vol. 4, no. 2, pp. 655-663, 2013, doi: 10.1039/C2SC21502K.

[232] X. Lin, A. P. Ivanov, and J. B. Edel, "Selective single molecule nanopore sensing of proteins using DNA aptamer-functionalised gold nanoparticles," *Chem Sci,* vol. 8, no. 5, pp. 3905-3912, May 1 2017, doi: 10.1039/c7sc00415j.

[233] J. Kong, N. A. Bell, and U. F. Keyser, "Quantifying Nanomolar Protein Concentrations Using Designed DNA Carriers and Solid-State Nanopores," *Nano Lett,* vol. 16, no. 6, pp. 3557-62, Jun 8 2016, doi: 10.1021/acs.nanolett.6b00627.

[234] J. Kong, J. Zhu, K. Chen, and U. F. Keyser, "Specific Biosensing Using DNA Aptamers and Nanopores," *Advanced Functional Materials,* vol. 29, no. 3, 2018, doi: 10.1002/adfm.201807555.

[235] J. Kong, J. Zhu, and U. F. Keyser, "Single molecule based SNP detection using designed DNA carriers and solid-state nanopores," *Chem Commun (Camb),* vol. 53, no. 2, pp. 436-439, Dec 22 2016, doi: 10.1039/c6cc08621g.

[236] A. Y. Y. Loh *et al.*, "Electric Single-Molecule Hybridization Detector for Short DNA Fragments," *Anal Chem,* vol. 90, no. 23, pp. 14063-14071, Dec 4 2018, doi: 10.1021/acs.analchem.8b04357.

[237] K. Chen, N. A. W. Bell, J. Kong, Y. Tian, and U. F. Keyser, "Direction- and Salt-Dependent Ionic Current Signatures for DNA Sensing with Asymmetric Nanopores," *Biophysical Journal,* vol. 112, no. 4, pp. 674-682, 2017, doi: 10.1016/j.bpj.2016.12.033.

[238] M. van den Hout, V. Krudde, X. J. A. Janssen, and N. H. Dekker, "Distinguishable Populations Report on the Interactions of Single DNA Molecules with Solid-State Nanopores," *Biophysical Journal,* vol. 99, no. 11, pp. 3840-3848, 2010/12/01/ 2010, doi: https://doi.org/10.1016/j.bpj.2010.10.012.

[239] X. Zhang *et al.*, "Translocation of Specific DNA Nanocarrier through an Ultrasmall Nanopipette: Toward Single-Protein-Molecule Detection with Superior Signal-to-Noise Ratio," *ACS Nano,* vol. 16, no. 9, pp. 15108-15114, 2022/9// 2022, doi: 10.1021/acsnano.2c06303.

[240] C. Tiede *et al.*, "Affimer proteins are versatile and renewable affinity reagents," *eLife,* vol. 6, p. e24903, 2017/06/27 2017, doi: 10.7554/eLife.24903.

[241] C. Tiede *et al.*, "Adhiron: A stable and versatile peptide display scaffold for molecular recognition applications," *Protein Engineering, Design and Selection,* vol. 27, no. 5, pp. 145-155, 2014, doi: 10.1093/protein/gzu007.

[242] M. Raina *et al.*, "Antibody mimetic receptor proteins for label-free biosensors," *Analyst,* 10.1039/C4AN01418A vol. 140, no. 3, pp. 803-810, 2015, doi: 10.1039/C4AN01418A.

[243] A. A.-S. Tang, C. Tiede, D. J. Hughes, M. J. McPherson, and D. C. Tomlinson, "Isolation of isoform-specific binding proteins (Affimers) by phage display using negative selection," *Science Signaling,* vol. 10, no. 505, p. eaan0868, 2017/11/14 2017, doi: 10.1126/scisignal.aan0868.

[244] P. Zhurauski *et al.*, "Sensitive and selective Affimer-functionalised interdigitated electrode-based capacitive biosensor for Her4 protein tumour biomarker detection," *Biosensors and Bioelectronics,* vol. 108, pp. 1-8, 2018/06/15/ 2018, doi: https://doi.org/10.1016/j.bios.2018.02.041.

[245] D. B. Ritchie and M. T. Woodside, "Probing the structural dynamics of proteins and nucleic acids with optical tweezers," *Current Opinion in Structural Biology,* vol. 34, pp. 43-51, 2015/10/01/ 2015, doi: https://doi.org/10.1016/j.sbi.2015.06.006.

[246] Y. R. Yang, Y. Liu, and H. Yan, "DNA Nanostructures as Programmable Biomolecular Scaffolds," *Bioconjugate Chemistry,* vol. 26, no. 8, pp. 1381-1395, 2015/08/19 2015, doi: 10.1021/acs.bioconjchem.5b00194.

[247] S. Li, A. H. C. Wong, and F. Liu, "Ligand-gated ion channel interacting proteins and their role in neuroprotection," *Frontiers in Cellular Neuroscience,* Mini Review vol. Volume 8 - 2014, 2014. [Online]. Available: https://www.frontiersin.org/journals/cellular-neuroscience/articles/10.3389/fncel.2014.00125.

[248] A. R. Chandrasekaran, "Programmable DNA scaffolds for spatially-ordered protein assembly," *Nanoscale,* 10.1039/C5NR08685J vol. 8, no. 8, pp. 4436-4446, 2016, doi: 10.1039/C5NR08685J.

[249] S. Ramakrishnan, G. Krainer, G. Grundmeier, M. Schlierf, and A. Keller, "Structural stability of DNA origami nanostructures in the presence of chaotropic agents," *Nanoscale,* 10.1039/C6NR00835F vol. 8, no. 19, pp. 10398-10405, 2016, doi: 10.1039/C6NR00835F.

[250] F. Kukolka *et al.*, "A Single-Molecule Förster Resonance Energy Transfer Analysis of Fluorescent DNA–Protein Conjugates for Nanobiotechnology," *Small,* vol. 2, no. 8-9, pp. 1083-1089, 2006/08/01 2006, doi: https://doi.org/10.1002/smll.200600202.

[251] N. A. W. Bell and U. F. Keyser, "Specific Protein Detection Using Designed DNA Carriers and Nanopores," *Journal of the American Chemical Society,* vol. 137, no. 5, pp. 2035-2041, 2015/02/11 2015, doi: 10.1021/ja512521w.

[252] I. Burbulis, K. Yamaguchi, A. Gordon, R. Carlson, and R. Brent, "Using protein-DNA chimeras to detect and count small numbers of molecules," *Nature Methods,* vol. 2, no. 1, pp. 31-37, 2005/01/01 2005, doi: 10.1038/nmeth729.

[253] R. Chhabra *et al.*, "Spatially Addressable Multiprotein Nanoarrays Templated by Aptamer-Tagged DNA Nanoarchitectures," *Journal of the American Chemical Society,* vol. 129, no. 34, pp. 10304-10305, 2007/08/01 2007, doi: 10.1021/ja072410u.

[254] D. N. Selmi *et al.*, "DNA-Templated Protein Arrays for Single-Molecule Imaging," *Nano Letters,* vol. 11, no. 2, pp. 657-660, 2011/02/09 2011, doi: 10.1021/nl1037769.

[255] C. Sornay, V. Vaur, A. Wagner, and G. Chaubet, "An overview of chemo- and site-selectivity aspects in the chemical conjugation of proteins," *Royal Society Open Science,* vol. 9, no. 1, p. 211563, 2022/01/26 2022, doi: 10.1098/rsos.211563.

[256] C. D. Spicer and B. G. Davis, "Selective chemical protein modification," *Nature Communications,* vol. 5, no. 1, p. 4740, 2014/09/05 2014, doi: 10.1038/ncomms5740.

[257] P. M. S. D. Cal, G. J. L. Bernardes, and P. M. P. Gois, "Cysteine-Selective Reactions for Antibody Conjugation," *Angewandte Chemie International Edition,* vol. 53, no. 40, pp. 10585-10587, 2014/09/26 2014, doi: https://doi.org/10.1002/anie.201405702.

[258] M. A. Alibakhshi, J. R. Halman, J. Wilson, A. Aksimentiev, K. A. Afonin, and M. Wanunu, "Picomolar Fingerprinting of Nucleic Acid Nanoparticles Using Solid-State Nanopores," *ACS Nano,* vol. 11, no. 10, pp. 9701-9710, 2017/10// 2017, doi: 10.1021/acsnano.7b04923.

[259] C. Plesa, J. W. Ruitenberg, M. J. Witteveen, and C. Dekker, "Detection of Individual Proteins Bound along DNA Using Solid-State Nanopores," *Nano Letters,* vol. 15, no. 5, pp. 3153-3158, 2015/05/13 2015, doi: 10.1021/acs.nanolett.5b00249.

[260] V. Wang, N. Ermann, and U. F. Keyser, "Current Enhancement in Solid-State Nanopores Depends on Three-Dimensional DNA Structure," *Nano Letters,* vol. 19, no. 8, pp. 5661-5666, 2019/08/14 2019, doi: 10.1021/acs.nanolett.9b02219.

[261] T. Ding *et al.*, "Shaped DNA origami carrier nanopore translocation influenced by aptamer based surface modification," *Biosensors and Bioelectronics,* vol. 195, p. 113658, 2022/01/01/ 2022, doi: https://doi.org/10.1016/j.bios.2021.113658.

[262] P. Ketterer *et al.*, "DNA origami scaffold for studying intrinsically disordered proteins of the nuclear pore complex," *Nature Communications,* vol. 9, no. 1, p. 902, 2018/03/02 2018, doi: 10.1038/s41467-018-03313-w.

[263] G. Tikhomirov, P. Petersen, and L. Qian, "Programmable disorder in random DNA tilings," *Nature Nanotechnology,* vol. 12, no. 3, pp. 251-259, 2017/3// 2017, doi: 10.1038/nnano.2016.256.

[264] S. M. Douglas, H. Dietz, T. Liedl, B. Högberg, F. Graf, and W. M. Shih, "Self-assembly of DNA into nanoscale three-dimensional shapes," *Nature,* vol. 459, no. 7245, pp. 414-418, 2009/05/01 2009, doi: 10.1038/nature08016.

[265] D. Liu, Q. Li, J. Luo, Q. Huang, and Y. Zhang, "An SPRI beads-based DNA purification strategy for flexibility and cost-effectiveness," *BMC Genomics,* vol. 24, no. 1, p. 125, 2023/03/16 2023, doi: 10.1186/s12864-023-09211-w.

[266] M. M. DeAngelis, D. G. Wang, and T. L. Hawkins, "Solid-phase reversible immobilization for the isolation of PCR products," *Nucleic Acids Research,* vol. 23, no. 22, pp. 4742-4743, 1995, doi: 10.1093/nar/23.22.4742.

[267] P. Oberacker *et al.*, "Bio-On-Magnetic-Beads (BOMB): Open platform for high-throughput nucleic acid extraction and manipulation," *PLOS Biology,* vol. 17, no. 1, p. e3000107, 2019, doi: 10.1371/journal.pbio.3000107.

[268] A. Stortchevoi, N. Kamelamela, and S. S. Levine, "SPRI Beads-based Size Selection in the Range of 2-10kb," (in eng), *J Biomol Tech. ,* vol. 31(1):7-10., 2020, doi: doi:10.7171/jbt.20-3101-002.

[269] L. S. Lerman, "A Transition to a Compact Form of DNA in Polymer Solutions," *Proceedings of the National Academy of Sciences,* vol. 68, no. 8, pp. 1886-1890, 1971/08/01 1971, doi: 10.1073/pnas.68.8.1886.

[270] C. Cheng, J.-L. Jia, and S.-Y. Ran, "Polyethylene glycol and divalent salt-induced DNA reentrant condensation revealed by single molecule measurements," *Soft Matter,* 10.1039/C5SM00619H vol. 11, no. 19, pp. 3927-3935, 2015, doi: 10.1039/C5SM00619H.

[271] P. Oberacker, P. Stepper, D. Bond, K. Hipp, T. A. Hore, and T. P. Jurkowski, "Simple Synthesis of Functionalized Paramagnetic Beads for Nucleic Acid Purification and Manipulation," *Bio-protocol,* vol. 9, no. 20, p. e3394, 2019/10/20 2019, doi: 10.21769/BioProtoc.3394.

[272] J. T. Lis and R. Schleif, "Size fractionation of double-stranded DNA by precipitation with polyethylene glycol," *Nucleic Acids Research,* vol. 2, no. 3, pp. 383-390, 1975, doi: 10.1093/nar/2.3.383.

[273] M. T. Record Jr, C. P. Woodbury, and T. M. Lohman, "Na+ effects on transitions of DNA and polynucleotides of variable linear charge density," *Biopolymers,* vol. 15, no. 5, pp. 893-915, 1976/05/01 1976, doi: https://doi.org/10.1002/bip.1976.360150507.

[274] M. A. Quail, H. Swerdlow, and D. J. Turner, "Improved Protocols for the Illumina Genome Analyzer Sequencing System," *Current Protocols in Human Genetics,* vol. 62, no. 1, pp. 18.2.1-18.2.27, 2009/07/01 2009, doi: https://doi.org/10.1002/0471142905.hg1802s62.

[275] C. Chau, G. Mohanan, I. Macaulay, P. Actis, and C. Wälti, "Automated Purification of DNA Origami with SPRI Beads (Small 20/2024)," *Small,* vol. 20, no. 20, p. 2470155, 2024/05/01 2024, doi: https://doi.org/10.1002/smll.202470155.

[276] J. F. Berengut, W. R. Berg, F. J. Rizzuto, and L. K. Lee, "Passivating Blunt-Ended Helices to Control Monodispersity and Multi-Subunit Assembly of DNA Origami Structures," *Small Structures,* vol. 5, no. 4, p. 2300441, 2024/04/01 2024, doi: https://doi.org/10.1002/sstr.202300441.

[277] Q. Xiong, O.-S. Lee, C. A. Mirkin, and G. Schatz, "Ethanol-Induced Condensation and Decondensation in DNA-Linked Nanoparticles: A

Nucleosome-like Model for the Condensed State," *Journal of the American Chemical Society,* vol. 145, no. 1, pp. 706-716, 2023/01/11 2023, doi: 10.1021/jacs.2c11834.

[278] S. He *et al.*, "DNA precipitation revisited: A quantitative analysis," *Nano Select,* vol. 3, no. 3, pp. 617-626, 2022/03/01 2022, doi: https://doi.org/10.1002/nano.202100152.

[279] P. G. Arscott, C. Ma, J. R. Wenner, and V. A. Bloomfield, "DNA condensation by cobalt hexaammine(III) in alcohol–water mixtures: Dielectric constant and other solvent effects," *Biopolymers,* vol. 36, no. 3, pp. 345-364, 1995/09/01 1995, doi: https://doi.org/10.1002/bip.360360309.

[280] A. V. Baptist and A. Heuer-Jungemann, "Lyophilization Reduces Aggregation of Three-Dimensional DNA Origami at High Concentrations," *ACS Omega,* vol. 8, no. 20, pp. 18225-18233, 2023/05/23 2023, doi: 10.1021/acsomega.3c01680.

[281] E. Enlund, S. Julin, V. Linko, and M. A. Kostiainen, "Structural stability of DNA origami nanostructures in organic solvents," *Nanoscale,* 10.1039/D4NR02185A vol. 16, no. 28, pp. 13407-13415, 2024, doi: 10.1039/D4NR02185A.

[282] J. Wang, Z. Li, and I. Willner, "Dynamic Reconfigurable DNA Nanostructures, Networks and Materials," *Angewandte Chemie International Edition,* vol. 62, no. 18, p. e202215332, 2023/04/24 2023, doi: https://doi.org/10.1002/anie.202215332.

[283] A. Rajendran, M. Endo, and H. Sugiyama, "Single-Molecule Analysis Using DNA Origami," *Angewandte Chemie International Edition,* vol. 51, no. 4, pp. 874-890, 2012/01/23 2012, doi: https://doi.org/10.1002/anie.201102113.

[284] M. Oranzie *et al.*, "Aptamer-Driven Biosensor Technology for the Quantitative Analysis of C-Reactive Protein," *ChemElectroChem,* vol. 12, no. 7, p. e202400667, 2025/04/01 2025, doi: https://doi.org/10.1002/celc.202400667.

[285] S. R. Chinnadayyala *et al.*, "Electrochemical Detection of C-Reactive Protein in Human Serum Based on Self-Assembled Monolayer-Modified Interdigitated Wave-Shaped Electrode," *Sensors*, vol. 19, no. 24, doi: 10.3390/s19245560.

[286] N. R. Sproston and J. J. Ashworth, "Role of C-Reactive Protein at Sites of Inflammation and Infection," *Frontiers in Immunology,* Review vol. Volume 9 - 2018, 2018. [Online]. Available: https://www.frontiersin.org/journals/immunology/articles/10.3389/fimmu.2018.00754.

[287] I. Smyrlaki, A. Shaw, Y. Yang, B. Shen, and B. Högberg, "Solid Phase Synthesis of DNA Nanostructures in Heavy Liquid," *Small,* vol. 19, no. 4, p. 2204513, 2023/01/01 2023, doi: https://doi.org/10.1002/smll.202204513.

[288] S. Zhao *et al.*, "Efficient Intracellular Delivery of RNase A Using DNA Origami Carriers," *ACS Applied Materials & Interfaces,* vol. 11, no. 12, pp. 11112-11118, 2019/03/27 2019, doi: 10.1021/acsami.8b21724.

[289] C. Yuan *et al.*, "Functionalized DNA Origami-Enabled Detection of Biomarkers," in *ChemBioChem* vol. 25, ed: John Wiley and Sons Inc, 2024.

[290] T. Tørring, N. V. Voigt, J. Nangreave, H. Yan, and K. V. Gothelf, "DNA origami: a quantum leap for self-assembly of complex structures," *Chemical Society Reviews,* 10.1039/C1CS15057J vol. 40, no. 12, pp. 5636-5646, 2011, doi: 10.1039/C1CS15057J.

[291] M. Wilchek and E. A. Bayer, "[2] Introduction to avidin-biotin technology," in *Methods in Enzymology*, vol. 184, M. Wilchek and E. A. Bayer Eds.: Academic Press, 1990, pp. 5-13.

[292] S. Freitag *et al.*, "X-ray crystallographic studies of streptavidin mutants binding to biotin," *Biomolecular Engineering,* vol. 16, no. 1, pp. 13-19, 1999/12/31/ 1999, doi: https://doi.org/10.1016/S1050-3862(99)00048-0.

[293] J. Ye, J. Teske, U. Kemper, and R. Seidel, "Sequential Pull-Down Purification of DNA Origami Superstructures," *Small,* vol. 17, no. 17, p. 2007218, 2021/04/01 2021, doi: https://doi.org/10.1002/smll.202007218.

[294] B. H. Northrop, S. H. Frayne, and U. Choudhary, "Thiol–maleimide “click” chemistry: evaluating the influence of solvent, initiator, and thiol on the reaction mechanism, kinetics, and selectivity," *Polymer Chemistry,* 10.1039/C5PY00168D vol. 6, no. 18, pp. 3415-3430, 2015, doi: 10.1039/C5PY00168D.

[295] D. P. Nair *et al.*, "The Thiol-Michael Addition Click Reaction: A Powerful and Widely Used Tool in Materials Chemistry," *Chemistry of Materials,* vol. 26, no. 1, pp. 724-744, 2014/01/14 2014, doi: 10.1021/cm402180t.

[296] P. Cordell, G. Carrington, A. Curd, F. Parker, D. Tomlinson, and M. Peckham, "Affimers and nanobodies as molecular probes and their applications in imaging," *Journal of Cell Science,* vol. 135, no. 14, 2022, doi: 10.1242/jcs.259168.

[297] M. B. Pepys and G. M. Hirschfield, "C-reactive protein: a critical update," *The Journal of Clinical Investigation,* vol. 111, no. 12, pp. 1805-1812, 06/15/ 2003, doi: 10.1172/JCI18921.

[298] D. Zhao, Z. R. Gregorich, and Y. Ge, "High throughput screening of disulfide-containing proteins in a complex mixture," *PROTEOMICS,* vol. 13, 2013.

[299] C. Chang, M. Isokawa, T. Funatsu, and M. Tsunoda, "Optimization of tris(2-carboxyethyl) phosphine reduction conditions for fast analysis of total biothiols in mouse serum samples," *Heliyon,* vol. 5, no. 5, p. e01598, 2019/05/01/ 2019, doi: https://doi.org/10.1016/j.heliyon.2019.e01598.

[300] S. H. Shamsuddin, D. G. Jayne, D. C. Tomlinson, M. J. McPherson, and P. A. Millner, "Selection and characterisation of Affimers specific for CEA recognition," *Scientific Reports,* vol. 11, no. 1, p. 744, 2021/01/12 2021, doi: 10.1038/s41598-020-80354-6.

[301] R. D. Smith and K. J. Light-Wahl, "The observation of non-covalent interactions in solution by electrospray ionization mass spectrometry: Promise, pitfalls and prognosis," *Biological Mass Spectrometry,* vol. 22, no. 9, pp. 493-501, 1993/09/01 1993, doi: https://doi.org/10.1002/bms.1200220902.

[302] J. M. Walker, *The Proteomics Protocols Handbook* (Springer protocol handbook). Humana Totowa, NJ, 2007, pp. XVIII, 988.

[303] E. Al-Enezi *et al.*, "Affimer-Based Europium Chelates Allow Sensitive Optical Biosensing in a Range of Human Disease Biomarkers," *Sensors*, vol. 21, no. 3, doi: 10.3390/s21030831.

[304] C. N. Yiannios and J. V. Karabinos, "Oxidation of Thiols by Dimethyl Sulfoxide," *The Journal of Organic Chemistry,* vol. 28, no. 11, pp. 3246-3248, 1963/11/01 1963, doi: 10.1021/jo01046a528.

[305] J. C. Han and G. Y. Han, "A Procedure for Quantitative Determination of Tris(2-Carboxyethyl)phosphine, an Odorless Reducing Agent More Stable and Effective Than Dithiothreitol," *Analytical Biochemistry,* vol. 220, no. 1, pp. 5-10, 1994/07/01/ 1994, doi: https://doi.org/10.1006/abio.1994.1290.

[306] G. T. Hermanson, "Chapter 3 - The Reactions of Bioconjugation," in *Bioconjugate Techniques (Third Edition)*, G. T. Hermanson Ed. Boston: Academic Press, 2013, pp. 229-258.

[307] E. Chargaff, "Chemical specificity of nucleic acids and mechanism of their enzymatic degradation," *Experientia,* vol. 6, no. 6, pp. 201-209, 1950/06/01 1950, doi: 10.1007/BF02173653.

[308] J. A. Burns, J. C. Butler, J. Moran, and G. M. Whitesides, "Selective reduction of disulfides by tris(2-carboxyethyl)phosphine," *The Journal of Organic Chemistry,* vol. 56, no. 8, pp. 2648-2650, 1991/04/01 1991, doi: 10.1021/jo00008a014.

[309] E. B. Getz, M. Xiao, T. Chakrabarty, R. Cooke, and P. R. Selvin, "A Comparison between the Sulfhydryl Reductants Tris(2-carboxyethyl)phosphine and Dithiothreitol for Use in Protein Biochemistry," *Analytical Biochemistry,* vol. 273, no. 1, pp. 73-80, 1999/08/15/ 1999, doi: https://doi.org/10.1006/abio.1999.4203.

[310] R. Kobayashi, R. Patenia, S. Ashizawa, and J. Vykoukal, "Targeted mass spectrometric analysis of N-terminally truncated isoforms generated via alternative translation initiation," *FEBS Letters,* vol. 583, no. 14, pp. 2441-2445, 2009/07/21 2009, doi: https://doi.org/10.1016/j.febslet.2009.05.042.

[311] M. Dupré, S. Cantel, J. Martinez, and C. Enjalbal, "Occurrence of C-Terminal Residue Exclusion in Peptide Fragmentation by ESI and MALDI Tandem Mass Spectrometry," *Journal of the American Society for Mass Spectrometry,* vol. 23, no. 2, pp. 330-346, 2012/02/01 2012, doi: 10.1007/s13361-011-0254-1.

[312] H. H. Nguyen *et al.*, "Long-Term Stability and Integrity of Plasmid-Based DNA Data Storage," *Polymers*, vol. 10, no. 1, doi: 10.3390/polym10010028.

[313] C. Kielar *et al.*, "On the Stability of DNA Origami Nanostructures in Low-Magnesium Buffers," *Angewandte Chemie International Edition,* vol. 57, no. 30, pp. 9470-9474, 2018/07/20 2018, doi: https://doi.org/10.1002/anie.201802890.

[314] Y. Xin, A. A. Zargariantabrizi, G. Grundmeier, and A. Keller, "Magnesium-Free Immobilization of DNA Origami Nanostructures at Mica Surfaces for Atomic Force Microscopy," *Molecules*, vol. 26, no. 16*,* doi: 10.3390/molecules26164798.

[315] R. Owczarzy, B. G. Moreira, Y. You, M. A. Behlke, and J. A. Walder, "Predicting Stability of DNA Duplexes in Solutions Containing Magnesium and Monovalent Cations," *Biochemistry,* vol. 47, no. 19, pp. 5336-5353, 2008/05/01 2008, doi: 10.1021/bi702363u.

[316] S. Manochehry, E. M. McConnell, and Y. Li, "Unraveling Determinants of Affinity Enhancement in Dimeric Aptamers for a Dimeric Protein," *Scientific Reports,* vol. 9, no. 1, p. 17824, 2019/11/28 2019, doi: 10.1038/s41598-019-54005-4.

[317] P. Zhang *et al.*, "Quantitative Measurement of Spatial Effects of DNA Origami on Molecular Binding Reactions Detected using Atomic Force Microscopy," *ACS Applied Materials & Interfaces,* vol. 11, no. 24, pp. 21973-21981, 2019/06/19 2019, doi: 10.1021/acsami.9b01691.

[318] M. Endo and H. Sugiyama, "Single-Molecule Imaging of Dynamic Motions of Biomolecules in DNA Origami Nanostructures Using High-Speed Atomic Force Microscopy," *Accounts of Chemical Research,* vol. 47, no. 6, pp. 1645-1653, 2014/06/17 2014, doi: 10.1021/ar400299m.

[319] A. Johnson, Q. Song, P. Ko Ferrigno, P. R. Bueno, and J. J. Davis, "Sensitive Affimer and Antibody Based Impedimetric Label-Free Assays for C-Reactive Protein," *Analytical Chemistry,* vol. 84, no. 15, pp. 6553-6560, 2012/08/07 2012, doi: 10.1021/ac300835b.

[320] S. Dutt, B. I. Karawdeniya, Y. M. N. D. Y. Bandara, N. Afrin, and P. Kluth, "Ultrathin, High-Lifetime Silicon Nitride Membranes for Nanopore Sensing," *Analytical Chemistry,* vol. 95, no. 13, pp. 5754-5763, 2023/4// 2023, doi: 10.1021/acs.analchem.3c00023.

[321] A. Meller, L. Nivon, E. Brandin, J. Golovchenko, and D. Branton, "Rapid nanopore discrimination between single polynucleotide molecules," in "PNAS," 2000, vol. 97. [Online]. Available: www.pnas.org

[322] H. Bayley and P. S. Cremer, "Stochastic sensors inspired by biology," *Nature,* vol. 413, no. 6852, pp. 226-230, 2001/09/01 2001, doi: 10.1038/35093038.

[323] J. Li, R. Hu, X. Li, X. Tong, D. Yu, and Q. Zhao, "Tiny protein detection using pressure through solid-state nanopores," *Electrophoresis,* vol. 38, no. 8, pp. 1130-1138, 2017/4// 2017, doi: 10.1002/elps.201600410.

[324] C. C. Chau, S. E. Radford, E. W. Hewitt, and P. Actis, "Macromolecular Crowding Enhances the Detection of DNA and Proteins by a Solid-State

Nanopore," *Nano Letters,* vol. 20, no. 7, pp. 5553-5561, 2020/7// 2020, doi: 10.1021/acs.nanolett.0c02246.

[325] C. Dekker, "Solid-state nanopores," *Nature Nanotechnology,* vol. 2, no. 4, pp. 209-215, 2007/04/01 2007, doi: 10.1038/nnano.2007.27.

[326] A. Fragasso, S. Schmid, and C. Dekker, "Comparing Current Noise in Biological and Solid-State Nanopores," *ACS Nano,* vol. 14, no. 2, pp. 1338-1349, 2020/02/25 2020, doi: 10.1021/acsnano.9b09353.

[327] S. Confederat, I. Sandei, G. Mohanan, C. Wälti, and P. Actis, "Nanopore fingerprinting of supramolecular DNA nanostructures," *Biophysical Journal,* vol. 121, no. 24, pp. 4882-4891, 2022, doi: 10.1016/j.bpj.2022.08.020.

[328] M. Raveendran, A. J. Lee, C. Wälti, and P. Actis, "Analysis of 2D DNA Origami with Nanopipettes," *ChemElectroChem,* vol. 5, no. 20, pp. 3014-3020, 2018/10/12 2018, doi: https://doi.org/10.1002/celc.201800732.

[329] Q. Shen *et al.*, "Functionalized DNA-Origami-Protein Nanopores Generate Large Transmembrane Channels with Programmable Size-Selectivity," *Journal of the American Chemical Society,* vol. 145, no. 2, pp. 1292-1300, 2023/01/18 2023, doi: 10.1021/jacs.2c11226.

[330] K. Szuttor, F. Weik, J.-N. Grad, and C. Holm, "Modeling the current modulation of bundled DNA structures in nanopores," *The Journal of Chemical Physics,* vol. 154, no. 5, p. 054901, 2021, doi: 10.1063/5.0038530.

[331] M. Wanunu, J. Sutin, B. McNally, A. Chow, and A. Meller, "DNA translocation governed by interactions with solid-state nanopores," *Biophysical Journal,* vol. 95, no. 10, pp. 4716-4725, 2008/11// 2008, doi: 10.1529/biophysj.108.140475.

[332] J. Li and D. S. Talaga, "The distribution of DNA translocation times in solid-state nanopores," *Journal of Physics Condensed Matter,* vol. 22, no. 45, 2010/11// 2010, doi: 10.1088/0953-8984/22/45/454129.

[333] L. Zhu, Z. Zhang, and Q. Liu, "Deformation-Mediated Translocation of DNA Origami Nanoplates through a Narrow Solid-State Nanopore," *Analytical Chemistry,* vol. 92, no. 19, pp. 13238-13245, 2020/10// 2020, doi: 10.1021/acs.analchem.0c02396.

[334] I. Kushner and J. A. Somerville, "Estimation of the molecular size of C-reactive protein and Cx-reactive protein in serum," *Biochimica et Biophysica Acta (BBA) - Protein Structure,* vol. 207, no. 1, pp. 105-114, 1970/04/28/ 1970, doi: https://doi.org/10.1016/0005-2795(70)90140-6.

[335] M. K. Sarangi *et al.*, "Evidence for a bind-then-bend mechanism for architectural DNA binding protein yNhp6A," *Nucleic Acids Research,* vol. 47, no. 6, pp. 2871-2883, 2019/4// 2019, doi: 10.1093/nar/gkz022.

[336] D. N. Kim, F. Kilchherr, H. Dietz, and M. Bathe, "Quantitative prediction of 3D solution shape and flexibility of nucleic acid nanostructures," *Nucleic Acids*

Research, vol. 40, no. 7, pp. 2862-2868, 2012/4// 2012, doi: 10.1093/nar/gkr1173.

[337] H. Chen, T. W. Weng, M. M. Riccitelli, Y. Cui, J. Irudayaraj, and J. H. Choi, "Understanding the mechanical properties of DNA origami tiles and controlling the kinetics of their folding and unfolding reconfiguration," *Journal of the American Chemical Society,* vol. 136, no. 19, pp. 6995-7005, 2014/5// 2014, doi: 10.1021/ja500612d.

[338] J. Zhou and J. Rossi, "Aptamers as targeted therapeutics: current potential and challenges," *Nature Reviews Drug Discovery,* vol. 16, no. 3, pp. 181-202, 2017/03/01 2017, doi: 10.1038/nrd.2016.199.

[339] I. Mela *et al.*, "DNA Nanostructures for Targeted Antimicrobial Delivery," *Angewandte Chemie International Edition,* vol. 59, no. 31, pp. 12698-12702, 2020/07/27 2020, doi: https://doi.org/10.1002/anie.202002740.

[340] G. R. Heath, E. Micklethwaite, and T. M. Storer, "NanoLocz: Image Analysis Platform for AFM, High-Speed AFM, and Localization AFM," *Small Methods,* vol. 8, no. 10, p. 2301766, 2024/10/01 2024, doi: https://doi.org/10.1002/smtd.202301766.

[341] J. Yang, N. Zhao, Y. Liang, Z. Lu, and C. Zhang, "Structure-flexible DNA origami translocation through a solid-state nanopore," *RSC Advances,* vol. 11, no. 38, pp. 23471-23476, 2021/7// 2021, doi: 10.1039/d1ra04267j.

[342] A. Khoshouei *et al.*, "Designing Rigid DNA Origami Templates for Molecular Visualization Using Cryo-EM," *Nano Letters,* vol. 24, no. 16, pp. 5031-5038, 2024/04/24 2024, doi: 10.1021/acs.nanolett.4c00915.

Appendix A : Appendix for Chapter 3

.1 caDNAno file

The caDNAno file of the DNA origami tile (4FST) used in the SPRI purification chapter.

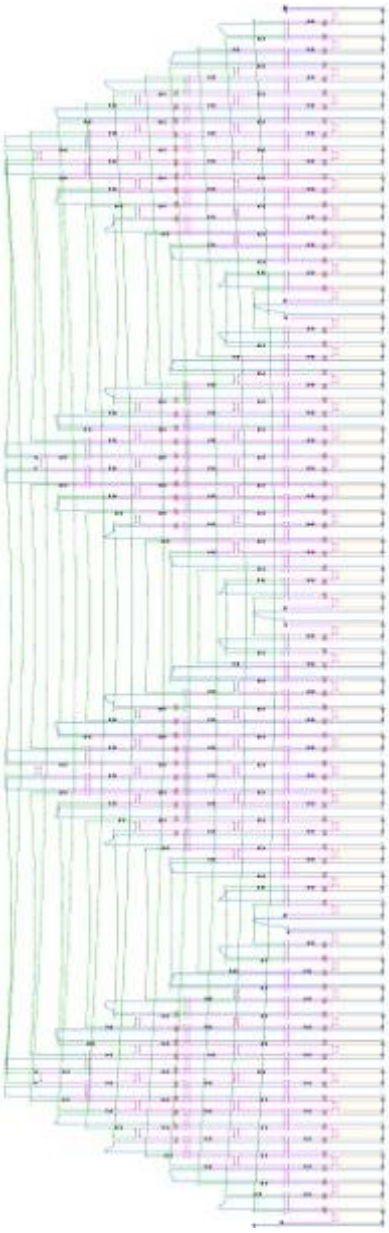

Figure 0:1 caDNAno file image of DNA origami tile used in Chapter 3 for SPRI purification study.

Sequence of M13mp18 (Scaffold) used for folding origami

AATGCTACTACTATTAGTAGAATTGATGCCACCTTTTCAGCTCGCGCCCCAAATGA
AAATATAGCTAAACAGGTTATTGACCATTTGCGAAATGTATCTAATGGTCAAACTAA
ATCTACTCGTTCGCAGAATTGGGAATCAACTGTTATATGGAATGAAACTTCCAGAC
ACCGTACTTTAGTTGCATATTTAAAACATGTTGAGCTACAGCATTATATTCAGCAAT

TAAGCTCTAAGCCATCCGCAAAAATGACCTCTTATCAAAAGGAGCAATTAAAGGTA
CTCTCTAATCCTGACCTGTTGGAGTTTGCTTCCGGTCTGGTTCGCTTTGAAGCTCG
AATTAAAACGCGATATTTGAAGTCTTTCGGGCTTCCTCTTAATCTTTTTGATGCAAT
CCGCTTTGCTTCTGACTATAATAGTCAGGGTAAAGACCTGATTTTTGATTTATGGT
CATTCTCGTTTTCTGAACTGTTTAAAGCATTTGAGGGGGATTCAATGAATATTTATG
ACGATTCCGCAGTATTGGACGCTATCCAGTCTAAACATTTTACTATTACCCCCTCT
GGCAAAACTTCTTTTGCAAAAGCCTCTCGCTATTTTGGTTTTTATCGTCGTCTGGTA
AACGAGGGTTATGATAGTGTTGCTCTTACTATGCCTCGTAATTCCTTTTGGCGTTA
TGTATCTGCATTAGTTGAATGTGGTATTCCTAAATCTCAACTGATGAATCTTTCTAC
CTGTAATAATGTTGTTCCGTTAGTTCGTTTTATTAACGTAGATTTTTCTTCCCAACG
TCCTGACTGGTATAATGAGCCAGTTCTTAAAATCGCATAAGGTAATTCACAATGAT
TAAAGTTGAAATTAAACCATCTCAAGCCCAATTTACTACTCGTTCTGGTGTTTCTCG
TCAGGGCAAGCCTTATTCACTGAATGAGCAGCTTTGTTACGTTGATTTGGGTAATG
AATATCCGGTTCTTGTCAAGATTACTCTTGATGAAGGTCAGCCAGCCTATGCGCCT
GGTCTGTACACCGTTCATCTGTCCTCTTTCAAAGTTGGTCAGTTCGGTTCCCTTAT
GATTGACCGTCTGCGCCTCGTTCCGGCTAAGTAACATGGAGCAGGTCGCGGATTT
CGACACAATTTATCAGGCGATGATACAAATCTCCGTTGTACTTTGTTTCGCGCTTG
GTATAATCGCTGGGGGTCAAAGATGAGTGTTTTAGTGTATTCTTTTGCCTCTTTCG
TTTTAGGTTGGTGCCTTCGTAGTGGCATTACGTATTTTACCCGTTTAATGGAAACTT
CCTCATGAAAAAGTCTTTAGTCCTCAAAGCCTCTGTAGCCGTTGCTACCCTCGTTC
CGATGCTGTCTTTCGCTGCTGAGGGTGACGATCCCGCAAAAGCGGCCTTTAACTC
CCTGCAAGCCTCAGCGACCGAATATATCGGTTATGCGTGGGCGATGGTTGTTGTC
ATTGTCGGCGCAACTATCGGTATCAAGCTGTTTAAGAAATTCACCTCGAAAGCAAG
CTGATAAACCGATACAATTAAAGGCTCCTTTTGGAGCCTTTTTTTTGGAGATTTTCA
ACGTGAAAAAATTATTATTCGCAATTCCTTTAGTTGTTCCTTTCTATTCTCACTCCG
CTGAAACTGTTGAAAGTTGTTTAGCAAAATCCCATACAGAAAATTCATTTACTAACG
TCTGGAAAGACGACAAAACTTTAGATCGTTACGCTAACTATGAGGGCTGTCTGTG
GAATGCTACAGGCGTTGTAGTTTGTACTGGTGACGAAACTCAGTGTTACGGTACA
TGGGTTCCTATTGGGCTTGCTATCCCTGAAAATGAGGGTGGTGGCTCTGAGGGTG
GCGGTTCTGAGGGTGGCGGTTCTGAGGGTGGCGGTACTAAACCTCCTGAGTACG
GTGATACACCTATTCCGGGCTATACTTATATCAACCCTCTCGACGGCACTTATCCG
CCTGGTACTGAGCAAAACCCCGCTAATCCTAATCCTTCTCTTGAGGAGTCTCAGC
CTCTTAATACTTTCATGTTTCAGAATAATAGGTTCCGAAATAGGCAGGGGGCATTA
ACTGTTTATACGGGCACTGTTACTCAAGGCACTGACCCCGTTAAAACTTATTACCA
GTACACTCCTGTATCATCAAAAGCCATGTATGACGCTTACTGGAACGGTAAATTCA
GAGACTGCGCTTTCCATTCTGGCTTTAATGAGGATTTATTTGTTTGTGAATATCAAG
GCCAATCGTCTGACCTGCCTCAACCTCCTGTCAATGCTGGCGGCGGCTCTGGTG
GTGGTTCTGGTGGCGGCTCTGAGGGTGGTGGCTCTGAGGGTGGCGGTTCTGAG

GGTGGCGGCTCTGAGGGAGGCGGTTCCGGTGGTGGCTCTGGTTCCGGTGATTTT
GATTATGAAAAGATGGCAAACGCTAATAAGGGGGCTATGACCGAAAATGCCGATG
AAAACGCGCTACAGTCTGACGCTAAAGGCAAACTTGATTCTGTCGCTACTGATTAC
GGTGCTGCTATCGATGGTTTCATTGGTGACGTTTCCGGCCTTGCTAATGGTAATG
GTGCTACTGGTGATTTTGCTGGCTCTAATTCCCAAATGGCTCAAGTCGGTGACGG
TGATAATTCACCTTTAATGAATAATTTCCGTCAATATTTACCTTCCCTCCCTCAATC
GGTTGAATGTCGCCCTTTTGTCTTTGGCGCTGGTAAACCATATGAATTTTCTATTG
ATTGTGACAAAATAAACTTATTCCGTGGTGTCTTTGCGTTTCTTTTATATGTTGCCA
CCTTTATGTATGTATTTTCTACGTTTGCTAACATACTGCGTAATAAGGAGTCTTAAT
CATGCCAGTTCTTTTGGGTATTCCGTTATTATTGCGTTTCCTCGGTTTCCTTCTGGT
AACTTTGTTCGGCTATCTGCTTACTTTTCTTAAAAAGGGCTTCGGTAAGATAGCTAT
TGCTATTTCATTGTTTCTTGCTCTTATTATTGGGCTTAACTCAATTCTTGTGGGTTAT
CTCTCTGATATTAGCGCTCAATTACCCTCTGACTTTGTTCAGGGTGTTCAGTTAATT
CTCCCGTCTAATGCGCTTCCCTGTTTTTATGTTATTCTCTCTGTAAAGGCTGCTATT
TTCATTTTTGACGTTAAACAAAAAATCGTTTCTTATTTGGATTGGGATAAATAATATG
GCTGTTTATTTTGTAACTGGCAAATTAGGCTCTGGAAAGACGCTCGTTAGCGTTGG
TAAGATTCAGGATAAAATTGTAGCTGGGTGCAAAATAGCAACTAATCTTGATTTAA
GGCTTCAAAACCTCCCGCAAGTCGGGAGGTTCGCTAAAACGCCTCGCGTTCTTAG
AATACCGGATAAGCCTTCTATATCTGATTTGCTTGCTATTGGGCGCGGTAATGATT
CCTACGATGAAAATAAAAACGGCTTGCTTGTTCTCGATGAGTGCGGTACTTGGTTT
AATACCCGTTCTTGGAATGATAAGGAAAGACAGCCGATTATTGATTGGTTTCTACA
TGCTCGTAAATTAGGATGGGATATTATTTTTCTTGTTCAGGACTTATCTATTGTTGA
TAAACAGGCGCGTTCTGCATTAGCTGAACATGTTGTTTATTGTCGTCGTCTGGACA
GAATTACTTTACCTTTTGTCGGTACTTTATATTCTCTTATTACTGGCTCGAAAATGC
CTCTGCCTAAATTACATGTTGGCGTTGTTAAATATGGCGATTCTCAATTAAGCCCT
ACTGTTGAGCGTTGGCTTTATACTGGTAAGAATTTGTATAACGCATATGATACTAAA
CAGGCTTTTTCTAGTAATTATGATTCCGGTGTTTATTCTTATTTAACGCCTTATTTAT
CACACGGTCGGTATTTCAAACCATTAAATTTAGGTCAGAAGATGAAATTAACTAAA
ATATATTTGAAAAAGTTTTCTCGCGTTCTTTGTCTTGCGATTGGATTTGCATCAGCA
TTTACATATAGTTATATAACCCAACCTAAGCCGGAGGTTAAAAAGGTAGTCTCTCA
GACCTATGATTTTGATAAATTCACTATTGACTCTTCTCAGCGTCTTAATCTAAGCTA
TCGCTATGTTTTCAAGGATTCTAAGGGAAAATTAATTAATAGCGACGATTTACAGAA
GCAAGGTTATTCACTCACATATATTGATTTATGTACTGTTTCCATTAAAAAAGGTAA
TTCAAATGAAATTGTTAAATGTAATTAATTTTGTTTTCTTGATGTTTGTTTCATCATC
TTCTTTTGCTCAGGTAATTGAAATGAATAATTCGCCTCTGCGCGATTTTGTAACTTG
GTATTCAAAGCAATCAGGCGAATCCGTTATTGTTTCTCCCGATGTAAAAGGTACTG
TTACTGTATATTCATCTGACGTTAAACCTGAAAATCTACGCAATTTCTTTATTTCTGT
TTTACGTGCAAATAATTTTGATATGGTAGGTTCTAACCCTTCCATTATTCAGAAGTA

TAATCCAAACAATCAGGATTATATTGATGAATTGCCATCATCTGATAATCAGGAATA
TGATGATAATTCCGCTCCTTCTGGTGGTTTCTTTGTTCCGCAAAATGATAATGTTAC
TCAAACTTTTAAAATTAATAACGTTCGGGCAAAGGATTTAATACGAGTTGTCGAATT
GTTTGTAAAGTCTAATACTTCTAAATCCTCAAATGTATTATCTATTGACGGCTCTAA
TCTATTAGTTGTTAGTGCTCCTAAAGATATTTTAGATAACCTTCCTCAATTCCTTTCA
ACTGTTGATTTGCCAACTGACCAGATATTGATTGAGGGTTTGATATTTGAGGTTCA
GCAAGGTGATGCTTTAGATTTTTCATTTGCTGCTGGCTCTCAGCGTGGCACTGTTG
CAGGCGGTGTTAATACTGACCGCCTCACCTCTGTTTTATCTTCTGCTGGTGGTTCG
TTCGGTATTTTTAATGGCGATGTTTTAGGGCTATCAGTTCGCGCATTAAAGACTAA
TAGCCATTCAAAAATATTGTCTGTGCCACGTATTCTTACGCTTTCAGGTCAGAAGG
GTTCTATCTCTGTTGGCCAGAATGTCCCTTTTATTACTGGTCGTGTGACTGGTGAA
TCTGCCAATGTAAATAATCCATTTCAGACGATTGAGCGTCAAAATGTAGGTATTTC
CATGAGCGTTTTTCCTGTTGCAATGGCTGGCGGTAATATTGTTCTGGATATTACCA
GCAAGGCCGATAGTTTGAGTTCTTCTACTCAGGCAAGTGATGTTATTACTAATCAA
AGAAGTATTGCTACAACGGTTAATTTGCGTGATGGACAGACTCTTTTACTCGGTGG
CCTCACTGATTATAAAAACACTTCTCAGGATTCTGGCGTACCGTTCCTGTCTAAAA
TCCCTTTAATCGGCCTCCTGTTTAGCTCCCGCTCTGATTCTAACGAGGAAAGCAC
GTTATACGTGCTCGTCAAAGCAACCATAGTACGCGCCCTGTAGCGGCGCATTAAG
CGCGGCGGGTGTGGTGGTTACGCGCAGCGTGACCGCTACACTTGCCAGCGCCC
TAGCGCCCGCTCCTTTCGCTTTCTTCCCTTCCTTTCTCGCCACGTTCGCCGGCTTT
CCCCGTCAAGCTCTAAATCGGGGGCTCCCTTTAGGGTTCCGATTTAGTGCTTTAC
GGCACCTCGACCCCAAAAAACTTGATTTGGGTGATGGTTCACGTAGTGGGCCATC
GCCCTGATAGACGGTTTTTCGCCCTTTGACGTTGGAGTCCACGTTCTTTAATAGTG
GACTCTTGTTCCAAACTGGAACAACACTCAACCCTATCTCGGGCTATTCTTTTGAT
TTATAAGGGATTTTGCCGATTTCGGAACCACCATCAAACAGGATTTTCGCCTGCTG
GGGCAAACCAGCGTGGACCGCTTGCTGCAACTCTCTCAGGGCCAGGCGGTGAAG
GGCAATCAGCTGTTGCCCGTCTCACTGGTGAAAAGAAAAACCACCCTGGCGCCCA
ATACGCAAACCGCCTCTCCCCGCGCGTTGGCCGATTCATTAATGCAGCTGGCACG
ACAGGTTTCCCGACTGGAAAGCGGGCAGTGAGCGCAACGCAATTAATGTGAGTTA
GCTCACTCATTAGGCACCCCAGGCTTTACACTTTATGCTTCCGGCTCGTATGTTGT
GTGGAATTGTGAGCGGATAACAATTTCACACAGGAAACAGCTATGACCATGATTAC
GAATTCGAGCTCGGTACCCGGGGATCCTCTAGAGTCGACCTGCAGGCATGCAAG
CTTGGCACTGGCCGTCGTTTTACAACGTCGTGACTGGGAAAACCCTGGCGTTACC
CAACTTAATCGCCTTGCAGCACATCCCCCTTTCGCCAGCTGGCGTAATAGCGAAG
AGGCCCGCACCGATCGCCCTTCCCAACAGTTGCGCAGCCTGAATGGCGAATGGC
GCTTTGCCTGGTTTCCGGCACCAGAAGCGGTGCCGGAAAGCTGGCTGGAGTGCG
ATCTTCCTGAGGCCGATACTGTCGTCGTCCCCTCAAACTGGCAGATGCACGGTTA
CGATGCGCCCATCTACACCAACGTGACCTATCCCATTACGGTCAATCCGCCGTTT

GTTCCCACGGAGAATCCGACGGGTTGTTACTCGCTCACATTTAATGTTGATGAAA
GCTGGCTACAGGAAGGCCAGACGCGAATTATTTTTGATGGCGTTCCTATTGGTTA
AAAAATGAGCTGATTTAACAAAAATTTAATGCGAATTTTAACAAAATATTAACGTTTA
CAATTTAAATATTTGCTTATACAATCTTCCTGTTTTTGGGGCTTTTCTGATTATCAAC
CGGGGTACATATGATTGACATGCTAGTTTTACGATTACCGTTCATCGATTCTCTTG
TTTGCTCCAGACTCTCAGGCAATGACCTGATAGCCTTTGTAGATCTCTCAAAAATA
GCTACCCTCTCCGGCATTAATTTATCAGCTAGAACGGTTGAATATCATATTGATGG
TGATTTGACTGTCTCCGGCCTTTCTCACCCTTTTGAATCTTTACCTACACATTACTC
AGGCATTGCATTTAAAATATATGAGGGTTCTAAAAATTTTTATCCTTGCGTTGAAAT
AAAGGCTTCTCCCGCAAAAGTATTACAGGGTCATAATGTTTTTGGTACAACCGATT
TAGCTTTATGCTCTGAGGCTTTATTGCTTAATTTTGCTAATTCTTTGCCTTGCCTGT
ATGATTTATTGGATGTT

.2 Quantification of intact and broken origami

Quantification of intact DNA origami and broken origami based on the rules outlined in materials and method. Figure below (Figure 0:2)

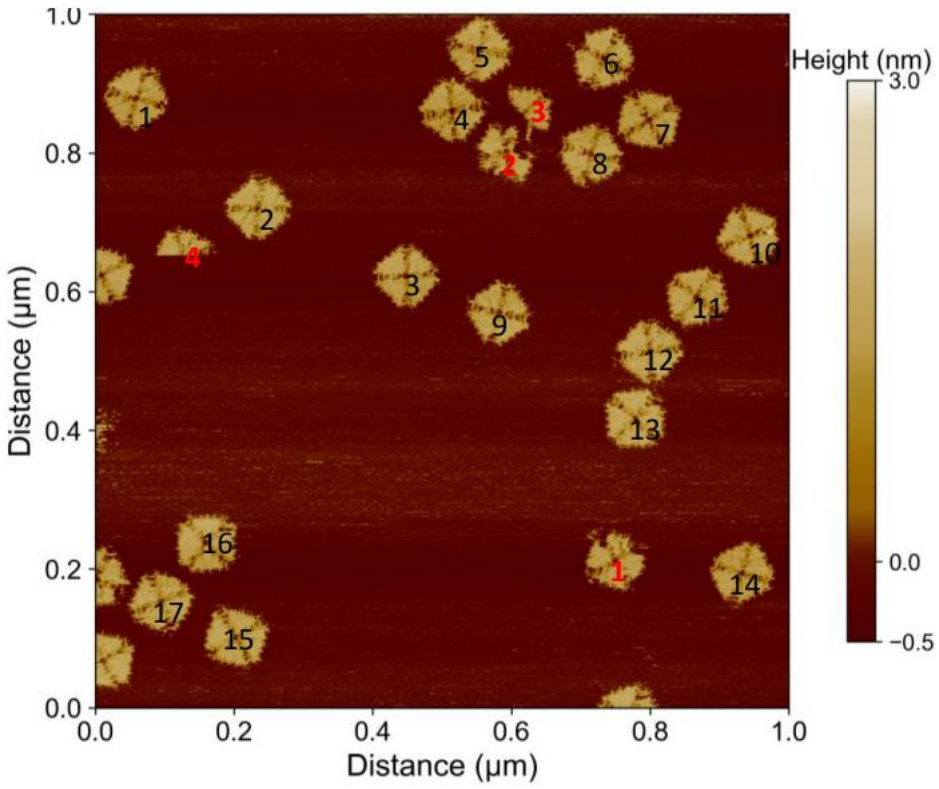

Figure 0:2 AFM image of example demonstrating how counting of intact and broken origami was done.

Appendix A :Appendix for Chapter 4

.1 Mass Spectrometry analysis in phosphate buffer

Mass spectrometry was carried out for detecting affimer-oligonucleotide formation in 40 mM phosphate buffer.

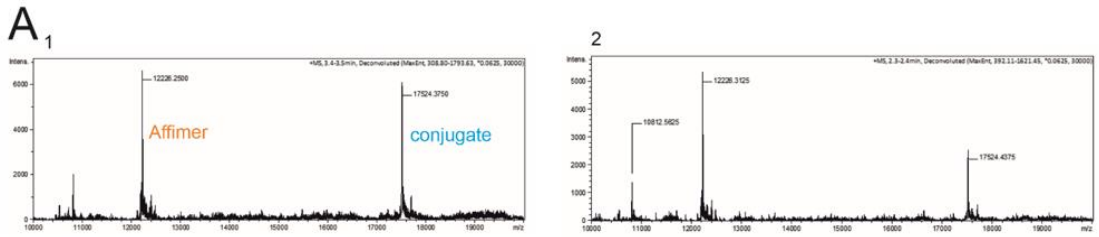

Figure 0:1 Mass spectra of affimer conjugate formation in 40 mM phosphate buffer.

.2 SDS-PAGE analysis of purified Affimer-oligonucleotide

Repeat of SDS-PAGE gel done with sample affimer-oligonucleotide purified after Ni-NTA chromatography. The E1-E5 demonstrates subsequent elution. Few proportions of monomer and dimer exists in the gel lanes. This demonstrates the reproducibility of Affimer-oligoucleotide conjugate.

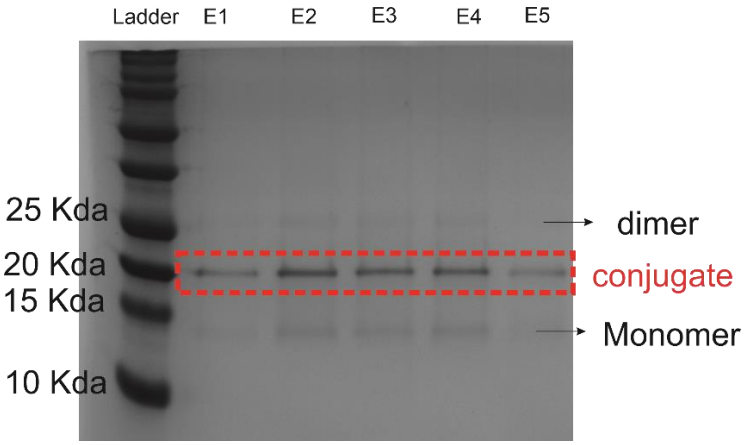

Figure 0:2 SDS PAGE gel of purified affimer-oligonucleotide. Lane 1 – ladder, Lane 2-6 – multiple rounds of elutions during purification.

Appendix A :Appendix for Chapter 5

.1 caDNAno file

caDNAno file image for 4FSF origami frame used in Chapter 4 for functionalisation of affimer and CRP.

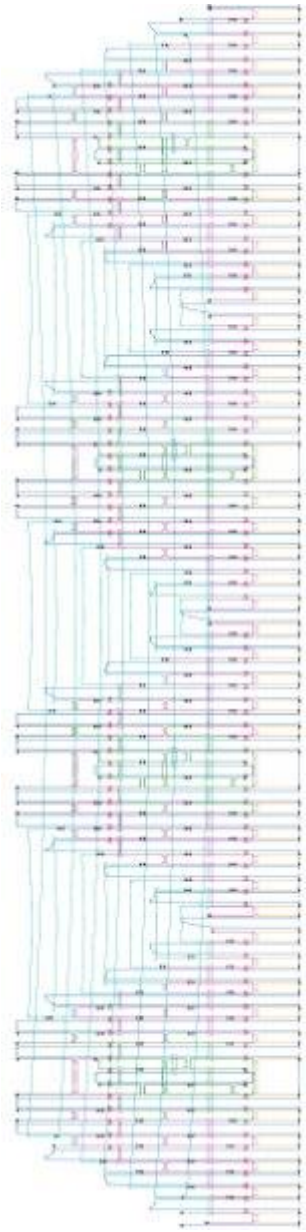

Figure 0:1 caDNAno image for 4FSF origami frame used for functionalisation studies.

.2 AFM Images of streptavidin functionalisation to 4FSF

Additional AFM images for 4FSF frame functionalised with streptavidin via 4 binding points (4 biotins).

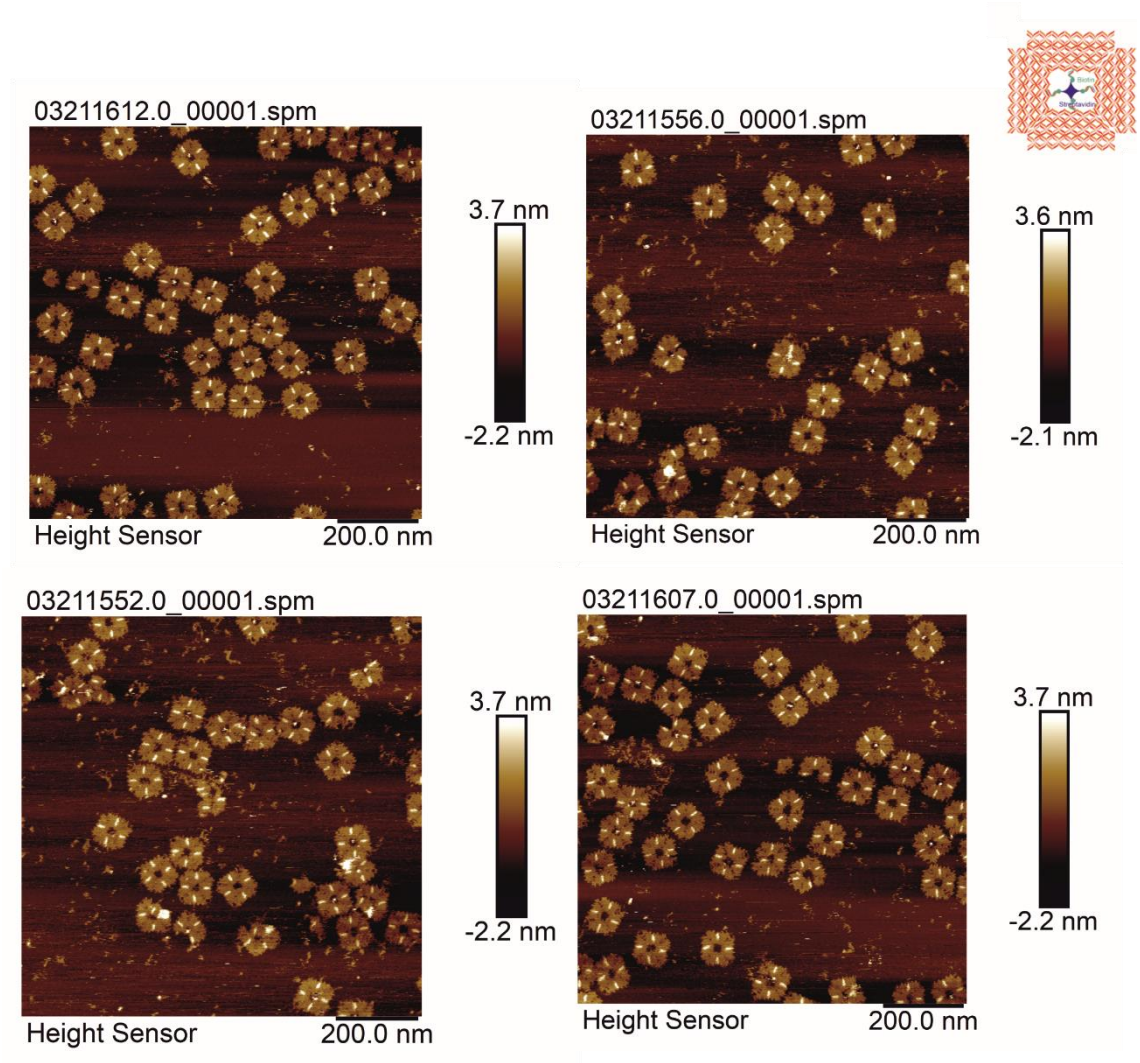

Figure 0:2 AFM images of 4FSF origami frame functionalised with streptavidin via four biotins.

Additional AFM images for 4FSF frame functionalised with streptavidin via 2 binding points (2 biotins).

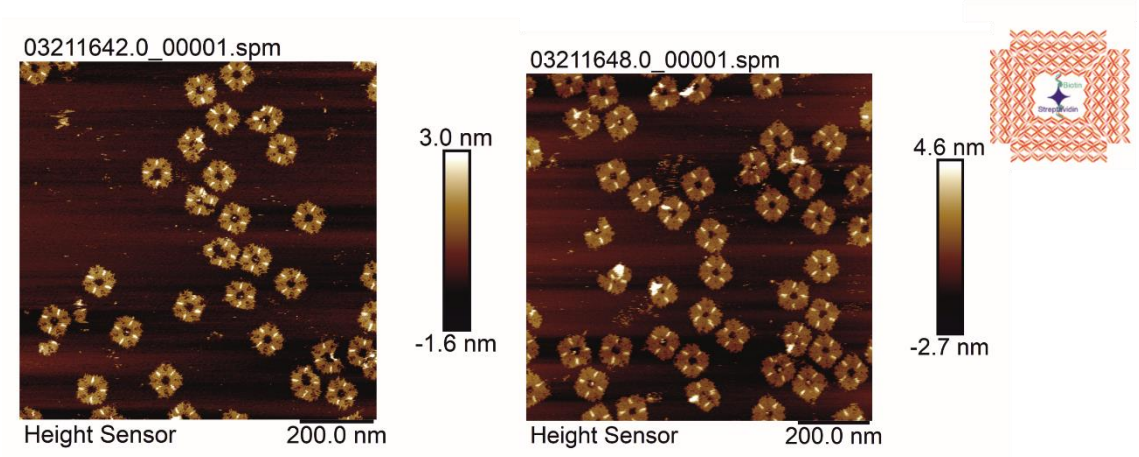

Figure 0:3 AFM images of 4FSF origami attached with streptavidin via 2 binding sites (2 biotins)

.3 AFM Images of CRP functionalisation to 4FSF

Examples of quantification of CRP attachment to DNA origami. This is done based on the rules outlined in Chapter 2 (materials and method).

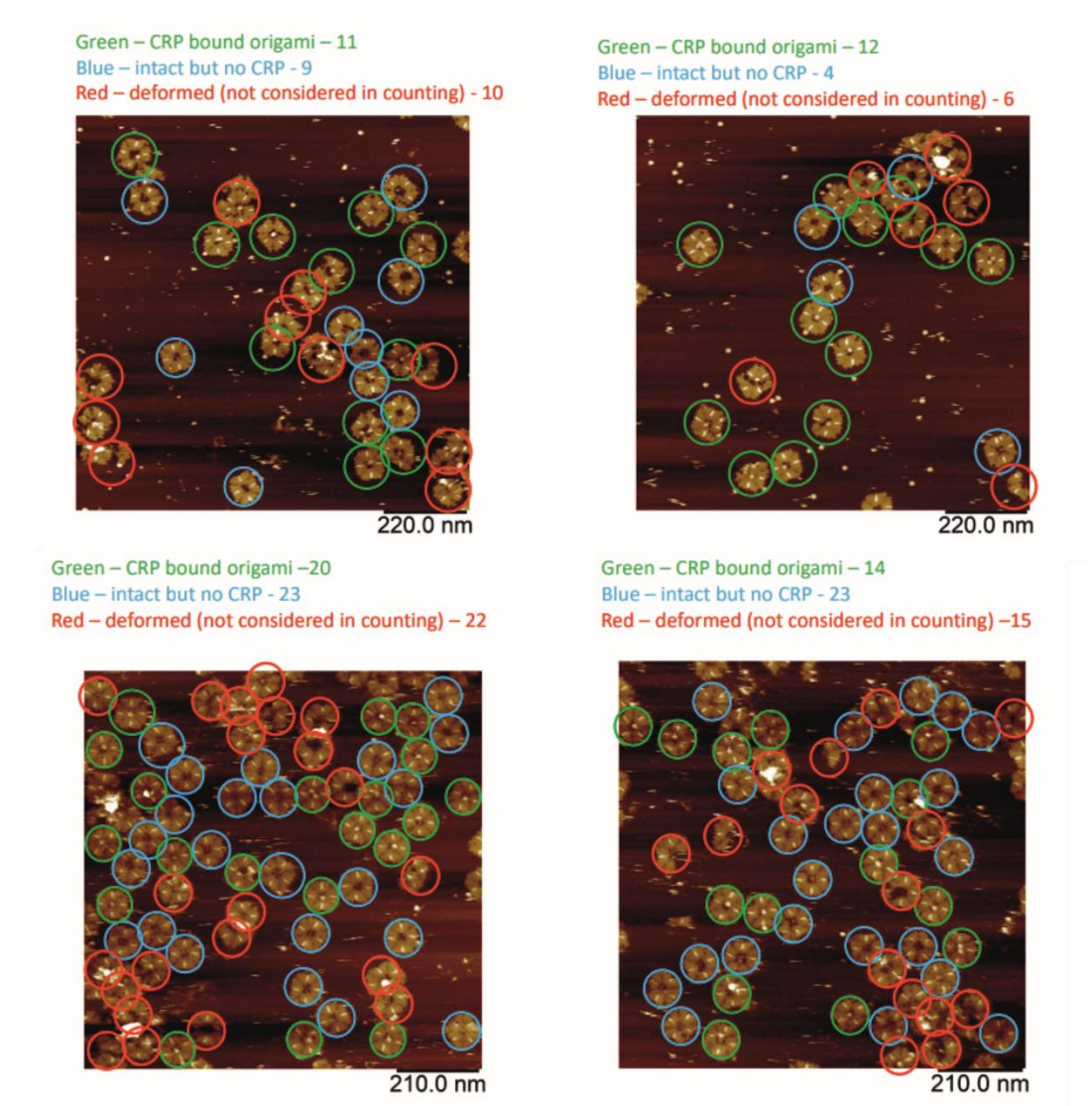

Figure 0:4 Quantification of CRP bound to 4FSF origami.

Appendix A :Appendix for Chapter 6

.1 SEM analysis

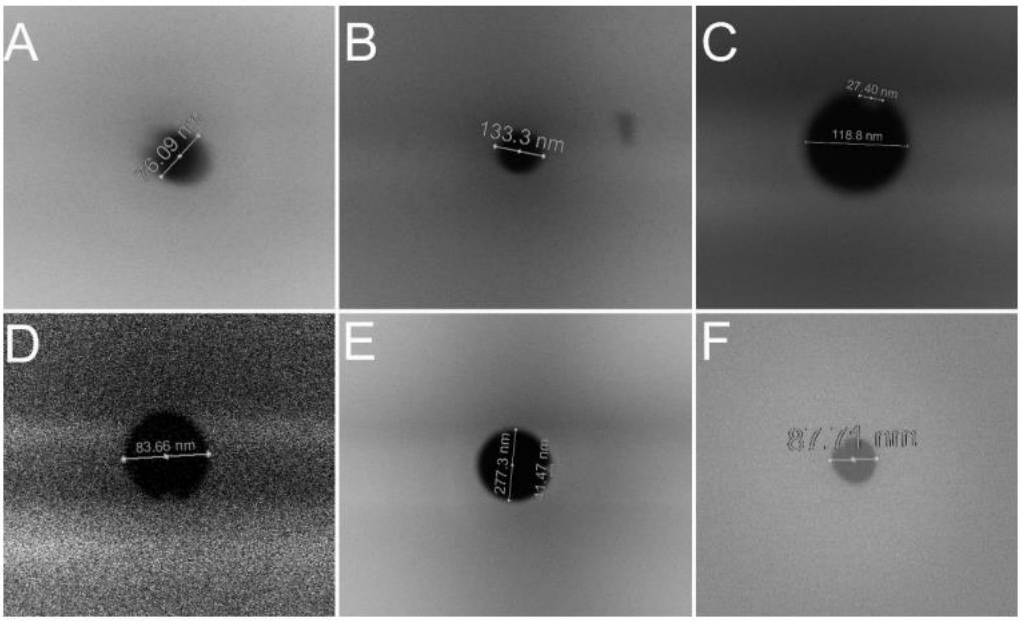

Figure 0:1 SEM images of nanopipettes pulled with different parameters.

Pulling parameters for program A for quartz capillaries with inner diameter 0.5 mm and outer diameter 1.0 mm.

Heat	Filament	Velocity	Delay	Pull
750	4	30	140	90
620	3	40	130	150

Table 0-1 Pulling Parameters for nanopipette.

The only difference applied was in the heat parameter for the other pipettes. The changes in heat applied are:

B	600
C	595
D	550
E	595

F	610

Table 0-2 Changes in the heat parameter in line 2 for producing different size of nanopores.

.2 Nanopore optimisation for translocation of 4FSF origami with affimers

I optimised the nanopipette parameters to differentiate affimer bound to 4FSF DNA origami frame. For this, I first pulled a pipette with program number 64, then changed the parameters as shown in the table below.

+10% heat -10% pull (Pgm 48)	+10% pull (Pgm 23)	+10% heat +10% pull (Pgm 52)
-10% heat (Pgm 30)	Pgm 64	+10% heat (Pgm 31)
-10% heat +10% pull (Pgm 54)	-10% pull (pgm 29)	-10% heat -10% pull (Pgm 60)

Table 0-3 Table representing the different programs used for optimisation of right nanopore for discrimination of number of affimers.

Heat	Filament	Velocity	Delay	Pull
750	4	30	150	80
650	3	40	135	149

Table 0-4 Table representing the parameters for program no. 64.

Program no.	parameters	Pull time	Resistance in 0.1 M KCl	Resistance in 35K 50% PEG, 0.1 M KCl
64	750 4 30 150 80 650 3 40 135 149	16s	67.7 MΩ	177 MΩ
23	750 4 30 150 80 650 3 40 135 164	17s	39 MΩ	200 MΩ
29	750 4 30 150 80 650 3 40 135 134	16s	55 MΩ	130 MΩ
30	750 4 30 150 80 585 3 40 135 149		26 MΩ	99 MΩ
31	750 4 30 150 80 715 3 40 135 149	14s	158 MΩ	245 MΩ
48	750 4 30 150 80 715 3 40 135 134	17s	70 MΩ	153 MΩ
52	750 4 30 150 80 715 3 40 135 164	17.4s	148 MΩ	270 MΩ
54	750 4 30 150 80 585 3 40 135 164	18.7s	45.5 MΩ	148 MΩ
60	750 4 30 150 80 585 3 40 135 134		48.8 MΩ	152 MΩ

Table 0-5 Table representing the parameters used for pulling nanopipettes with different programs. The pull time is shown in column 3, resistance in 0.1 M KCl in column 4, and resistance in 50% 35K PEG, 0.1 M KCl in column 5.

For the optimisation, I chose 4FSF origami with 10 affimers as I know it produces a percentage of around ~70% in range 2. Then I extracted the peak area followed by bootstrapping analysis to obtain the percentage of origami population in range 2 for 4FSF + 10 Affimers translocated through each of the programs. I noticed that the percentage

in range 2 is 69.5 when 4FSF + 10 Affimers were translocated through nanopore pulled with program 31. The percentage of origami population in range 2 for 4FSF + 10 affimers translocated through any other program is lower than 69.5 %. This confirms the importance of validating the pore parameters and choosing the right program to pull the pipettes to have the right pore characteristics. The translocation of the same construct through different pipettes interestingly generated different population percentage indicating different behaviour while translocation.

Program	Range 1	Range 2
64	59.9	39.9
23	68.7	31.2
29	74	25.8
30	56.8	43
31	30	**69.7**
48	77.3	22.6
52	87.4	12.5
54	61.4	38.5
60	52.4	47.5

Table 0-6 Table demonstrating the percentage of origami in range 1 and 2 for the same construct (4FSF + 10 Affimers) translocated through nanopores pulled with different parameters.